Sorbonne Université

Ecole doctorale 397 Physique et Chimie des Matériaux

UMR 7588 : Institut des NanoSciences de Paris

Study of (C20mim) + (NTf2) - ionic liquid Langmuir films mixed with graphene oxide sheets or deposited on aqueous gold ion subphases and irradiated by grazing incidence X-rays

Par Helen IBRAHIM

Thèse de doctorat de Physico-chimie des matériaux

Dirigée par Michel Goldmann et François Muller

Présentée et soutenue publiquement le 18 décembre

Devant un jury composé de :

Mme Sophie Cantin-Rivière	Examinateur
M. Eduardo Filipe	Examinateur
M. Benoît Forget	Président
Mme Marianne Impéror	Rapporteur
Mme Fabienne Testard	Rapporteur
M. Michel Goldmann	Directeur de thèse
M. François Muller	Co-directeur de thèse

Acknowledgements

Cette thèse a été réalisée au sein de l'équipe PHYSUF qui fait partie de l'Institut des Nanosciences de Paris (INSP) et en collaboration avec l'Ecole Centrale d'Electronique (ECE). Je tiens à remercier ces deux instituts de m'avoir donné la chance de me joindre à cette aventure. La recherche est loin d'être une activité individuelle. Sans le soutien de mes superviseurs, de mes collègues, de mes amis et de ma famille, je n'aurais pas pu accomplir ce travail.

Je tiens en premier lieu à remercier les membres du jury, qui m'ont fait l'honneur d'étudier mon travail : Marianne Impéror, Fabienne Testard, Sophie Cantin-Rivière, Benoît Forget et Eduardo Filipe. Je leur suis très reconnaissante de l'intérêt qu'ils ont porté à ma thèse.

Je tiens ensuite à remercier mes deux directeurs de thèse, Michel Goldmann et François Muller. Michel étais le directeur avec lequel tout doctorant souhaite travailler. Je le remercie de sa disponibilité et de sa patience pour m'expliquer les théories, même pour la énième fois! Je le serai toujours reconnaissante pour ce que j'ai appris de nos échanges culturels, historiques, politiques... Nos discussions ont contribué à mon épanouissement tant sur le plan scientifique que personnel. Un grand merci à François, mon Co-directeur de thèse. Merci pour sa patience et son aide pendant ces trois années. Merci pour ses conseils sur l'enseignement à l'ECE.

Je tiens également à remercier toute l'équipe de l'INSP, en particulier Denis Limagne et Marie-Claude. Merci à Denis pour son aide et sa patience face à mon utilisation maladroite des appareils électroniques. Merci à Marie-Claude pour son soutien moral, sa gentillesse et sa bonne compagnie. Je profite également pour remercier Philippe Fontaine et Arnaud Hemmerle pour leur disponibilité et leur présence durant les expériences au synchrotron SOLEIL.

Ces années de thèse n'auraient pas été aussi agréables sans mes amis multinationaux du laboratoire: Tomas, Pedro, Haifa et Angeline. J'estime avoir eu beaucoup de la chance de faire leur connaissance et d'avoir partagé avec eux de beaux souvenirs pour l'éternité. Je leur remercie pour le soutien qu'ils m'ont apporté au quotidien. Merci pour les moments de fous rires, les discussions mouvementées et pour les soirées (même si elles ont eu lieu la plupart du temps chez moi et que j'étais votre chef libanaise).

Mon séjour en France ainsi que le déroulement de ma thèse auraient été beaucoup plus compliqués sans le soutien de ma deuxième famille, la famille Tarabay. Merci infiniment à Nawal, Tony, Joseph, Eliana, Céline, Pierre, et Julien. Je leur serai toute ma vie reconnaissante.

Merci à mes deux amies avec lesquelles nous nous sommes accompagnées depuis notre licence de physique jusqu'au doctorat Mackrine et Carine (P.S. : Mackrine est aussi mon amie d'enfance). Santé à de nombreuses autres années de succès pleines de soirées de folies!

Merci à ma famille. Merci de toujours croire en moi et de la liberté qu'elle m'a donnée. Sans son soutien, sa bienveillance et ses encouragements, rien n'aurait été possible. Enfin merci à Andrew pour tout.

Contents

Abbreviations and acronyms

Experimental techniques

LB Langmuir-Blodgett

ILS Inverse Langmuir-Schaefer.

GIXD Grazing Incidence X-ray Diffraction

XRR X-ray Reflectivity

XRF X-ray Fluorescence

BAM Brewster Angle Microscope

AFM Atomic Force Microscope

Chemical products

IL Ionic liquid

GO Graphene oxide

$[C_{20}mim]^+$ 1-eicosyl-3-methylImidazolium

$[NTf_2]^-$ Bis(trifluoromethylsulfonyl)imide

$H[AuCl_4] \cdot 3H_2$ Gold(III) chloride trihydrate salt

Résumé

Le réchauffement climatique est l'un des problèmes qui menacent notre planète. Il est principalement attribué aux émissions excessives de gaz à effet de serre résultant d'activités humaines aléatoires dans l'industrie, la technologie, l'agriculture .... L'excès de ces gaz induit le changement de la température de la terre et provoque donc des catastrophes naturelles. À cet égard, il est essentielle de trouver des dispositifs durables et régénératifs comme les cellules solaires, les piles à combustible, les générateurs de vagues et des appareils de stockage d'énergie...

Les supercondensateurs sont des appareils prometteurs de stockage d'énergie. Leur principe de fonctionnement est basé sur le stockage des charges électrostatiques dans une double couche électrique (EDL) de Helmholtz [1], à l'interface entre l'électrode et l'électrolyte. Figure 3 est une illustration d'un supercondensateur.

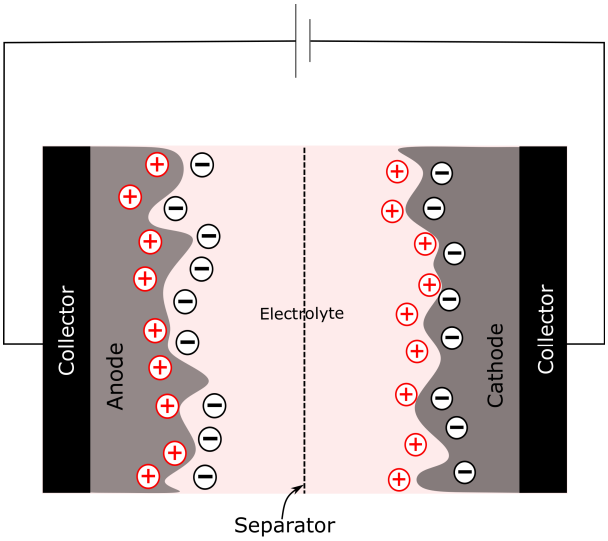

Figure 1: Représentation schématique d'un supercondensateur.

Sa densité d'énergie est exprimée dans l'équation ci-dessous [2] :

$$E = \frac{1}{2}CV^2 \tag{1}$$

Où "V" est sa tension de fonctionnement. "C" est la capacitance spécifique de l'EDL du supercondensateur et est estimée dans l'équation 4. Son expression est également utilisée pour calculer celle d'un condensateur.

$$C = \frac{\epsilon_r \epsilon_0 S}{d} \tag{2}$$

Où "ϵ_0" est la permittivité du vide et "ϵ_r" la permittivité relative de l'électrolyte. "d" est la distance séparant l'électrode de l'électrolyte. "S" est la surface d'interaction entre l'électrode et l'électrolyte. Les supercondensateurs se caractérisent donc par leur capacitance élevée : ils acceptent et livrent les charges beaucoup plus rapidement que les condensateurs ou les batteries. Toutefois, en termes de stockage de la densité d'énergie, ils sont intermédiaires. Leur performance est entravée par l'accès restreint des ions de l'électrolyte à la surface de l'électrode, donc par la faible surface d'interaction "S". Cela leur empêche de faire concurrence aux autres appareil de stockage d'énergie sur le marché.

Afin d'améliorer la densité d'énergie des supercondensateurs, les conditions physico-chimiques contrôlant l'accès des ions à l'électrode doivent être déterminées. Dans ce contexte, il est essentiel d'étudier l'interface formée entre l'électrode et l'électrolyte. L'électrode doit avoir une conductivité électrique élevée et une large densité de surface, tel que le **graphène**. L'électrolyte doit avoir une conductivité ionique élevée, une faible tension de vapeur et être de préférence un produit vert, tel que le **liquide ionique** (IL), d'où **les supercondensateurs à base de graphène et liquide ionique**. Il est donc nécessaire d'élaborer et d'étudier l'interface formée entre le graphène (l'électrode) et le liquide ionique (l'électrolyte). De nombreuse recherches théorique et de simulation ont été menées pour comprendre l'interaction entre le graphène et le liquide ionique à leur interface [2, 3, 4]. La littérature suggère que les molécules d'IL à l'interface des feuillets de graphène se trouvent dans un empilement de couches. La couche adsorbée sur les feuillets est formée par des molécules d'IL couchées parallèlement sur les feuillets. La couche la plus externe est formée par des molécules d'IL perpendiculaires ou inclinées. Les couches intermédiaires sont formées par des molécules sans orientation préférentielle [2]. À notre connaissance, cette interface n'a pas encore fait l'objet d'une étude expérimentale.

La procédure des films de Langmuir est reconnue pour sa capacité à former des films bidimensionnels et est détaillée dans le chapitre 1 de cette thèse. Elle est donc adapté à l'élaboration d'une telle interface. Les feuillets de graphène sont hydrophobes et donc ne peuvent pas être étudier par les films de Langmuir. En revanche, les feuillets d'oxyde de graphène (GO) sont amphiphiles grâce aux groupements fonctionnels qui décorent leurs plans de base et leurs bords. Récemment, des études ont montré que les supercondensateurs à base d'oxyde de graphène sont considérés comme efficaces [5]. L'électrode de graphène est sensible à l'oxydation à long terme pendant les cycles de charge/décharge. En outre, il est possible d'obtenir le graphène par la réduction de l'oxyde de graphène. Il est donc commode de choisir le GO comme alternative au graphène à étudier à l'interface avec le liquide ionique.

D'après la littérature, l'introduction des nanoparticules (NPs) métalliques dans les supercondensateurs améliore leur performance [6, 7]. En particulier, la décoration des feuillets de graphene par des NPs d'or augmente la capacitance des supercondensateurs [8]. D'autre part, les IL se révèlent comme stabilisant pour la synthèse des NPs d'or [9]. La radiolyse de surface par rayons X est une procédure de formation des nanostructures métalliques contrôlées par le film de Langmuir qui agit comme une moule [10]. Nous avons donc tenté d'utiliser cette méthode pour former des nanostructures d'or contrôlées par le film de Langmuir pur de l'IL par radiolyse de surface par rayons X.

Les objectifs de cette thèse

L'un des objectifs de cette thèse est d'élaborer une interface entre les molécules d'IL et les feuillets GO à l'aide des films de Langmuir, puis de la sonder. L'autre objectif est d'élaborer des films organométalliques d'IL et d'or par la procédure de radiolyse de surface, puis de les étudier à l'interface avec le GO. En raison de contraintes de temps, cet objectif n'a pas pu être complètement réalisé. Nous avons pu étudier les films d'IL de Langmuir déposés sur des sous-phases d'ions d'or de différentes concentrations. Ils ont ensuite été irradiés avec des rayons X sous incidence rasante afin de tenter de réduire les ions d'or en atomes par radiolyse de surface. La coalescence de ces atomes est censée être contrôlée par le film d'IL servant de moule.

Les techniques expérimentales

Dans cette thèse, les films de Langmuir d'IL mélangés avec le GO ou déposés sur des sous-phases ioniques, ont été sondés à l'échelle macroscopique et nanométrique. Les techniques expérimentales employées incluent des mesures d'isotherme Π-A, de microscope à angle de Brewster (BAM), de microscope à force atomique (AFM)et des mesures de diffusion des rayons X comme la réflectivité des rayons X (XRR), la diffraction des rayons X sous incidence rasant (GIXD) et la fluorescence par rayons X (XRF). La mesure d'isotherme Π-A est l'étude du film à l'échelle macroscopique à l'interface eau-air. Elle permet d'étudier la variation de la pression superficielle du film en fonction de la surface moléculaire et ainsi d'identifier ses différentes phases. Le BAM permet de visualiser les films sous forme de domaines à l'échelle mésoscopique à la surface des sou-phases aqueuses. L'AFM mesure l'épaisseur des films déposés sur un substrat solide et estime si les domaines du film sont de natures différentes. La mesure XRR sonde la densité électronique des films dans la direction perpendiculaire à l'interface eau-air. Elle permet de mesurer avec précision l'épaisseur des films et d'estimer la répartition de ses composants le long de l'axe vertical. La mesure GIXD révèle l'ordre cristallin des films, sa phase et la structure des molécules dans le cas où elles sont organisées à la surface des sou-phases aqueuses. La mesure XRF détermine la composition chimique des films à la surface des sou-phases aqueuses.Ces techniques sont présentées en détails dans le chapitre 2.

Le choix du liquide ionique

Cette étude fait partie du chapitre 3. Nous avons choisi d'étudier le $[C_{20}mim]^+[NTf_2]^-$, un liquide ionique à base d'Imidazolium de formule moléculaire : $C_{26}H_{47}N_3F_6O_4S_2$. Son cation est le $[C_{20}mim]^+$ et est asymétrique, composé d'une tête hydrophile Imidazolium et d'une chaîne alkyle hydrophobe, formée de 20 atomes de carbone. Son anion est le $[NTf_2]^-$ et est l'un des anions les moins hydrophiles. La coexistence des espèces hydrophiles et hydrophobes au sein de ce liquide ionique lui confère un équilibre amphiphile nécessaire à la formation de films de Langmuir stables à l'interface eau-air. Il est l'un des rares liquides ioniques qui peuvent être étudiés par la procédure de Langmuir. Nous avons montré que le film de Langmuir de $[C_{20}mim]^+[NTf_2]^-$ passe d'une monocouche à une multicouche à travers deux plateaux de collapse, le premier est observé à $\Pi = 17{,}5$ mN.m^{-1} et le second à $\Pi = 23$ mN.m^{-1} Tassler et al. [11] ont étudié sa structure par GIXD et ont

sondé sa densité électronique dans la direction perpendiculaire à l'interface eau-air par XRR. Ils ont montré qu'avant le premier plateau, le film n'est pas organisé et est formé en une monocouche où les têtes d'Imidazolium sont dans l'eau et les chaînes d'alkyles sont dirigées vers l'air. Pour des pressions de surface entre les deux plateaux de collapse, le film est organisé dans une coexistence d'une couche en 2D et 3D où les chaînes alkyles sont interdigitées.

Le film de Langmuir de $[C_{20}mim]^+[NTf_2]^-$ mélangé avec le GO

Cette étude fait partie du chapitre 4. Avant de préparer le films mixte de $[C_{20}mim]^+[NTf_2]^-$ mélangé avec le GO, les films purs ont été étudiés. Nous avons utilisé le solvant N-Méthyle-2-Pyrrolidone (NMP), un des solvant commun aux deux composants pour l'élaboration des films. Il n'est pas volatil et est miscible dans l'eau. 30 heures sont nécessaire pour la dissolution de 680 µL de NMP dans une sous-phase d'eau pure de 120 mL. Les films préparés avec ce solvant présentent donc des traces de NMP au cours de nos mesures. Le film pur de $([C_{20}mim]^+[NTf_2]^-)_{NMP}$ est formé en déposant 680 µL d'une solution de 0.037 mg.mL^{-1} de $[C_{20}mim]^+[NTf_2]^-$ avec NMP à la surface d'eau pure. Le film pur de $(GO)_{NMP}$ est élaboré en déposant 680 µL d'une solution de 0.01 mg.mL^{-1} de GO avec NMP, à la surface d'eau pure.

Pour la préparation du mélange mixte de (IL+GO), 5 mL d'une dispersion de 0.02 mg.mL^{-1} de $(GO)_{NMP}$ sont ajoutés à 5 mL d'une solution de 0.074 mg.mL^{-1} de $(IL)_{NMP}$, après les avoir soniqué chacune séparément pour 40 min. La concentration finale de ce mélange est de 0.047 mg.mL^{-1} : 0.01 mg.mL^{-1} de GO + 0.037 mg.mL^{-1} d'IL . Il est ensuite mis sous agitation mécanique pour 24h. Pour l'élaboration des films mixtes de Langmuir à l'interface eau-air, 680 µL de cette solution sont déposés.

La vitesse de compression est fixée à 15 cm^2.min^{-1}, après avoir attendu 45 min. La température de la sous-phase est maintenue à 20°C.

Étude macroscopique des films purs et mixte à la surface d'eau

Dans le chapitre 4, les films purs et mixte ont été étudiés à l'échelle macroscopique. Nous avons tracé les isothermes Π-A des films purs et du mélange en fonction de la surface de la cuve et non en fonction de l'aire moléculaire. En fait, les feuillets de GO existent en différentes tailles et n'ont donc pas tous la même balance amphiphilique. Les petits feuillets sont plus hydrophiles que les grands et donc ne peuvent pas être adsorbé en un film de Langmuir. Comme il est impossible de connaître le nombre de feuillets GO restant adsorbés, il est plus significatif de tracer les isothermes en fonction de la surface de la cuve.

Les mesures des isothermes Π-A des films purs et du film mixte à l'interface eau-air donne les informations suivantes :

- L'aire de lift-off du film de $(IL)_{NMP}$ est $A_{cuve} = 225$ cm^2, celui du film de $(GO)_{NMP}$ à $A_{cuve} = 60$ cm^2 et celui du mélange à $A_{cuve} = 162$ cm^2.

– Le NMP ne modifie pas le comportement des composants purs. Il reste adsorbé en une quantité modeste.

– L'isotherme est intermédiaire entre celle des purs purs et sa pression de collapse est différente de celle des films purs. Ceci indique que les deux composants du films mixtes interagissent ensemble.

– Le film mixte est formé spontanément par un empilement de deux couches à l'interface eau-air.

Suite à cette étude, nous avons construit deux modèles qui proposent de décrire la configuration des feuillets de GO et des molécules d'IL dans la bicouche au lift-off:

1. Première configuration :
   La couche en contact avec l'eau est formée dans une partie par toutes les feuillets de GO déposées et dans une autre partie par la moitié des molécules d'IL déposées. La couche en contact avec l'air est formée par l'autre moitié des molécules d'IL déposées.

2. Deuxième configuration :
   La couche en contact avec l'eau est formée par un total de 70% des molécules d'IL déposées. La couche en contact avec l'air est formée dans une partie par 30% des molécules d'IL déposées et dans une autre partie par toutes les feuillets GO déposées.

Après le lift-off, la pression de surface de la bicouche augmente progressivement jusqu'à 12.5 $mN.m^{-1}$ où un plateau commence. À travers ce plateau, la surface de la cuve allouée au film est réduite de 20%. Rappelons que le film d'IL pur, à travers un plateau, subit une transition d'une monocouche à une multicouche. Cela suggère l'éventualité que 20 % des molécules d'IL aient pu migrer de la couche en contact avec l'eau vers la couche en contact avec l'air. À $\Pi = 30$ $mN.m^{-1}$, le film mixte collapse

Caractérisation par diffusion des rayons X à l'interface eau-air

Les mesures de XRR

La densité électronique moyenne du film mixte a été sondée dans la direction de l'axe perpendiculaire à l'interface par XRR, sous différentes pressions de surface. Ces mesures montrent que le film mixte est formé par une bicouche à l'interface eau-air à $\Pi = 11$ $mN.^{-1}$ (avant le plateau). L_1 est la couche en contact avec l'eau et est formé en 77% des molécules de IL et d'environ 23% des molécules de NMP qui se dissolvent dans la sous-phase lorsque le film est comprimé. L_2 est la couche en contact avec l'air et est formée à partir des feuillets de GO et des molécules d'IL. Dans cette couche, d'après les mesures de XRR, les molécules d'IL t soit couchées parallèlement au dessus des feuillets GO, soit inclinées, à côté des feuillets, au dessus des molécules d'IL de L_1. Se référer à ces Figures 4.16 et 4.17 au chapitre 4 pour trouver les modèles proposés pour décrire la bicouche avant le plateau.

A travers le plateau observé à $\Pi = 12.5$ $mN.^{-1}$, environ 25% des molécules de IL migrent de L_1 vers L_2 et environ 70% des molécules du NMP plongent dans la sous-phase. La compression ultérieur du film entraîne la migration supplémentaire des molécules de

IL de L_1 vers L_2. Les molécules d'IL qui migrent vers L_2 peuvent se superposer soit aux molécules d'IL couchées à la surface de GO, soit aux molécules d'IL de L_1. Se référer à ces Figures 4.19, 4.20 et 4.21 au chapitre 4 pour trouver les modèles proposés pour décrire la bicouche après le plateau.

Les mesures de GIXD

La structure de la bicouche a ensuite été caractérisée par des mesures de GIXD à l'interface eau-air. Avant le plateau, observé à Π = 12.5 mN.m^{-1}, nous n'avons pas réussi à observer aucun pics de diffraction, ce qui suggère que le film n'est pas organisé. A Π = 21 mN.m^{-1} et puis à Π = 27 mN.m^{-1} nous avons observé 2 pics de diffraction hors plan (voir Figure 4.26 et Figure 4.27). Ce signal de diffraction est relatif à une même structure. Il indique l'organisation des chaînes des molécules d'IL dans un réseau rectangulaire à deux molécules, de paramètres suivants : a = 5.21 Å and b = 9.10 Å et d'aire A = 47 Å^2.molécule^{-1}. L'aire moléculaire est alors A = 23 Å^2.molécule^{-1}. L'étude des rodscans de ces deux pics montre que les chaînes alkyles sont inclinées de 7° vers les second proche voisin comme illustré dans le chapitre 4, Figure 4.30. L'épaisseur de cette structure est d'environ 30 Å.

Cette structure d'IL est supposé être formée en L_2 et non en L_1 pour deux raisons :

1. L_1 étant enfoui sous L_2 et ayant une épaisseur de 10 Å ne peut pas comprendre une structure de 30 Å d'épaisseur.

2. L_1 contient des traces de solvant dont sa présence est connu pour empêcher l'organisation des molécules organiques.

Caractérisation par AFM sur un substrat solide

Le film mixte a ensuite été transféré sur des substrats solides par la procédure de Langmuir-Blodgett à Π = 11 mN.m^{-1} (avant le plateau) et à Π = 25 mN.m^{-1} (après le plateau). Ces mesures ont permis de réduire nos options pour choisir de manière adéquate les modèles décrivant le film avant et après le plateau.

Avant le plateau, les mesures d'AFM montrent une première couche d'épaisseur 10 Å sur laquelle se trouve un deuxième couche d'épaisseur 14 Å. La première couche est attribuée à L_1, la couche formée des molécules d'IL et de NMP selon les mesures de XRR. La deuxième couche est attribué à L_2, la couche formée des feuillets de GO et des molécules d'IL. L'épaisseur d'un feuillet étant de l'ordre de 10 Å, soit environ 4 Å de moins que celle de L_2, les molécules d'IL dans L_2 doivent être couchées parallèlement aux feuillets de GO. A partir de ce résultat, nous avons pu éliminer le modèle présenté dans la Figure 4.20 et adopté le modèle présenté dans la Figure 4.21 pour décrire la bicouche avant le plateau (Chapitre 4). Dans ce modèle, on constate que l'orientation des molécules d'IL à l'interface avec les feuillets de GO n'est pas la même dans L_1 que dans L_2. Elles sont inclinées par rapport aux feuillets dans L_1 mais sont couchées parallèlement à ceux-ci dans L_2 (voir Figure 4.21). Rappelons que dans L_1, les molécules d'IL sont à l'interface avec l'eau d'une part et avec les feuillets d'autre part mais dans L_2, elles sont d'une part à l'interface avec l'air et d'autre part avec les feuillets. Ces résultats ouvrent la voie à

une nouvelle hypothèse suggérant que le comportement des molécules à l'interface avec les feuillets GO n'est pas unique mais dépend de l'autre interface limitant les molécules.

Après le plateau, on observe une troisième couche d'environ 30 Å d'épaisseur recouvrant les feuillets formés de GO + les molécules d'IL couchées. Cette nouvelle couche est attribuée aux molécules d'IL ayant migré de L_1 à L_2 à travers le plateau. Son épaisseur de cette couche suggère qu'elle est relative à la structure observée par les mesures du GIXD. À partir de ce résultat, nous avons pu éliminer les modèles illustrés dans les Figures 4.19, 4.20 et adopté le modèle illustré dans la Figure 4.21 pour décrire la bicouche après le plateau (Chapitre 4).

Les films de Langmuir d'IL déposés sur des sous-phases ionique d'or

Nous avons ensuite étudier les films de Langmuir de $[C_{20}mim]^+[NTf_2]^-$ déposés sur deux sous-phase de concentrations différentes de sels d'Or(III) chlorure trihydraté $H[AuCl_4]\cdot 3H_2$. Cette étude est détaillée dans le chapitre 5. La concentration d'ions d'or dans la sous-phase est définie par le rapport entre le nombre d'ions d'or et le nombre de molécules d'IL déposées à la surface. La première concentration étudiée correspond à 30 $[AuCl_4]^-$/IL et la deuxième à 600 $[AuCl_4]^-$/IL. Le nombre de molécules d'IL initialement déposé correspond à une aire moléculaire d'environ 1.32 nm^{-2}. Ces systèmes ont été caractérisé à l'échelle macroscopique/nanométrique et ensuite irradiés pendant environ 8 heures sous incidence rasante. Ces systèmes ont été caractérisés à l'échelle macroscopique/nanométrique, puis irradiés pendant environ 8 heures sous incidence rasante. L'objectif est de réduire les ions d'or par radiolyse et de leur permettre de fusionner en nanostructures contrôlées par le film de Langmuir. Les sous-phases contiennent de l'éthanol à une concentration d'environ 10^{-2} mol.L^{-1} pour masquer ("scavenger") les radicaux libres produits par la radiolyse de l'eau.

30 $[AuCl_4]^-$/IL :

Étude macroscopique à la surface de la sous-phase ionique

Essentiellement, le comportement du film est presque similaire à celui déposé sur l'eau pure. Le film présente 2 régions de pression croissante et un plateau à Π = 18,5 mN.m^{-1}. L'étude comparative de son isotherme Π-A avec celle du film déposé sur l'eau pure conduit aux points suivants :

- L'interaction des ions d'or avec le film organique ne déplace l'aire de lift-off que de 6 % vers les aire les plus grandes.
- Les deux films ont la même compressibilité. et sont supposés être formés en monocouches en phase (LE).
- Les deux films sont formés en monocouche et ensuite collapse en multicouche. Le collapse se fait à travers deux plateaux (un à Π = 17,5 mN.m^{-1} et l'autre à Π = 23 mN.m^{-1}) dans le film déposé sur l'eau pure et à travers un plateau formé à Π = 18,5 mN.m^{-1} dans le film déposé sur la sous-phase ionique.

– Le plateau est obtenue à une pression supérieure (Π = 18,5 mN.m^{-1}) à celui formé lorsque le film est déposé sur de l'eau pure Π = 17,5 mN.m^{-1}. Ceci suggère que l'interaction des ions d'or avec le film stabilise la monocouche.

Caractérisation par GIXD à la surface de la sous-phase ionique

La structure de ce film a ensuite été sondée par des mesures de GIXD à la surface de la sous-phase ionique. Avant le plateau formé à Π = 18.5 mN.m^{-1}, nous n'avons réussi à observer aucun signal de diffraction. A Π = 30 mN.m^{-1} (après le plateau), un pic de diffraction centré à Q_{xy} = 15.17 nm^{-1} a été observé. Ce pic est sous la forme d'une tige de Bragg et est situé dans le plan du diffraction. Après avoir intégré son intensité dans la direction de Q_z et étudié son rodscan, nous avons montré qu'il est attribué aux chaînes alkyles d'IL, organisées perpendiculairement à l'interface dans un réseau hexagonal en 2D. Le paramètre de ce réseau est a = 0.47 nm et l'aire moléculaire est A = 0.19 nm^2. D'après Tassler et al.[11], le film de $[C_{20}mim]^+[NTf_2]^-$ déposé sur l'eau pure est organisé en une coexistence d'une structure 2D et 3D. L'interaction des ions d'or avec le film semble donc empêcher l'organisation du film en une structure 3D.

Radiolyse de surface par les rayons X

Nous avons continué à l'irradier par les rayons X sous incidence rasante pour tenter de réduire les ions d'or par radiolyse.L'application de cette procédure au niveau de la surface permet la formation des nanostructures d'or cristallin orientées et contrôlées par le film de Langmuir. Après environ 2 heures d'irradiation, deux anneaux de diffraction ont été observés . Après avoir intégré leur intensités azimutalement (à Q constante) nous avons montré qu'ils sont attribués aux pics de diffraction (111) et (200) de l'or. Les structures inorganiques sont, dans ce cas, désorientés. D'après la largeur à mi-hauteur de ces pics, la taille des structures inorganiques est estimée de l'ordre de 15 nm.

Caractérisation par AFM sur un substrat solide

Après 8 heurs d'irradiation sous incidence rasante, le film a été transféré sur un substrat solide par la procédure de Langmuir Schaefer-Inversé et ensuite caractérisé par AFM. Nous avons observé des Nanoparticules sphérique de tailles moyenne d'environ 15 nm. Il est donc conclu que la radiolyse de surface par les rayons X en utilisant le film $[C_{20}mim]^+[NTf_2]^-$ comme moule conduit à la formation de nanoparticules d'or sphériques d'une taille de 15 nm.

600 $[AuCl_4]^-$/IL :

Étude macroscopique à la surface de la sous-phase ionique

Pour une concentration de 600 $[AuCl_4]^-$/IL, le comportement du film varie considérablement par rapport à celui du film déposé sur l'eau pure. L'isotherme comporte deux régions de pressions croissante et un plateau à 26 mN.m^{-1}. L'étude comparative de son isotherme Π-A avec celle du film déposé sur l'eau pure conduit aux points suivants :

– L'aire de lift-off est décalé d'environ 35% vers les aire les plus petite par rapport à celui du film déposé sur l'eau pur. Ce décalage pourrait être dû à la substitution

des anions à la surface. Les ILs ayant $[NTf_2]^-$ comme anion sont connus pour leur capacité à extraire les anions d'or des solutions aqueuses par substitution d'anions. Dans notre cas, nous supposons que le $[[NTf_2]^-$ a été remplacé par 1 ou 2 anions de $[[AuCl_4]^-$. L'interaction entre les complexes et les cations est manifestement électrostatique. Comme l'aire de la section transversale de cet anion est plus petite que celle de $[[NTf_2]^-$, le lift-off est déplacé vers les aire les plus petites.

– Le film est moins compressible lorsque la concentration de la sous-phase correspond à 600 $[AuCl_4]^-$/IL.

– Le film collapse d'une monocouche en une multicouche à travers le plateau. Sa compressibilité étant différente de celle du film déposé sur l'eau pure, on suppose que le collapse ne conduit pas à la même structure que celle sur l'eau pure ou sur la sous-phase de concentration 30 $[AuCl_4]^-$/IL.

Sur la base de ces observations, il est conclu que le comportement du film varie en fonction de la concentration en ions d'or.

Caractérisation par GIXD à la surface de la sous-phase ionique

Afin de détecter une possible organisation induite par le comportement du film suite à la dissolution de 600 $[AuCl_4]^-$/IL en sous-phase, il a été étudié par GIXD. A $\Pi = 20$ $mN.m^{-1}$ (avant le plateau), nous avons observé 10 pics de diffractions. Après avoir intégré leurs intensités dans la direction de Q_z et étudié leurs rodscans, nous avons montré qu'ils sont relatifs à deux structures en coexistence. La première est organique formée des chaînes alkyl d'IL, organisées dans un réseau oblique en 2D . Les paramètres du réseau de la structure organique sont les suivants: $a_1 = 1.6$ nm; $b_1 = 1.32$ nm; $\gamma = (\vec{a_1}, \vec{b_1}) = 140°$ and son aire est de $A_1 = 1.35$ nm^2. Cette structure comporte 3 molécules d'IL par maille. La deuxième est inorganique, formée de $[AuCl_4]^-$ et probablement de $[NTf_2]^-$, arrangés dans un empilement 3D des réseaux hexagonaux 2D . Les paramètres du réseau de la structure inorganique sont les suivants: $a_2 = b_2 = 2.34$ nm et son aire est de $A_2 = 4.74$ nm^2. Le rapport entre le paramètre de la structure organique ($a_1 = 1.6$ nm) et celui de la structure inorganique ($a_2 = b_2 = 2.34$ nm) étant de $\frac{3}{2}$, les deux structures forment une surstructure selon la direction d'un seul axe.

Nous avons ensuite observé à $\Pi = 35$ $mN.m^{-1}$ (après le plateau), 7 pics de diffractions. Après avoir intégré leurs intensité dans la direction de Q_z et étudié leurs rodscans, nous nous avons montrer qu'ils sont relatifs à deux structures en coexistence. Ici encore, la première structure est organique formée des chaînes alkyl et la deuxième est inorganique formée de $[AuCl_4]^-$ et probablement de $[NTf_2]^-$. La structure inorganique conserve la même organisation que celle observée avant le plateau. Cependant la structure organique change et les molécules à cette pression de surface deviennent organisées dans un réseau rectangulaire en 2D. Les paramètres du réseau de la structure organique sont les suivants: $a_1 = 0.46$ nm; $b_1 = 0.97$ nm; $\gamma = (\vec{a_1}, \vec{b_1}) = 90°$ et son aire est de $A_1 = 0.44$ nm^2. Cette structure comporte deux molécules d'IL par maille. Le rapport entre le paramètre de la structure organique ($a_1 = 0.46$ nm) et celui de la structure inorganique ($a_2 = b_2 = 2.34$ n) étant de 5, les deux structures forment une surstructure selon la direction d'un seul axe.

Ces mesures nous ont permis de constater que la concentration d'ions d'or dépassait un certain seuil de concentration pour l'apparition de la surstructure. Les raisons de

sa formation ne sont jusqu'à présent pas très claires. On suppose que la substitution d'anions entre le film de Langmuir et le complexe d'or pourrait jouer un rôle dans sa formation.

Radiolyse de surface par les rayons X

Nous avons ensuite tenté de réduire les ions d'or par la radiolyse de surface par les rayons X, à $\Pi = 20$ mN.m^{-1} et également à $\Pi = 26$ mN.m^{-1} Les intensités de toutes les pics de la surstructure diminuent progressivement à partir de 2.5 heurs d'irradiation pour s'annuler après un total 8 heurs d'irradiation. Cette observation indique la dégradation de la surstructure. Aucun signal provenant de la formation des nanostructures inorganique a pu être détecté. Les mesures de fluorescence ont confirmée ce résultat. Il semble que l'interaction du complexe anionique de l'or avec les cations IL soit forte, de sorte qu'elle empêche l'interaction des ions d'or avec l'électron solvaté produit par la radiolyse. Cela suggère que la formation d'une surstructure empêche les ions d'or d'être réduits.

Conclusions et perspectives

Selon les isothermes Π-A , les mesures XRR et AFM, le film mixte est formé par un empilement de deux couches. La couche en contact avec l'eau, L_1, est occupée par des molécules d'IL inclinées et du NMP. La couche en contact avec l'air, L_2, est occupée par des feuillets de GO et des molécules d'IL couchées parallèles sur ceux-ci. À travers un plateau observé à $\Pi = 12{,}5$ mN.m^{-1}, 70% des molécules de NMP se dissout dans l'eau et 25% des molécules d'IL migrent de L_1 vers L_2. Ces molécules migrantes s'organisent presque perpendiculairement dans un réseau rectangulaire sur le dessus des molécules d'IL se couchant parallèlement aux feuillets de GO. Les configurations des couches sont décrites par les modèle illustrés dans la Figure 2 : à gauche avant le plateau (pour $\Pi < \Pi_{plateau} = 12{,}5$ mN.m^{-1}) et à droite après le plateau (pour $\Pi > \Pi_{plateau} = 12{,}5$ mN.m^{-1}).

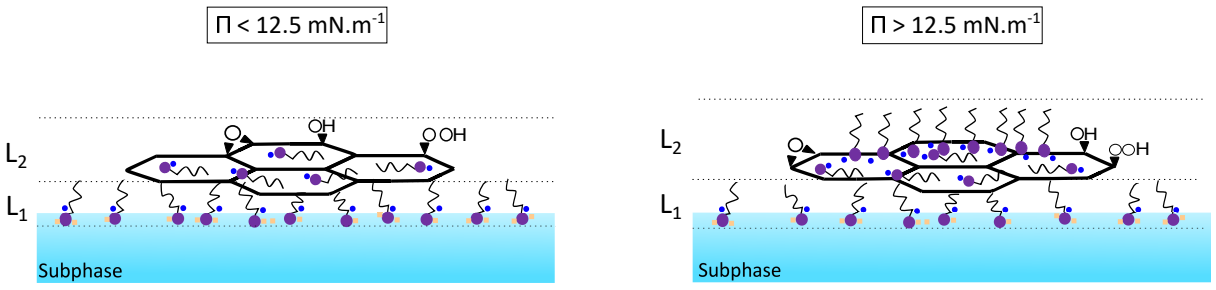

Figure 2: Les modèles décrivant la bicouche avant le plateau à $\Pi < 12.5$ mN.m^{-1} (à gauche) et après le plateau à $\Pi > 12.5$ mN.m^{-1} (à droite).

Trois conclusions peuvent être tirées :

1. Bien que les chaînes alkyles aient tendance à se couchées parallèlement aux plans de carbone, leur orientation à la surface des feuillets GO suit celle des têtes d'Imidazolium. Dans le cas où les molécules d'IL se trouvent entre la surface de l'eau et la surface des feuillets GO, l'interaction des têtes d'Imidazolium avec l'eau porte l'interaction $\Pi - \Pi$ avec les feuillets GO. Dans un tel cas, les têtes d'Imidazolium préfèrent être

dans l'eau plutôt que d'être couchées parallèles aux feuillets GO. Par conséquent, les chaînes alkyles préfèrent être inclinées par rapport aux feuillets plutôt que d'être couchés parallèles à celles-ci. Cependant, dans le cas où les molécules d'IL se trouvent entre les feuillets GO et l'air, l'interaction des têtes d'Imidazolium avec les feuillets porte l'interaction avec l'air. Dans un tel cas, les têtes d'Imidazolium ainsi que les chaînes alkyles préfèrent être parallèles à la surface des feuillets de GO.

2. Cette étude contribue à notre compréhension de l'interaction des molécules d'IL, situées à une certaine interface (air, eau....), avec les feuillets de GO. Les résultats indiquent que le comportement des molécules d'IL à l'interface avec les feuillets GO est déterminé par leur interaction avec la seconde interface (air, eau....). Il n'est donc pas possible de généraliser le type d'interaction pour décrire l'orientation des molécules d'IL à la surface des feuillets GO.

3. Les feuillets GO qui restent adsorbées à la surface de l'eau, même si elles sont amphiphiles, ont tendance à être hydrophobes car elles préfèrent interagir avec les chaînes alkyles de l'IL plutôt qu'avec l'eau.

Dans le chapitre 5, les films de Langmuir de $[C_{20}mim]^+[NTf_2]^-$ déposés sur deux sous-phases aqueuses contenant des ions d'or en différentes concentrations ont été étudiés .

Pour une concentration de 30 $AuCl_4^-$/IL , le film de Langmuir d'IL se comporte de manière comparable à celui déposé sur l'eau pure. L'interaction des ions d'or avec le film organique montre qu'elle empêche l'organisation du film en 3D. La radiolyse de surface par les rayons X, en utilisant le film d'IL comme moule, a aboutit à la formation des nanoparticules d'or de taille de 15 nm.

Pour une concentration de 600 $AuCl_4^-$/IL , le système semble avoir dépassé une concentration seuil en ions d'ors. Le film se comporte d'une façon considérablement différente de celui déposé à la surface de l'eau pure. Par conséquent, une surstructure apparaît. Elle consiste en une structure 3D inorganique formée sous une structure 2D organique. Les conditions de dépassement de la concentration seuil et donc de l'apparition du super-réseau ne sont pas claires. Il est suggéré que la présence du $[NTf_2]^-$ à la surface pourrait avoir réduit la solubilité des ions d'or dans l'or près de la surface. En conséquence, les ions d'or ont été capturé dans la structure 3D, probablement avec le $[NTf_2]^-$. Il est également suggéré que les interactions électrostatiques entre $[AuCl_4]^-$ and $[C_{20}mim]^+$ suite à l'échange d'anion, pourrait avoir capturer les ions d'or dans le film de Langmuir d'IL. Par conséquent, les électrons solvatés ne pouvaient pas interagir avec les ions d'or près de la surface. Dans cette situation, la radiolyse de la surface par les rayons X ne pouvait pas conduire à la réduction et à la formation des nanostructures d'or dirigées par le film de Langmuir de l'IL.

Abstract

Supercapacitors based on graphene oxide (GO) and ionic liquid (IL) are emerging as promising devices for energy storage. However, due to the limited access of electrolyte ions (IL) to the electrode (GO), they still lack the desired energy density. In this context, we aimed to determine the physico-chemical conditions for the formation of the IL/GO (electrolyte/electrode) interface. We used Langmuir procedure to form such an interface and study it by II-A isotherms, atomic force microscopy and surface X-ray scattering. We show that the film get spontaneously formed of the stacking of two layers L_1/L_2 on the air-water interface. L_1 is in contact with water and is formed of tilted IL molecules. L_2 is in contact with air and is formed of GO sheets covered with lying IL molecules. Through the film's compression, some IL molecules migrate from L_1 to L_2 and get organized in a 2D lattice. The results show that the configuration of the IL/GO interface in L_1 differs from that in L_2. This finding indicates that the IL/GO interaction is not unique but depends on the interaction of IL with the interface on which it is located (air, water...). The introduction of gold nanoparticles (NPs) to supercapacitors proved to improve their performance. We therefore studied the IL film deposited on aqueous subphases containing gold ions and attempted to form gold nanostructures by surface X-ray radiolysis using the film as a template. We show that there is a threshold concentration of gold ions for the appearance of a superstructure that prevents the reduction of ions. The conditions for its appearance remain unclear. Below the threshold concentration, 15 nm gold NPs are formed.

Les supercondensateurs à base d'oxyde de graphène (GO) et du liquide ionique (IL) émergent comme dispositifs de stockage d'énergie prometteurs. Toutefois, en raison de l'accès restreint des ions de l'électrolyte (IL) à l'électrode (GO), leur densité d'énergie est limitée. Dans ce contexte, nous avons cherché à déterminer les conditions physico-chimiques à l'origine de la formation de l'interface IL/GO. Nous avons utilisé la procédure de Langmuir pour former une telle interface et l'avons étudiée via des mesures de Π-A isothermes, microscope à force atomique et diffusion des rayons X de surface. Nous montrons que le film se forme spontanément en une pile de 2 couches L_1/L_2 à l'interface eau-air. L_1 est en contact avec l'eau et est formée par des molécules d'IL tiltées et du solvant. L_2 est en contact avec l'air et est formée par des feuillets de GO recouvertes de molécules d'IL couchées. Avec la compression, des molécules d'IL migrent vers L_2 et s'organisent en 2D. Ces résultats montre que l'interaction IL/GO n'est pas unique mais dépend de l'interaction d'IL avec l'interface sur laquelle il est situé (eau, air...). L'ajout des nanoparticules (NPs) d'or aux supercondensateurs ont prouvé qu'elles améliorent leur performance. Nous avons donc étudié le film d'IL déposé sur des sousphases aqueuses contenant des ions d'or et avons tenté de former des nanostructures d'or par radiolyse de surface aux rayons X en utilisant le film comme moule. Nous montrons qu'il y a un seuil de concentration pour l'apparition d'une surstructure qui empêche la réduction des

ions d'or. Les conditions de sa formation restent incertaines. En dessous du seuil de concentration, des NPs d'or de taille de 15 nm se forment.

Introduction

Global warming is one of the problems threatening our planet. It is mainly attributed to the excessive emission of greenhouse gases resulting from random human activity in industry, technology, agriculture... We are therefore facing climate change and natural disaster. In order to curb the random emission of greenhouse gases, there is an urgent need for sustainable and regenerative devices such as fuel cells, solar cells, wave generators conversion devices and energy storage systems.

Supercapacitors, also known by ultra-capacitors or high-capacity devices are promising devices for energy storage. Their operating concept is based on the principle of storing electrostatic charges at the level of the electrode/electrolyte interface. The charges accumulate in the form of the electric double layer (EDL) model proposed by Helmholtz in 1879 [1]. Figure 3 is a schematic representation of a supercapacitor.

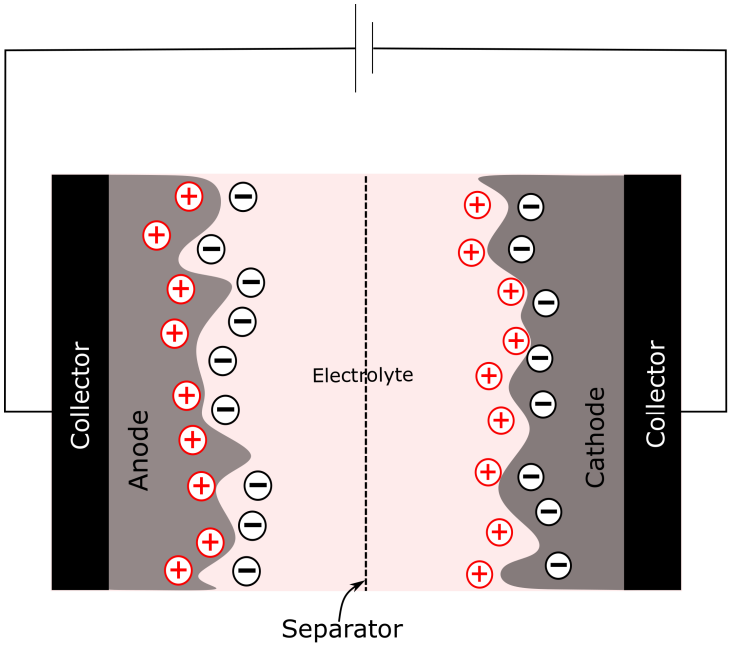

Figure 3: Schematic representation of a supercapacitor.

The energy density of a supercapacitor is expressed as follows [2] :

$$E = \frac{1}{2}CV^2 \tag{3}$$

Where "V" is its operating voltage. "C" is the specific capacitance of the EDL of the supercapacitor, which is estimated by Equation 4. Its expression is the same used to

compute the capacitance of conventional capacitors.

$$C = \frac{\epsilon_r \epsilon_0 S}{d} \tag{4}$$

Where "ϵ_0" is the vacuum permittivity , "ϵ_r" the relative permittivity of the electrolyte. "d" is the distance between the electrode et the electrolyte. "S" is the interaction surface between the electrode and the electrolyte. In conventional capacitors, the distance between the electrode and the electrolyte is of the order of a few micrometers [12], which implies a capacitance of the order of a few microfarads or nanofarads. In supercapacitors, it is estimated from the radius of the solvated ions of the electrolyte to be about a few angstroms [13], which implies a capacity of the order of a few kilofarads [14]. Therefore, supercapacitors exhibit high capacitance so can accept and deliver charges much faster than capacitors and batteries. However, in terms of voltage delivery, they are intermediaries between capacitors and batteries, making them unable to compete commercially with them. The performance of supercapacitors is somewhat limited due to the restricted access of electrolyte ions to the electrode. Understanding the mechanism that controls the interaction of electrolyte ions with the electrode is key to optimizing the access of ions to the electrode. In this context, it is necessary to study the physico-chemical conditions to form the electrode/electrolyte interface.

The electrode must have a high electrical conductivity and a large specific surface area such as **graphene**. The electrolyte must have a high ionic conductivity, a low vapor pressure, be insulating and preferably green, such as **ionic liquid** (IL). Hence the "Graphene - Ionic Liquid based supercapacitors". In order to understand the mechanism of the electrode/electrolyte interaction, it is necessary to conduct a structural characterization on a graphene/IL interface. Numerous theoretical research and simulation studies have been devoted to understanding the behavior of graphene (electrode) and IL (electrolyte) at their interface [2, 3, 4]. To our knowledge, the graphene/IL interface has not yet been studied experimentally, the need for this current research.

Langmuir is a known procedure for controlling the formation of two-dimensional films. It is therefore adapted to form such an interface. Graphene films are however hydrophobic and cannot therefore be studied by the Langmuir procedure. On the other hand, GO sheets, thanks to the oxygenated functional groups that decorate them, are amphiphilic. They are also characterized by a high surface area like graphene. They do not have an electrical conductivity as high as graphene, but recent studies have shown that GO-based supercapacitors can be efficient devices [5]. Graphene electrodes are also sensitive to long-term oxidation during charge/discharge cycles. In addition, it is also possible to obtain graphene from the GO by reduction. It is therefore convenient to choose GO as an alternative to graphene to investigate it at the interface with IL. One of the objectives of this thesis is therefore to elaborate the GO/IL interface using Langmuir films and then to study it by X-ray scattering and AFM.

According to the literature, the introduction of metallic nanoparticles (NPs) between the electrode and the electrolyte of supercapacitors enhances their performance. In particular, decorating graphene sheets with gold NPs improves the capacitance of supercapacitors[8]. On the other hand, ILs prove to be stabilizers for the synthesis of gold nanoparticles [9]. Surface X-ray radiolysis is a procedure for the formation of metallic

crystalline nanostructures controlled by a Langmuir film that acts as a [10] template. The other objective of this thesis is therefore to elaborate organometallic films of IL and gold by surface X-ray radiolysis, then to study them at the interface with GO. Due to time constraints, this last step could not be carried out. We will simply present the results on the systems of Langmuir films spread over gold ionic subphases of different concentrations. Those systems will be irradiated by X-ray in a grazing incidence geometry to perform surface radiolysis and form gold nanocrystals directed by the IL Langmuir film.

Chapter 1

Langmuir films

Contents

1.1 Notions for monolayers at the air-water interface

1.1.1 Amphiphilic molecules

"Amphiphile" is a word that derives from the Greek term "amphis-philia" which means "both love". It indicates the affinity of a chemical compound for two types of environments [15]. For example, a molecule composed of a hydrophilic polar part and a hydrophobic apolar part has an affinity for air and water. Figure 1.1 is a sketch showing a general amphiphilic molecule composed of a polar head and an apolar chain. For this reason, it is possible to be spontaneously adsorbed at the air-water interface [16].

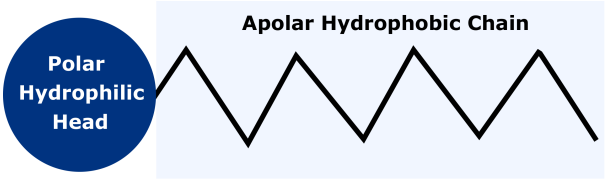

Figure 1.1: Sketch of an amphiphilic molecule.

1.1.2 Surface tension

In a dense phase, each molecule undergoes in all directions the cohesive forces of neighboring molecules, giving a total force of zero. However, at the surface of this phase, the molecules are surrounded by fewer neighboring molecules relative to the volume, giving a non-zero total force. The free surface energy is therefore positive. Figure 1.2 is a sketch showing the forces that the molecules undergo on the surface and in the volume of water. The surface then behaves as if it were covered with a stretchable elastic film and creates a surface tension "γ". The latter, corresponds to the work "ω" required to increase the area A of a surface by one unit:

$$\partial\omega = \gamma\partial A \tag{1.1}$$

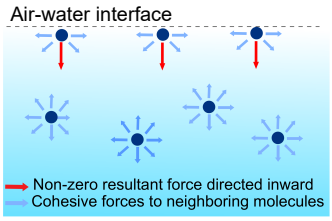

Figure 1.2: Illustration of the forces that undergo water molecules.

1.1.3 Thermodynamic of an interface

Gibbs thermodynamically described the interface between two fluids as a plane situated at z = 0 separating "Fluid 1" and "Fluid 2". Each fluid is composed of a certain number of molecules equal to [17]:

$$N_{1,2} = \rho_{1,2}V_{1,2} \tag{1.2}$$

Where $\rho_{1,2}$ is the density of each fluid far from the interface.

The total volume of the two systems is:

$$V = V_1 + V_2 \tag{1.3}$$

Where V_1 and V_2 are the volumes of each fluid.

The extensive quantities of the interface are its entropy S^s, its internal energy U^s, its volume V^s and the number of molecules N^s. They are defined as follows:

$$\begin{aligned} S^s &= S - S_1 - S_2 \\ U^s &= U - U_1 - U_2 \\ V^s &= V - V_1 - V_2 = 0 \\ N^s &= N - N_1 - N_2 \end{aligned} \tag{1.4}$$

The intensive quantities of the interface are its pressure P, its temperature T and its chemical potential μ. As the system is in equilibrium, the intensive quantities are the same for both fluids.

The free energy or Helmholtz energy of the surface is then defined as follows:

$$F^s = U^s - TS^s = -PV^s + \mu N^s + \gamma A \tag{1.5}$$

However, in the case of an ideal interface which is defined as an **infinitely sharp surface** separating two media, $N^s = 0$. The free energy of the surface thus becomes as follows :

$$F^s = \gamma A \tag{1.6}$$

This equation therefore indicates that the surface tension is the free energy density of a defined surface.

1.1.4 Films of amphiphilic molecules at the air-water interface

Depending on the relationship between the hydrophobic and hydrophilic parts of amphiphilic molecules, several types of films adsorbed at the water-air interface can be considered:

- Three-dimensional film once compressed : when the hydrophobic part is dominant over the hydrophilic part. If the film is compressed, 3D aggregates are formed [18].
- Gibbs monolayer : when the amphiphilic molecules tend to be more hydrophilic. In order to maintain a thermodynamic equilibrium between the surface and the subphase, some of them dissolve in water [18]. The film is generally in a condensed state at low temperature and in a gaseous state at high temperature. However, it is incapable of phase transition at constant temperature, making it unsuitable for our studies [19].
- Langmuir monolayer: when amphiphilic molecules have the right balance between hydrophilic and hydrophobic parts. A two-dimensional stable film can thus be formed at the air-water interface. Unlike the situation with Gibbs films, the phase transition of a Langmuir monolayer is possible at constant temperature. The study of these films allows the two-dimensional thermodynamic understanding of the monolayers adsorbed at the interfaces.

The three possible types of films that can be adsorbed at air-water interface are illustrated in Figure 1.3.

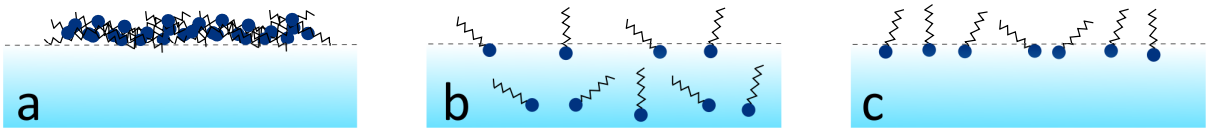

Figure 1.3: a. 3D film of amphiphilic molecules with hydrophobic tendency, b. Gibbs film and c. Langmuir film.

1.2 Langmuir films at the air-water interface

1.2.1 Historical overview

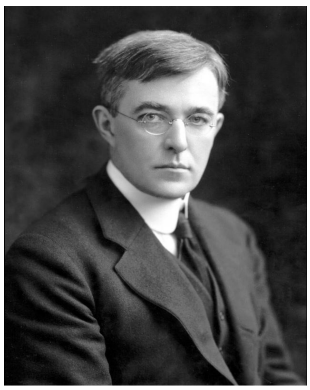

Figure 1.4: Irving Langmuir (1881-1957).

In the time of Hammurabi (1800 B.C.), sailors used to pour oil into the turbulent waters of the ocean to calm it [20]. This method was passed down from generation to generation, but no one attempted to understand the theory behind it until 1774. This year dates back to the time when the American statesman and philosopher Benjamin Franklin sought to interpret it. He discovered that a drop of oil on a small pond in Clapham Common spread to form a monomolecular layer. He explained this by the fact that oil particles can move freely on the surface of the water to reduce its surface tension [21]. The thickness of the monomolecular layer of oil was later estimated, by Lord Rayleigh in 1890, to be about 16,3 Å. At about the same time, Agnes Pockels, a self-taught scientist, succeeded, thanks to her experiments in her kitchen, to estimate the minimum surface area occupied by a molecule at about 20 $Å^2$ [22]. These studies were crowned by Irving Langmuir in 1910 who improved Pockels' experimental techniques for measuring the thermodynamic properties of a lipid film. This procedure provided scientists with a tool to monitor and understand the two-dimensional phase transition of the monolayer [23]. In collaboration with his colleagues: Katherine B. Blodgett and Vincent J. Schaefer, they developed two transfer techniques on solid wafer.

1.2.2 Procedure for the elaboration of a Langmuir film

To form Langmuir films, using a syringe, amphiphilic molecules, dissolved in a solvent, are deposited on the water surface of a Langmuir trough [19]. Langmuir troughs are in general entirely coated with Teflon, a material that is chemically almost inert to avoid any type of interaction with the molecules. The Teflon lets the water to have a level higher than the level of the edges of the trough and thus to form a meniscus. The molecules are then compressed using two mobile barriers to progressively reduce the surface area of the trough allocated to the film [19]. The thermodynamic properties of the film which are the surface of the trough allocated to the film "A_{trough}" and the surface pressure of the film "Π", at constant temperature "T" thus vary. "A_{trough}" and "Π" are the equivalent of volume V and pressure P in the state equations of 3D systems. This variation results in two-dimensional phase transitions of the Langmuir monolayer. The surface pressure of the film is measured by the Wilhelmy Plate Tensiometer which will be later explained. During compression, the variation of "Π" relative to the variation of the molecular area

"A" is recorded. The resulting curve is called the Π-A isotherm. Figure 1.5 is an annotated picture of our laboratory Langmuir trough.

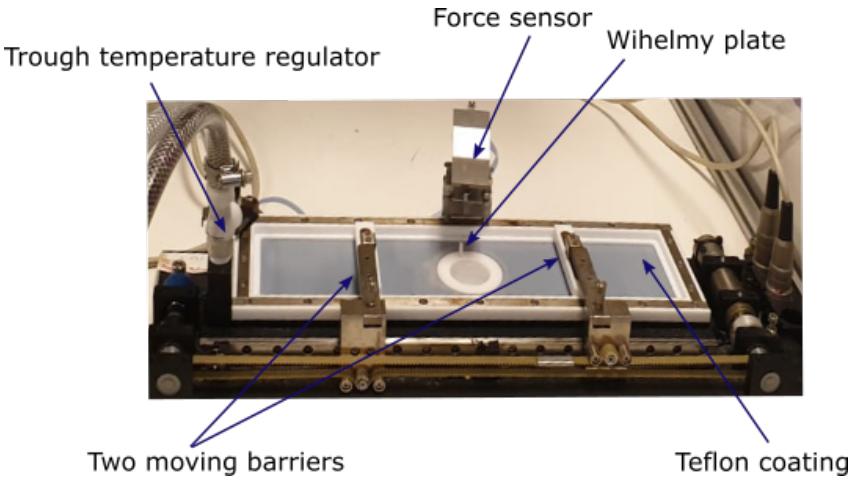

Figure 1.5: Photo of a Langmuir trough.

It is preferable to use a volatile and water-immiscible solvent such as chloroform. However, for some of our experiments, we had to use a non volatile and water-miscible solvent after unsuccessful attempts to dissolve our molecules in a volatile solvent. The main drawback of miscible solvents is their affinity for both media: the surface of water where the molecules are adsorbed and the volume of water. The Langmuir monolayer will therefore coexist with some residual solvent molecules.

1.2.3 Thermodynamic properties

The different phases that a Langmuir monolayer can undergo depend on the thermodynamic properties "A" "Π" and "T" of the film. The following paragraphs deal with these properties and the tools to measure them.

Area

Molecular area "A"is the average area occupied by an amphiphilic molecule adsorbed at an interface and expressed usually in $nm^2.Molecule^{-1}$. It is determined by the ratio between the surface area of the trough and the number of molecules deposited on the surface. It is thus calculated by the following relation :

$$A = \frac{A_{trough}}{N_A \times C \times V} \tag{1.7}$$

Where A_{trough} is the surface of the Langmuir trough, expressed in cm^2. N_A is the Avogadro number. C is the concentration of the solution and V is the volume of the deposited solution.

Surface pressure

The surface pressure "Π" is defined as the decrease in the surface tension of water due to the presence of amphiphilic molecules adsorbed on the surface. It is expressed in $mN.m^{-1}$

and is calculated by the following relation :

$$\Pi = \gamma_0 - \gamma \tag{1.8}$$

where γ_0 is the surface tension of the air-water interface without molecules adsorbed on water. It is constant and, for example, $\gamma_0 = 72.8$ mN.m^{-1} at 18°C. While γ is the surface tension of the interface in the presence of adsorbed amphiphilic molecules. γ varies according to the decrease of the area "A" occupied by the molecules.

The Wilhelmy Plate Tensiometer provides us with the pressure values. It consists of putting one side of a vertical plate of L×H×d dimensions in the water and connecting the other side to a balance. The latter measures the forces that pull the plate down, such as the force of gravity, Archimedes' buoyancy and the action of the surface tension of the interface. The total vertical force F is expressed as:

$$F = mg + \rho_e g(h.d.L) + 2(d + L)\gamma \cos(\theta) \tag{1.9}$$

Where m, d, H and L are respectively the mass, thickness, height and width of the plate. "h" is the length of the section of the plate immersed in water."θ" is the contact angle formed by the intersection between water-plate interface. The plate material is chosen to ensure total wettability, so that the contact angle can be considered to be approximately equal to zero. Taking into account the invariance of the force of gravity and buoyancy experienced by the plate (whether or not there are molecules adsorbed on the surface of the water) the commercial surface pressure balance is calibrated to provide Π directly based on this relation :

$$\Pi = \Delta F \propto \gamma_0 - \gamma \tag{1.10}$$

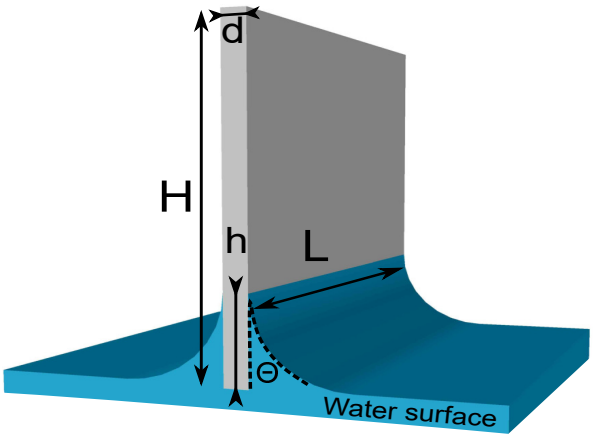

Figure 1.6: Scheme of Wilhelmy plate;

Temperature

The experiments must be carried out at constant temperature. Therefore, the trough is equipped with a thermostatic bath that provides a constant and uniform temperature to the subphase. Since the Langmuir film and the subphase are in quasi-static equilibrium, the temperature of the film is then imposed by that of the subphase.

1.2.4 Compressibility

By analogy with volume compressibility, it is possible to define the surface compressibility "χ" of a Langmuir monolayer. It is expressed in m.N^{-1}. It indicates the compression capacity of the film and thus informs us of its physical state over a well-defined range of surface pressure. It is calculated by the following relation:

$$\chi = -\frac{1}{A}\left(\frac{\partial A}{\partial \Pi}\right)\Big|_{T,N} \tag{1.11}$$

Where N is the number of the molecules adsorbed at the interface and T is the temperature of the monolayer.

1.2.5 Interactions between molecules in a Langmuir monolayer

To maintain a Langmuir film stable at the air-water interface, one should consider the interactions between the amphiphilic molecules. They are subject to three kind of interactions : head-head, head-chain and chain-chain.

- **Chain-chain Interactions**: is of the Van der waals type, described by Leonard-Jones' potential which shows that long-distance interactions are attractive and short-distance interactions are repulsive. This is the most important type of interaction that helps maintain the stability of a Langmuir film. It has been shown that at equilibrium, the typical distance between alkyl chains is about 4.8 Å
- **Head-head Interactions** : is of repulsive type; at long distance is of dipolar type and at short distance is of the steric repulsive type. The presence of ions in the subphase (as we will discuss later), may induce an attractive interaction.
- **Chain-head Interactions** : In fact, the head-chain distances are much more important than the head-to-head and chain-chain distances. Since interactions decrease as the distance increases, chain-head interactions are negligible.

1.2.6 Π-A Isotherm

Definition

The Π-A isotherm describes the evolution of the surface pressure as a function of the surface area occupied by each molecule at constant temperature. This macroscopic measurement allows the study of the thermodynamic of the Langmuir film. A generic Π-A isotherm showing the possible phase transitions that a short-chain Langmuir film can undergo is represented in Figure 1.7. Note that depending on the temperature and the nature of the amphiphilic molecules, it is possible not to observe all the phase transitions of the Langmuir film. From a Π-A isotherm one can extract the following thermodynamic characteristics of a Langmuir film [24]:

1. The pressure, therefore the surface tension of amphiphilic molecules, at a given surface and temperature, thanks to the relation 4.3.
2. The pressure of the collapse corresponding, in some cases, to the transition from a 2D to a 3D system.
3. The compressibility using the relation 1.11. It is therefore possible estimate the different phases of the film.

Phase transitions

In 1933, Ehrenfest introduced two classes of phase transitions [25]:

- The first order transition occurs when the first derivative of free energy with respect to one of its thermodynamic parameters is discontinuous. For example, entropy changes discontinuously during the phase transition from ice to water.
- The second order transition occurs when the first derivative of free energy is continuous while its second derivative is not. This is the case with ferro-paramagnetic or conductor-superconductor transitions. This second classification has been problematic to date because its conditions are not systematically verified during the transition.

The phase transitions that can be detected in a Langmuir film are for most of them of first order. They are evidenced by the observation of a plateau, between two successive phases, indicating a coexistence of the two phases. However, second order transition phases can also occur. They are identified by a modest change in the slope of the Π-A isotherm. The phases that one can evidence on the isotherm are:

– Gas phase (G): At a very large molecular area - 100 times larger than the cross-section of the molecule - the Langmuir film is in the gas phase. The molecules do not interact with each other so the surface pressure is at almost 0 $mN.m^{-1}$. This phase is very difficult to be detected experimentally.

– Liquid expanded (LE) phase: This phase occurs after compressing the molecules and observing a change of the slope of the isotherm. It evidences the first interactions between the molecules. The surface pressure is then not null and the compressibility is of the order of some tens $m.N^{-1}$.

– Liquid condensed (LC) phase: In this phase, the molecules are arranged in a state close to their maximum compactness. The area occupied by each one is close to the cross-section of the molecule so the film is not very compressible (around or less then 10 $m.N^{-1}$).

– Solid phase (S): At high surface pressures, the film becomes rigid and the molecules form a compact two-dimensional network. The transition of the film into the solid phase is evidenced by a break in the slope of the isotherm.

When the area available for each molecule becomes smaller than it cross-section, the film pressure reaches the critical collapse pressure. The molecules rise up on top of each other to form a three-dimensional film or plunge into the subphase. The film is said to have collapsed.

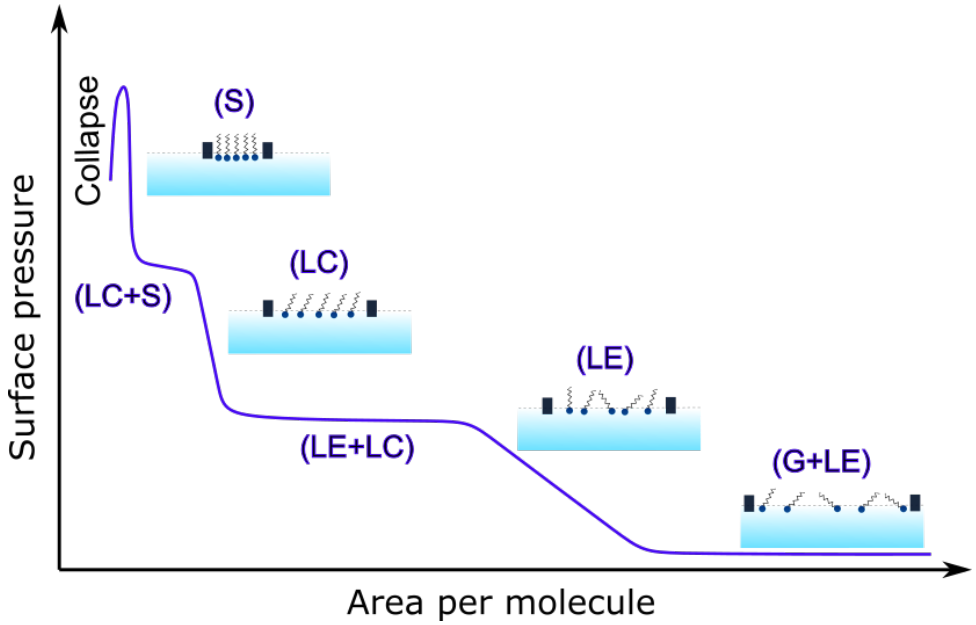

Figure 1.7: A generic Π-A isotherm of a Langmuir film deposited at the air-water interface.

1.2.7 Generic phase diagram

Thanks to the X-ray studies of 2D systems of fatty acid, Kagner and al. were able to develop a generic phase diagram common to all amphiphilic molecules of long alkyl chains [26, 27, 28]. It is equivalent to the Clayperon phase diagram for three-dimensional studies. It differentiates each mesophase by a set of parameters that describe the molecules, such as their tilt, rotation angle, orientation, elementary lattice... The diagram illustrated in Figure 1.8 shows the great diversity of phases that a Langmuir monolayer of amphiphilic molecules of long alkyl chains can have [27]. The condensed phases are grouped into: straight phases and tilted phases.

- **Tilted phases** :
  At low surface pressure, the molecular lattice is formed by tilted molecules organized according to four phases; L_2'', L_2 subdivided into L_{2d} and L_{2h}, L_2' and Overbeck Ov phases.
  - The L_2'' phase is obtained at low temperature where the molecules are organized in a centered rectangular lattice. The tilted molecules are oriented towards their nearest neighbor (NN) and their rotation around their axis is not possible.
  - The L_2 phase, according to Kagner et al [29] who were inspired by Landau's theory, is subdivided into two phases; L_{2h} phase at low temperature and L_{2d} phase at high temperature. In both phases, the molecules are tilted towards their nearest neighbor (NN). The main difference between them lies in the rotation configuration of the molecules: in the L_{2d} phase, the molecules are free to rotate around their axis, but in the L_{2h} phase, they are not.
  - The L_2' phase where the molecules are tilted towards their second nearest neighbor (NNN) and organized in a distorted hexagonal lattice which is equivalent to a centered rectangular lattice.

- The Ov phase is obtained at high temperature and was first evidenced by Brewster angle microscopy and then structured by Grazing incidence X-ray diffraction [30].

– **Straight phases** :
At high surface pressure, straight phases that include CS, LS and S phases are observed. They are characteristic of a Langmuir film composed of molecules perpendicular to the interface.

- The CS phase conforms with a compact, centered rectangular lattice where the molecules cannot rotate around their axis (the delta is fixed).
- The LS phase is represented by a perfectly hexagonal lattice where the molecules are free to rotate around their axis.
- The S phase occurs when the lattice becomes rectangular centered and we have again the molecules unable to rotate.

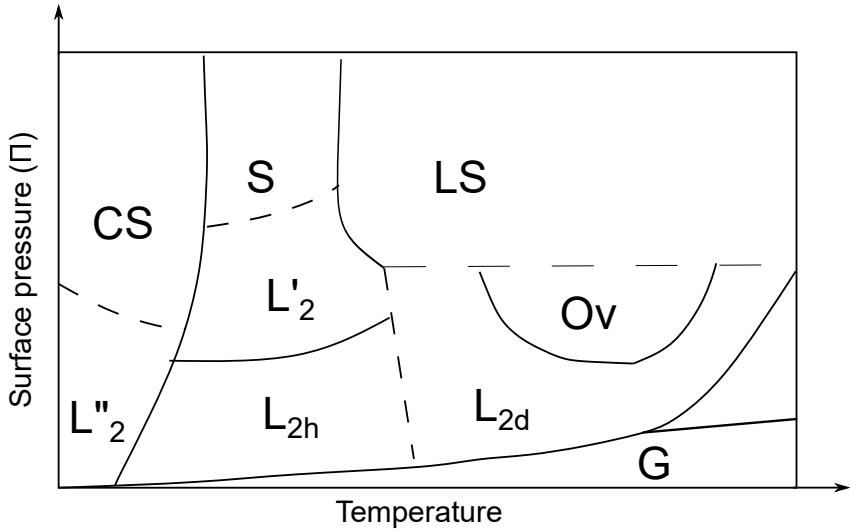

Figure 1.8: Generic phase diagram of molecules of long alkyl chains. The solid lines represent the first order phase transition and the dotted line represent the second order phase transition [28].

1.3 Langmuir films on solid substrates

Langmuir films are as well studied on solid substrates (wafers) by transferring them from water surface. Two main transfer procedures can be considered : Langmuir-Blodgett (LB) and Inverse Langmuir-Schaefer (ILS).

1.3.1 Preparation of the wafer

The wafers most used in Langmuir's experiments are of silicon type. The wafer must be cleaned beforehand with the Piranha solution to remove all organic residues and to make

its surface hydrophilic. Piranha solution is composed by a volume of 1/3 hydrogen peroxide (H_2O_2) and 2/3 sulfuric acid(H_2SO_4). The cleaning protocol consists in immersing the wafer for 10 minutes in the Piranha solution. Then, it must be rinsed several times with distilled water. A layer of silica SiO_2 is thus formed on its surface making it hydrophilic. It becomes therefore a favorable medium for the adsorption of the hydrophilic polar head of the Langmuir films while the alkyl chains remain in contact with the air.

1.3.2 Langmuir-Blodgett (LB) transfer

Using a stand holder, the wafer is suspended vertically and immersed in water perpendicular to its surface. After depositing the molecules, they are compressed to the desired surface pressure, which must be kept constant during transfer. The substrate is then removed from the water surface using the stand holder. The latter allows delicate control of the movement of the insert at speeds of a few mm/min. It also prevents the system from being exposed to lateral vibrations. Thanks to capillary phenomena, the film is correctly deposited on the hydrophilic substrate with adhesion.

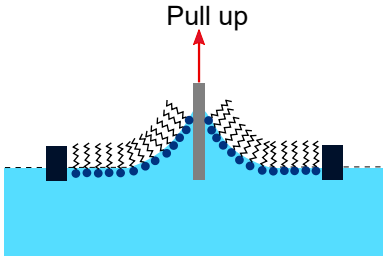

Figure 1.9: Illustration of the Langmuir-Blodgett (LB) transfer procedure.

1.3.3 Inverse Langmuir-Schaefer (ILS) transfer

Similarly to the Langmuir-Blodgett technique, the transfer is realized at a constant surface pressure. However, in this case, the wafer is held horizontally underneath the Langmuir film (at the bottom of the trough). The transfer is carried out by evacuating the water behind the barriers until the layer is deposited on the wafer: the polar heads in contact with the wafer and the chains in the air. This type of transfer is mainly used for low surface pressure measurements where the layer is not dense.

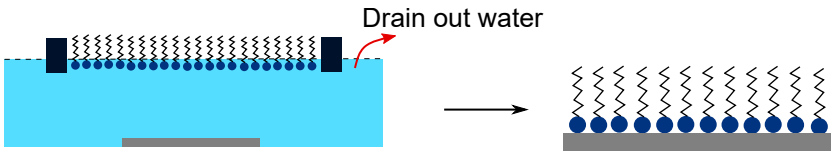

Figure 1.10: Illustration of the Inverse Langmuir-Schaefer transfer (ILS) transfer procedure.

Chapter 2

Characterization of Langmuir films

Contents

Despite the importance of Langmuir films, they were not widely studied initially due to the lack of their characterization techniques at the molecular level. The growing interest in Langmuir films only emerged with the advent of synchrotron facilities. The intense and well-collimated radiation generated by X-ray synchrotrons made it possible to study the structural composition and organization of Langmuir films. Specifically, the development, beginning in the 1980s, of the theories and setups for performing grazing incidence X-ray diffraction (GIXD) and X-ray reflectivity (XRR) and X-ray fluorescence (XRF) adapted to surface and interface measurements [31, 32, 33, 34]. The study of Langmuir films has become essential to understand interactions between biological molecules (drugs, proteins, peptides, ions ...) and organic-inorganic systems [35, 36]. XRR technique allows a precise measurement of the thickness and the electon density profile of a Langmuir film. GIXD measurements demonstrated the existence of a crystalline order in two-dimensional systems. By GIXD, it is possible to estimate the geometry, structure and the phase of the monolayer adsorbed on the water surface. XRF is used to determine the chemical composition of the film. In addition to the X-ray characterization techniques, Langmuir films can be studied at the microscopic scale by Atomic Force Microscopy (AFM) and at the mesoscopic scale by Brewster Angle Microscopy (BAM). AFM measures the thickness of Langmuir films deposited on wafers. BAM allows to visualize films deposited on the surface of water at the mesoscopic scale.

2.1 Notions for X-ray characterization

2.1.1 Historical overview of X-rays

The discovery of X-rays was a scientific bombshell and triggered a wide range of studies of matter. In 1889, Wilhelm Conrad Röntgen (Figure 2.1) was examining the light emitted from a cathode ray tube in a dark room. He accidentally observed a faint yellow green light from the fluorescence of cardboard coated with barium platinocyanide, originally used to protect (cover) his experiment from light [34]. To his astonishment, this phenomenon was reproduced even when he covered the tube with aluminum, glass, wood... But he discovered that a thin sheet of plumb or platinum was able to stop this invisible radiation [37]. In order to test the ability and limits of this invisible ray to penetrate objects, he exposed his wife's hand to this radiation. The image to the right of Figure 2.1 shows a photo of the bone in the hand of Roentgen's wife wearing a wedding ring, after it was exposed to this radiation. It was the very first image showing any part of the inside of the human body. An amateur photographer, Röntgen, announced the discovery of X-rays by publishing an article that referred to this photo as scientific documentation, instead of the fluorescent cardboard photo. Not having found an appropriate name, he named it "X-ray" after the usual algebraic name for the unknown. For his discovery of these revolutionary radiations, he was honoured with the Nobel Prize in Physics in 1901.

2.1.2 Interaction X-rays/matter

X-rays are electromagnetic waves composed of an electric field and a magnetic field. They propagate in the direction of the wave vector ($K = \frac{2\pi}{\lambda}$), where λ is the wavelength of the radiation and is of the order of the interatomic distance. They also have a very high energy E, comparable to the binding energy of the electrons to the nucleus. These properties make them the principal investigator of matter. Moreover, they are characterized by a

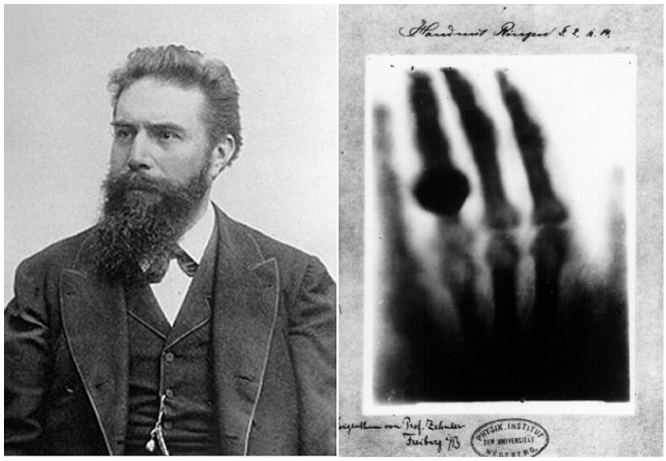

Figure 2.1: Left: Wilhelm Conrad Röntgen (1845-1923). Right : The very first X-ray photo showing a part of the inside of the human body, Mrs. Röntgen's left hand, including her wedding ring [38].

corpuscular nature that describes them by photons of quantified energy :
$E = h\frac{C}{\lambda} = h\nu$ where h is Planck's constant and ν is their frequency. Thanks to their dualistic wave/particle nature, two types of interaction of X-rays with matter can be highlighted :

1. Inelastic scattering : When a photon of $E = h\nu$ impinges an atom, it will scatter with a lower energy than the incident one. For instance:
   - Compton scattering : The energy of the photon is partially absorbed by a free or quasi-free electron. Consequently, the electron scatters in one direction and the incident photon in another but with $h\nu' \leq h\nu$. This interaction makes it possible to understand the electronic waves functions.
   - Photoelectric effect : The energy of the photon is absorbed by an electron from an inner layer of the atom. It will therefore be torn off and the atom will be excited. To return to its fundamental state, the atom undergoes another electronic transition accompanied by the emission of a photon. The energy of this photon is different from that of the incident one and corresponds to the energy difference between the exited and the fundamental level of the atom. This phenomenon is at the origin of fluorescence, which is used to determine the chemical composition of a material.
2. Elastic scattering : When an electromagnetic wave is incident on an atom, the latter begins to oscillate and becomes an electric dipole that re-emits the beam at the same energy as the incident one. By replicating this phenomenon on a group of atoms, the elastically scattered waves may interfere with each other, leading to X-ray reflectivity or diffraction phenomena.

The analysis of the perturbation of X-rays following their interaction with atoms allows a thorough understanding of the chemical composition, electronic states and atomic structure of matter.

2.1.3 Critical angle

For X rays, optical index n of a medium is calculated by the equation below :

$$n = 1 - \delta - i\beta \quad \text{where} \begin{cases} \delta = \frac{2\pi\rho r_0}{K^2} \\ \\ \beta = \frac{\mu}{2K} \end{cases} \tag{2.1}$$

δ characterises the scattering and β the absorption of a medium.

- ρ is the electron density of the medium.
- K = $\frac{2\pi}{\lambda}$ is the wave number of the X-ray.
- $r_0 = 2{,}82.10^{-13}$ the radius of the electron.
- μ is the coefficient of the linear absorbance of the medium.
- $\varrho = \rho r_0$ is scattering length density SLD.

For X-rays, δ and β are positive and in the order of 10^{-6} and 10^{-8} respectively. Given that n_{air} is a unit, the refractive index of any studied system is then less than n_{air} [37].

Consider X-rays propagating from a medium of optical index n_1 to another of n_2 with $n_1 > n_2$. If they impinge on the interface at an angle of incidence (the angle separating the incident beam and the interface) less than a critical angle α_c − specific to this interface and calculated by the Snell-Descartes law of classical optics in equation 2.2 − total external reflection occurs.

$$\cos\alpha_c = \frac{n_2}{n_1} \tag{2.2}$$

For X-ray, $n_1 = n_{air} = 1$ and $n_2 = n_{water} = 1 - \delta_{water}$ where $\delta_{water} << 1$ and β_{water} is negligible. Equation 2.2 becomes :

$$\cos\alpha_c = 1 - \delta_{water}$$
$$\sqrt{1 - \sin^2\alpha_c} = 1 - \delta_{water}$$

Since $\alpha_c << 1 \longrightarrow \sin\alpha_c \approx \alpha_c$ and $\delta_{water} << 1 \longrightarrow \delta^2_{water} \approx 0$. Therefore, we can express the critical angle of the air-water interface as follows:

$$\alpha_c = \sqrt{2\delta_{water}} \tag{2.3}$$

Therefore, equation 2.3 is the expression of the critical angle of the air-water interface, under which the incident X-rays are totally reflected in the air.

2.1.4 Evanescent wave and depth of penetration

Although under grazing incidence X-rays are totally reflected, some of them penetrate the second medium in a small region close to the interface. The penetrated radiation is intended to interact with the second medium in order to evaluate whether or not it is a total reflection situation. The wave propagating through the second medium is called an

evanescent wave whose intensity decreases exponentially with the distance of the vertical penetration. The penetration depth ξ of this wave, generated in the direction of Z and propagating parallel to the surface, is calculated as follows:

$$\xi = \frac{\lambda\sqrt{2}}{4\pi\sqrt{\sqrt{(\alpha_i^2 - 2\delta^2)^2 + 4\beta^2} - (\alpha_i^2 - 2\delta)^2}} \tag{2.4}$$

For example, suppose X-rays are propagating at 8 kev from medium 1 which is air of n_1=1 through the medium 2 which is water of $n_2 < n_1$ ($\delta_2 \approx 2{,}8.10^{-6} >> \beta_2 \approx 11{,}1.10^{-9}$). The critical angle for this system is therefore α_c= 2,3 mrad and the depth of penetration of the evanescent wave is $\xi = 5$ nm for $\alpha_i < 0.5\ \alpha_c$ [39]. Figure 2.2 compares the evolution of the depth penetration of the evanescent wave in relation to the angle of incidence of an incident wave of 8 kev and another of 22 Kev.

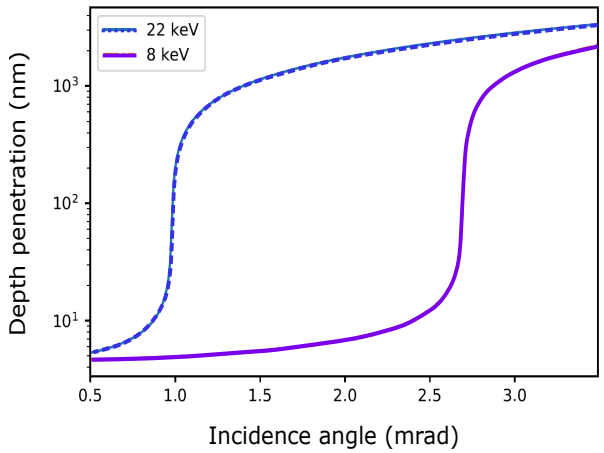

Figure 2.2: The evolution of the depth penetration of the evanescent wave in relation to the angle of incidence, for two energies.

2.1.5 X-ray scattering by a free particle (Thomson scattering by a free electron)

Let us consider a charged particle "q", placed at the origin "O" of a cartesian system and in the path of a high-energy plane electromagnetic wave [40], [41]. The electric field "E" and the magnetic field "B" will then exert a Lorentz force on the particle that will set it in motion:

$$\vec{F} = q\vec{E} + q\vec{V} \wedge \vec{B} \tag{2.5}$$

Where V is the velocity of the particle. The resolution of Maxwell's equations in th vacuum leads to the following relation between the amplitudes of electrical and magnetic field:

$$B_0 = \frac{E_0}{C}$$

V is supposed to remain sub-relativistic $\Longrightarrow \frac{V}{C} << 1$, inducing neglect of the contribution of the magnetic field. The displacement of the particle will therefore be mainly due to the electrical component of the given Lorentz force.

According to the fundamental principle of dynamics, the equation of motion is written:

$$q\vec{E} = q\vec{\epsilon}E_0 e^{i(\omega t - \vec{K}_i.\vec{r})} = m_q \frac{\partial^2 \vec{r}}{\partial t^2} \tag{2.6}$$

This equation describes the harmonic oscillation of the particle, where $\vec{\epsilon}$ is the vector polarization of the incident wave, ω its angular frequency and E_0 the amplitude of the electric field. We suppose that the electric field which generates the oscillations is that of the equilibrium position of the particle (r = 0) because it oscillates at low speed and short period. The equation of motion (2.6) becomes:

$$\frac{\partial^2 r}{\partial t^2} + \frac{q}{m_q} E_0 e^{i(\omega t)} = 0 \tag{2.7}$$

The oscillating particle is then assimilated to an electric dipole of moment $\vec{D}$ = q$\vec{r}$ and considered as a new source of X-rays which re-emits electromagnetic waves, in all directions and having the same frequency as the incident beam. This is the case when a wave is elastically scattered by a free particle. E_{dq} the scattered electric field by a charged particle q, intercepted in M (OM >> $2r_0$ where r_0 is the oscillation amplitude of the particle), is then expressed as follows:

$$\begin{aligned} E_{dq} &= \frac{1}{C^2 R}(\frac{\partial^2 \vec{D}}{\partial t^2} \times \vec{n}) \times \vec{n} \\ E_{dq} &= \frac{q^2}{m_d C^2} \frac{1}{OM} E_0 \sin(\theta).e^{i(wt - \vec{K_d}.\overrightarrow{OM})} \end{aligned} \tag{2.8}$$

Where C is the velocity of light. $\vec{D}$ is the electric dipole of moment. $\vec{n}$ is the unit vector of the propagation of the scattered radiation in the direction of $\overrightarrow{OM}$. θ is the angle between the vertical axis and the direction of the scattered beam and $\vec{K_d}$ is the scattered wave vector(K_d =K_i=$\frac{2\pi}{\lambda}$).

I_{dq} is the intensity of the scattered wave by a charge free particle, located at the origin "O". It is equal to the modulus squared of the electric field and expressed as follows :

$$I_{dq} = E_{dq} E^*_{dq} = \mid E_{dq} \mid^2 \tag{2.9}$$

From the equation 2.8 which describes the wave scattered by a charged particle, we establish in the following paragraph the expression of the wave scattered by a charged density (an atom). Note that the intensity of the scattered beam, developed in the equation 2.9, is proportional to the square modulus of the electric field, thus inversely proportional to the square modulus of the mass of the particle. Since protons and neutrons are heavier than electrons, the scattered wave from an atom is mainly due to electrons.

2.1.6 X-ray scattering by a charged density (atom)

Now consider an atom of volume "V" of density "ρ", composed of "Z" electrons, each acting as a free particle repaired by $\overrightarrow{OP}$, its position with respect to the origin O. When electromagnetic waves ($\vec{E_i}$=$\vec{E_0}$.e$^{i(\omega t - \vec{K}_i.\vec{r})}$) are incident on the atom, They will be scattered elastically in all directions by each electron as illustrated in Figure 2.3 [40, 41]. Assuming that the scattered waves by the electrons of the atom are intercepted at a distant point M, where $\overrightarrow{PM}$= $\overrightarrow{OM}$ - $\overrightarrow{OP}$ and $\overrightarrow{OM}$ >> $\overrightarrow{OP}$, we can consider the approximations of Fraunhofer:

1. When the fronts of the incident wave are spherical, the scattered waves, intercepted in M, are approximate to plane waves.

2. The lines connecting the position of the electrons of the atom to M are considered parallel, so that all scattered waves intercepted by M have the same wave vector $\vec{K}_d$ and OM $\sim$ PM.

Based on these approximations, the elementary electric field scattered by a charge density $\rho(\overrightarrow{OP})$ is expressed as follows:

$$\begin{aligned} dE_d &= \rho(\overrightarrow{OP})dV.\frac{q^2}{m_q C^2}\frac{1}{OM}E_0\sin(\theta).e^{-i(\vec{K}_i.\overrightarrow{OP})}.e^{i(\omega t-\vec{K}_d.(\overrightarrow{OM}-\overrightarrow{OP})} \\ dE_d &= \rho(\overrightarrow{OP})dV.\frac{q^2}{m_q C^2}\frac{1}{OM}E_0\sin(\theta).e^{i(\omega t-\vec{K}_d.\overrightarrow{OM})}.e^{i(\vec{Q}.\overrightarrow{OP})} \\ dE_d &= \rho(\overrightarrow{OP})dV.E_{dq}.e^{i(\vec{Q}.\overrightarrow{OP})} \end{aligned} \tag{2.10}$$

where E_{dq} is the electric field scattered by a an electron located at the origin (expressed according to Thomson' s equation 2.8. θ is the angle formed between the vertical and the scattered wave as shown in Figure 2.3. $\vec{Q} = \vec{K}_d - \vec{K}_i$ is the scattering vector whose magnitude is equal to:

$$Q = \frac{4\pi\sin\theta}{\lambda}$$

Therefore, the electric field re-emitted by an atom of $\rho(\overrightarrow{OP})$is:

$$\begin{aligned} E_d &= E_{dq}\int_V \rho(\overrightarrow{OP}).e^{i(\vec{Q}.\overrightarrow{OP})}dV \\ E_d &= E_{dq}.\mathrm{TF}(\rho(\overrightarrow{OP})) \end{aligned} \tag{2.11}$$

It is expressed by the product of the electric field re-emitted by an electron located at the origin : E_{dq} and the Fourier transform of the charged density : $\mathrm{TF}(\rho(\overrightarrow{OP}))$.

The intensity of the electric field is calculated by the square modulus of E_d as follows:

$$I_d = E_d E_d^* = \mid E_{dq} \mid^2 . \mid \mathrm{TF}(\rho(\overrightarrow{OP})) \mid^2 = I_{dq}. \mid \mathrm{TF}(\rho(\overrightarrow{OP})) \mid^2 \tag{2.12}$$

Where I_{dq} is the intensity of the wave scattered by an isolated electron located at O.

2.2 X-ray Reflectivity (XRR)

XRR measurement is a powerful non-destructive technique for surfaces and interfaces structural analysis. It has proven invaluable for the accurate determination of film thickness at the angstrom scale. Technically, XRR technique only measures the variation of the intensity of the scattered wave from a sample. A thorough knowledge of the theory behind this measurement is therefore necessary to extract the informations carried by our sample : its thickness, electron density and roughness. It is obviously more complicated than the other nanoscopic characterization techniques, i.e. scanning tunneling microscopy (STM) or transmission electron microscopy (TEM), which directly show the image of the surface but it exceeds them in its accuracy [42]. The first XRR measurements date back to 1954, when Parratt explored the surface of copper-clad glass [43]. This technique can be applied using synchrotron radiation as well as X-rays provided by university laboratories. It is suitable for the study of solid and liquid interfaces.

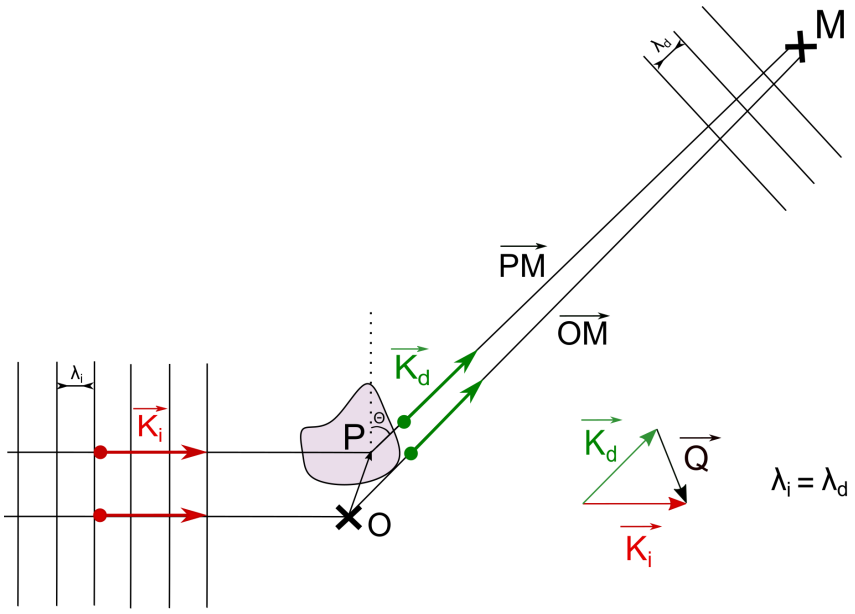

Figure 2.3: Illustration of X-ray scattering by an atom of charge density $\rho(r)$.

2.2.1 Fresnel's Equations for Reflection and Transmission

Based on Maxwell's relations, the equations of propagation of the electric field $\vec{E}$ and the magnetic field $\vec{B}$ of a plane electromagnetic wave are expressed as follows :

$$\Delta\vec{E} - K^2\vec{E} = \vec{0}$$
$$\Delta\vec{B} - K^2\vec{B} = \vec{0}$$

The solutions to the propagation equations for $\vec{E}$ and $\vec{B}$ are :

$$\vec{E} = E^0 \exp\left(i(\omega t - \vec{K}.\vec{r})\right).\vec{u}_e$$
$$\vec{B} = B^0 \exp\left(i(\omega t - \vec{K}.\vec{r})\right).\vec{u}_h$$

Where E^0 and B^0 are the amplitude of $\vec{E}$ and $\vec{B}$ respectively. ω is the angular frequency, $\vec{K}$ the wave vector, $\vec{u}_e$ and $\vec{u}_b$ the unit vectors and $\vec{r}$ the position vector of any point M in space for which we solve these calculations.

Consider the "Fresnel's interface", an infinitely sharp and flat interface located at z = 0, separating two homogeneous media of different refractive index n_i and n_t. When an electromagnetic wave of transverse polarization - $\vec{E}$ propagates $\perp$ to the incidence plane (yOz) - is emitted on the "Fresnel's interface" at an angle of incidence greater than the critical angle of the system ($\alpha_i > \alpha_c$), two phenomena can be considered :

1. The wave is **transmitted** in the second medium of n_t, forming an angle "α_t" with the interface.

2. The wave is **reflected** in a specular direction; the incident wave and the outgoing reflected wave make the same value of angle with the interface which coincides with (xOy) plane ($\alpha_i = \alpha_r$).

The geometry of the reflectivity experience in the case of Fresnel interface is represented by a sketch in Figure 2.4.

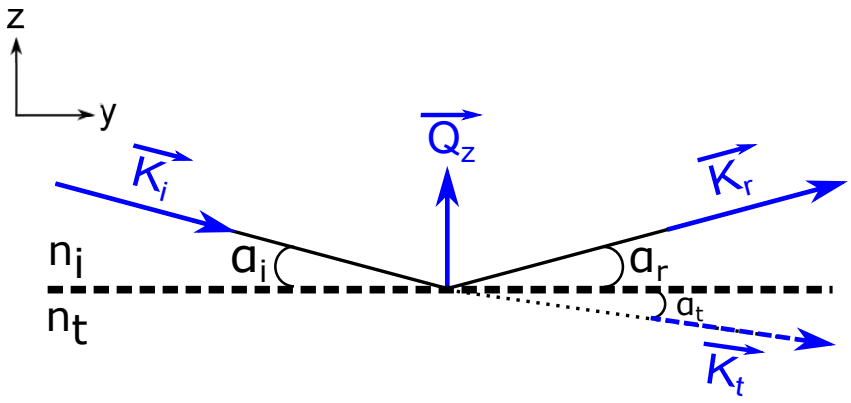

Figure 2.4: Scheme of an electromagnetic wave reflected and transmitted at the Fresnel interface

The process being elastic, the wave numbers corresponding to the incident (index i), reflected (index r) and transmitted (index t) waves, are written as :

$$\frac{K_t}{n_t} = K_i = K_r = K_0 \tag{2.13}$$

Having $\alpha_i = \alpha_r$, the wave vectors are calculated as follows:

$$\begin{aligned} \vec{K}_i &= K_0 \cos(\alpha_i)\vec{u}_y - K_0 \sin(\alpha_i)\vec{u}_z \\ \vec{K}_r &= K_0 \cos(\alpha_i)\vec{u}_y + K_0 \sin(\alpha_i)\vec{u}_z \\ \vec{K}_t &= K_0 n_t \cos(\alpha_t)\vec{u}_y - K_0 n_t \sin(\alpha_t)\vec{u}_z \end{aligned} \tag{2.14}$$

"Q_z" denotes the scattering vector which is none other than :

$$\vec{Q}_z = \vec{K}_r - \vec{K}_i \tag{2.15}$$

According to Maxwell's equations, $\vec{E}$ is related to to $\vec{B}$ by:

$$\overrightarrow{rot}(\vec{E}) = -\frac{\partial \vec{B}}{\partial t} = i\omega.\vec{B}$$

Where,

$$\overrightarrow{rot}(\vec{E}) = \left(\frac{\partial E_x}{\partial z}\right).\vec{u}_y - \left(\frac{\partial E_x}{\partial y}\right).\vec{u}_z$$

Hence,

$$B.\vec{u}_y = \frac{1}{i\omega}\left(\frac{\partial E_x}{\partial z}\right).\vec{u}_y \tag{2.16}$$

Considering the equations 2.14, the continuity of the tangential component of the electric field it passes through the interface is expressed as follows:

$$\begin{aligned} &\left(\vec{E}_i + \vec{E}_r\right).\vec{u}_x = \vec{E}_t.\vec{u}_x \\ \longrightarrow \quad &\left(E_i^0 + E_r^0\right)\exp\left(-iyK_0\cos(\alpha_i)\right) = E_t^0 \exp\left(-iyK_0 n_t \cos(\alpha_t)\right) \end{aligned}$$

Which results in the Snell-Descartes law :

$$K_0 \cos(\alpha_i) = K_0 n_t \cos(\alpha_t) \tag{2.17}$$

and

$$E_i^0 + E_r^0 = E_t^0 \tag{2.18}$$

Considering the equations 2.14 and 2.16, the continuity of the transverse component of the magnetic field as it passes through the interface is expressed as follows:

$$\begin{aligned} &\left(\vec{B}_i^0 + \vec{B}_r^0\right).\vec{u}_y = \vec{B}_t^0.\vec{u}_y \\ \longrightarrow \quad &K_0\left(E_i^0 - E_r^0\right)\sin(\alpha_i) = K_0 n_t\left(E_t^0\right)\sin(\alpha_t) \end{aligned} \tag{2.19}$$

In order to process the calculation of the intensity of the reflected beam "R", we must first express the reflection coefficient "r" , the coefficient of transmission "t" and the relation between them. "r" is the ratio of the amplitude of the reflected wave to that of the incident wave and "t" is the ratio of the amplitude of the transmitted wave to that of the incident wave :

$$1 + r = t \quad \text{where} \quad r = \frac{E_r^0}{E_i^0} \quad \text{and} \quad t = \frac{E_t^0}{E_i^0} \tag{2.20}$$

By integrating the equation 2.20 into the equation 2.19, we can express the Fresnel coefficients; "r" and "t"; in s-polarization ($\vec{E} \perp$ to the incidence plane) as follows:

$$r_\perp = \frac{\sin\alpha_i - n_t \sin\alpha_t}{\sin\alpha_i + n_t \sin\alpha_t} \quad \text{and} \quad t_\perp = \frac{2\sin\alpha_i}{\sin\alpha_i + n_t \sin\alpha_t} \tag{2.21}$$

For analog reasoning, the Fresnel coefficients in p-polarization ($\vec{E}$ // to the incidence plane) are expressed as follows :

$$r_{//} = \frac{n_t \sin\alpha_i - \sin\alpha_t}{n_t \sin\alpha_i + \sin\alpha_t} \quad \text{and} \quad t_{//} = \frac{2\sin\alpha_i}{n_t \sin\alpha_i + \sin\alpha_t} \tag{2.22}$$

However, since $\alpha_i << 1$ and $\alpha_t << 1$, the Fresnel coefficients are equivalents in s-polarization and p-polarization $\Longleftrightarrow$ $r_\perp \approx r_{//} \approx r$ and $t_\perp \approx t_{//} \approx t$ as.

Considering the Snell-Descartes relation (equation 2.17), the expression of the coefficient of reflection becomes:.

$$r = \frac{\sin\alpha_i - \sqrt{(n_t^2 - \cos^2(\alpha_i))}}{\sin\alpha_i + \sqrt{(n_t^2 - \cos^2(\alpha_i))}} \tag{2.23}$$

From the Fresnel coefficients that we have developed, we will, in the following paragraph, establish the expression of the intensity "R_F" of the beam reflected by the Fresnel interface.

2.2.2 Intensity of X-ray reflected by the Fresnel interface

The intensity of the beam reflected by the Fresnel interface is expressed by means of the square modulus of the reflection coefficient as follows :

$$R_F = r\bar{r} = \left|\frac{\sin\alpha_i - \sqrt{(n_t^2 - \cos^2(\alpha_i))}}{\sin\alpha_i + \sqrt{(n_t^2 - \cos^2(\alpha_i))}}\right|^2 \tag{2.24}$$

Taking into accounts :

- Equation 2.3 which modulates the expression of the critical angle of the air-water interface for x-ray studies : $\alpha_c = \sqrt{2\delta_{water}}$
- $n_t^2 = n_{water}^2 = 1 - 2\delta_{water} = 1 - \alpha_c^2$
- $\sin \alpha_i = \alpha_i$ when $\alpha_i << 1$.

R_F can be simplified to :

$$R_F = \left| \frac{\alpha_i - \sqrt{(\alpha_i^2 - \alpha_c^2)}}{\alpha_i + \sqrt{(\alpha_i^2 - \alpha_c^2)}} \right|^2$$

For convenience, the reflected intensity is expressed as a function of the magnitude of the scattering vector "Q" :

$$\vec{Q} = \vec{K}_r - \vec{K}_i$$

From the equation2.14, we obtain :

$$\vec{Q} = 2K_0 \sin(\alpha_i)\vec{u}_z = \vec{Q}_z$$

Which results in:

$$||\vec{Q}_z|| = \frac{4\pi \sin(\alpha_i)}{\lambda} \approx \frac{4\pi(\alpha_i)}{\lambda} \quad \text{and} \quad ||\vec{Q}_z c|| = \frac{4\pi \sin(\alpha_c)}{\lambda} \approx \frac{4\pi(\alpha_c)}{\lambda}$$

Therefore, the intensity of the reflected beam expressed as function of the scattering vector becomes :

$$R_F = \left| \frac{Q_z - \sqrt{(Q_z^2 - Q_z^2 c)}}{Q_z + \sqrt{(Q_z^2 - Q_z^2 c)}} \right|^2 \tag{2.25}$$

This relation describes the reflected signal by the Fresnel interface, a perfectly sharp and smooth interface.

The reflectivity signal presents three different regimes:

1. $\mathbf{Q}_z < \mathbf{Q}_c$: we observe a plateau of total reflection.
2. $\mathbf{Q}_z = \mathbf{Q}_c$: we observe a kink at the critical angle indicating the initiation of the decrease in intensity due to the beginning of X-ray absorption.
3. $\mathbf{Q}_z > \mathbf{3Q}_c$: the intensity will be driven by an exponential decrease and become proportional to Q_z^{-4}.

2.2.3 Intensity of X-ray reflected by a stratified interface

We are interested in the study of Langmuir films deposited at the air-water interface. We will therefore relax the Fresnel interface assumption and consider an electron density profile across the interface in the z-direction. Our interface is thus considered as laminated, consisting of a succession of interfaces separating media with different refractive indices. Henceforth, the study of Langmuir films by XRR requires to modulated them to stratified interfaces.

In the following paragraphs, two expressions of the intensity of specular reflectivity from a stratified interface based on two theories: **kinematic theory** and **dynamic theory** are established.

The kinematic theory [31, 41, 42] is based on Born's first approximation, which neglects the multiple reflections by the subjacent layers. Figure 2.5 is a sketch of the reflection of the beam by a stratified interface. It shows that the reflection comes from two "sources": the first reflection of the incident beam by each interface (black) and their multiple reflection (grey). However, since multiple reflections are also detected in the specular direction, neglecting them can lead to misinterpretation of XRR signals.Therefore, this theory cannot be adopted to interpret our systems. Nevertheless, as it allows a simple design of the reflected intensity as a function of the gradient of the density profile, it will be discussed. The expression of the reflectivity according to the kinematical approximation is the so-called the "Master-Formula".

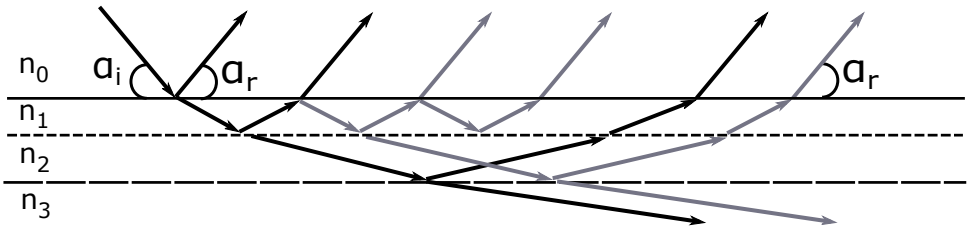

Figure 2.5: Sketch showing the first (black) and multiple reflections (grey) of an electromagnetic wave through a stratified interface in the specular direction

To process our XRR experimental results, we opted for the dynamic theory from which Parratt's formalism [39, 42, 43] derives. The advantage of this theory is its ability to describe the intensity of the reflected beam recursively, taking into account the first and multiple reflections.

kinematical scattering theory

To proceed with the calculation of the reflectivity, it is necessary to recall Equation 2.12. It expresses the intensity I_d of an electromagnetic wave scattered by a charged density $\rho(r)$, [31, 41]:

$$\begin{aligned} I_d &= I_{dq}.\left|\int_V \rho(r).e^{i(\vec{Q}.\vec{r})}dV\right|^2 \\ \Longrightarrow \qquad I_d &\propto I_0.\left|\int_V \rho(r).e^{i(\vec{Q}.\vec{r})}dV\right|^2 \end{aligned} \tag{2.26}$$

Since detection is in the specular direction, the only component of the scattering vector is the z-axis component Q_z. It is assumed that the density is homogeneous along the (x,y) interface plane but varies continuously along the z-axis :

$$\rho(x, y, z) =< \rho_{xy} > (z)$$

The volume V corresponds to the thickness of the interface multiplied by the illuminated surface A where :

$$A \propto \frac{S}{\alpha_i} \propto \frac{S}{Q_z}$$

S is the section of the incident beam.

Therefore, the expression of the intensity of the beam scattered by the interface in the specular direction is :

$$I_d(z) \propto I_0 \frac{1}{Q_z^2} \left| \int < \rho_{xy} > (z).e^{i(Q_z.z)} dz \right|^2$$

The intensity can as well be expressed by the derivative of the average density along the z-axis by integration per part. The reflectivity of a stratified interface is therefore obtained by the following formula :

$$R = \frac{I_d(z)}{I_0} \propto \frac{1}{Q_z^4} . \left| \frac{1}{\rho_\infty} \int \frac{d\big(< \rho_{xy} > (z)\big)}{dz} .e^{i(Q_z.z)} dz \right|^2$$

Where:

- ρ_∞ denotes the electron density of the substrate.
- $\frac{d\left(<\rho_{xy}>(z)\right)}{dz}$ is the derivative with respect to the z-direction of the mean electron density of the surface in the (x,y) plane.
- $\frac{1}{Q_z^4} \propto \mathrm{R}_F$ for $\mathrm{Q}_z \geq 3\mathrm{Q}_c$.

For $\alpha_i >> \alpha_c$, the reflectivity signal is described by the so-called Master-Formula [44] as follows :

$$\begin{aligned} R &= R_F \left| \frac{1}{\rho_\infty} \int \frac{d\big(< \rho_{xy} > (z)\big)}{dz} .e^{i(Q_z.z)} dz \right|^2 \\ R &= R_F.\mathrm{TF}^2\left(\tfrac{d(<\rho_{xy}>(z))}{dz}\right) \end{aligned} \tag{2.27}$$

The incorporation of the electron density derivative in the expression of the reflectivity emphasizes that the beam is reflected by the electron density gradient across the interface.

In conclusion, the reflectivity signal by a stratified interface is equal to the Fresnel reflectivity signal R_f modified by the absolute square of the Fourier transform of the electron density gradient.

As mentioned above, the kinematic approximation neglects the multiple reflections. Many formalisms have therefore been developed to deal with multiple reflections. We are particularly interested in Parratt's algorithm. Based on a dynamic approximation, it describes each reflection in an iterative way.

Dynamical scattering theory, Parratt formalism

Parratt's formalism [43], inspired by that of Abelès [45], is a dynamic description of the reflection of the waves, first and multiple, by a stratified interface. It consists in modelling the system in slices: the sample (i. e. Langmuir film) to be scanned is considered as an interface divided into N slices, located between the vacuum and a substrate (liquid or solid). Each layer j of the sample is characterized by its thickness d_j , its electron density j and its roughness σ_j. In our convention, j = 0 for vacuum and j = N+1 for the substrate. Figure 2.6 is a representative sketch of the reflection and transmission of waves by a sliced modulated system as described by Parratt.

Parratt's formalism describes the reflectivity in a recursive way. It links the amplitude of the reflected wave R_j to that transmitted T_j at the interface between layer j and layer j + 1 with the following recursion formula :

$$X_j = \frac{R_j}{T_j} = \exp(-iQ_{z,j}z_j)\frac{r_{j,j+1} + X_{j+1}\exp(iQ_{z,j+1}z_j)}{1 + r_{j,j+1}X_{j+1}\exp(iQ_{z,j+1}z_j)} \tag{2.28}$$

Here :

- $r_{j,j+1}$ is the Fresnel reflection coefficient calculated in 2.20 which takes into account only the first reflections from the interface separating layers j and j+1.
- $Q_{z,j}$ denotes the vertical component of the scattering vector within layer j and is expressed as:

  $$Q_{z,j} = 2k_{z,j}$$

  Where

  $$k_{z,j} = k_0\sqrt{n_j^2 - \cos\alpha_i}$$

In order to calculate the signal reflected by the interface between layers j-1 and j, it is imperative to first calculate the signal reflected by the interface between layers j and j+1. The computation is therefore done in a recursive way starting with the last layer and by considering :

1. $R_{N+1} = X_{N+1} = 0$, since there is no reflection by the substrate assumed to be infinitely thick.
2. $T_0 = 1 \longrightarrow X_0 = R_0$ since the incident wave is normalized to unity.

After N+1 iterations, according to Parratt's formalism, the expression of the intensity of the specular reflectivity, "r", is obtained by :

$$r = |X_0|^2 = |R_0|^2$$

The reflectivity spectrum is formed by the constructive interference between waves reflected by the different layers of a stratified interface, i.e. a Langmuir film deposited at the air-water interface. The reflectivity curve will exhibit periodic oscillations and deep minima, known as Kiessig fringes as it is illustrated in Figure 2.7. In an attempt to construct a hypothesis that suggests a first description of the film, it is interesting to analyze the shape of the reflectivity spectrum. For example, the amplitude of the

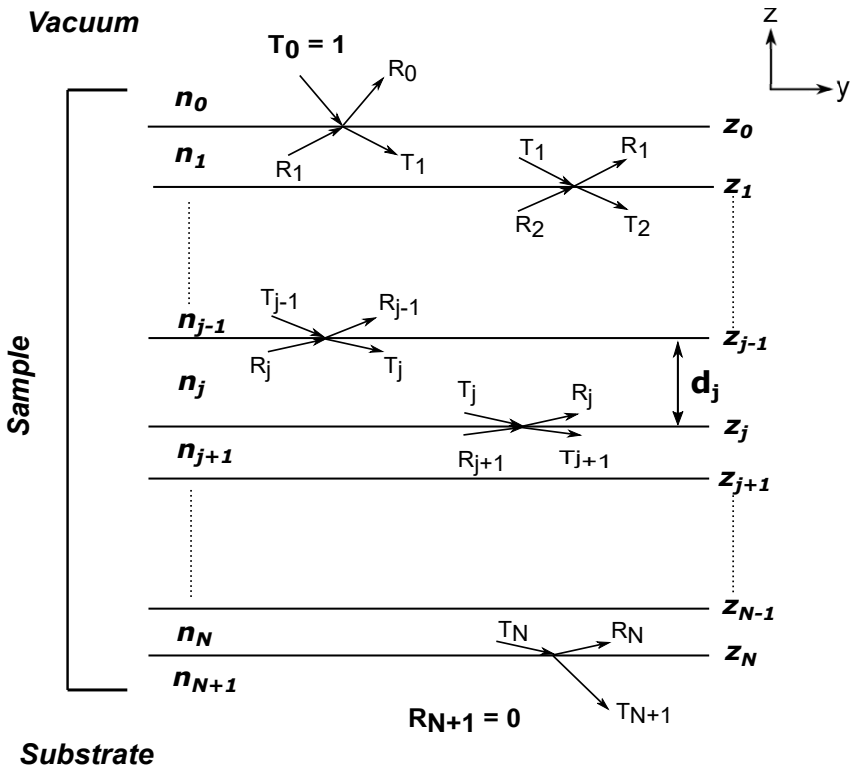

Figure 2.6: Schematic of a system sliced in N layers of N+1 net interfaces positioned at z_j. The multilayers are at the interface between the vacuum and a substrate of infinite thickness. The thickness of each layer is $d_j = z_j - z_{j-1}$. The scheme shows the transmission T_j and the reflection R_j of the beam from the layers with $T_0 = 1$ and $R_{N+1} = 0$.

oscillations is the result of the difference in electron density of the layers. The thickness "d" of the film can be calculated according to the periodicity of the oscillations (the inter-fringes distance) as follows :

$$d = \frac{2\pi}{\Delta Q_z}$$

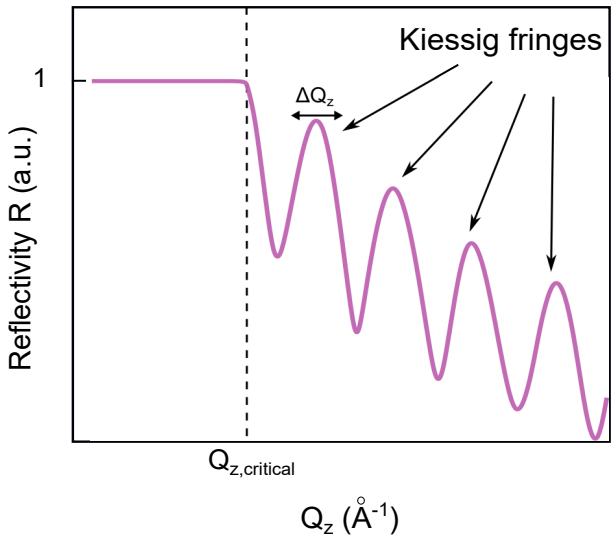

Figure 2.7: A sketch of a reflectivity spectrum that exhibits the Kiessig fringes.

2.2.4 Intensity of X-ray reflected by a rough stratified interface

At the surface of a liquid, capillary waves, produced by surface tension effects, cause fluctuations in height z(x,y) relative to an average interface position $\langle z(x,y)\rangle_{xy}$. These fluctuations will induce parasitic X-ray scattering in non-specular directions. The intensity detected in non-specular directions is obtained at a non-zero Q_{xy} and/or at a Q_z not perpendicular to the interface plane. As a result, the reflected signal measured in the specular direction at $Q_{xy} = 0$ will be less than that would be detected in an ideal case (a perfectly flat, smooth surface) [42, 41]. Equation 2.29 expresses"σ", the roughness of a surface, as a function of these height fluctuations.

$$\sigma = \sqrt{\left\langle \left(z(x,y) - \langle z(x,y)\rangle_{xy} \right)^2 \right\rangle_{xy}} \tag{2.29}$$

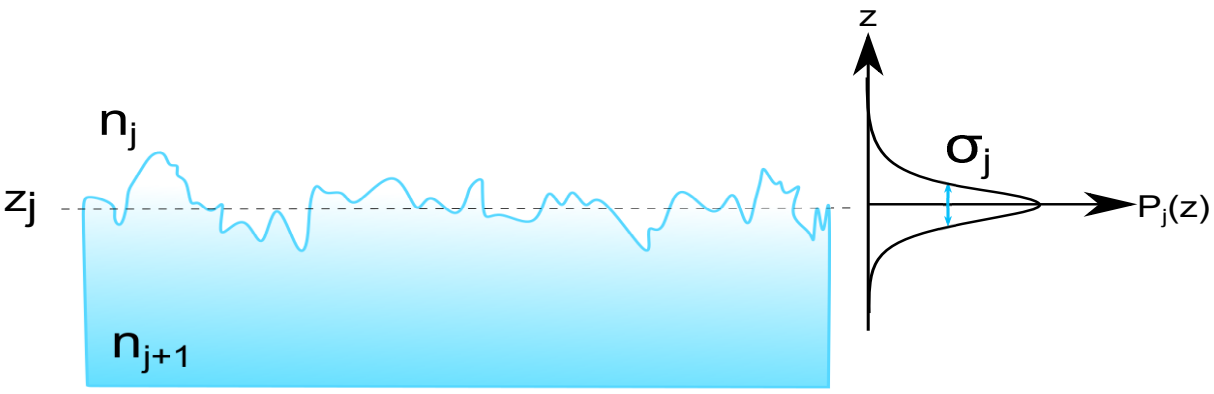

Figure 2.8: Sketch showing the z-height fluctuations in the horizontal plane (x,y) of a surface as a representation of a rough surface. $P_j(z)$ is a z distribution function, and shows the probability of finding a sharp interface at z_j+z.

Similarly, the electron density profile across an interface will be affected by the presence of roughness. It will therefore follow a progressive rather than abrupt evolution when the interface is rough. Figure 2.9 shows a comparison of the evolution of electron density across a helium-water interface in an ideal case (dotted lines) and in a real case; a rough surface (solid lines).

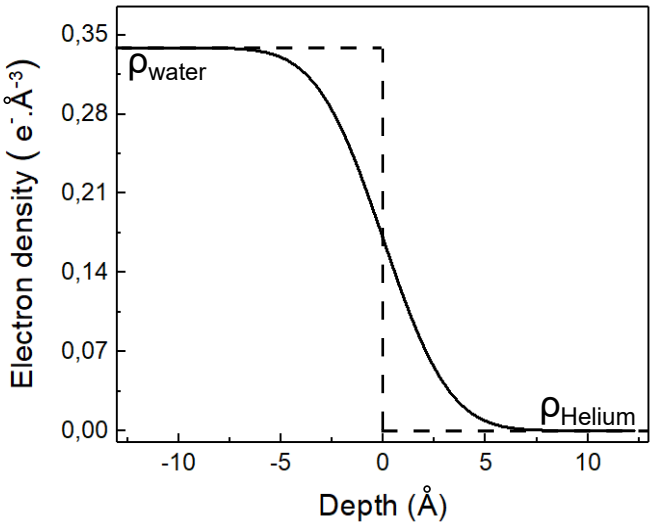

Figure 2.9: Electron density profile across an ideal interface (dotted lines) and a real interface (solid lines)

The roughness effect is emphasized by a further exponential decrease in the measured reflectivity signal as a function of the scattering vector Q_z. The reflectivity expressions are therefore modified by an exponential function term of σ as follows:

$$\text{Reflectivity}_{rough} = \text{Reflectivity}_{ideal}.\exp\left(-\tfrac{1}{2}Q_z^2\sigma^2\right)$$

The kinematical theory expressed in equation 2.27 becomes:

$$R' = R_F\left|\frac{1}{\rho_\infty}\int\frac{d\big(<\rho_{xy}>(z)\big)}{dz}.e^{i(Q_z.z)}dz\right|^2.\exp\left(-\tfrac{1}{2}Q_z^2\sigma^2\right) \tag{2.30}$$

Likewise, the dynamic theory in the form of Parratt formalism expressed in equation 2.28 becomes:

$$X'_j = \frac{R_j}{T_j} = \exp(-iQ_{z,j}z_j)\frac{r'_{j,j+1} + X_{j+1}\exp(iQ_{z,j+1}z_j)}{1 + r'_{j,j+1}X_{j+1}\exp(iQ_{z,j+1}z_j)} \tag{2.31}$$

Where $r'_{j,j+1} = r_{j,j+1}\exp\left(-\tfrac{1}{2}Q_{z,j}Q_{z,j+1}\sigma_j^2\right)$.
In the case of $\alpha_i >> \alpha_c$, we can approximate $Q_{z,j} = Q_{z,j+1} = Q_z$.

Figure 2.10 shows the effect of the roughness on the reflectivity spectrum a silica surface. It is obvious that the increase in roughness is accompanied by a further exponential decrease in the reflectivity signal [44].

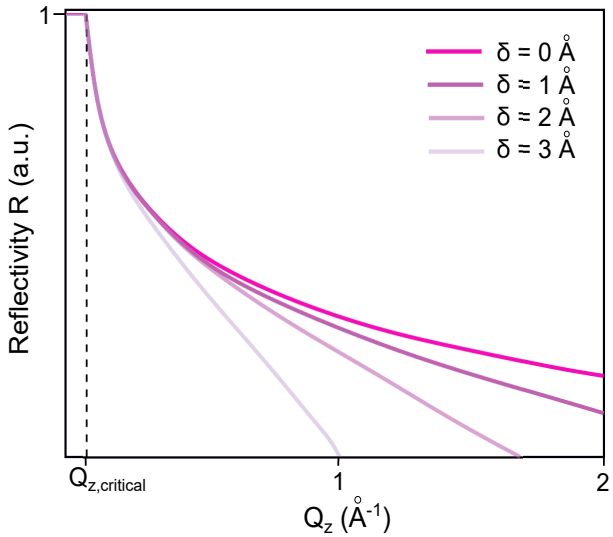

Figure 2.10: The effect of the roughness on the shape of specular Fresnel reflectivity spectra from a silica surface.

2.3 X-ray diffraction (XRD)

Historical overview of crystals

Since antiquity, crystals have fascinated mankind. The origin of the word "crystal" derives from *"crystallos"*, which means ice cube, attributed by the ancient Greek to quartz to believe that the gods composed it from frozen water. The Sumerians, Egyptians, Greeks, Romans...integrated them into their lives for aesthetic and cosmetic reasons and to believe in their power to spell the talisman [46]... Admiration for crystals was limited by a superficial framework until the 18^{th} century, when Romé de Lisle and Haüy realized that the geometric shape of crystals is related to a certain arrangement of atoms within entities. However, crystallography, the science of the properties and structure of crystals at the atomic scale, was only established in the 20^{th} century with the first X-ray diffraction experiment by Friedrich, Knipping and Laue. Crystallography paved the way for revolutionary discoveries concerning the physical, biological and chemical properties of matter [47].

2.3.1 X-ray diffraction by a 3D crystal

A three-dimensional crystal is a network constructed by the translation of a pattern of atoms by three basic vectors $\vec{a_1}$, $\vec{a_2}$, $\vec{a_3}$ [41]. It is thus described by a periodic volume distribution of the atoms, each repaired by its position $\overrightarrow{R}_{pqr}$=p.$\vec{a_1}$+q.$\vec{a_2}$+r.$\vec{a_3}$ where p,q, and r $\in \mathbb{Z}^+$. When X-rays are incident on a crystal, they are elastically scattered by each atom. The diffraction pattern is the result of the constructive interference between these scattered waves. $\rho_0(\overrightarrow{OP})$ is the electron density of an atom centered at the origin of the network. The total electron density of the crystal $\rho(\overrightarrow{OP})$ is the sum of the contributions of the atoms in the network and is expressed as follows :

$$\rho(\overrightarrow{OP}) = \sum_{p,q,r} \rho_0(\overrightarrow{OP} - \overrightarrow{R}_{pqr}) \tag{2.32}$$

According to Equation 2.12, the intensity of the wave scattered by a charged density

varies as a function of the square modulus of the Fourier transform of the charged density . It is therefore necessary to establish a detailed expression of the Fourier transform of a charged density for the analysis of the diffracted intensity as follows :

$$\begin{aligned}
\mathrm{TF}(\rho(\overrightarrow{OP})) &= \int \rho(\overrightarrow{OP}).e^{i(\vec{Q}.\overrightarrow{OP})}dV \\
\mathrm{TF}(\rho(\overrightarrow{OP})) &= \int \sum_{p,q,r} \rho_0(\overrightarrow{OP} - \overrightarrow{R}_{pqr}).e^{i(\vec{Q}.\overrightarrow{OP})}dV \\
\mathrm{TF}(\rho(\overrightarrow{OP})) &= \iiint \sum_{p,q,r} \rho_0(\overrightarrow{OP} - \overrightarrow{R}_{pqr}).e^{i(\vec{Q}.\overrightarrow{OP})}d^3r \\
\mathrm{TF}(\rho(\overrightarrow{OP})) &= \sum_{p,q,r} e^{i(\vec{Q}.\overrightarrow{R})} \iiint \rho_0(\overrightarrow{OP} - \overrightarrow{R}_{pqr}).e^{i(\vec{Q}.(\overrightarrow{OP}-\overrightarrow{R}))}d^3r
\end{aligned} \tag{2.33}$$

One can notice that the Fourier transform of $\rho_0(\overrightarrow{OP})$ is expressed by means of the product of two terms :

- $\mathrm{S}(\vec{Q}) = \sum_{p,q,r} e^{i(\vec{Q}.\overrightarrow{R})}$, the ***lattice sum*** which describes the geometric organization of the atoms in the network.
- $\mathrm{F}(\vec{Q}) = \iiint \rho_0(\overrightarrow{OP} - \overrightarrow{R}_{pqr}).e^{i(\vec{Q}.(\overrightarrow{OP}-\overrightarrow{R}))}d^3r$, the ***structure factor*** which informs us of the atomic composition and the topology of the atoms in the network.

The Fourier transform of the electronic density of the crystal is expressed as :

$$\mathrm{TF}(\rho(\overrightarrow{OP})) = S(\vec{Q})F(\vec{Q})$$

The lattice sum for a infinite crystal can be written as follows ;

$$\mathrm{S}(\vec{Q}) = \sum_{p=1}^{\infty} e^{ip(\vec{Q}.\vec{a_1})} \sum_{n=1}^{\infty} e^{in(\vec{Q}.\vec{a_2})} \sum_{r=1}^{\infty} e^{ir(\vec{Q}.\vec{a_3})} \tag{2.34}$$

The scattered intensity $\propto |S(\vec{Q})|^2$ is non zero if a discrete set of scattering vectors $\vec{Q}$ belongs to the reciprocal network. In other words if the set of $\vec{Q}$ satisfies the Laue conditions, represented in the below equation:

$$\vec{Q}.\vec{R} = 2\pi n \quad \mathrm{n} \in \mathbb{Z}^+ \tag{2.35}$$

We define then $\overrightarrow{Q}_{hkl} = \mathrm{h}.\vec{a}_1{}^* + \mathrm{k}.\vec{a}_2{}^* + \mathrm{l}.\vec{a}_3{}^*$, a vector of the reciprocal network whose basic vectors are $\vec{a}_1{}^*$, $\vec{a}_2{}^*$ and $\vec{a}_3{}^*$ and h, k, l $\in \mathbb{Z}^+$, called Miller index. Moreover, $\vec{Q}$ is perpendicular to a set family of discrete reticular planes separated by constant distance d. According to Bragg's law : $\{2\mathrm{dsin}\,\theta = \mathrm{n}\lambda\}$, where θ is the angle between the scattered wave and the reticular plane and n $\in \mathbb{Z}^+$, d is expressed as follows:

$$d = \frac{2\pi}{Q} \tag{2.36}$$

Laue's conditions are then written in the following form:

$$\begin{aligned}
\vec{Q}.\vec{a}_1 &= 2\pi h & \vec{a}_1{}^*.\vec{a}_1 &= 2\pi \\
\vec{Q}.\vec{a}_2 &= 2\pi k & \vec{a}_2{}^*.\vec{a}_2 &= 2\pi \\
\vec{Q}.\vec{a}_3 &= 2\pi l & \vec{a}_3{}^*.\vec{a}_3 &= 2\pi
\end{aligned}$$

By satisfying Equation 2.35, at the "nodes" of the perfect infinite reciprocal lattice, the shape of the intensity of the diffraction peaks or Bragg peaks is a Dirac peak of zero width. However, the reality imposes to consider crystals of finite extension, so that the thickness of the Bragg peaks is not equal to 0 but inversely proportional to the size of the crystal . The periodicity of the crystal is then limited to N_1, N_2, N_3 to which tend respectively p,q,r instead of ∞. Therefore, the intensity of the diffracted beam is expressed by:

$$I(\vec{Q}) = I_0 I_{dq} \mid F(\vec{Q}) \mid^2 \prod_{j=1}^{3} \left| \frac{\sin(\frac{N_j \vec{Q}.\vec{a_j}}{2})}{\sin(\frac{\vec{Q}.\vec{a_j}}{2})} \right| \tag{2.37}$$

In conclusion, the study of x-ray diffraction by a crystal allows to determine the reciprocal lattice of the crystal and hence to identify its structure.

2.3.2 X-ray diffraction by a 2D crystal, Langmuir film

To describe the diffraction of X-rays by a two-dimensional crystal, the same reasoning as for a three-dimensional crystal will be followed [31, 41]. However, in this case, one must consider only the in-plane translation of a periodically repeated pattern within a crystal lattice. The lattice sum which describes the translation of the pattern thus becomes :

$$\mathrm{S}(\vec{Q}) = \sum_{p=1}^{\infty} e^{ip(\vec{Q}.\vec{a_1})} \sum_{n=1}^{\infty} e^{in(\vec{Q}.\vec{a_2})} \tag{2.38}$$

The vectors of the direct lattice $\overrightarrow{R}_{pqr}$ and of the reciprocal lattice $\overrightarrow{Q}_{hkl}$ are expressed as follows:

$$\begin{aligned} \overrightarrow{R}_{pq} &= p.\vec{a_1} + q.\vec{a_2} \\ \overrightarrow{Q}_{hk} &= h.\vec{a_1}^* + k.\vec{a_2}^* + Q_z\vec{z} = \overrightarrow{Q}_{xy}^{[hk]} + \overrightarrow{Q}_z \end{aligned} \tag{2.39}$$

Laue's conditions results then in:

$$\begin{aligned} \vec{Q}.\vec{a}_1 &= 2\pi h & \qquad \vec{a_1}^*.\vec{a}_1 &= 2\pi \\ \vec{Q}.\vec{a}_2 &= 2\pi k & \qquad \vec{a_2}^*.\vec{a}_2 &= 2\pi \end{aligned}$$

It is noticeable that only the component of the scattering vector $\vec{Q}_{xy}$ which is parallel to the lattice is taken into account in the diffraction of two-dimensional crystals. The resulting diffraction pattern is therefore not composed of "nodes" as in a three-dimensional crystal, but of vertical rods, called Bragg rodes. In our work, the two-dimensional films are Langmuir films, where the amphiphilic molecules form the lattice pattern.

The analysis of X-ray diffraction pattern allows to understand the symmetry and the geometry of its unit cell as well as the orientation of the molecules and the phase of the film.

Theoretical intensity of the scattered beam by a Langmuir film

Similarly to the 3D crystals, the theoretical intensity of the diffracted signal by a 2D system is expressed as follows [41, 31]:

$$I_{hk}(\vec{Q}) = I_0 I_{dq} \mid F(\vec{Q}) \mid^2 \prod_{j=1}^{2} \left| \frac{\sin(\frac{N_j \vec{Q}.\vec{a_j}}{2})}{\sin(\frac{\vec{Q}.\vec{a_j}}{2})} \right| \tag{2.40}$$

The position, the full-width half-maximum FWHM and the intensity of the diffraction pic are obtained by the adjustment of the diffracted signal by Gaussian or Lorentz functions. By incorporating them into appropriate equations, we manage to reveal the structure and parameters of the pattern of an organized Langmuir film.

Structure factor of Langmuir films

The structure factor describes the intern structure of the molecules assimilated to cylinders of homogeneous electron density ρ_e(r)= $\frac{Z}{S.h}$ [31]. Where Z is the number of electrons, S is the cross section of the cylinder and h its height. Using a suitable cylindrical coordinate system (r, z, Φ), F($\vec{Q}$) is expressed as follows:

$$F(\vec{Q}) = \int_0^h dz \int_0^{2\pi} d\Phi \int_0^R \frac{2Z}{S.h} e^{i(\vec{Q}.\vec{r})} r.dr \tag{2.41}$$

Hence:

$$\mid F(\vec{Q}) \mid^2 = \left(\frac{2Z}{S.h}\right)^2 \left| \frac{\sin\left(\frac{Q_z h}{2}\right)}{\left(\frac{Q_z h}{2}\right)} \right|^2 |J_1(QR)|^2 \tag{2.42}$$

The structure factor is a function of the cardinal sine function, which is the Fourier transform of a step function, and of J_1,which is the cylindrical Bessel function. J_1 varies slightly at large angles so it can be neglected. The structure factor becomes as follows :

$$\mid F(\vec{Q}) \mid^2 = 4\rho_e^2 \left| \frac{\sin\left(\frac{Q_z h}{2}\right)}{\left(\frac{Q_z h}{2}\right)} \right|^2 \tag{2.43}$$

From this equation, it is deduced that the intensity of the out-of-plane Bragg's peak (Q_z) must be adjusted by a cardinal sine squared function as illustrated in Figure 2.11. The width of the peak is inversely proportional to the length of the molecules.

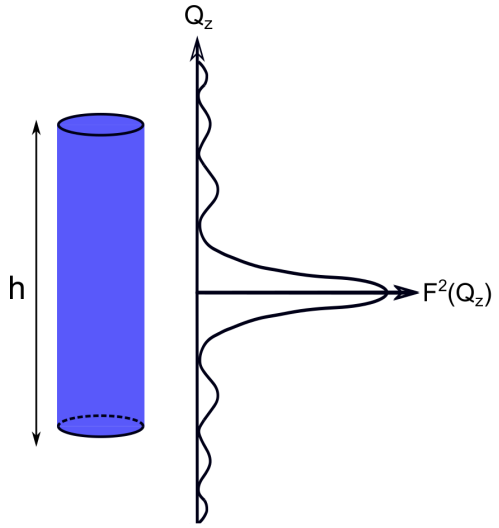

Figure 2.11: Representation of the structure factor squared of a molecule, assimilated to a cylinder of homogeneous density, perpendicular to the water surface.

Geometry of molecules within a 2D crystalline lattice

The range of the order of a crystal is defined as the distance over which the organization can be predicted from the network translations. For a temperature strictly above 0 K, thermal fluctuations of the molecules prevent the establishment of a long-range positional order of a two-dimensional crystalline film [41]. Peierls and Landau predicted the impossibility of forming an infinite two-dimensional crystal [48, 37]. In 1973, Kosterlitz, and Thouless [49], proposed a new order for the two-dimensional system called topological order in which no long-term order of a conventional type exists. Using the concepts of topology, a branch of mathematics, they described phase transitions in two-dimensional films at low temperature. Their theoretical discovery earned them the Nobel Prize in 2016. A quasi long-range orientational order is thus possible to occur in a two-dimensional crystal at temperature different than zero K. For 2D systems, it was then appropriate to define a new type of phase characterized by a quasi long-range positional order and a quasi long-range orientational order, intermediate between the liquid phase and the solid phase in 3D systems. It is known as "*mesophase*". All the elongated molecules, assimilated to cylinders, of a diffraction plane at the interface are oriented in one direction and each has four degrees of freedom. Therefore, the position of a molecule at the interface (illustrated in Figure 2.12) is described by four variables: two related to the translation (x, y) of the molecule parallel to the interface and two angles which are t, the azimuth Ψ respectively the tilt and rotation of the molecule with respect to an axis perpendicular to the interface. The axis of the molecules has a unitary vector $\vec{n}$:

$$\vec{n} = \begin{cases} \cos\psi . \sin t \\ \sin\psi . \sin t \\ \cos t \end{cases} \tag{2.44}$$

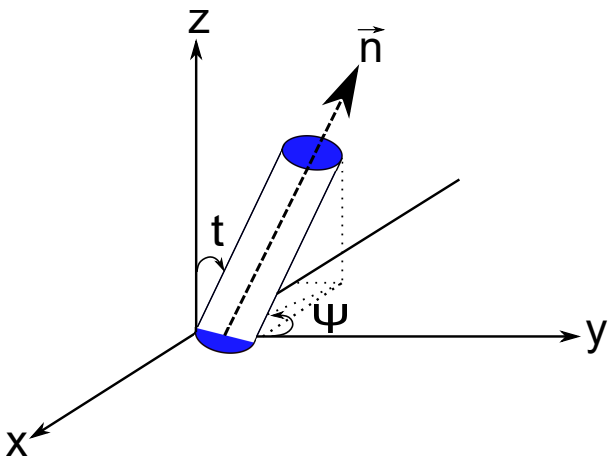

Figure 2.12: Representation of the tilt t, azimuth Ψ and the rotation angle δ of the molecules with regards to its axis n.

Elementary cell geometry

Consider a two dimensional direct network described by:

$$\vec{a}_1 = a[\cos(\gamma)\vec{i} - \sin(\gamma)\vec{j}] \quad \text{and} \quad \vec{a}_2 = b\vec{i} \qquad \text{where } \gamma = (\vec{a}_1, \vec{a}_2) \tag{2.45}$$

Where $\vec{i}$ and $\vec{j}$ are the unit vectors of the cartesian coordinate system.

Respecting the Laue's conditions, the basic vectors of the reciprocal network are calculated as follows:

$$\begin{aligned} \vec{a_1}^* &= 2\pi \frac{\vec{a}_2 \wedge \vec{z}}{\vec{a}_1.(\vec{a}_2 \wedge \vec{z})} = \frac{2\pi}{a \sin\gamma} \begin{pmatrix} 0 \\ -1 \end{pmatrix} \\ \vec{a_2}^* &= 2\pi \frac{\vec{z} \wedge \vec{a}_1}{\vec{a}_1.(\vec{a}_2 \wedge \vec{z})} = \frac{2\pi}{b \sin\gamma} \begin{pmatrix} \sin(\gamma) \\ \cos(\gamma) \end{pmatrix} \end{aligned} \tag{2.46}$$

Two-dimensional films can be organized in three possible networks: an oblique, rectangular or hexagonal network as illustrated in Figure 2.13. The unit cell of the oblique and rectangular lattices is composed of two molecules and that of the hexagonal lattice is composed of one molecule. However, as we consider that the rectangular and the hexagonal lattice are basically the same but differ in their symmetry (a rectangular lattice is asymmetric whereas the hexagonal lattice is symmetric) we have chosen a cell composed of two atoms to describe the hexagonal lattice. On the basis of the number and position of observed first-order peaks, it is possible to estimate the geometry of the lattice and to calculate its parameters as follows [17]:

– **Oblique lattice**: The number of observed first-order peaks is three : $Q_{xy}^{[11]}$, $Q_{xy}^{[1\bar{1}]}$ and $Q_{xy}^{[02]}$. In this case, by convention, $\gamma > \frac{\pi}{2}$ and the parameters of the unit cell are calculated as follows [17]:

$$\begin{aligned} \cos(\gamma) &= \frac{(Q_{xy}^{[1\bar{1}]}/Q_{xy}^{[02]})^2 - (Q_{xy}^{[11]}/Q_{xy}^{[02]})^2}{\sqrt{2(Q_{xy}^{[11]}/Q_{xy}^{[02]})^2 + (Q_{xy}^{[1\bar{1}]}/Q_{xy}^{[02]})^2 - 1}} \\ a &= \frac{4\pi/\sin(\gamma)}{\sqrt{2(Q_{xy}^{[11]})^2 + 2(Q_{xy}^{[1\bar{1}]})^2 - (Q_{xy}^{[02]})^2}} \\ b &= \frac{4\pi/\sin(\gamma)}{Q_{xy}^{[02]}} \end{aligned} \tag{2.47}$$

– **Rectangular lattice**: The number of observed first-order peaks is two. One is doubly degenerate ($Q_{xy}^{[11]}$=$Q_{xy}^{[1\bar{1}]}$) and the second one is $Q_{xy}^{[02]}$. The parameters of the unit cell are calculated according to the equations below:

$$\begin{aligned} \gamma &= \frac{\pi}{2} \\ a &= \frac{4\pi}{\sqrt{4(Q_{xy}^{[11]})^2 - (Q_{xy}^{[02]})^2}} \\ b &= \frac{4\pi}{Q_{xy}^{[02]}} \end{aligned} \tag{2.48}$$

– **Hexagonal lattice** : A first-order peak triply degenerate is observed $Q_{xy}^{[11]}$=$Q_{xy}^{[1\bar{1}]}$=$Q_{xy}^{[02]}$. The parameters of the cell composed of two atoms are calculated as follows:

$$\begin{aligned} \gamma &= \frac{\pi}{2} \\ b &= a\sqrt{3} = \frac{4\pi}{Q_{xy}^{[02]}} \end{aligned} \tag{2.49}$$

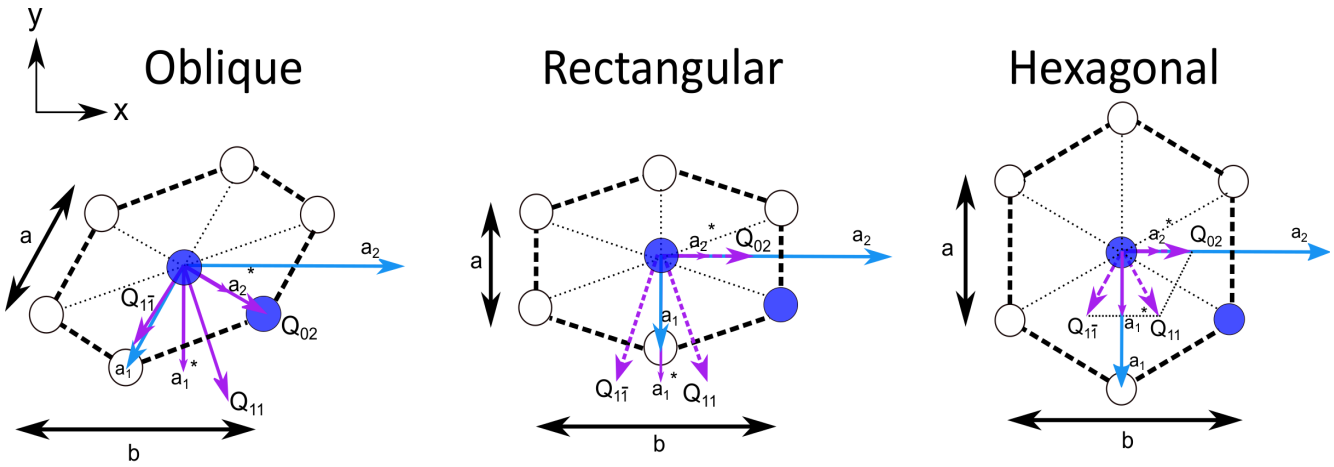

Figure 2.13: The two atoms of the unit cell of an oblique, rectangular and hexagonal network are represented respectively by blue disks, their nearest neighbors by hollow circles. $\vec{a}_1$, $\vec{a}_2$ (light blue) are the basic vectors of the direct lattice and $\vec{a}_1^*$, $\vec{a}_2^*$ (purple lines) those of the reciprocal lattice. $\vec{Q}_{xy}^{[11]}$, $\vec{Q}_{xy}^{[1\bar{1}]}$ and $\vec{Q}_{xy}^{[02]}$ (purple dashes) are the scattering vectors corresponding to the three first-order peaks of non-zero intensity.

To adjust the diffraction peaks, either a Gaussian or a Lorentz function is used. We can estimate the correlation length φ of the crystal from the full-width half-maximum Δ of the peak [37]:

$$\begin{aligned} \varphi &\sim \frac{2}{\Delta_{Lorentz}} \\ \varphi &\sim \frac{2\pi}{\Delta_{Gauss}} \end{aligned} \tag{2.50}$$

Note that since two-dimensional crystals can only be ordered in a quasi-long positional order, we refer to the correlation length to designate the length at which the crystal retains its organization.

Thickness of the Langmuir film

The structure factor, which describes the inner geometry of the molecule, is at its maximum when $\vec{Q}.\vec{n} = 0$. Therefore, for a given value of the component in the plane Q_{xy}, the value of Q_z for which the structure factor thus the intensity are maximum is equal to :

$$Q_z = Q_{xy}.\tan(t).\mid\cos(\Psi)\mid \tag{2.51}$$

Determining the position of the maximum of the intensity of the out-of-plane Bragg rod is an effective way to estimate the tilt of the molecule's chain and the thickness of Langmuir film.

The thickness of Langmuir film can be estimated from the full-width half-maximum FWHM of the peak function that fits Q_z. We can adjust the out of plane peaks by a sine cardinal square peak function of the following form :

$$y = y_0 + \left[A \frac{\sin\left(\frac{\pi(Q_z - Q_{z,max})}{\Delta_{Q_z}}\right)}{\left(\frac{\pi(Q_z - Q_{z,max})}{\Delta_{Q_z}}\right)} \right]^2 \tag{2.52}$$

Where y_0 and A are the baseline and area of the peak function respectively. $Q_{z,max}$ denotes the Q_z at which the peak is at its maximum intensity, i.e. $Q_{z,max} = 0$ if the maximum of the diffraction peak is in the plane. Δ_{Q_z} is the FWHM of the peak, according to , the film thickness h can be estimated by :

$$h = \frac{2\pi}{\Delta_{Q_z}} \tag{2.53}$$

Tilt and azimuth of the molecules

It is possible to estimate the tilt and azimuth of the molecules from the out-of-plane scattering vector $\vec{Q}_z$. The molecules will be perpendicular to the plane of the Langmuir film when $Q_z = 0$. However, when $Q_z \neq 0$, the molecules expect to be tilted and oriented towards a nearest neighbor or a second nearest neighbor or an intermediary direction. The application of the condition ($\vec{Q}.\vec{n} = 0$), in which the structure factor is maximal (Equation 2.51) to first-order peaks leads to the expression of the azimuth and inclination Ψ of the molecules. The detailed calculations of t and Ψ for an oblique and hexagonal lattice can be found in [17] . The tilt $t \in [0, \frac{\pi}{2}]$ and the azimuth $\Psi \in [0, \frac{\pi}{2}]$. In the following paragraph, the possible orientations of the molecules forming an ordered **rectangular network** are presented :

- **Intermediary orientation** : The doubly degenerated peak ($Q_{xy}^{[11]} = Q_{xy}^{[1\bar{1}]}$) have different out of plane peaks where $Q_z^{[11]} > Q_z^{[1\bar{1}]}$. As for $Q_{xy}^{[02]}$, it is also out of plane, $Q_z^{[02]} \neq 0$.
  The azimuth is then expressed by :

$$\cot(\Psi) = \frac{a_2}{a_1} \frac{Q_z^{[02]}}{\left(2Q_z^{[1\bar{1}]} - Q_z^{[02]}\right)} \tag{2.54}$$

  And the tilt by:

$$\tan(t) = \frac{a_2 Q_z^{[02]}}{4\pi \cos(\Psi)} \tag{2.55}$$

- Orientation towards the **nearest neighbor (NN)** : The doubly degenerated peak ($Q_{xy}^{[11]} = Q_{xy}^{[1\bar{1}]}$) is out of plane where $Q_z^{[11]} = Q_z^{[1\bar{1}]} \neq 0$. However, $Q_{xy}^{[02]}$ is in plane so $Q_z^{[02]} = 0$. In such situation $\Psi = \frac{\pi}{2}$ and the expression of molecule's tilt is :

$$\tan(t) = \frac{a_1 Q_z^{[1\bar{1}]}}{2\pi} \tag{2.56}$$

- Orientation towards the **next nearest neighbor (NNN)** : The doubly degenerated peak ($Q_{xy}^{[11]} = Q_{xy}^{[1\bar{1}]}$) and $Q_{xy}^{[02]}$ are both out of plane. $Q_z^{[11]} = Q_z^{[1\bar{1}]} \neq 0$ and $Q_z^{[02]} \neq 0$. In such situation , $\Psi = 0$ and the expression of the molecule's tilt is :

$$\tan(t) = \frac{a_2 Q_z^{[02]}}{4\pi} \tag{2.57}$$

2.3.3 Geometry of Grazing Incidence X-ray Diffraction (GIXD)

When X-rays are incident on a two-dimensional film deposited on a substrate (solid or liquid), two scattered signals can be collected: one from the film and one from the substrate. However, the measured intensity of a diffracted X-ray beam is proportional to the volume of the irradiated object and thus to the penetration length of the beam. Consequently, the signal coming from the substrate will be dominant compared to that coming from the film. The isolation of the wave diffracted by the film from that diffracted by the substrate will not be possible. In order to increase the ratio of the signal scattered by the film to that scattered by the substrate, it is essential to limit the depth of penetration of the X-rays in the volume of the substrate.

As previously discussed, the penetration depth of the evanescent wave can be less than 10 nm. This corresponds approximately to the thickness of a Langmuir monolayer deposited on an aqueous subphase. The total reflection geometry, which generates an evanescent wave, therefore meets the criteria necessary to probe only the Langmuir monolayer and reduce the intensity of the wave diffused by the subphase. This geometry is therefore the one adopted in GIXD measurements to determine the two-dimensional periodicity of a Langmuir monolayer.

2.4 X-ray fluorescence (XRF)

X-ray fluorescence (XRF) is a non-destructive characterization technique that permits to identify the elemental composition of the sample. It results from an inelastic scattering following the impinge of an x-ray beam a sample.

2.4.1 Principle

When an atom is irradiated with X-rays, the electrons are torn from the inner shell of the atoms, the excitation of the atom. Since, the excited state of the atom is unstable, so that to return to its fundamental state, an electron from a higher-energy shell will fill the vacuum and release energy, notably in the form of X-rays. The emitted radiation quanta then correspond to the difference in energy between the excited state and the ground state of the atom. As they are a characteristic of each atom, their analysis makes it possible to recognize the chemical composition of the sample. Hence the principle of fluorescence spectroscopy permits the identification of the elements according to the energy they release following their excitation by X-rays.

The electronic transitions are labeled based on the energy of the different outer shells. One can consider mainly three transitions : K corresponds to the lowest electronic level

followed by L and M.

The number of atoms composing a Langmuir monolayer is much smaller than that of three-dimensional systems. The intensity of the signal coming from XRR, GIXD and XRF coming from a Langmuir monolayer is then much lower than that coming from three-dimensional systems. It is therefore primordial to opt for synchrotron facilities to benefit from intense and well collimated (without divergence) X-rays.

2.5 Synchrotrons

Synchrotron radiations were first detected in the 1940s in General Electric particle accelerator, but were considered parasitic that caused loss of energy of the particles. In the 1960s, Synchrotron x-rays began to emerge as an exceptional source of radiation that overcame the deficiencies of x-ray tubes. Synchrotron radiations have proved essential for a thorough understanding of the condensed matter [50].

2.5.1 Utility of Synchrotron radiation

Synchrotron radiation is of interest due to its exceptional characteristics listed below :

1. High intensity, 10^6 higher than that provided by ordinary laboratories.
2. Wide spectral range; from infrared to hard X-ray.
3. Tunable energy
4. Well collimated cone of light.
5. High brightness/brilliance which indicates the number of photons per second in considering the size of the source and the angle of divergence.

We used the synchrotron facilities: SOLEIL in France and PETRA III in Germany.

2.5.2 Principle of synchrotron radiations

Synchrotron radiation are electromagnetic waves, produced by a relativistic charged particle (electron or positron) when it is accelerated in a curvilinear path under applied magnetic fields. A synchrotron is mainly composed of five principle elements: electron source, linear accelerator, booster ring, storage ring and beamlines. The electron source or electron gun is generated by the thermionic emission of electrons from a hot filament. Under the effect of an electric field, the bunch of electrons will be accelerated in the linear accelerator to an energy of thousands of Mev. Then, the electrons will be transferred to the booster ring composed of two curved sections linked by two straight section. In the booster ring, the electrons are accelerated to an energy of few Gev (2.75 Gev for SOLEIL). After that, the electrons will be transferred to the storage ring, the main component of a synchrotron. The storage ring consists in a periodic set of quasi circular sections, each composed of straight section plus curved section formed of bending magnets (BM). In this section of the synchrotron, electrons travel at a relativistic speed $\sim$(0.999C). The straight sections of the storage ring contain "insertion devices" that are used to produce a

high intensity of synchrotron radiation. The radiation will then be transferred to beamlines where we conduct our measurements. Figure 2.14 shows the main parts, mentioned above, to operate a synchrotron.

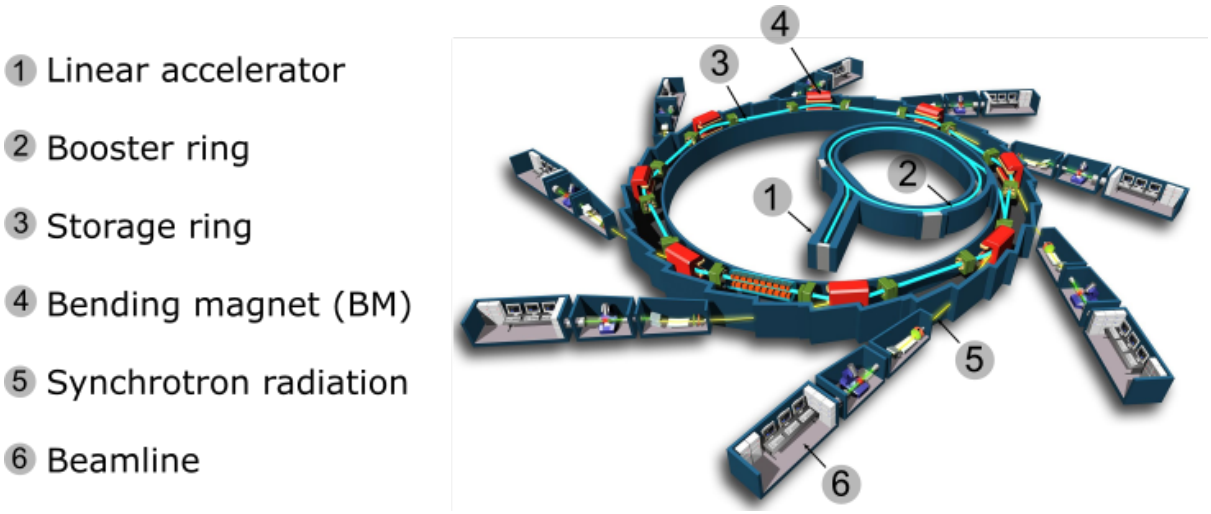

Figure 2.14: Schematic representation of the main operating parts of a synchrotron

Enhancement of characteristics (flux, brilliance, energy) of synchrotron radiation

In order to enhance and control the characteristics of the flux of emitted photons, "insertion devices" are inserted in the straight section of the storage ring. They serve to drive the electron beam with periodic magnetic fields, forcing them to oscillate around its natural path. The resulting cone of synchrotron radiation is therefore well-collimated. There is two type of the "insertion devices" : the wigglers and the undulators. Theses devices consist in a set of N periodic multipole small magnets of inverse polarization. For the wigglers, each one acts as a magnet bending, the waves do not interfere together but add up incoherently. The superposition of waves wiggling from each wiggle enhances the flux and brilliance of the energy of the polychromatic radiation. For the undulator, the waves interfere with each other coherently leading to the emission of a monochromatic radiation but of high brilliancy (10^4 higher than that of Bending magnets) for certain wavelength (see Figure 2.15). One can deduce that the bending magnets and wiggler deliver an almost continuous energy spectrum known as a white beam, while undulator radiates pseudo-monochromatic energy bands.

Synchrotrons deliver radiation of many features, based on which we have categorized synchrotrons. To date, four generations of synchrotrons exists and deliver different characteristics of radiations. For example, the 3^{rd} generation is brighter than the 2^{nd} generation. Figure 2.16 shows the evolution of the brightness of the four generations of synchrotrons over the years as a function of the additional devices specific to each. SOLEIL and PETRA III are synchrotrons of 3^{rd} generation.

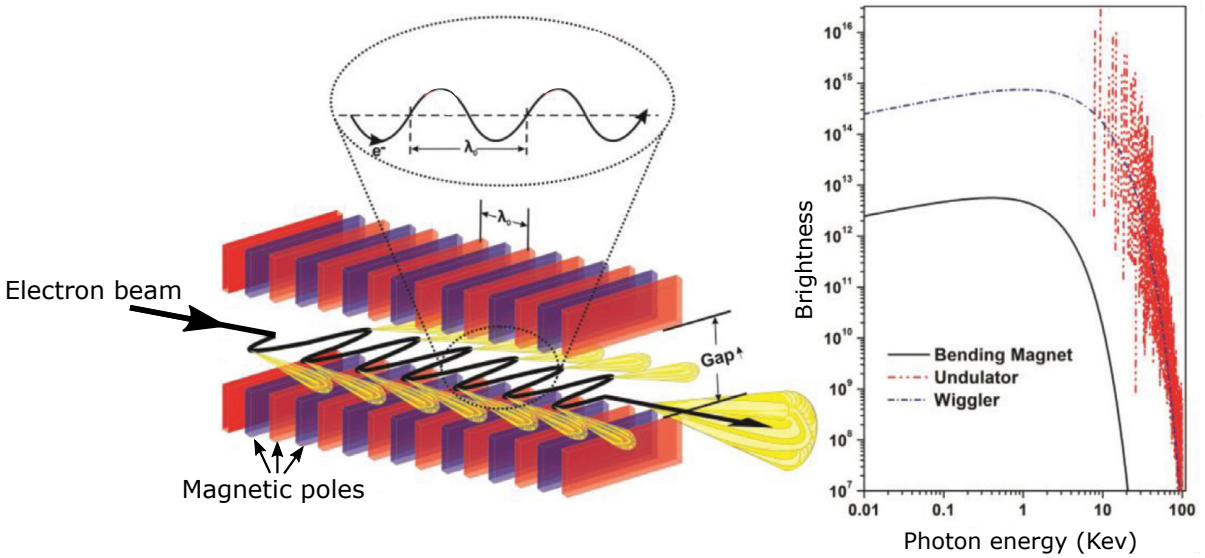

Figure 2.15: On the left, a diagram showing the movement of an electron beam through the wigglers inserted at the straight section of the storage ring. On the right, a spectrum comparing the brightness as a function of the energy of the synchrotron radiation emitted through the bending magnets, undulators and wigglers [50].

2.5.3 Beamline

For each experiment, it is essential to condition the beam to the type of sample: tuning of the energy, choice of the angle of incidence, beam size, etc. Therefore, each beamline consists of main elements that allow us to optimize, emit and detect the beam. Here are these elements :

1. **The primary slits** serve to define the size of the beam.
2. **The monochromator** consists of a double crystal presented at the Bragg condition. It is used to select the corresponding monochromatic beam from the beam source.
3. **The mirrors** control the angle of incidence. They also help to reduce background noise by eliminating the harmonics generated by the monochromator. This results in sharper and more accurate spectra.
4. **The attenuators**, which are made of aluminium, are used to protect the detector from very strong signal intensity.
5. **The sample** is deposited on an adjustable support. In our case, it consists of a Langmuir film.
6. **The Soller's slit** are for GIXD measurements. They optimize the angular resolution of the diffracted beam in the plane of the interface.
7. **The detector**

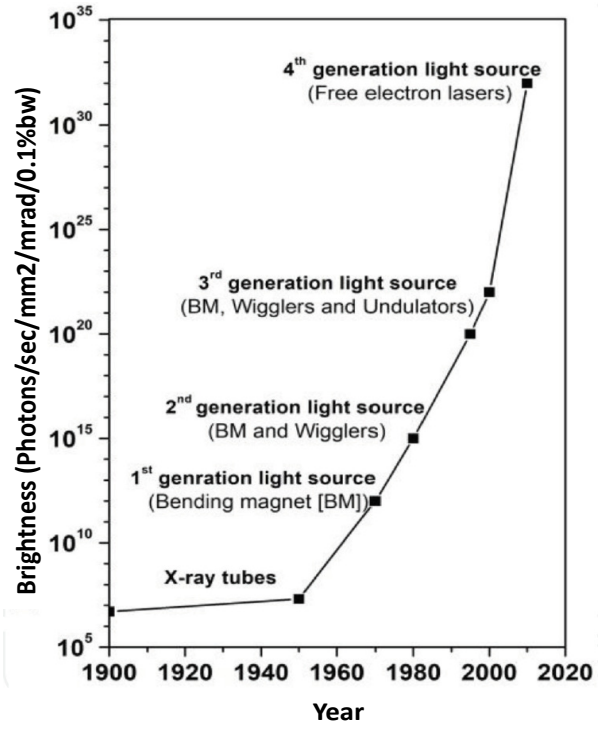

Figure 2.16: Evolution of brightness of synchrotron radiations from the different over time. The image is taken from [50].

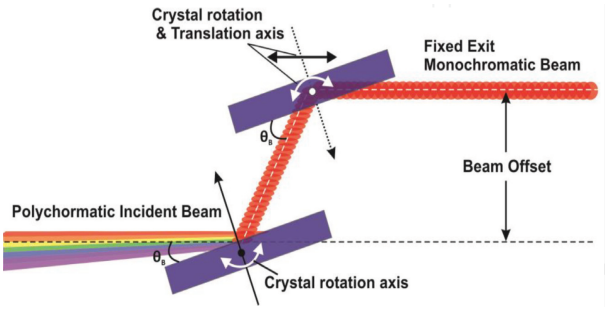

Figure 2.17: Schematic illustration of the double crystal monochromator in the beamline. This image is taken from [50].

2.5.4 Synchrotron Langmuir trough

The Langmuir trough must be suitable for X-ray measurements. The measurement of the surface pressure isotherm is carried out in a manner similar to that done in ordinary laboratories. The trough is isolated from the outside atmosphere by a hermetic cover. In order to avoid the arbitrary scattering of X-rays by the air molecules surrounding the trough, we circulate a continuous flow of helium. The trough is also equipped with Kepton windows that allow beam penetration and scattering with minimal interaction with the window. The water meniscus of the trough must be significant (higher than the lateral edges of the trough) to ensure successful measurements in the grazing incidence geometry. The position of the trough relative to the incident beam is controlled by a movable plate that holds it from below. Finally, it is mounted on an anti-vibration device to eliminate mechanical vibrations.

In the next part of this chapter, we will discuss the characterization techniques provided by our laboratory for the mesoscopic and microscopic analysis of Langmuir films. These include: atomic force microscopy (AFM) and Brewster angle microscopy (BAM).

2.6 Brewster angle microscopy (BAM)

Brewster's angle microscopy (BAM) was developed by Henon and Meunier in 1991 based on the principle of ellipsometry [51]. It is a technique for visualizing the inhomogeneities of a film of molecular thickness on the surface of water (or liquid subphase) on a mesoscopic scale. BAM technique obviously relies on Brewster's angle theory, named after Sir David Brewster who discovered it in 1812.

2.6.1 Principle

According to the Snell-Descartes law 2.17 and the Fresnel coefficient elaborated in 2.22 and 2.21, the reflectivity coefficient of a p-polarization ($r_{//}$) and s-polarization ($r_{\perp}$) are expressed as:

$$r_{//} = \frac{n_t \cos\theta_i - n_i \cos\theta_t}{n_t \cos\theta_i + n_i \cos\theta_t} = \frac{\tan\left(\theta_i - \theta_t\right)}{\tan\left(\theta_i + \theta_t\right)}$$
$$r_{\perp} = \frac{n_i \sin\alpha_i - n_t \sin\alpha_t}{n_i \sin\alpha_i + n_t \sin\alpha_t} = -\frac{\sin\left(\theta_i - \theta_t\right)}{\sin\left(\theta_i + \theta_t\right)}$$

As we work now within the framework of classical optics and not anymore in X-rays "world", we have replaced α with θ, the angle formed by the normal to the interface and the light beam ($\theta = \frac{\pi}{2}$ - α). Here $n_i = n_{air} = 1$

Consider the particular case of a light beam sent in p-polarization on the Fresnel interface under Brewster's angle θ_b i.e. :

$$(\theta_i + \theta_t) = \frac{\pi}{2} \quad \text{and} \quad \theta_i = \theta_b = \arctan\left(\frac{n_t}{n_i}\right)$$

In the case of Fresnel interface, the refractive index varies abruptly from n_i to n_t across

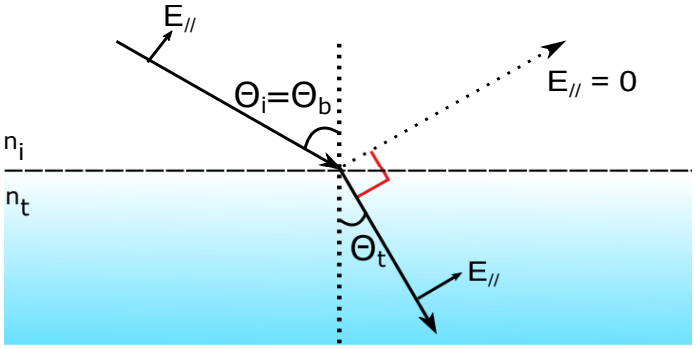

Figure 2.18: Reflection at Brewster angle

interface situated at z = 0. For an incidence at the Brewster angle, reflection of p-polarized light is not possible. This can be interpreted in two versions:

1. From a physical point of view: The light is reflected in medium "i" due to its scattering by the dipoles (atoms) oscillating perpendicularly to the direction of propagation of the refracted wave in medium "t". Since the wave cannot be scattered in the same direction as the oscillations of the dipoles, which in our case is that of the supposedly reflected light, reflection cannot take place.

2. From a mathematical point of view: the reflection coefficient $r_{//}$ is null because its denominator tends towards infinity leading to the suppression of the reflectivity.

Figure 2.19 shows that $r_{//}$ is set at zero at Brewster angle for air-water interface but $r_{\perp}$ can never worth zero.

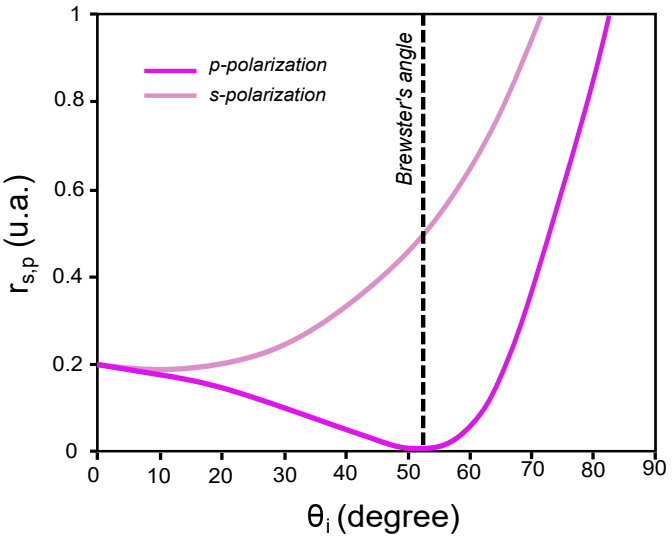

Figure 2.19: Fresnel reflection coefficients in p and s polarization ($r_{//}$ and $r_{\perp}$) as a function of the angle of incidence (θ_i).

Consider now the same situation as before, but taking into account the roughness, thickness, electron density and optical anisotropy of a real interface or of a Langmuir film situated at $z \in [0; L]$. Recall that in this case, the refractive index change continuously - and not abruptly - from n_i to n_t through the electronic density profile that characterizes the real interfaces (see Figure 2.20) [52]. In this case, the reflection coefficient is not zero but at its minimum, so the reflectivity does not vanish completely. This underlines the fact that the reflected intensity depends strongly on the physical and chemical properties of the film.

In this perspective, BAM was designed to visualize, on a macroscopic scale, the monomolecular films deposited on the water surface. Its principle consists in sending a p-polarized laser beam at the Brewster angle, which is 53.1° for the air-water interface, and then measuring the variation in intensity of the beam reflected by the inhomogeneous surface. The first light contrasts are observed between a Langmuir film and the water surface. It is also possible to follow the first-order phase transition where two phases of anisotropy, different density and thickness coexist. Thus, the film will be formed of multiple inhomogeneous domains that reflect light at different intensities. BAM can therefore be used to detect, as a spatial function, the light intensity contrast of the reflectivity

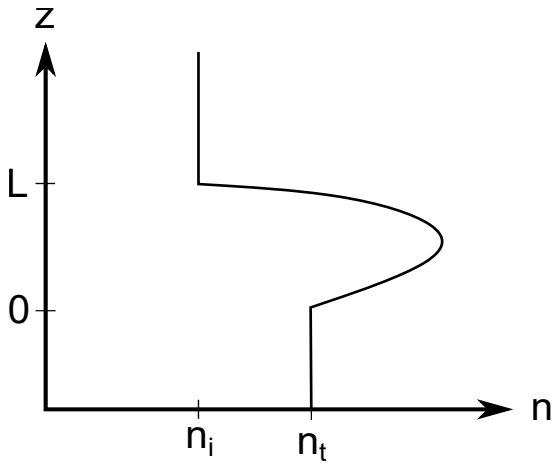

Figure 2.20: Diagram of the refractive index variation across an interface located at z $\in$ $[0; L]$ and separating two media of different refractive indices.

coming from the inhomogeneous thickness, density and anisotropy of the film. Finally, it is possible to construct the image of the film using a lens.

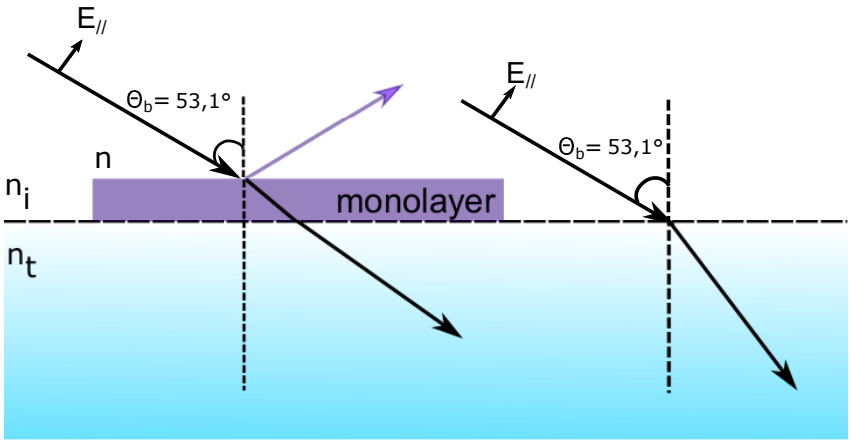

Figure 2.21: Principle of the Brewster angle microscope

2.6.2 Experimental set-up

The wavelength of the laser beam is equal to $\lambda = 523$ nm. The domains observed by BAM are of the order of tens of micrometers. We have an objective lens (x10) that allows the formation of the image of the surface of the water and a CCD (Charged-Coupled Device) camera that records the information. However, the objective lens is not perpendicular to the surface of the water and therefore not perpendicular to its optical axis. This leads to the recording of partially clear images, only the lines of the image of the area on the water belonging to the optical axis of the lens will be sharp.

2.7 Atomic force microscopy (AFM)

The invention of the scanning tunneling microscopy (STM), which earned Rohrer and Binning the Nobel Prize in 1986, was the driving force behind the development of atomic

force microscopy (AFM) by IBM researchers Binning, Quate and Gerber [53]. AFM is a local probe microscopy which belongs to the family of scanning probe microscopy (SPM). It allows the imaging of a surface in air or liquid media, at different temperatures and for different types of samples (conductive, non-conductive, biological, organic, etc.). The image obtained is three-dimensional with a vertical resolution ranging from a few tens of microns to one nanometre and a horizontal resolution ranging from a few tens of microns to a few hundred nanometres. It is a technique which, in terms of resolution, is at the interface between optical microscopy and x-ray scattering techniques.

2.7.1 Principle

AFM measurement allows the study of Langmuir films transferred on solid substrates by Langmuir-Blodgett or Inverse-Langmuir-Schaefer procedures. The principle of AFM consists of scanning the sample by an extremely sharp probe tip - ideally a cone ending in a single atom - attached to the end of a cantilever as shown in Figure 2.22. It is assumed that tip-sample interactions are limited to atomic repulsion forces at short-range and Van der Waals' attractive forces at long-range. In fact, the interaction is approximated by the model of the Lennard-Jones potential, illustrated in Figure 2.24. "V(r)" represents the potential for interaction between a pair of uncharged atoms (or molecules) separated by a distance "r". This model highlights the competition between the long-range and short-range interactions and is expressed by the following equation:

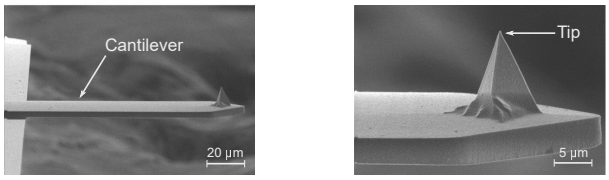

Figure 2.22: Tip and cantilever observed by electronic microscopy [54].

$$V(r) = 4\epsilon\left[\left(\frac{\sigma}{r}\right)^{12} - \left(\frac{\sigma}{r}\right)^{6}\right] \tag{2.58}$$

ϵ is homologous to a potential and it sets the depth of the potential well (minimum energy). σ is homologous to a length and is the distance at which the potential is zero. The first term describes the repulsion potential: the short-range interactions and the second one describes Van der Walls' attraction potential: the long-range interactions. One can obviously trace the force of interaction from the potential energy by the following formula :

$$\vec{F} = -\overrightarrow{\text{grad}}V(r) \tag{2.59}$$

The cantilever, acting as a force sensor, deflects when the tip and the sample interact with each other. Therefore, if we record at any point the cantilever deflection, we will be able to accede to the topography of the sample and to construct its image. Its operating principle is illustrated in the figure 2.23 and its measuring principle is detailed below :

- The sample is scanned horizontally, using a piezoelectric ceramic system that allows the tip to be moved relative to the sample or vice versa.
- When the tip interacts with the sample, a laser beam is reflected by the deflected cantilever and redirected by a mirror to be detected by a set of photodiodes.
- The intensity received by each diode which is a function of the height and the twist of the tip is used in a feedback loop to maintain the deflection of the cantilever.

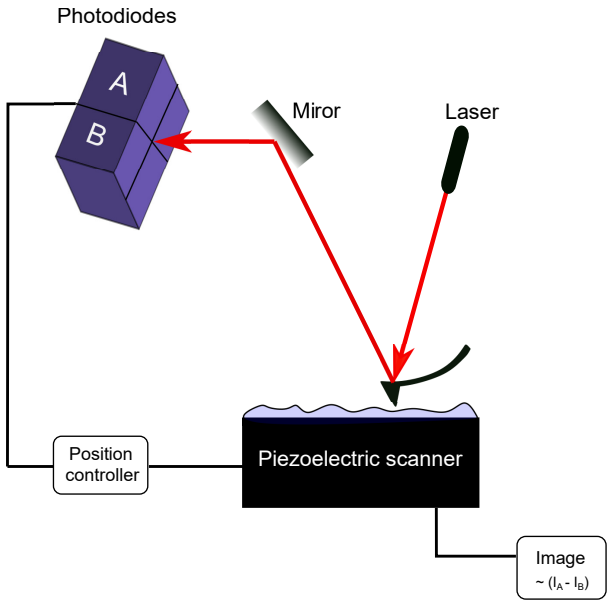

Figure 2.23: Representative scheme of the operating principle of an AFM.

This process is necessary to keep the system scanning the sample with a constant force.

- The signal will be processed by a measurement acquisition system and will eventually lead to the reconstruction of a three-dimensional image of the sample.

2.7.2 Imaging modes

Atomic force microscopy operates in three main modes as illustrated in Figure 2.24:

- Contact mode
- Non contact mode
- Intermittent mode or tapping mode which we used in our measurements

Contact mode

The contact mode implies that the tip is at an infinitely small distance from the atoms of the sample, so the forces involved are of the repulsive type. As mentioned above, it is necessary to maintain a constant measuring force, which in our case means maintaining a constant interaction between the tip and the sample. Therefore, the deflection of the cantilever must be enslaved by moving the sample in the vertical direction to keep the interaction between them constant. This mode offers the best image resolution, but it is not recommended and is not suitable for probing soft samples such as Langmuir organic films. This is because the adhesion and friction forces generated during the interaction between the tip and the soft sample may destroy the tip and/or the sample.

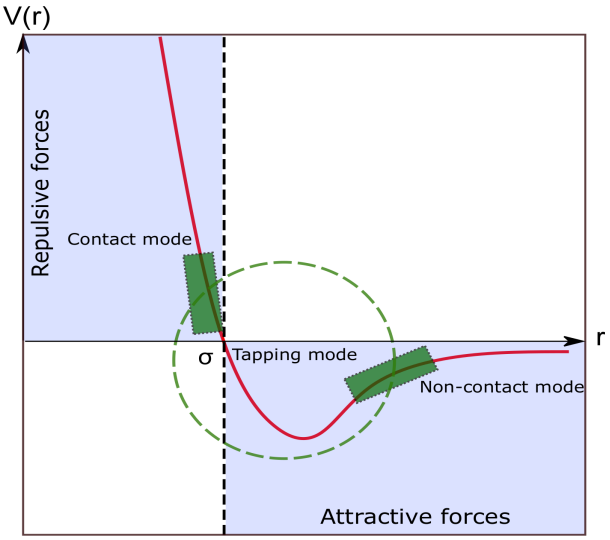

Figure 2.24: The Lennard-Jones potential shown as a function of the tip-sample distance. It also shows the different AFM imaging modes.

Non contact mode

In this mode, we assimilate the tip to a forced harmonic oscillator that is excited by a piezoelectric system at or near its resonant frequency. It oscillates at low amplitude and away from the surface of the sample. Here, the type of the interaction is Van der Waals. When the tip interacts with the sample the resonance frequency of the cantilever shifts. In order to maintain a constant gradient of the interaction forces, there is a need to move vertically the cantilever to keep the resonance frequency constant. This mode is rarely used in topographic measurements. Indeed, due to the fact that the tip oscillates away from the sample surface, the interaction forces are low, of the order of 10 nN, and thus the topographic image is of low resolution in z direction.

Intermittent mode or tapping mode

As in the non-contact mode, the tip is excited at or near its resonant frequency. However, in this mode, the amplitude of the oscillation is large enough to allow the tip to oscillate in the region close to the potential well of the Lennard-Jones curve. Indeed, the tip oscillates vertically under a known frequency. When the tip oscillates in the repulsive region, the amplitude is damped and the phase of the oscillations is modified. As a result, the piezoelectric wedge moves vertically to bring the resonant frequency back to the set point. The photodiode thus detects the amplitude variation and phase shift and leads to the construction of the topography and a phase image of the sample. Indeed, the tip is sensitive to the chemical nature of the sample: viscosity, density... which causes a phase shift of the oscillations each time it comes into contact with zones of different chemical nature. The tapping mode is very interesting because it provides simultaneously two images carrying topographic and phase information on the sample. Another advantage of this mode is that it is, in terms of force intensity, intermediate between the contact and non-contact mode. The sample is therefore not destroyed by the tip and the images are of good resolution.

Chapter 3

Pure $[C_{20}mim]^+[NTf_2]^-$ Langmuir film and bibliographical study

Contents

This chapter presents the study of $[C_{20}mim]^+[NTf_2]^-$ pure Langmuir film deposited on the air-water interface. It also discusses some studies in the literature on the behavior of IL molecules at the interface with graphene. The radiolysis procedure of surface X-rays is also addressed in the framework of our study.

3.1 Ionic liquids (ILs)

3.1.1 Historical overview

In 1807, shortly after Volta claimed that a "pile" of alternating copper and zinc plates, immersed in an acid solution, could produce electric current, Humphrey Davy made a surprising discovery [55]. He used molten alkali metal salts to pass electricity through a voltaic pile under the influence of an electric field. He thus marked for the first time the pioneering behavior of ionic liquids (IL) in the field of energy storage. However, the discovery and synthesis of the first IL, **liquid at room temperature**, dates from 1914. In that year, Walden reported the properties and synthesis of ethylammonium nitrate with a melting point of 12°C, by neutralization of ethylamine with nitric acid [56, 57, 58]. Since then, numerous researches have been devoted to understanding the behavior of IL in energy storage devices such as supercapacitors and in many other fields.

3.1.2 Definition

The literature provides a set of synonyms suitable to describe ILs such as "low temperature molten salt", "room temperature molten salt", "liquid organic salt", "salts with a melting point lower than 100°C"... Today, the definition adequate enough to define ILs is as follows : **salts composed of an organic cation and an inorganic anion, having a melting point below the boiling point of water**. Given the number of ions that exist, the combinations to compose ILs are numerous. However, and despite the feasibility and ease of synthesizing ILs, the number of ILs discussed in the literature remains modest compared to their possible number. In fact, although all ILs have common properties such as low vapor pressure, high viscosity when they are fluids..., almost every IL has at least one characteristic different from the others that requires a fundamental study for each one [59, 60, 61]. The growing interest in ILs is attributed to their versatility, green chemistry and unique properties.

3.1.3 Families of ILs

ILs can be grouped into families that are based on the same cation. The main ones are: Imidazolium, Pyridinium, Pyrrolidinium, Pyrazoliums... whose molecular structures are illustrated in Figure 3.1(A). The combination of each of them with another anion gives them specific and different properties. Most anions are inorganic. Figure 3.1(B) shows the molecular structure of some of them.

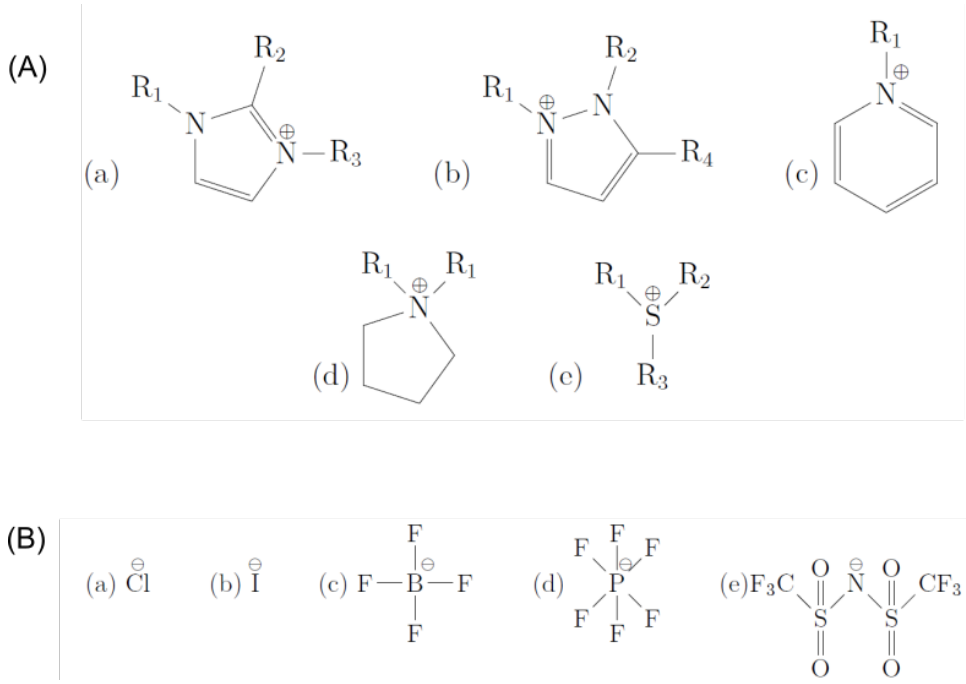

Figure 3.1: Molecular structure of **(A) cations families** of : (a) Imidazolium, (b) Pyrazolium, (c) Pyridinium, (d) Pyrrolidinium and (e) Sulfonium. Molecular structure of **(B) anions families** : (a) Chlorure, (b) Iodure, (c) Tétrafluoroborate, (d) Hexafluorophosphate.

3.1.4 Properties of ILs

ILs appear as promising electrolytes for energy storage devices [62, 63]. They are characterized by a wide stable potential window, ionic nature and low vapor pressure that allow them to overcome the problems of conventional aqueous electrolytes . They are also recyclable, non flammable and non-toxic, which makes them green solvents [64]. Green chemistry is a discipline that unifies the principles of efficient, low-cost and environmentally friendly chemical synthesis with good waste management. Its main concern is to curb the production and mishandling of hazardous chemicals...

3.1.5 Organization of ILs Langmuir films at the air-water interface

The general structural composition of an IL is an amphiphilic cation consisting of a polar head group, an apolar alkyl chains and a polar anion. The polar-apolar and polar-polar interactions are always in competition which leads to a segregation between the charged and uncharged parts of the IL. Triolo et al. [65] showed that this segregation is the reason for their structural organization at room temperature. Thanks to this competition between charged and uncharged domains, ILs possess an amphiphilic character. Some of them are able to form stable Langmuir films at the air-water interface. For example, Bonatout et al. studied $[C_{18}mim]^+[NTf_2]^-$, an Imidazolium-based IL, by Langmuir films at the air-water surface [39]. Its cation consists of an Imidazolium ring and an alkyl chain of 18 carbon atoms. Its anion is one of the least hydrophilic anions. The coexistence of the polar and apolar domains within the same entity allow $[C_{18}mim]^+[NTf_2]^-$ to form a stable Langmuir film. It is formed in an unorganized monolayer at low surface pressures

but in an organized trilayer at a collapse plateau.

Among the ILs that are capable of forming stable Langmuir films on water surface, we are particularly interested in the 1-eicosyl-3-methylimidazolium bis(trifluoromethylsulfonyl)imide **$[C_{20}mim]^+[NTf_2]^-$**.

3.2 $[C_{20}mim]^+[NTf_2]^-$

It is an Imidazolium-based IL of molecular formula : $C_{26}H_{47}N_3F_6O_4S_2$. Its molecular structure is illustrated in Figure 3.2. It is in the form of a white powder at room temperature. Its cation $[C_{20}mim]^+$ is asymmetric and is composed of a hydrophilic Imidazolium ring and a hydrophobic alkyl chain composed of 20 carbon atoms and is anion is $[NTf_2]^-$.

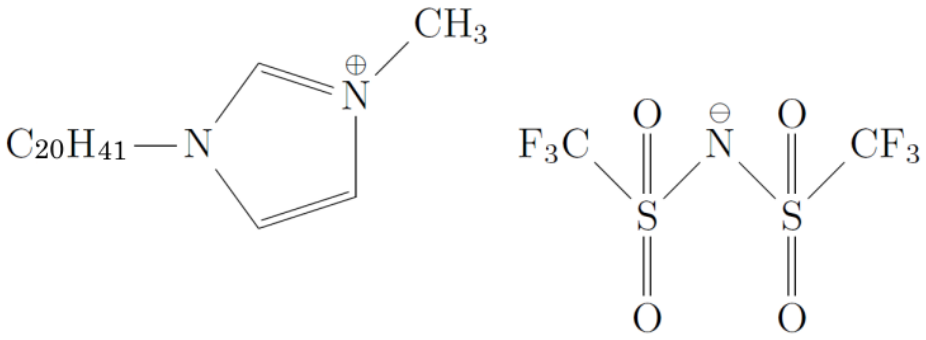

Figure 3.2: Molecular structure of the ionic liquid $[C_{20}mim]^+[NTf_2]^-$.

To our knowledge, $[C_{20}mim]^+[NTf_2]^-$ is barely studied in the literature. However, many fundamental studies have been devoted to the global understanding of the Imidazolium-based ILs. Montalban et al. studied the effect of temperature, anion nature and alkyl chain length on the density of Imidazolium-based ILs [66]. They observed that the density of ILs increases with decreasing alkyl chain length. They expressed the volume of alkyl Imidazolium cations in the Equation 3.1 as a function of temperature and the number of carbons in the alkyl chain. They also expressed the volume of a list of anions, including $[NTf_2]^-$, as a function of temperature in the Equation 3.2. All our measurements were performed at constant temperature T = 293.15 K.

$$V_{al-imid} = (0.08159 + 0.01697 \times N_C)(1328 + 1.120 \times T) \tag{3.1}$$

Where $V_{al-imid}$ is the volume of alkyl Imidazolium cations and is expressed in nm^3. N_C is the number of carbons in the alkyl chain. T is the temperature and is expressed in Kelvin. We thus obtain $V_{C_{20}mim} = 697$ Å^3.

$$V_{NTf_2} = 188.2 + 16.17 \times 10^{-2} \times T \tag{3.2}$$

Where V_{NTf_2} is the volume of $[NTf_2]^-$ and is expressed in nm^3.T is the temperature and is expressed in Kelvin. We thus obtain $V_{NTf_2} = 235$ Å^3.

The theoretical length of an elongated C_{20} alkyl chain is calculated by :
$L_{max} = 1.26 \times N_C + 1.46 = 27$ Å. The diameter of an Imidazolium ring is approximately

5 Å [4] leading to a total length of an elongated cation $[C_{20}mim]^+$ to be about 32 Å. Based on Holbrey et al. [67]the estimated dimension of an elongated crystalline structure of the anion, $[NTf_2]^-$, is ∼9.38Å × ∼3Å × ∼3Å.

3.2.1 Macroscopic description at the air-water interface

In order to describe the behaviour of the $[C_{20}mim]^+[NTf_2]^-$ film on water surface, we measured the Π-A isotherm. Figure 3.3 (a) and Figure 3.3 (b) show respectively the Π-A isotherm and the inverse of the compressibility of $[C_{20}mim]^+[NTf_2]^-$ Langmuir film deposited at the air-water interface. Recall that the inverse of the compressibility corresponds to $\chi^{-1} = -A\frac{\partial \Pi}{\partial A}$. We have chosen to plot χ^{-1} instead of χ to avoid scale problems because perfectly flat plateaux are infinitely compressible. The deposited amount of IL molecules corresponds to A = 1.32 nm^2.$molecule^{-1}$. Three increasing regions can be identified : **region (i)**, **region(ii)** and **region (iii)**.

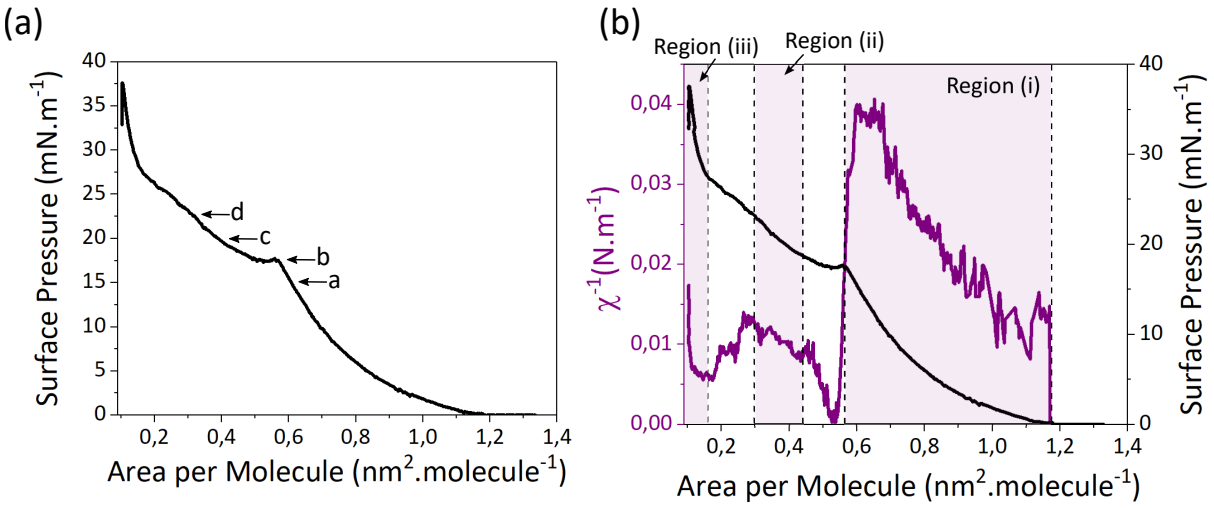

Figure 3.3: Π-A isotherm of $[C_{20}mim]^+[NTf_2]^-$ Langmuir film deposited at the air-water interface.

For molecular areas greater than A = 1.17 nm^2.$molecule^{-1}$, the surface pressure of the IL film is Π = 0 $mN.m^{-1}$ and χ^{-1} = 0 $N.m^{-1}$. This indicates that the film undergoes a plateau of a phase coexistence, which one of the phases is a diluted phase. **The plateau is then followed by region (i) which is limited between A = 1.17 nm^2.$molecule^{-1}$ and A = 0.56 nm^2.$molecule^{-1}$.** In this region, the surface pressure increases gradually from Π = 0 $mN.m^{-1}$ to Π = 17.5 $mN.m^{-1}$. The inverse of the compressibility increases to χ^{-1} = 0.04 $N.m^{-1}$ (χ = 25 $m.N^{-1}$). The film in region (i) is in a (LE) phase. At the end of region (i), the slope of the inverse of the compressibility drops, indicating the beginning of the formation of a plateau. It extends to (Π = 19 $mN.m^{-1}$; A = 0.43 nm^2.$molecule^{-1}$). **The plateau is then followed by region (ii) which is limited between A = 0.43 nm^2.$molecule^{-1}$ and A = 0.30 nm^2.$molecule^{-1}$.** In this region, the surface pressure of the film increases from Π = 19 $mN.m^{-1}$ to Π = 23 $mN.m^{-1}$. The inverse of the compressibility decreases with respect to region (i) and reaches χ^{-1} = 0.012 $N.m^{-1}$ (χ = 83 $m.N^{-1}$). At A = 0.30 nm^2.$molecule^{-1}$, the slope

of the inverse of the compressibility drops indicating the beginning of the formation of a second plateau. It extends to (Π = 27 mN.m^{-1}; A = 0.17 nm^2. molecule^{-1}). **The plateau is then followed by region (iii) which is limited between A = 0.17 nm^2. molecule^{-1} and = 0.10 nm^2. molecule^{-1}.** In this region, the surface pressure increases to Π = 37.5 mN.m^{-1} and then drops, indicating film collapse. The inverse of the compressibility is χ^{-1} = 0.018 N.m^{-1} (χ = 55 m.N^{-1}).

Discussion

As mentioned in section 3.1.5, the balance between the hydrophilic and hydrophobic parts of an IL is the condition to form a stable Langmuir film at the air-water interface. As the Imidazolium rings are hydrophilic and the alkyl chains hydrophobic, the rings must be in contact with water while the chains must be oriented towards the air. As for $[NTf_2]^-$, its hydrophobicity and electrostatic interactions with the ring suggest a position close to the ring but in contact with the air. An elongated aklyl chain has a cross-section of about 0.18 nm^2 [37]. A flat Imidazolium ring has a cross section close to 0.5 nm^2 while a vertically ordered Imidazolium ring has a cross section close to 0.3 nm^2 [68, 69]. Thus, the surface of $[C_{20}mim]^+$ formed of elongated alkyl chains is defined by the cross section of the Imidazolium ring. The cross section of the $[NTf_2]^-$ is 0.09 nm^2 when vertical to the water surface and 0.28 nm^2 when horizontal to the water surface. When the $[NTf_2]^-$ is in the same horizontal plane as the ring, an elongate IL must have a molecular area between 0.77 nm^2 and 0.40 nm^2.

The lift-off area of $[C_{20}mim]^+[NTf_2]^-$ Langmuir film is A = 1.17 nm^2. It is therefore determined by the area occupied by the alkyl chains. $[NTf_2]^-$, in this case, can be considered as occupying a position in the same horizontal plane of the rings, but in contact with the air. The compressibility of the film in region (i) is χ = 25 m.N^{-1}, which corresponds to a (LE) phase. The film in this region is formed as a monolayer. At the end of region (i), a first plateau is observed at A = 0.56 nm^2.molecule^{-1} and extends to A = 0.43 nm^2.molecule^{-1}. The molecular area of the film, at the end of the plateau, is close to the minimum area (A = 0.40 nm^2.molecule^{-1}) that can be occupied by an elongated IL whose $[NTf_2]^-$ is the same horizontal plane as the ring. Across this plateau, the film considers one of the three following situations. (1) A reorganization of the compounds on the surface of the water while the film remains as a monolayer. (2) The collapse of the anions. (3) The collapse of the IL in a multilayer film. In the first two situations, the film thickness should remain the same as it was just before the plateau or increase by a maximum of 0.9 nm, if the anions collapse vertically with the cations. In the third situation, the film thickness should at least double after the plateau.

The compressibility of the film in region (ii) increases compared to to region (i). In principle, the higher the surface pressure, the less compressible the film is. However, if the monolayer collapses to a multilayer across this plateau, one should consider a 3D compressibility. It is related to 2D compressibility by the relation χ_{3D}= eχ_{2D}, where e is the layer thickness.

At the end of region (ii), a second plateau is observed at A = 0.30 nm^2.molecule^{-1} and extends to A = 0.17 nm^2.molecule^{-1}, which is smaller than that of an elongated

$[C_{20}mim]^+[NTf_2]^-$. Across the two plateaux, the molecular area of the film thus decreases by a factor of 3.2. They can be considered a two collapse plateaux.

After the plateau, region (iii) starts. It is of compressibility of about $\chi = 55$ m.N^{-1}. The film in this region is 3D and degrades at $\Pi = 37.5$ mN.$^{-1}$.

BAM measurements

Tassler et al. [11] studied the film by BAM measurements and recorded the images obtained at different surface pressures (see Figure 3.3). At $\Pi = 15$ mN.m^{-1}, a surface pressure lower than that of the first plateau, a dark phase of a homogeneous surface can be observed (Figure 3.4-a). It indicates that the film is formed of a monolayer, which is in agreement with the Π-A isotherm. At the end of the first increasing region, at $\Pi = 16.9$ mN.m^{-1} (Figure 3.4-b), a coexistence of phases appears. One can observe the dark phase attributed to the monolayer, highlighted before the plateau, in a coexistence with a light grey phase in the form of circular plate domains. After further compression on the plateau, the circular plates increase in number and begin to coalesce gradually (Figure 3.4-c). At surface pressures higher than that of the plateau, the number of circular plates increases further, the dark phase disappears but a third, lighter phase appears (Figure 3.4-d).

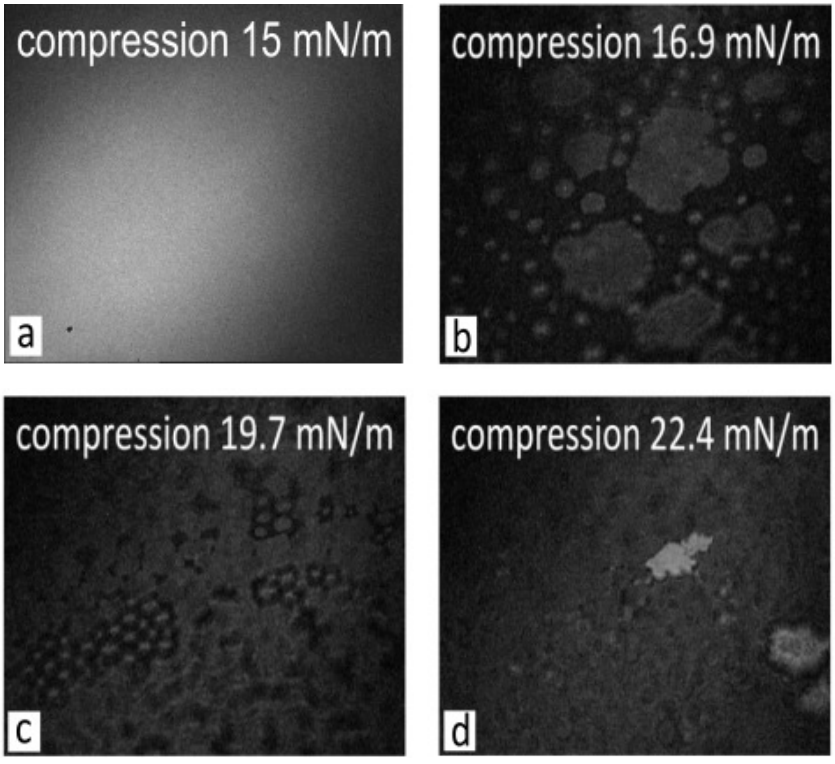

Figure 3.4: BAM images obtained on $[C_{20}mim]^+[NTf_2]^-$ Langmuir film deposited at the air-water interface at different surface pressures (reproduced from [11]).

3.2.2 Transfer on solid substrates

We transferred the films on silicon substrates by Langmuir-Blodgett in order to study them by AFM. The wafers were cleaned by Piranha so they were hydrophilic. We performed two transfers, one at $\Pi = 15$ mN.m^{-1} (before the first plateau) and a second one at $\Pi = 22$ mN.m^{-1} (between the two plateaux) (see Figure 3.5).

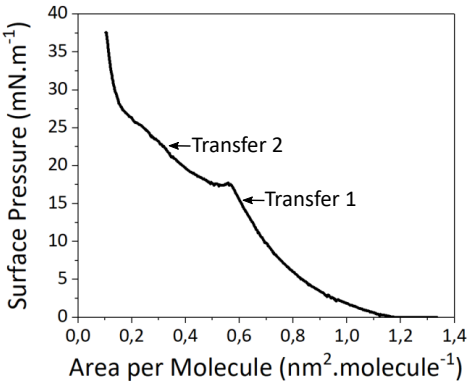

Figure 3.5: Π-A isotherm of $[C_{20}mim]^+[NTf_2]^-$ Langmuir film deposited at the air-water interface.

Figure 3.6 shows the AFM topographic image of the film transferred at $\Pi = 15$ mN.m^{-1}. A homogeneous surface is observed. It could correspond to an IL monolayer covering the entire wafer. However, the film, at this surface pressure, is in a (LE) phase ($\chi = 25$ m.N^{-1}), so not very dense. The transfer considers a possible failure. In such a case, the observed homogeneous surface could correspond to silicon wafer.

Figure 3.7 (a) and Figure 3.7 (b) are respectively the topographic and phase images of the film transferred at $\Pi = 25$ mN.m^{-1}. Domains of d $\sim$ 8 nm thick, formed on a homogeneous surface, are observed. The domains and the homogeneous surface are 10° phase shifted which indicates that they are of a different nature. The thickness of $[C_{20}mim]^+[NTf_2]^-$ formed of elongated alkyl chain can vary between 3.2 nm and 4.1 nm, depending on the position of the anion (whether its in the same vertical or horizontal plane of the cation). The thickness of the domains therefore suggests that they may be formed of bi or multilayers of $[C_{20}mim]^+[NTf_2]^-$. The homogeneous surface is assumed to be the silicon surface.

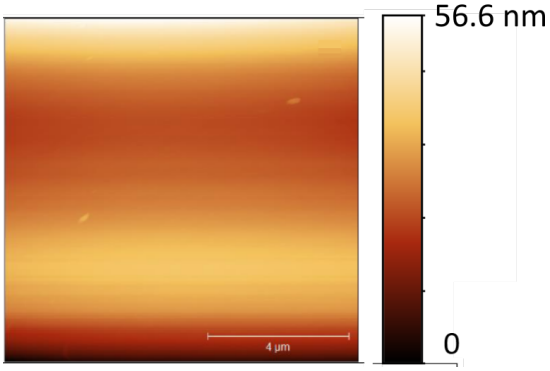

Figure 3.6: AFM topographic image measured on $[C_{20}mim]^+[NTf_2]^-$ Langmuir-Blodgett film deposited on Si/SiO_2 at $\Pi = 15$ mN.m^{-1}.

On the basis of the macroscopic study and AFM images, it can be concluded the following :
At surface pressures lower than $\Pi_{plateau} = 17.5$ mN.m^{-1}, the IL film is formed as a monolayer. It then collapses into a multilayer through a first plateau. The thickness of the multilayer domains suggests that the collapse occurred by the superposition of the IL, vertically. After further compression, the collapse of the film continues through a second plateau. At $\Pi = 37.5$ mN.m^{-1}, the film degrades.

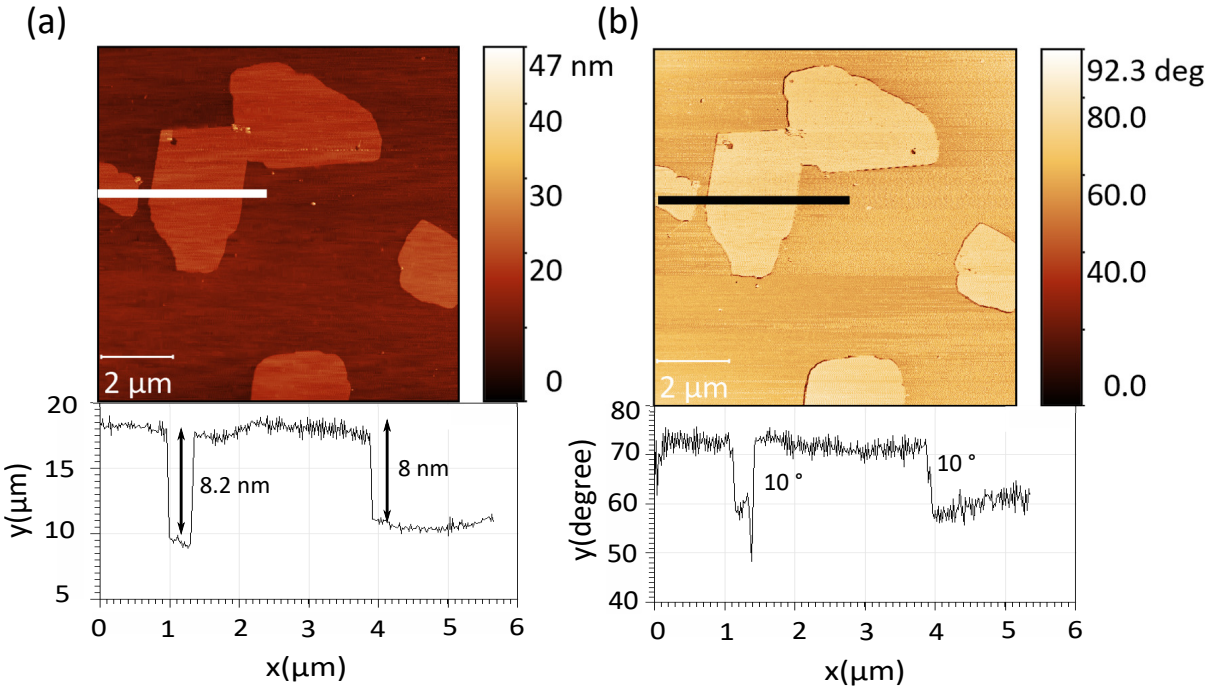

Figure 3.7: AFM topographic (a) and phase (b) images measured on $[C_{20}mim]^+[NTf_2]^-$ Langmuir-Blodgett film deposited on Si/SiO_2 at $\Pi = 25$ mN.m^{-1}.

3.2.3 Characterization by X-ray scattering at the air-water interface

XRR measurements

Tassler et al. performed XRR measurements at PETRA III synchrotron, on $[C_{20}mim]^+[NTf_2]^-$ Langmuir film deposited at the air-water interface. Figure 3.8-A and Figure 3.8-B are respectively the XRR measurements and the electron density profiles of the film at different surface pressures. They observed that the film is formed, in the first growing region of the isotherm, by a monolayer where the alkyl chains are directed towards the air. Then, at surface pressures higher than that of the first plateau, the molecules are vertically superposed and form a multilayer.

GIXD measurements

They also studied the film's structure by GIXD measurements at the SIRIUS beamline at SOLEIL. At surface pressures lower than that of the first plateau, they didn't succeed in observing any diffraction peaks. The film at these pressures is in (LE) phase so it is not dense. At $\Pi = 24.5$ mN.m^{-1}, nine diffraction peaks were observed. Figure 3.9 (a) and Figure 3.9 (b) show respectively the diffraction map and the integrated peak intensity on Q_z of a selection of the observed diffracted peaks. They adjusted the peaks by Lorentzian functions, and collected their parameters in Table 3.1. On the basis of these measurements, they suggested that $[C_{20}mim]^+[NTf_2]^-$ Langmuir is organized in a coexistence of a 2D rectangular network of interdigitated chains and a 3D network.

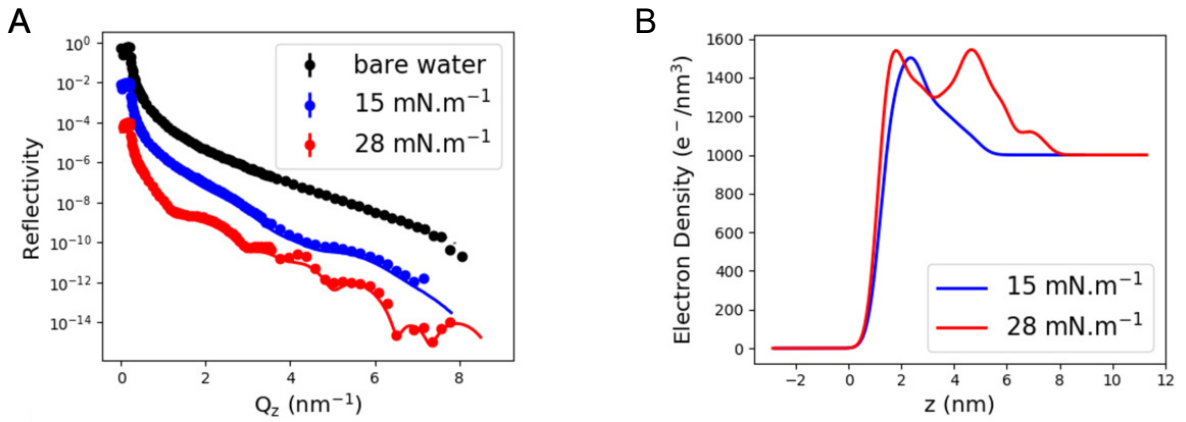

Figure 3.8: The evolution of : (A) XRR measurements and (B) the electron density profile of the $[C_{20}mim]^+[NTf_2]^-$ Langmuir film deposited at the air-water interface (reproduced from [11]).

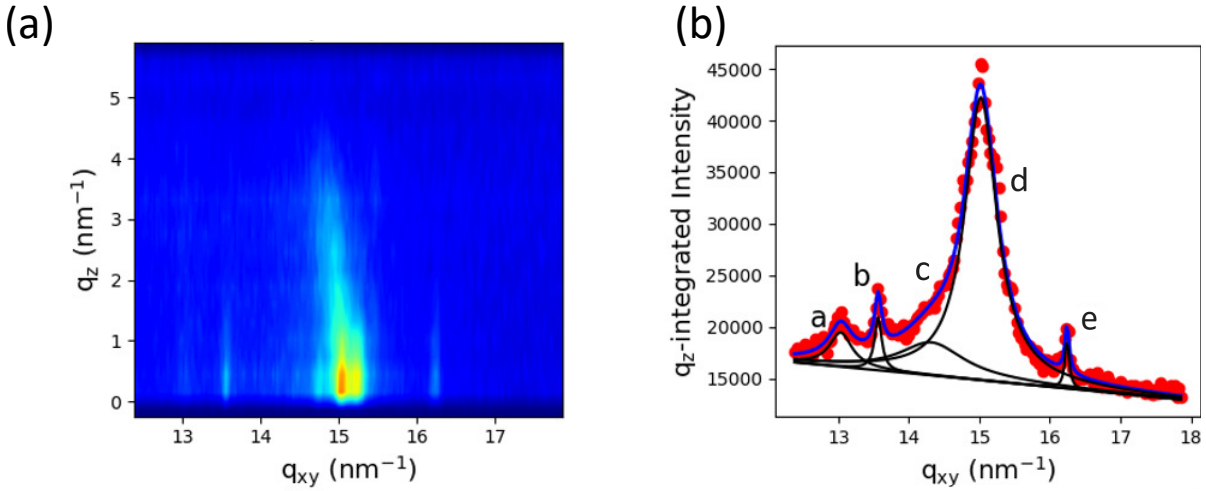

Figure 3.9: The X-ray diffraction (a) map, (b) intensity integrated over Q_z in the horizontal plane of $[C_{20}mim]^+[NTf_2]^-$ Langmuir film spread over pure water, at $\Pi = 25$ mN.m^{-1}(reproduced from [11]).

$[C_{20}mim]^+[NTf_2]^-$ Langmuir film spread over pure water is formed of an unorganized monolayer until its surface pressure reaches that of a collapse plateau at $\Pi = 17.5$ mN.m^{-1}. Through this plateau, the film collapses into a multilayer organized in a coexistence of 2D rectangular networks of interdigitated alkyl chains and 3D networks. The additional compression of the film causes the molecules to collapse further.

	Q_{xy} (nm^{-1})	FWHM ΔQ_{xy} (nm^{-1})	Intensity (a.u.)
a	13.033	0.195	2041
b	13.565	0.062	1005
c	14.322	0.557	5608
d	15.02	0.227676	23791
e	16.243	0.037	550
f	7.381	0.035	11545
g	7.612	0.042	4116
h	7.527	0.033	5190
i	7.729	0.051	9941

Table 3.1: Adjustment parameters of the integrated intensity of the diffraction peaks over Q_z of $[C_{20}mim]^+[NTf_2]^-$ Langmuir film spread over pure water, at $\Pi = 24.5$ mN.m−1 (reproduced from [11]).

3.3 IL and graphene oxide Langmuir mixed films

The need to understand the behavior of IL at the interface with the graphene electrode of supercapacitors has motivated this research. Langmuir is a known procedure for controlling the formation of two-dimensional films, so we adopt it form such an interface. However, graphene films are hydrophobic and are therefore not suitable candidates to be studied by the Langmuir procedure. On the other hand, GO sheets, thanks to the oxygenated functional groups that decorate them, are amphiphilic. Recent studies have shown that GO-based supercapacitors can be efficient devices [5]. Graphene electrodes are also sensitive to long-term oxidation during charge/discharge cycles. In addition, it is also possible to obtain graphene from the GO by reduction. It was therefore convenient to choose GO as an alternative to graphene to investigate it at the interface with IL. Our goal is to first elaborate the GO/IL interface by the Langmuir film procedure, then study it by X-ray scattering and AFM.

In the following section, theoretical and simulation studies are discussed on graphene, graphene oxide and their interaction with IL molecules.

3.3.1 Graphene

Historical overview

Graphite consists of a 3D stack of graphene sheets, formed of covalently bonded carbon atoms arranged in a 2D honeycomb network as illustrated in Figure 3.10. Scientists have always agreed on the exceptional properties of a single sheet of graphene, but before 2004, their studies were purely theoretical. That year, Gein and Novoselov succeeded for the first time in isolating a graphene sheet from graphite powder using scotch tape [70]. For their achievement, they were awarded the Nobel Prize in 2010 [71]. Note that there is many other methods to obtain a single graphene sheet. However, they are either more sophisticated or have a less pure yield than the "scotch-tape" method. They include

chemical vapor deposition (CVD), mechanical exfoliation, epitaxial growth and a chemical process by reduction of graphene oxide sheets produced by the Hummers method [72, 73, 74, 75].

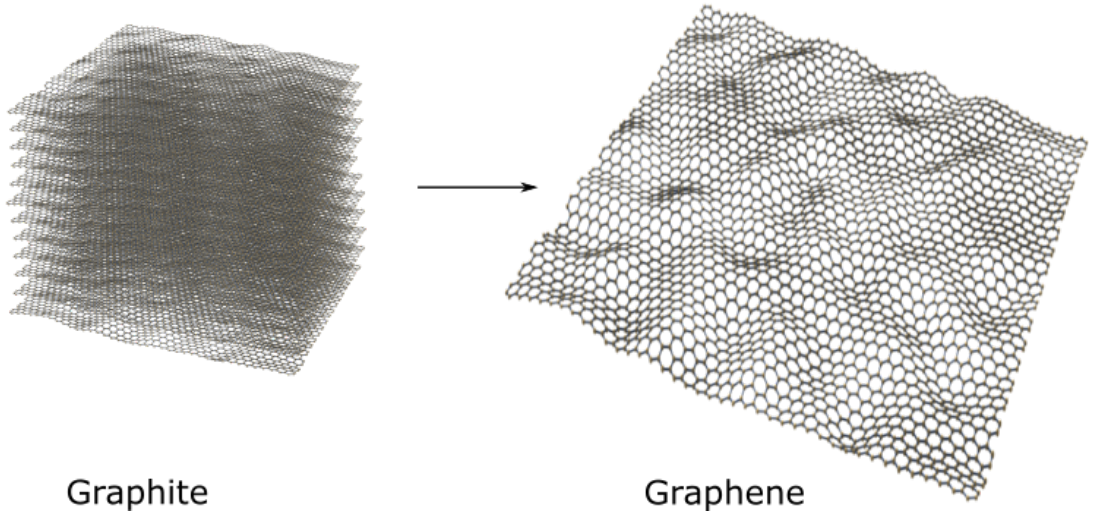

Figure 3.10: Illustration of the structures of graphite and graphene.

Structure and properties of graphene

Since experiments have shown the feasibility of isolating a single sheet of graphene from graphite, it was revealed the most popular and sought-after material. Figure 3.11 shows the evolution of the number of reports containing the search term "graphene" (in the SciFinder Scholar database) which increased considerably after 2004. Graphene combines a set of properties including the ability of its electrons to move smoothly over the surface of the sheet and at a very fast constant speed (one thousand kilometers per second). In fact, the fourth of the 4 valence electrons shared between the 2 carbon atoms of the elementary graphene lattice is alone in an orbit that gives it a native sp^2 hybridization state [76]. This particular structure of graphene makes it highly electrically conductive at room temperature. It has practically the structure of a zero-gap semiconductor. It also has a large specific surface area (2600 m^2/g) since all the atoms constituting the graphene sheet are on its surface [77]. It has an optical transparency of nearly 98%. In addition, graphene is characterized by its mechanical strength while being elastic and flexible, thanks to the covalent bonds between carbon atoms [39, 71] .

For these reasons, graphene is harnessed in various fields such as solar cells[79], transparent touch screens[80], light panels[81], energy storage systems [82] etc...

3.3.2 Graphene oxide (GO)

Graphene oxide is the oxidized form of graphene where oxygenated functional groups are distributed along the edges and the basal plane of graphene sheets. The Hummers method [75], introduced in 1957, is the best known method for mass production of GO sheets. It consists in oxidizing graphite powder by adding an oxidizing agent. The result is a graphite oxide powder consisting of layers of graphene oxide sheets whose base

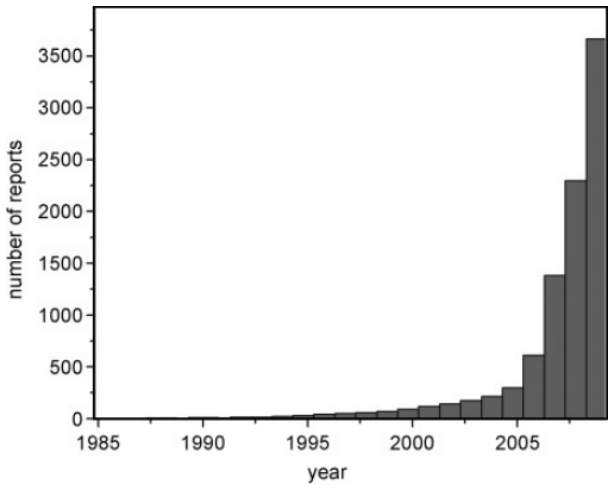

Figure 3.11: Number of reports containing the search term "graphene" by year [78].

planes are weakly bonded together. The powder can hence be easily exfoliated in water or many other solvents through sonication, resulting in a dispersion of GO single sheets. Depending on the quantity and nature of the oxidizing agents, added to the conditions of the experiment and the quality of the graphite powder, the structural models to describe GO sheets may differ [39]. In the following paragraph, the models proposed, over time, to describe the structure of GO sheets are presented.

3.3.3 Structural models of GO

There are mainly 5 models that describe the structure of a GO sheet :

1. In 1939, Hoffman and Holst proposed that the GO sheet is formed by a graphene sheet with epoxy groups attached to its basal plane with a C/O ratio equal to 2 [83].

2. In 1947, Ruess suggested to add hydroxyl groups to Hoffman model [84].

3. In 1969, Scholz and Boehm presented a new model showing wavy GO sheets with ketones instead of epoxy and hydroxyl groups attached on it [85].

4. In the 1990s, Lerf and Klinowski introduced a model based on that of Hoffman and Holst and Ruess but with the addition of carboxyl groups on the edges of the sheets. Today, this model is widely adopted to describe the structure of GO [86], [87].

5. In 2006, Dékány et al. added another model to describe the structure. They based their model on Scholz and Boehm's model, but added groups of 1,3-ether [88].

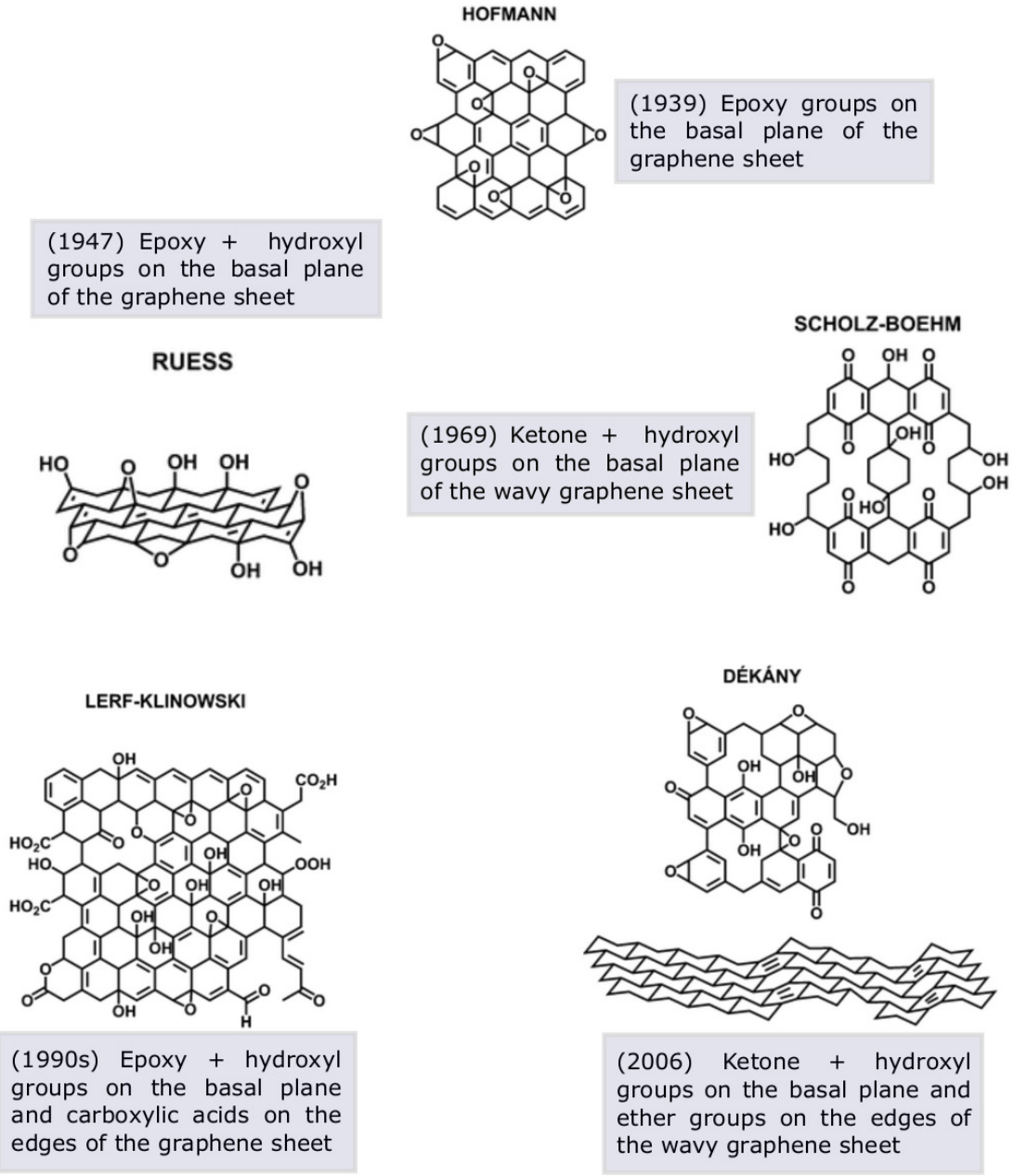

Figure 3.12: Different models to describe the structure of GO sheet(reproduced from [89]).

3.3.4 Lerf-Klinowski model

The Lerf-Klinowski model shown in Figure 3.13 is the model that has proven to be the most suitable to describe GO sheets. It mainly describes the structure of GO by two distinct regions: a sp^2-hybridized unoxidized region of carbon atoms (graphene pristine region) and a sp^3-hybridize functionalized region of carbon atoms [89]. GO sheet therefore consists of an arrangement of carbon atoms in a 2D honeycomb network, identical to that of graphene, decorated with oxygenated functional groups on its basal plane and its edges.

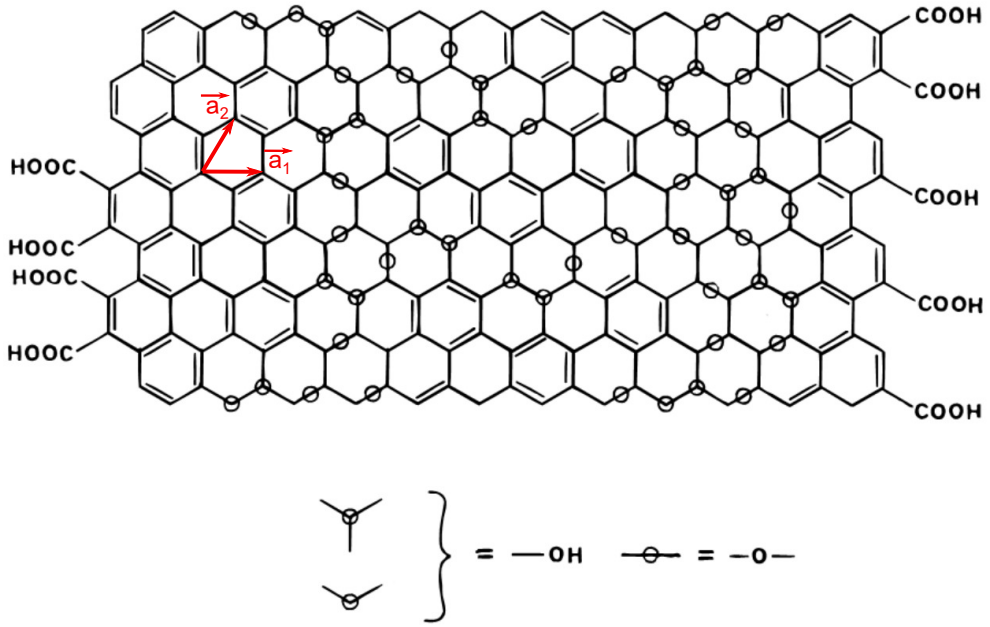

Figure 3.13: The structural model of GO as proposed by Lerf et al.(reproduced from [90]).

3.3.5 Properties of GO

The presence of oxygenated functional groups on the GO sheets disturbs the hybridization sp^2 and generates the hybridization state sp^3. GO is characterized by a finite electronic band gap and is therefore a less electrically conductive than graphene. Depending on the percentage of these functional groups, GO sheets can be amphiphilic unlike graphene sheets, which are hydrophobic. As described in Lerf-Klinowski's model, the oxygenated functional groups decorating GO sheets, which are epoxy (-O-), hydroxyl (-OH) and carboxylic group (-COOH), are hydrophilic. Their coexistence with an area of carbon atoms that are hydrophobic gives the GO sheet an amphiphilic character. Depending on the size of the GO sheets and the amounts of oxidizing agents, the percentage of functional groups may vary in relation to the number of carbon atoms. The smaller the size of the sheet, the higher the ratio of these groups to carbon atoms. Thus, unlike graphene, GO sheets can be dispersed in a wide range of organic solvents and water and can form Langmuir films at the air-water interface. Moreover, GO has been shown to be effective for cleaning polluted water due to its ability to adsorb a variety of organic and inorganic pollutants [91, 92]. In addition, it has been proven to enhance the mechanical and electrical properties of different polymers or matrices when combined to them [93]. It is a promising precursor of graphene by reduction [77, 94]. In fact, to date the production of graphene in commercial or university research laboratories is hindered by high production costs, low yield, complicated production methods, etc... This has a major impact on the limitation of industrial applications of graphene [95]. The main challenge in producing graphene from graphite is to break the Van der Waals interactions between the sheets, which are strong due to their large specific area. However, the introduction of oxygenated functional groups between the sheets will reduce their specif area and weaken the interaction between sheets. Hence, graphite oxide can be easily exfoliated into GO sheets with low cost mass production. By reducing the GO sheets, it is therefore possible

to mass-produce graphene sheets in a simple and inexpensive process.

3.3.6 GO in water

The interaction between the IL and GO sheets is studied by Langmuir films on the water surface. In addition, GO sheets are initially dispersed in an aqueous solution. However, water can interact with oxygenated functional groups and modify their properties. Therefore, it is necessary to study the consequences of water on the chemical properties of the GO sheets before proceeding with the IL and GO study.

Mouhat et al. performed molecular dynamics simulations (MDS) to study the behavior of GO sheets in water [96]. They modeled the GO sheet as a graphene sheet whose basal plane is in interaction with epoxy (-O-) and hydroxyl (-OH) groups. They suggested neglecting the presence of (-COOH) on the GO sheet by considering their number relative to that of (-O-) (-OH) as insignificant. The results showed that the sheets present in water can carry either a modest negative charge due to deprotonation of (-OH) groups or a net neutral charge due to the formation of water molecules. Their conclusion was mainly based on the following observations which are also represented in Figure 3.14:

1. For epoxy groups: the (-O-) bonds break after opening of an epoxide function, leading to a zwitterionic form of the graphene oxide. Subsequently, a negative charge appears, but is accompanied by a positive charge from an adjacent carbon atom, resulting in a net neutral charge of the GO sheet.

2. For hydroxyl groups, two phenomena were observed:

   i) Deprotonation of hydroxyl groups resulting in negative charges compensated by an excess of positive charges in water (hydronium cation). This process results in a modest negative charge of the sheets.

   ii) Spontaneous dehydration of GO sheets. As the hydroxyl groups are close together, -OH group jumps to the next and forms water molecules and alcoholate. This process results in a net neutral charge.

At the end of their study, they indicated that the GO replica, given these results, looked more like a reduced GO than a GO. This confirms the need to add carboxyl groups to the structural model of GO. To conclude: the contribution of (-O-) and (-OH) groups to the negative charges carried by GO sheets is modest or negligible and the presence of (-COOH) groups at the edges of GO sheets cannot be neglected.

Kim et al, another group of researchers experimentally studied the dispersion of GO in water [97]. They modeled GO sheet this time with the presence of epoxy (-O-), hydroxyl (-OH) and carboxyl (-COOH) groups. They considered the GO sheets as surfactants with hydrophilic edges and hydrophobic basal planes when in aqueous solution. They reported that the sheets are negatively charged and that due to the electrostatic repulsion, the dispersion is kept stable. In fact, carboxylate anions ($-COO^-$) which are formed following deprotonation of (-COOH) groups in water are mainly at the origin of the negative charges present on the sheets. They did not take into account the contribution of (-O-) and (-OH) groups to the appearance of negative charges. Figure 3.15 shows the structure of GO sheets following it interaction with water. They have demonstrated that the

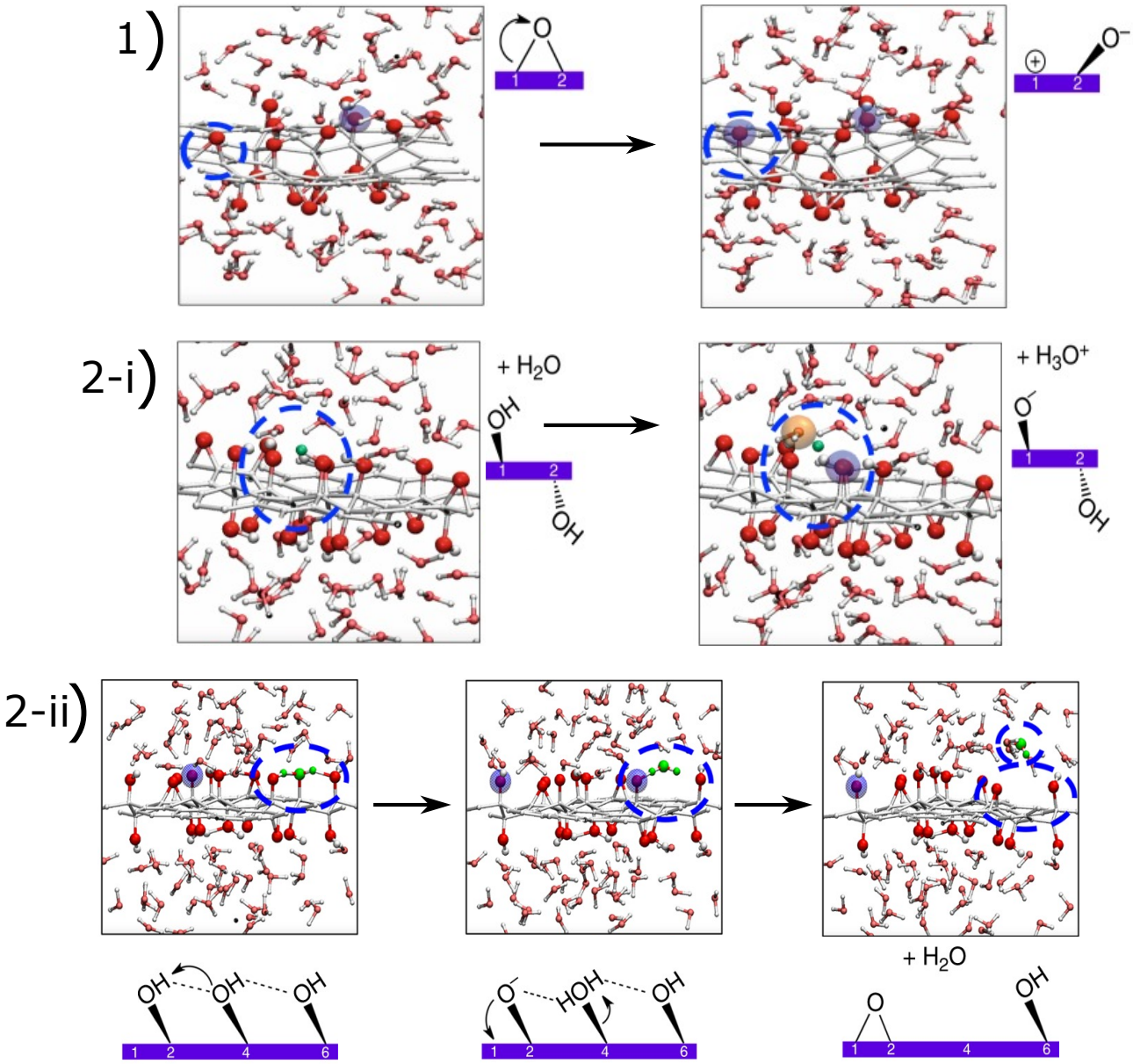

Figure 3.14: Snapshots taken from MDS. In **1)** an opening of an epoxide function. No net charge is created on the sheet. In **2-i)** deprotonation of hydroxyl group, leading to a surface alcoholate (blue shaded circles) and an excess proton (orange) in the liquid water. This results in GO negatively charged sheet. In **2-ii)** spontaneous dehydration of GO sheet following protons transfer due to the presence of a strong hydrogen bond network. In green color is the water molecule (reproduced from [96]).

hydrophilicity of GO sheets, and thus their dispersion stability, increase with increasing the pH of the aqueous solution. In fact, it is recognized that base solutions promote the deprotonation process of compounds, so in this case they promote the formation of negative charges on GO sheets. But this does not mean that deprotonation is impossible to achieve in pure water (without any basic agent). According to our experiments, the pH of the GO dispersion solution in pure water was close to 5, which suggests the presence of acid groups that cannot be other than (-COO^-).

Based on these results, GO sheets dispersed in pure water are negatively charged because of (-COO^-) groups that "decorate" their edges as illustrated in Figure 3.15.

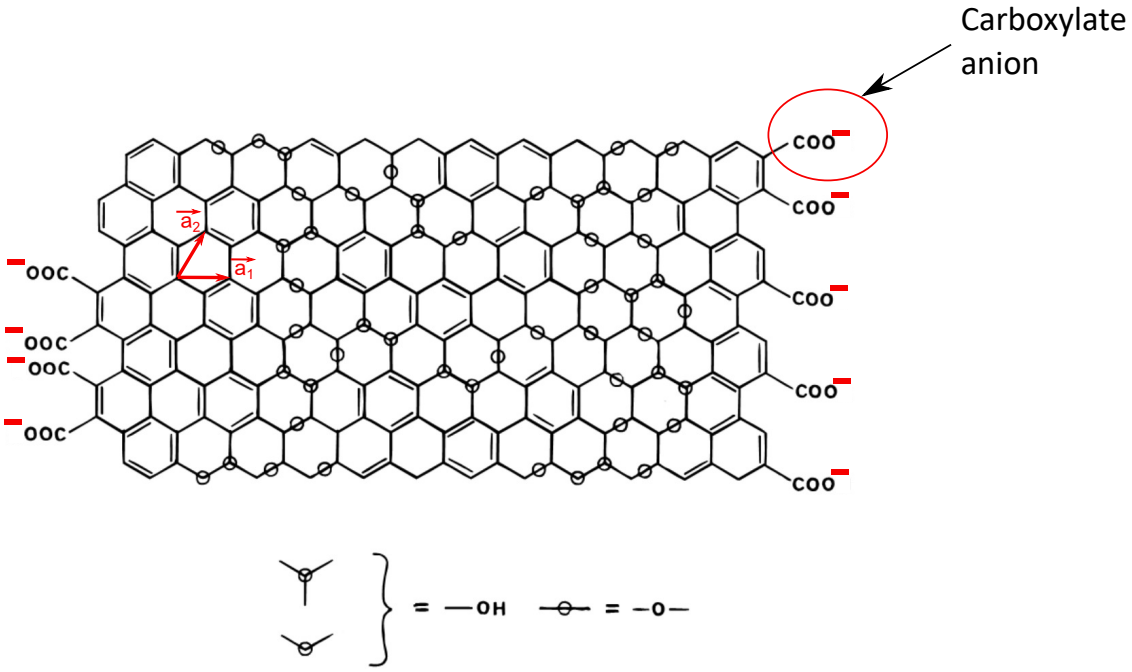

Figure 3.15: The structure of GO sheet dispersed in water. It shows the formation of carboxylate anions at its edges as a result of deprotonation of carboxyl groups in water.

It is also interesting to note that Dimriev et al. observed that the exposure of GO sheets to water for more than 2 months is able to degrade them into smaller, more hydrophilic sheets [98]. They suggested that, over the long term, water molecules attack the sp^3 hybrid carbon atoms, break the C-C bonds and induce the cleavage of the sheets. They showed images obtained by scanning electron microscope (SEM) measurements on GO sheets deposited on Si/SiO_2 wafers, coming from two different aqueous dispersions: a fresh dispersion and an 2 months old dispersion. They observed that GO are formed in large sheets when freshly dispersed in water (Figure 3.16(a,b)) and small broken sheets when exposed to water for 2 months (Figure 3.16(c,d)).

Our experiences are in agreement with their study. We noticed that one year after purchasing our GO aqueous dispersion solution, we were no longer able to form GO Langmuir films. The adsorption of GO sheets on water surface in Langmuir films was therefore no longer possible. This confirms that the GO sheets had to break into smaller and therefore more hydrophilic sheets with time.

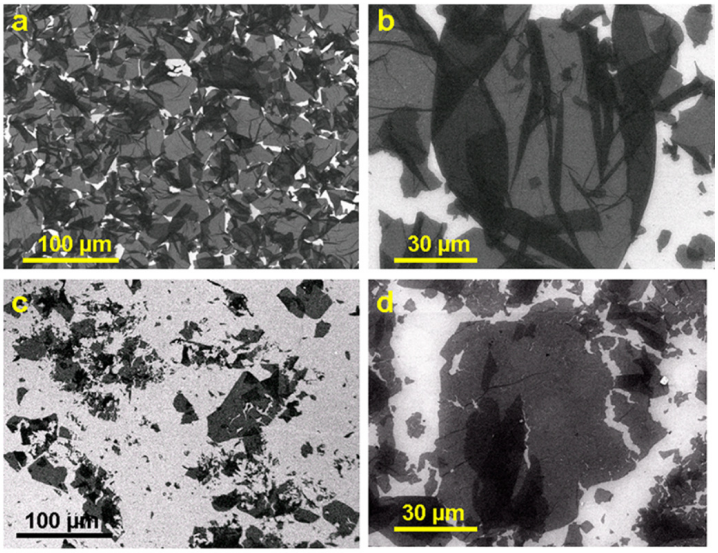

Figure 3.16: SEM images of GO sheets deposited on Si/SiO_2 wafers: (a,b) from a freshly prepared solution, (c,d) from a solution prepared 2 months ago (reproduced from [98])

3.3.7 Organization of GO Langmuir films at the air-water interface

Bonatout et al. have studied GO by Langmuir films on water surface and by Langmuir-Blodgett films on solid substrates. They demonstrated by XRR and GIXD that the film self-assembles to form a double layer of GO sheets linked by water molecules on water surface. They estimated the thickness of the bilayer to be about 20 Å. Figure 3.17 shows the evolution of XRR spectra and their electron density profile GO film at different surface pressures. Figure 3.18 shows the diffraction peaks, attributed to the organized bilayer of GO sheets. They suggested a model, shown in Figure 3.19, to describe the GO Langmuir film deposited at the air-water interface.

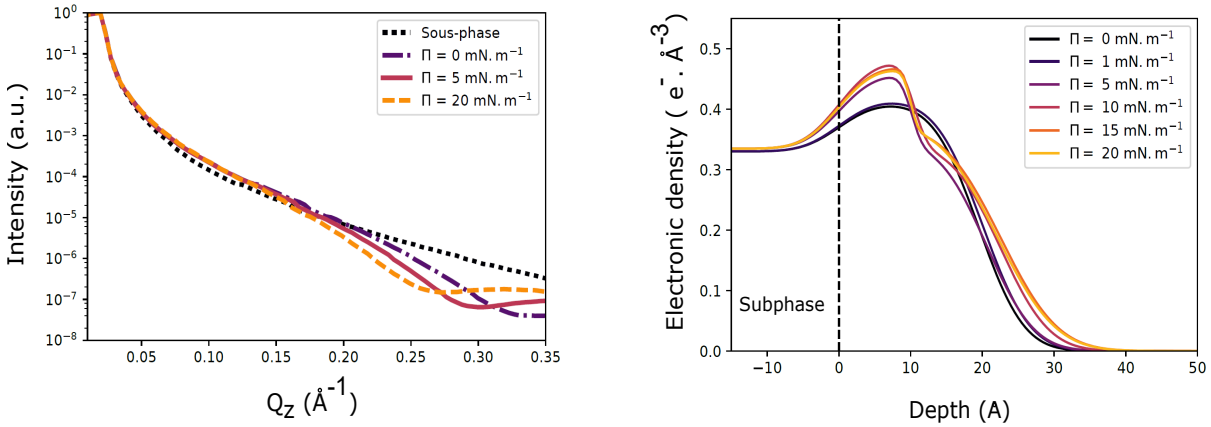

Figure 3.17: The evolution of the : (left) XRR and (right) the electron density profile of the GO Langmuir film deposited at the air-water interface during its compression (reproduced from [39], [99]).

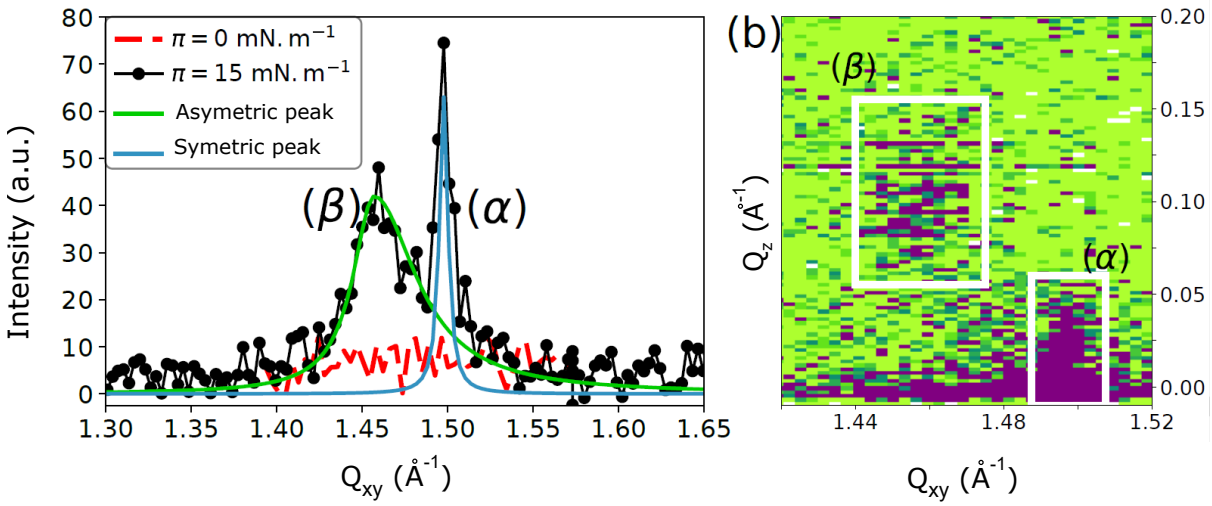

Figure 3.18: (a) GIXD spectre of the GO Langmuir film deposited at the air-water interface at Π=0 mN.m^{-1} and 15 mN.m^{-1} and (b) diffraction map of these peaks (reproduced from [39], [99]).

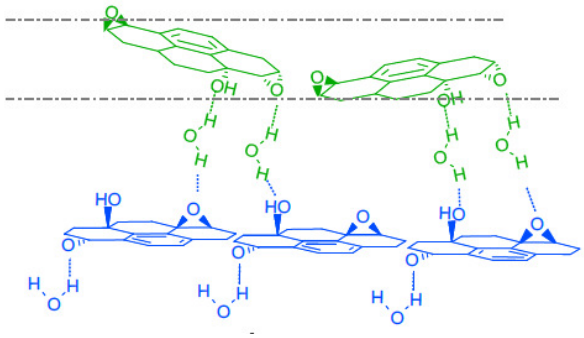

Figure 3.19: Schematic representation of the bilayer model of GO Langmuir film deposited on water surface as proposed by Bonatout et al.(reproduced from [39, 99]).

3.3.8 Transfer on solid substrates

They also studied by AFM Langmuir-Blodgett films of GO sheets deposited on Si/SiO_2 substrates. They observed that the film is formed in single sheets of GO of 10 Å at low surface pressures as shown in Figure 3.20(a). However, at high surface pressures, the film is formed of sheets interleaved at their edges as shown in Figure 3.20(b).

Results collected by AFM, XRR and GIXD showed that the structure of the GO film depends on the substrate, whether aqueous or solid. They proposed to interpret this discrepancy in results as follows : the film is formed by a bilayer on the water surface, however, during its transfer to a solid substrate, water drainage may have induced the loss of the upper GO layer.

The following section presents Molecular Dynamics (MDS) simulation studies, drawn from the literature, to understand the graphene/IL interface.

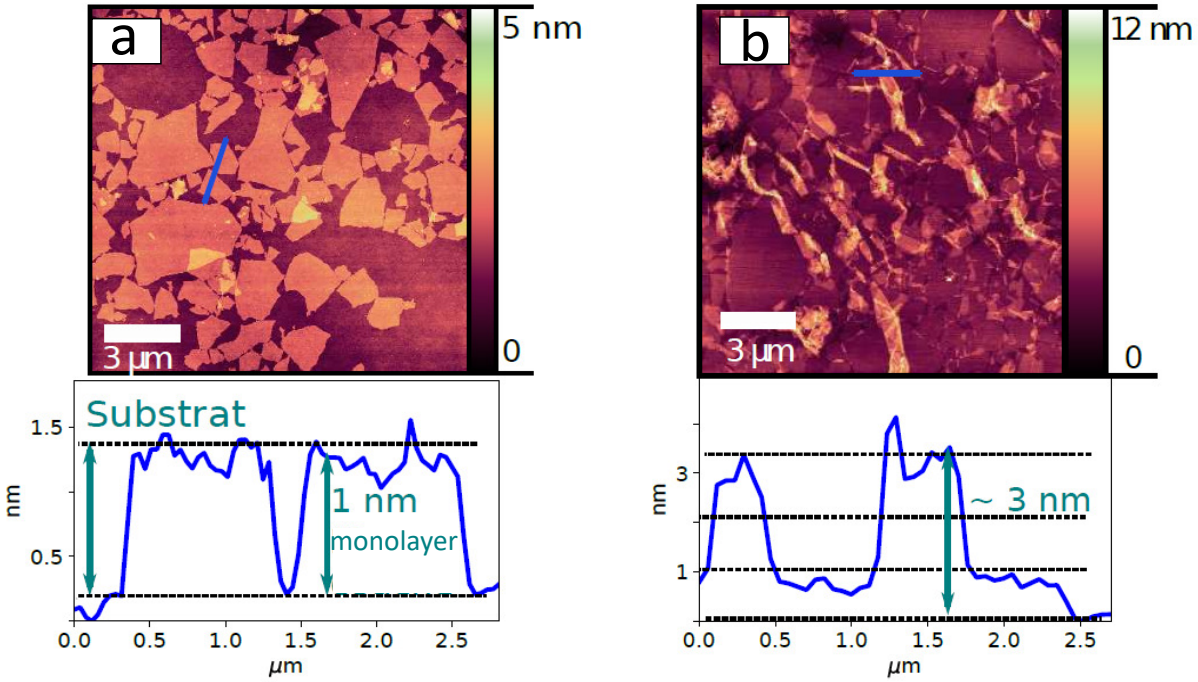

Figure 3.20: AFM images of GO Langmuir films transferred onto Si/SiO_2 wafers by Langmuir-Blodgett technique at (a) low and (b) high surface pressures (reproduced from [39, 99]).

3.3.9 Molecular dynamic simulation of ILs at Graphene interfaces

Uysal et al. studied the electric double layer (EDL) of 1-methyl-3-nonylImidazolium bis-(trifluoromethanesulfonyl)imide $[C_9mim]^+[NTf_2]^-$ ionic liquid at room temperature at the interface of an uncharged graphene electrode [3]. They studied the innermost layer of the EDL : the adsorbed layer in direct contact with the surface of the graphene. They obtained by molecular dynamics simulation (MDS) that the adsorbed layer consists of a layer of cations in direct contact with the graphene, and on top of it a layer of anions. The cation layer is 3.5 Å thick and appears to overscreen the surface of the graphene. This suggests that the Imidazolium rings as well as the alkyl chains lie parallel to the graphene surface. The Imidazolium ring must be adsorbed to the graphene sheet by Π-Π interactions and alkyl chains must be commensurate with the 2D graphene lattice. The second layer, which forms above the cation layer, is formed by the anions and no information is available on their orientation.

Moghadam et al. also studied by (MDS) the EDL of IL at the interface with an uncharged graphene surface [2]. They studied the innermost and outermost layer of the EDL. The innermost layer is called the adsorbed layer and is in direct contact with the graphene surface. The outermost layer is called the vacuum layer and is in contact with the vacuum. They chose to study three different types of ILs : $[EMIM]^+[ALA]^-$, $[EMIM]^+[ILE]^-$, and $[EMIM]^+[PF_6]^-$. They studied the orientation (the tilt) of the Imidazolium rings, alkyl chains and the anions. The orientation is defined by the angle formed between the normal vector of the graphene and the normal vector of the ring or the alkyl chain or the anion as shown in Figure 3.21. They obtained that the orientation

of the alkyl chain mainly follows that of the Imidazolium ring. On the other hand, the anions are randomly distributed. Figure 3.22 shows the probable orientation of the Imidazolium ring and the alkyl chain with respect to the graphene surface, in both layers..

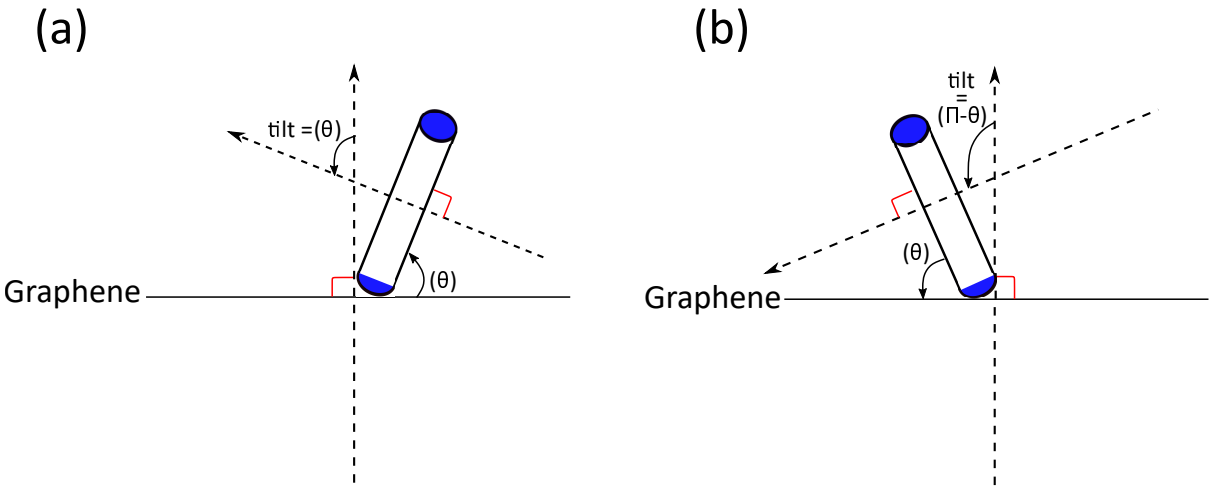

Figure 3.21: The orientation of a compound is defined by the angle formed between the normal vectors of graphene and the normal vector of the compound.

The orientation of the cations shows to be dependent on the nature of the anion. In fact, $[EMIM]^+[ALA]^-$, $[EMIM]^+[ILE]^-$ are amino acid Imidazolium-based ILs whose anions, respectively alaninate (ALA) and isoleucinate (ILE), have alkyl side chains of amino acid (AA). It has been observed that depending on the length of the alkyl chain, the orientation of IL at the interface varies. However, $[EMIM]^+[PF_6]^-$, also known as $[C_2mim]^+[PF_6]^-$ has $[PF_6]^-$ as an anion without alkyl chains. This anion resembles to the most classical anions used in the study of the graphene/IL interface. Its properties are also similar to those of $[NTf_2]^-$. We are therefore going to discuss in more detail the orientation of $[EMIM]^+[PF_6]^-$ when it is in vicinity of the graphene surface. The obtained orientations of the Imidazolium ring and the alkyl chain of $[EMIM]^+[PF_6]^-$, in the adsorbed layer, are 10° or 30° the. They estimated the thickness of this layer to be about 3.6 Å. In the vacuum layer, the Imidazolium ring has an equal probability of being oriented in 80° (Figure 3.21(a)) and 100° (Figure 3.21(b)) with respect to the graphene surface. However, the alkyl chains can have three possible orientation: 40°, 60° and 90°. These results suggest that Imidazolium rings as well as alkyl chains prefer to lie parallel to the graphene surface in the adsorbed layer. The thickness of the adsorbed layer suggests that the anions are also parallel to the graphene surface, which is in agreement with Uysal et al.. However, in the vacuum layer, the orientation of the IL is no longer parallel to the surface of the graphene and be either be perpendicular or tilted by 40° or 60° with respect to the graphene surface. As for the anions, they are randomly distributed, most probably next to the Imidazolium rings.

Figure 3.23 is schematic representation of the model proposed to describe the innermost and outermost layers of the EDL of $[EMIM]^+[PF_6]^-$ in the vicinity of the graphene surface.

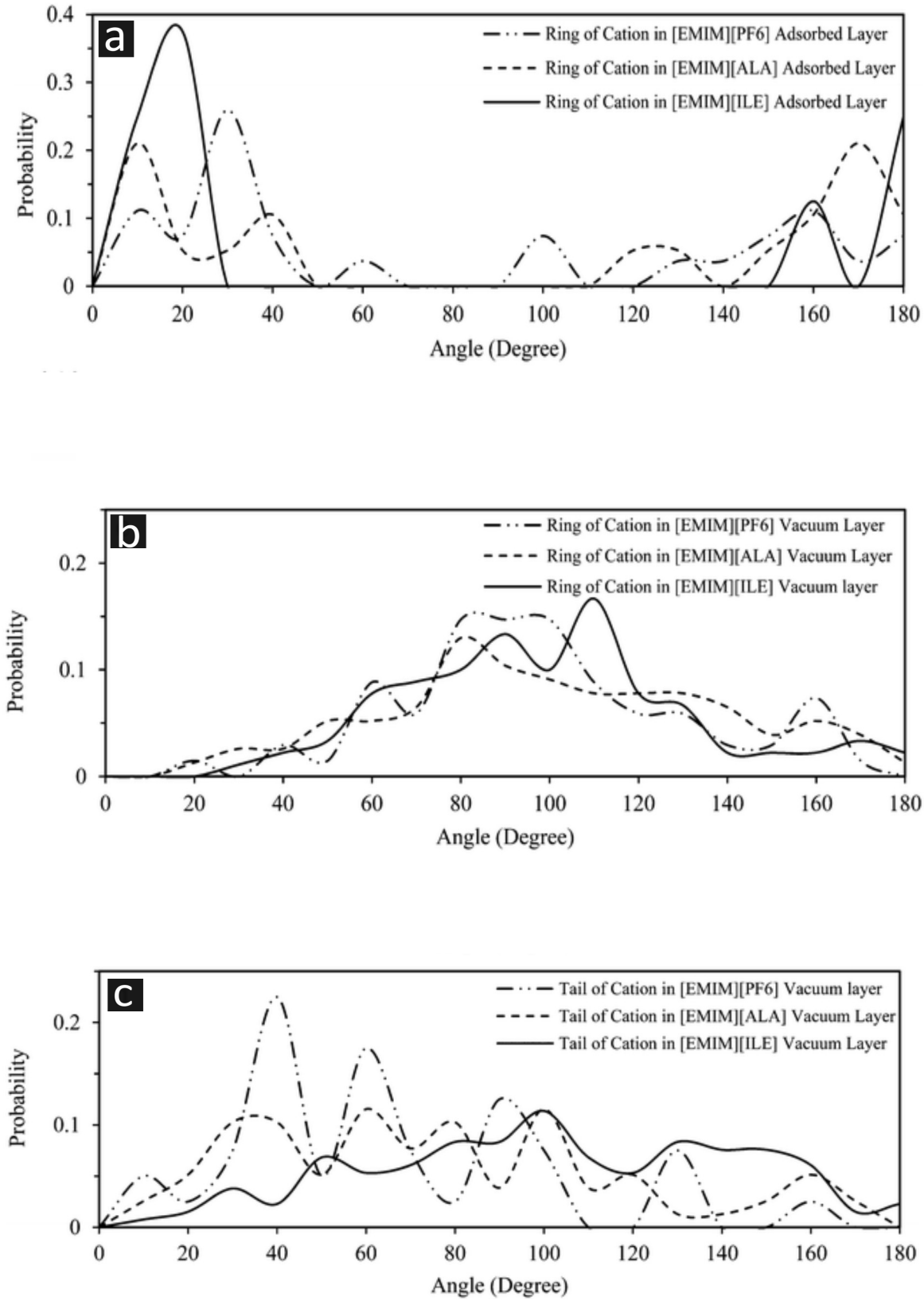

Figure 3.22: Angle distribution of (a) the ring of the cation at the first adsorbed layer, (b) the ring of cation at the vacuum layer, and (c) the tail of the cation at the vacuum layer (reproduced from [2]).

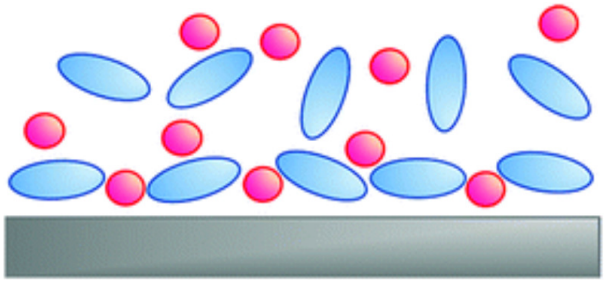

Figure 3.23: Schematic structure of the adsorbed layer and the vacuum layer of the EDL of $[EMIM]^+[PF_6]^-$ in the vicinity of the graphene surface where the red spheres represent the anion and the blue ovals represent the cations (reproduced from [2]).

Kislenko et al. another group of researcher [4], also studied by MDS the structure of the EDL of IL at the interface with an uncharged graphene surface. They chose to work with $[EMIM]^+[PF_6]^-$ also an imidazoliom-based IL known as $[C_4mim]^+[PF_6]^-$. They investigated the EDL of IL extending from the innermost layer, inclusive, to a distance of 20 Å form the graphene surface. They did not study the vacuum layer. The adsorbed layer is 5 Å thick and formed by cations and anions lying parallel to the graphene surface, which is in agreement with the previous studies [2, 3]. The position of the anions is slightly higher than that of the cations. Figure 3.24 (A) is a snapshot from the MDS that shows the orientation as well the position of ions in the adsorbed layer. They also obtained by MDS that the ions of the adsorbed layer are arranged in a 2D hexagonal network with a lattice parameter approximately four times larger than that of the graphene substrate. This means that IL and graphene form a commensurate superlattice. Figure 3.24 (B) shows the map of the distribution of the ions in the hexagonal lattice on top of a graphene surface. They also obtained that this IL is well-ordered in a region extending to 20Å from the graphene surface. In the region > 20 Å the EDL is obtained to be bulky of arbitrary orientations of the IL molecules.

To conclude, the EDL of ILs were studied at the interface with an uncharged graphene surface by MDS. The behavior of the ions of the ILs depends on their position relative to the graphene surface, whether in the adsorbed layer or in the vacuum layer or in an intermediate position. Basically, all studies agreed that the Imidazolium rings as well as the alkyl chains in the adsorbed layer prefer to lie parallel to the uncharged graphene surface due the $\Pi - \Pi$ interactions. However, they disagreed on the position of the anions in the adsorbed layer. Uysal et al. showed that the anions occupy a layer completely above that of the cations. On the other hand, Moghadam et al. showed that the anions are in the horizontal plane of the Imidazolium rings. However, Kislenko et al. obtained that the anions in the adsorbed layer are positioned slightly higher than the cations. This group has also obtained that IL ions and graphene form a commensurate superlattice in the adsorbed layer and that this organization is extended to a region within 20 Å of the graphene surface. From this distance, the IL is in bulk with no specific orientation or organization. Finally, according to Moghadam et al. the layer in contact with the vacuum is formed of molecules tilted and/or perpendicular to the graphene.

MDS studies of the graphene/ILs interface do not provide a unique and general description of the structure of the interface. It is therefore necessary to study it experimentally.

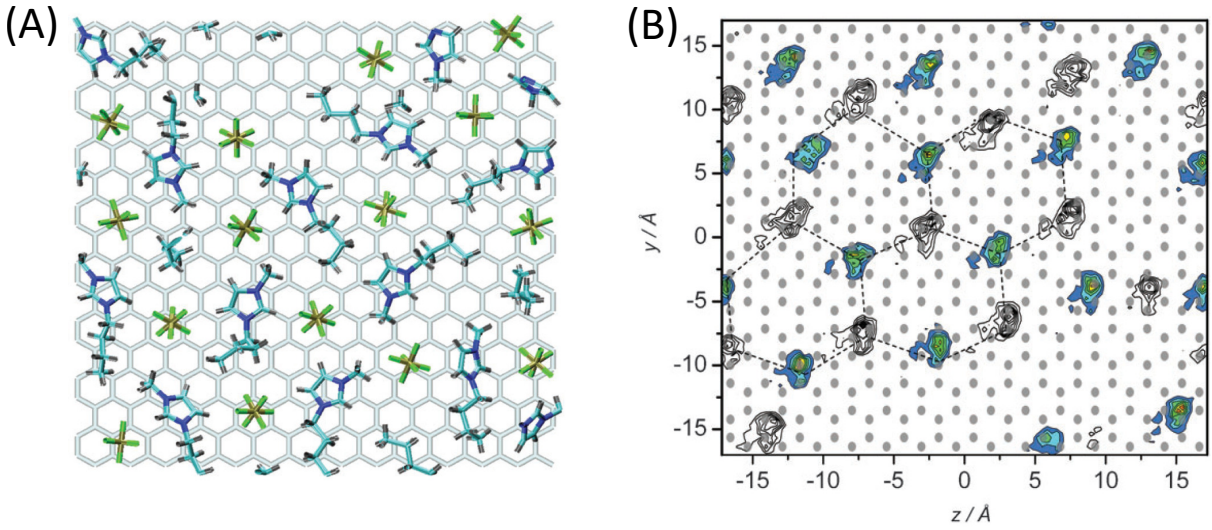

Figure 3.24: (A) snapshot taken from the MDS showing the orientation and positions of cations as well the anion in the adsorbed layer to an uncharged graphene surface (cations are represented in blue and anions in green). (B) The density contour map for the adsorbed ions formed in a 2D hexagonal lattice in the adsorbed layer. Grey circles indicate surface carbon atoms. The color map corresponds to $[PF_6]^-$ anions; the black-and-white contour map corresponds to Imidazolium rings.

3.4 Langmuir films deposited on gold ionic subphases

Decorating GO sheets with gold nanoparticles has proven to be an effective way to improve the energy storage capacity of supercapacitors [8]. On the other hand, ILs have recently emerged as stabilizers for the synthesis of a monodispersion of gold nanoparticles [9]. The main problem with supercapacitors remains in the interaction at the interface between the electrode and the electrolyte. From this perspective, it is interesting to first try to form organometallic films of gold and IL and then to study them at the interface with graphene oxide. Surface X-ray radiolysis is a procedure for forming metallic crystalline nanostructures controlled and directed by a monolayer of Langmuir which acts as a template [10]. This process can therefore be suitable for the elaboration of gold nanoparticles in interaction with a monomolecular layer of IL.

The principle of water radiolysis is exploited in various research fields such as hydrogen production, radiotherapy, corrosion prevention in nuclear power plants, ion reduction [100, 101, 102, 103]... The reduction of metal ions by radiolysis of aqueous solutions is excessively incorporated in the field of nanosciences. It has proven to be accurate and efficient in the synthesis of a monodispersion of polyvalent metal nanoparticles [104]. Combining the properties of organic and inorganic species is interesting to enhance their functionalities and properties (optical, electronic, catalytic ...). One of the strengths of this synthesis technique lies in its ability to precisely control the size and composition of the final products. It does not involve any chemical reducing agents that could be harmful and have undesirable effects on the final product. We are particularly interested in this principle for the metallic ions reductions using Langmuir films as templates. The metallic clusters formed are thus controlled and directed by the Langmuir film.

3.4.1 Historical overview of water radiolysis

The radiolysis of water was naturally demonstrated following the discovery of radioactivity (in 1896) [105]. In 1901, P. Curie and Debierne observed for the first time the emission of molecular hydrogen and molecular oxygen from radium bromide solutions [106, 107]. In 1902 and 1903, Giesel [102, 108, 109] repeated and confirmed the experiment. This prompted Debierne to study in depth the effect of radiation on water. He suggested that the ionisation of water produces free radicals H° and HO° which interact with each other to form water, hydrogen peroxide and molecular hydrogen. Radiation chemistry flourished during and after the Second World War, when the understanding of the effects of radiation on water emerged as an urgent need to test and develop an atomic bomb [110]. In the 1960s, the development of pulsed radiation [111] led to the discovery of the solvated electron (e^-_{aq}) as one of the products formed during the radiolysis of water [112]. This discovery was the key to the success of Belloni et al. [113] in the synthesis of metallic nanoclusters through the reduction of ions by the solvated electron. Water radiolysis has then emerged as a process for the reduction of metal ions into atoms and through their nucleation , the growth of nanometric-sized particles.

3.4.2 Principle of water radiolysis

Radiolysis of water is the dissociation of water molecules induced by ionizing radiation such as gamma rays or X-rays. When high-energy rays penetrate the medium, the molecules will be excited and ionized resulting in the production of radicals and molecular species and free electrons. These electrons will in turn excite and ionize other molecules in the solvent, costing them their kinetic energy. In this way, the electrons become thermalized, reach their stable equilibrium state and solvate in the water into e^-_{aq} [114]. The mechanism of radiolysis is fully elucidated in the following equation that shows the primary products of water radiolysis:

$$H_2O + radiation \longrightarrow e^-_{aq}, H^\circ, HO^\circ, HO^\circ_2, HO^-, H_3O^+, H_2, H_2O_2 \tag{3.3}$$

We evaluate each radiolysis experiment in terms of the following physical quantities:

- **The dose** : It corresponds the amount of energy absorbed by 1kg of the system. It is expressed in Gray (Gy) which is equivalent to $J.Kg^{-1}$ and depends on three factors :

  1. The flux of photon per time unit ϕ_{photon}
  2. The energy of the radiations E_{photon}
  3. The ration of the photon absorbed by the solution. For X-rays of $E_{photon} = 18$ Kev, it is worth 8.7 % for 1mm of the solution [35].

- **The dose rate R** : It expresses the dose as a function of time $Gy.s^{-1}$. It is the intensity of the absorbed radiation per unit of time and calculated by the following equation:

$$D = \frac{0,9.e_{sample}.\phi_{photon}.E_{photon}}{m_{sample}} \tag{3.4}$$

  Where e_{sample} and m_{sample} are respectively the thickness and the mass of the irradiated zone of the medium through which the radiation passes. Multiplying the dose rate by the irradiation time gives the dose expression in Gy.

– **Linear energy transfer LET** : It represents the amount of energy loss of a charged particle per unit length of travel when passing through a medium. It depends on the nature and energy of the radiation as well as the nature of the medium through which it passes.

– **The radiolytic yield *G*** : It is defined as the ratio of the concentration of radiolytic products for 1 Joule of deposited energy , and expressed in mol.J^{-1}. It highly depends on LET, pH of the solution, temperature. For further details see [115] and [114].

3.4.3 Principle of synthesis of gold nanoparticles by X-ray radiolysis

The primary products of the radiolysis of a low-concentration aqueous solution will react with the molecules of the solute to form new products. The solutions must also contain alcohol to scavenge the free radicals resulting from the water radiolysis mechanism. The alcohol plays a key role in the success of the ion reduction process. Consider the case of gold ions solution $Au^{III}Cl_4^-$, commonly noted $AuCl_4^-$, of concentration of 10^{-4} to 10^{-3} mol.L^{-1}. The principle reducing agents (e_{aq}^- and H°) generated by the water radiolysis will reduce the gold ions into atoms Au^0 by a process of three steps :

1. $Au^{III}Cl_4^-$ is reduce to $Au^{II}Cl_4^-$ by e_{aq}^- and H° as show equations 3.5 and 3.6 :

$$Au^{III}Cl_4^- + e_{aq}^- \longrightarrow Au^{II}Cl_4^{2-} \tag{3.5}$$

$$Au^{III}Cl_4^- + H^\circ \longrightarrow Au^{II}Cl_4^{2-} + H^+ \tag{3.6}$$

2. However, Au^{II} is not as stable as the I and III oxidation numbers, causing it to dimerize and then decompose into Au^I and Au^{III} as shown in equation 3.7.

$$Au^{II} + Au^{II} \longrightarrow [Au^{II}]_2 \longrightarrow Au^{I} + Au^{III} \tag{3.7}$$

3. Finally, the Au^I will be reduced by the reducing agent to form the Au^0 according to equations 3.8 and 3.9:

$$Au^{I}Cl_2^- + e_{aq}^- \longrightarrow Au^0Cl_2^{2-} \tag{3.8}$$

$$Au^{I}Cl_2^- + H^\circ \longrightarrow Au^0Cl_2^{2-} + H^+ \tag{3.9}$$

Au^0 and Au^I will dimerize together to form clusters of atoms surrounded by Cl^- according to the following equations :

$$\begin{aligned} Au^0Cl_2^{2-} + Au^{I}Cl_2^- &\longrightarrow (Au_2^+)_{Cl^-} \\ (Au_2^+)_{Cl} + (Au_2^+)_{Cl} &\longrightarrow (Au_4^+)_{Cl^-} \end{aligned} \tag{3.10}$$

We also added ethanol in the subphase at a concentration of about 10^{-2} mol.L^{-1} as we planned to further try to reduce the gold ions by surface X-ray radiolysis at the synchrotron.

3.4.4 X-ray surface radiolysis using Langmuir films as templates

In 2004, Goldmann et al. [10] applied the principle of radiolysis of water by synchrotron grazing incidence X-rays to a Langmuir film spread on an aqueous subphase containing silver ions. They succeeded in forming organometallic films of controlled shape and thickness. The grazing incidence and thus the total reflection geometry ensure that the reduction of metal ions occurs only a few nanometers from the surface, as shown in figure 3.25. This distance corresponds to the penetration length of the evanescent wave. The reduction is therefore limited to the surface ions only and is naturally directed by the Langmuir film. The film serves in fact as a template for the nucleation and growth of morphologically specific metal crystals. Simultaneously, they followed and determined the evolution of inorganic/organic structures by GIXD. Their results demonstrated the strength of limiting the principle of water radiolysis to Langmuir films deposited on the surface of the metal ion subphase to form crystalline metal nanostructures controlled and directed by the films. The study of this phenomenon contributes to the understanding, with new perspectives, of the interaction between organic and metallic structures.

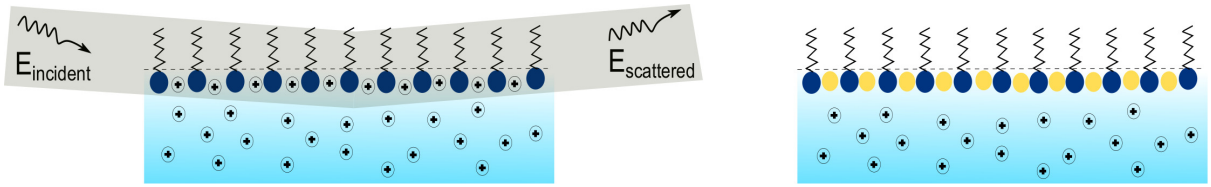

Figure 3.25: Schematic illustration of geometry of the X-ray surface radiolysis experiments applied to a Langmuir film spread over an ionic subphase.

Since then, X-ray surface radiolysis has been exploited to synthesize organometallic films of various Langmuir films and metal structures. For instance, Dutta et al. [116] succeeded in forming (111)-oriented gold nanoparticles using octadecanethiol monolayers as templates.

3.4.5 Superstructure of inorganic-organic Langmuir films

The adsorption of ions on the surface allows the stabilization and organization of Langmuir films. However, it was observed that when the concentration of ions exceeds a concentration threshold, an inorganic/organic superstructure forms [117]. A superstructure is the superimposition of an additional commensurate structure on a given crystalline structure. This phenomena has been observed and reported for the first time in 1991 for a Langmuir Films film of Cadmium Arachidate [118]. Numerous researches [117, 36, 119, 120, 121], since then, have been devoted to the study of superstructures of different Langmuir films and inorganic species. For instance Cantin et al. [117] studied behenic acid Langmuir monolayer deposited on a subphase containing cadmium chloride salt. Depending on the concentration of ions, they were able to demonstrate the transition of the film from an tilted L_2 phase to a superstructure via an intermediate phase. A concentration threshold was then defined to mark the limit of the formation of a superstructure. Dupres et al. [119] studied fatty acid monolayers deposited on subphases containing pure Cd^{2+}, Pb^{2+}, Mg^{2+}, or Mn^{2+}. They have demonstrated the formation of inorganic/organic superstructures when the concentration of cations in the subphase exceeds a threshold concentration. They have shown that the threshold, in addition to the concentration of

the subphase, depends on the pH of the subphase. They were also able to demonstrate that the shape of the isotherms can predict the formation of the superstructure. Recently, El Haitami et al. [121] studied a fatty acid monolayer deposited on Mg^{2+}/Mn^{2+} mixed subphases of various ratios. They followed the evolution of the Mn^{2+}-fatty acid monolayer superstructure as the mole fraction of Mg^{2+} increases in the subphase. They demonstrated the formation of a coexistence of two oblique phases at a certain ratio of Mg^{2+}/Mn^{2+}. They suggested that the ionic strength could play a key role, in addition to ion concentration, in the appearance of this phase coexistence.

Concentration unit

The adsorption of ions on the surface of a volume is governed by the thermodynamic equilibrium of the system. It therefore depends on the ratio between surface and volume of the system. Langmuir's troughs are of different dimensions all over the world. The concentration of a subphase, if expressed in $mol.L^{-1}$, would therefore be insignificant in terms of determining the number of inorganic ions adsorbed on the surface. Hence, to ensure the reproducibility of the experiments, regardless the dimension of the Langmuir trough, one must adopt another unit than $mol.L^{-1}$. By convention, the concentration is defined as the ratio of the number of inorganic ions to the number of organic molecules $r_{ions/molecules}$ [122]. It is calculated by the following equation:

$$r_{ions/molecules} = \frac{C_{ions}.V_{ions}}{C_{molecules}.V_{molecules}} \tag{3.11}$$

Chapter 4

$[C_{20}mim]^+[NTf_2]^-$ Langmuir films mixed with GO sheets

Contents

In this chapter, mixed films of $[C_{20}mim]^+[NTf_2]^-$ and GO sheets are studied at the air-water interface. The objective here is to understand the physico-chemical conditions for the formation of the interface between GO sheets and IL molecules. This could be a way to understand the mechanism of access of IL molecules to the graphene electrode interface in supercapacitors. We show that the mixed film consists of a double layer stack of GO sheets and IL molecules at the air-water interface. The IL molecules are in contact with water and the GO sheets, decorated with parallel IL molecules, are in contact with air. We also show that through a transition plateau, some IL molecules migrate from the water contact layer to the air contact layer. We have been able to demonstrate that the orientation of IL molecules at the interface with the GO sheets depends on the second interface that limits them. They are parallel to the GO sheets when they are in contact with air, but they are perpendicular or tiled to the GO sheets when they are in contact with water.

4.1 Preparation of the mixture

4.1.1 Solvent's choice

One of the special features of GO sheets is their large specific surface area. It is indeed one of the properties that made graphene or GO the compounds sought after to be the electrode of supercapacitors. However, GO sheets tend to aggregate into several sheets by $\Pi - \Pi$ stacking over time, which modifies their properties such as reducing their specific surface area. This problem can be avoided by choosing a suitable solvent to disperse the GO sheets into individual sheets. However, as we aim to study the GO/IL interface by Langmuir films, the solvent must, on the one hand, stabilize the GO dispersion in the long term and, on the other hand, dissolve the $[C_{20}mim]^+[NTf_2]^-$.

For the dissolution of IL, many solvents appear to be good candidates such as chloroform, NMP, DMF, ethylene glycol, DMSO [39, 123, 124] . On the other hand, solvents suitable for long-term dispersion stability of GO monosheets are limited. According to Dimitrios et al. [125], they should be characterized by a low vapor pressure and a surface tension similar to that of the graphene family. Depending on the oxidation degree of GO sheets, thus on the number of functional groups, GO surface tension is estimated to be between ~ 62 mN.m^{-1} and ~ 46 mN.m^{-1}. NMP, DMF and ethylene glycol have shown to be the three best solvents that ensure long-term dispersion stability of GO [125, 126]. They are also among the solvents that can dissolve $[C_{20}mim]^+[NTf_2]^-$. Table 4.1 shows the values of the vapor pressure, the surface tension of the three best organic solvent for GO monosheets dispersion and the solubility of the sheets.

Solvent	Vapor pressure (mmHg)	Surface tension (mN.m^{-1})	GO solubility (µg/mL)	References
DMF	2.85	37.1	1.96	[127], [125]
Ethylene glycol	0.06	47.7	5.5	[128], [125]
NMP	0.27	40.1	8.7	[129], [125]

Table 4.1: Properties of the three best solvent for long-term stability of GO monosheets dispersion.

We therefore limit our selection to three solvents suitable for the preparation of a good dispersion of GO monosheets and IL molecules in a mixed solution. On the other hand, for the formation of Langmuir films, the solvent must meet certain specific criteria. In fact, all three solvents are water-miscible and non-volatile, unlike the usual solvent, chloroform, which is used to form Langmuir films. The appropriate solvent to form Langmuir films must spread well over the surface. The very high toxicity of DMF [130] and its lowest solubility for GO sheets make it the least desirable solvent for our study. Large et al. [131], who studied the ability of certain water-miscible solvents (ethanol, acetone, isopropanol and NMP) to form Langmuir films, demonstrated that NMP was the best. In addition, NMP offers the highest solubility for GO sheets and is also a good solvent for IL. For these reasons, we choose NMP as the solvent to prepare our mixed solution of (GO + $[C_{20}mim]^+[NTf_2]^-$).

N-Methyl-2-Pyrrolidone, known as NMP, is a polar, organic and aprotic solvent. It is used in petrochemicals as an extraction solvent [132]. It is also characterized by being a paint remover solvent and is used in many fields because of its ability to dissolve a large number of organic and inorganic products [133]... Its chemical formula is : C_5H_9NO and its molecular structure is illustrated in Figure 4.1. Its density is $\rho_{NMP} = 1.03$ g.cm^3 [134].

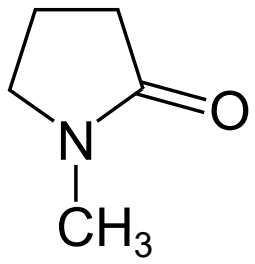

Figure 4.1: Molecular structure of NMP.

However, NMP is a water-miscible solvent and its dissolution kinetics in water are not known. Then, before proceeding to the study of Langmuir mixed films, the temporal evolution of the surface tension of water after the deposition of pure NMP on its surface must be measured.

We thus deposited 680 µL of NMP - a volume equivalent to the one we will spread on water surface to form GO/IL Langmuir film - on a water surface of a trough (A_{trough}= 180 cm^2; V_{trough} = 120 mL) at 20°C . We then recorded the evolution of the surface tension for 24 hours. We eliminated the variation in surface tension resulting from the evaporation of water. It is done by subtracting the evolution of the surface tension of pure water from that measured in the presence of NMP. The evolution over time of the surface tension $\gamma_0\,'(t)$ of the water in the presence of NMP on its surface is represented in Figure 4.2. We notice that the surface tension varies from $\gamma_0\,'(0) = 70.5$ mN.m^{-1} to $\gamma_0\,'(350) = 72.5$ mN.m^{-1}. Since the surface tension of pure water at 20°C is γ_0 =72.8 mN.m^{-1}, NMP is therefore assumed to be present on the water surface at t = 0 min. The surface pressure (Π) of the film must therefore be calculated taking into account $\gamma_0\,'(t)$, the surface tension of water with NMP according to Figure 4.2. It must therefore be calculated as follows :

$$\Pi = \gamma_0\,' - \gamma \tag{4.1}$$

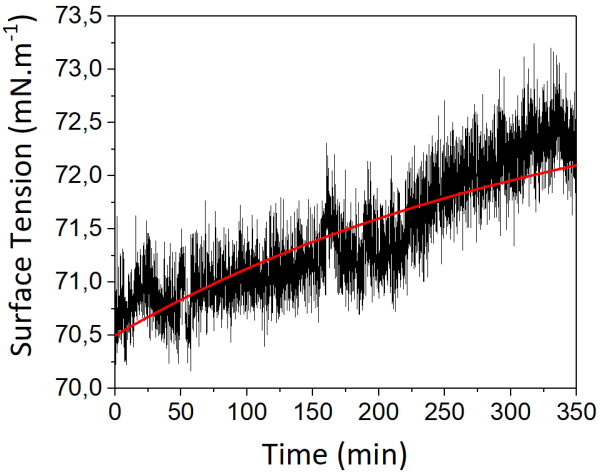

Figure 4.2: The evolution of the surface tension of water when 680 µL of NMP are deposited on its surface.

Where γ is the surface tension of water with presence of molecules which varies as a function of the film's compression.

It is possible to adjust the evolution over time of the surface tension $\gamma_0{}'(t)$ by a linear or exponential function. We have chosen an exponential function of the following form :

$$\gamma_0{}'(t) = \gamma_c - A \exp\left(\frac{-t}{\tau}\right) \tag{4.2}$$

Where γ_c is the constant to which tend the surface tension and is expressed in $\mathrm{mN.m^{-1}}$. τ is the time constant of the function and is expressed in minutes (min). A is the amplitude of the function and is expressed in $\mathrm{mN.m^{-1}}$. The adjustment has converged to :

$$\gamma_0{}'(t) = 73.04 - 2.54 \exp\left(\frac{-t}{350}\right) \tag{4.3}$$

Hence, γ_c tends to 73.04 $\mathrm{mN.m^{-1}}$ at $t \sim 5\tau = 1750$ min ~ 30 h. As γ_c is close to the surface tension of pure water ($\gamma_0 = 72.8$ $\mathrm{mN.m^{-1}}$), one can assume that the NMP needs about 30 hours to be completely dissolved in the subphase. This time range far exceeds that of our measurement.

We applied a waiting time of about 45 min after having deposited the solution and before starting to compress the film. According to Figure 4.3, $\gamma_0{}'(45) = 70.8$ $\mathrm{mN.m^{-1}}$. The Π-A isotherm was thus measured according to $\Pi = 70.8 - \gamma$. The films were also studied by XRR and GIXD measurements at three surface pressures, taking a total of 45 min. The complete measurement of the film therefore takes 90 min. According to Figure 4.3, $\gamma_0{}'(90) = 71.0$ $\mathrm{m^{-1}}$ which is 0.2 $\mathrm{mN.m^{-1}}$ lower than $\gamma_0{}'(45) = 70.8$ $\mathrm{mN.m^{-1}}$. However, the resolution of the surface pressure is 0.2 $\mathrm{mN.m^{-1}}$. It is therefore acceptable to consider that the conditions under which our measurements were carried out were invariant.

4.1.2 Preparation of the ($[C_{20}mim]^+[NTf_2]^-$ + GO) mixed solution in NMP

To prepare a mixture of GO and IL solution, we purchased an aqueous graphene oxide dispersion of 2 $mg.ml^{-1}$ from Sigma Aldrich and $[C_{20}mim]^+[NTf_2]^-$ powder from Iolitec. We first prepared two solutions : one of GO dispersed in NMP (0.020 $mg.mL^{-1}$; 5 mL) and another one of $[C_{20}mim]^+[NTf_2]^-$ dissolved in NMP (0.074 $mg.mL^{-1}$; 5 mL). We sonicated each for 40 min and then mixed and let them under mechanical stirring for 24h. The obtained final mixed solution (GO + $[C_{20}mim]^+[NTf_2]^-)_{NMP}$ was of concentration C = 0.047 $mg.mL^{-1}$ and composed of 0.01 $mg.mL^{-1}$ of GO and 0.037 $mg.mL^{-1}$ of $[C_{20}mim]^+[NTf_2]^-$.

For the elaboration of Langmuir mixed films, we used to spread 680 µL of this mixed solution after having sonicated it for 5 min. The thermodynamic equilibrium between the surface and the subphase is controlled by the dissolution of the NMP in the subphase. In order to keep it constant regardless of the trough dimension, the ratio between the trough's area A_{trough} and the subphase's volume $V_{subphase}$ has been kept constant : r = $A_{trough}/V_{subphase} \sim 1.5$ cm^{-1}. The compression velocity was set to 15 $cm^2.min^{-1}$ and the temperature of the trough was maintained at 20°C.

4.2 Macroscopic characterization at the air-water interface

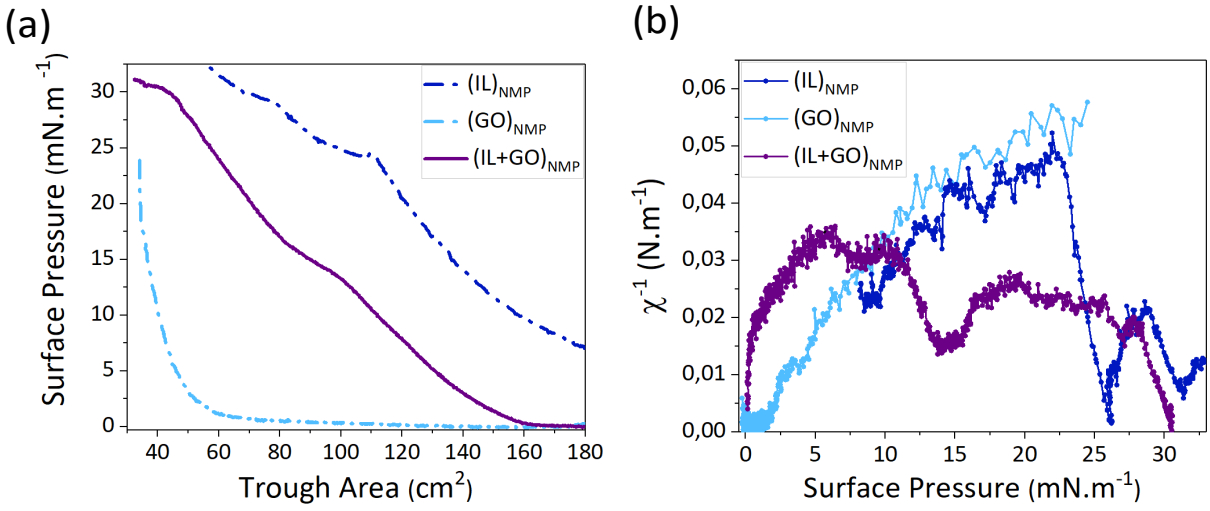

Figure 4.3: Π-A isotherms of $([C_{20}mim]^+[NTf_2]^-)_{NMP}$, $(GO)_{NMP}$ and (GO + $[C_{20}mim]^+[NTf_2]^-)_{NMP}$ Langmuir films deposited at the air-water interface at 20°C.

Figure 4.3 (a) and Figure 4.3 (b) show respectively the Π-A isotherms and the inverse of compressibilities of pure compounds and their mixture. Recall that the inverse of the compressibility corresponds to $\chi^{-1} = -A\frac{\partial \Pi}{\partial A}$. We have chosen to plot χ^{-1} instead of χ to avoid scale problems because perfectly flat plateaux are infinitely compressible. The amount of each compound forming pure Langmuir films is equivalent to that forming mixed Langmuir films. The surface pressure of the mixed Langmuir film is roughly

intermediate between that of pure films. As the pressure is an intensive quantity, the surface pressure of the film must be obtained by averaging the surface pressure of the pure Langmuir film. It can therefore be confirmed that both compounds are present at the air-water interface. In order to study in more details the behavior of Langmuir mixed film, it is necessary to understand the behavior of pure films beforehand.

Usually, Langmuir films are prepared using a volatile solvent, so that they would be solvent-free after 15 min of deposition. The behavior of the films on the water surface would only be relative to that of the molecules. In this study, Langmuir films are prepared with NMP, thus cannot be solvent-free within the time range of our measurements as shown in section 4.1.1. One must consider a possible effect of NMP on the macroscopic behavior of pure films on the water surface. It is therefore necessary to study and compare the Π-A isotherms of pure Langmuir films prepared with NMP with those prepared using volatile solvents.

4.2.1 Π-A isotherm : $[C_{20}mim]^+[NTf_2]^-$

Figure 4.4 (a) and Figure 4.4 (b) show respectively the Π-A isotherms and the inverse of compressibilities of $[C_{20}mim]^+[NTf_2]^-$ Langmuir films prepared in chloroform $(IL)_{chloroform}$ and in NMP $(IL)_{NMP}$. Since chloroform is a volatile solvent, $(IL)_{chloroform}$ Langmuir film can be considered solvent-free film after 15 min of deposition. To form the $(IL)_{NMP}$ Langmuir film, 680 µL of 0.057 mMol.L^{-1} of a solution of $[C_{20}mim]^+[NTf_2]^-$ dissolved in NMP were deposited on the water surface. This amount is equivalent to the amount that IL molecules occupy in Langmuir mixed film. To form the $(IL)_{chloroform}$ Langmuir film, 12 µL of 2 mMol.L^{-1} of a solution of $[C_{20}mim]^+[NTf_2]^-$ dissolved in chloroform were deposited on the water surface. The Π-A isotherm of the free-solvent IL ($(IL)_{chloroform}$) Langmuir film is described in chapter 3, in section 3.2.1.

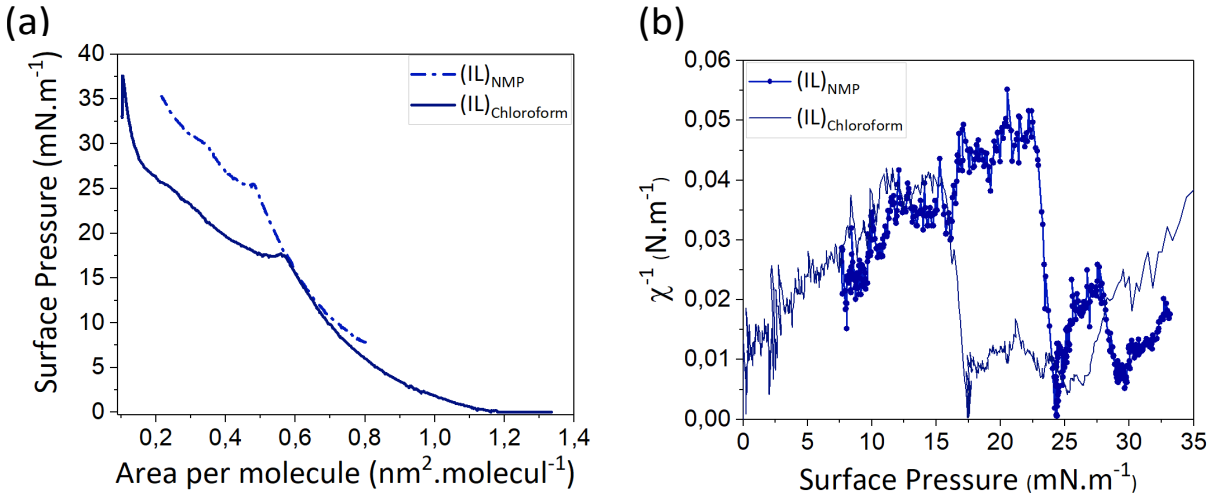

Figure 4.4: (a) Π-A isotherms of each of $(IL)_{NMP}$ Langmuir film and $(IL)_{chloroform}$ Langmuir film deposited at the air-water interface and (b) their corresponding inverse compressibilities.

The deposited amount of $(IL)_{NMP}$ corresponds to A_{NMP} = 0.8 nm^2.molecule^{-1} and Π_{NMP} = 7.83 mN.m^{-1}. Three increasing regions can be identified : **region (i)**, **region(ii)** and **region (iii)**.

Region (i) extends to (Π = 26.5 mN.m^{-1}; A = 0.48 nm^2.molecule^{-1}). The inverse of the compressibility increases to χ^{-1} = 0.05 N.m^{-1} (χ = 20 m.N^{-1}). The film in this region is in a (LE) phase. At A = 0.48 nm^2.molecule^{-1}, the slope of the inverse of the compressibility drops indicating the beginning of the formation of a plateau. It extends to (Π = 26.8 mN.m^{-1}; A= 0.40 nm^2. molecule^{-1}). **The plateau is then followed by region (ii) which is limited between A = 0.40 nm^2.molecule^{-1} and A = 0.34 nm^2.molecule^{-1}.** The surface pressure increases from Π = 26.8 mN.m^{-1} to Π = 31 mN.m^{-1}. The inverse of the compressibility in region (ii) decreases with respect to region (i). It reaches χ^{-1} = 0.015 N.m^{-1} (χ = 66 m.N^{-1}). At A = 0.34 nm^2. molecule^{-1}, the slope of the inverse of the compressibility drops indicating the beginning of the formation of a plateau. It extends to (Π = 31 mN.m^{-1}; A = 0.31 nm^2. molecule^{-1}). **The plateau is the followed by region (iii) which is limited between A = 0.31 nm^2.molecule^{-1} and A = 0.21 nm^2.molecule^{-1}.** The surface pressure increases to Π = 35 mN.m^{-1}. In this region, the inverse of the compressibility is χ^{-1} = 0.025 N.m^{-1} (χ = 40 m.N^{-1}). At the end of this region, water overflows from the trough due to the densification of the IL film.

Discussion

The two films behave broadly similar on a macroscopic scale, in both three increasing region are identified. At A = 0.8 nm^2.molecule^{-1}, the surface pressure of $(IL)_{NMP}$ Langmuir film is 2 mN.m^{-1} higher than that of the free-solvent Langmuir IL film. However, during the compression of the films, up to A = 0.56 nm^2.molecule^{-1}, the isotherm of $(IL)_{NMP}$ film converges to that of the free-solvent film. Based on these observations, one suggests that NMP is present on the water surface but in modest quantities. In this case, the lift-off of the $(IL)_{NMP}$ Langmuir film should be considered close to that of the free-solvent Langmuir IL film and corresponds to A_{trough} = 225 cm^2.

In region (i), $(IL)_{NMP}$ is slightly less compressible (χ = 20 m.N^{-1}) than the free-solvent film (χ = 25 m.N^{-1}) but both are considered monolayers in a (LE) phase. The presence of NMP molecules on the surface could be the reason for decreasing the film compressibility.

In region (ii), obtained after a first plateau, the compressibilities of the films increase with respect to region (i) after passing through a plateau. The free-solvent IL monolayer collapses into a multilayer, across this plateau. The system therefore becomes 3D and 2D compressibility can no longer be an adequate description of the film state. 3D compressibility must be considered and is related to 2D compressibility by the relation χ_{3D}= eχ_{2D}, where e is the layer thickness. $(IL)_{NMP}$ is therefore assumed to as well collapse into a multilayer across this plateau. The plateau is obtained at a higher surface pressure and at a molecular area 14% less when the film is $(IL)_{NMP}$. Since NMP is a suitable solvent for IL molecules and is miscible with water, its presence on the water surface may have induced a longer interaction between IL molecules and water. One may therefore suggest that the presence of NMP better stabilizes the IL film on the water surface.

In region (iii), obtained after a second plateau, the films compressibilities are as well higher than that of region (i). The free-solvent IL multilayer is assumed to collapse further , across this plateau. Since the compressibilities of both films are close, it is assumed that the $(IL)_{NMP}$ film as well collapses further through this plateau.

At the end of region (iii), the films collapse while this is achieved earlier for $(IL)_{NMP}$ Langmuir film. This would imply an effect of the presence of NMP with IL molecules.

To conclude, IL films undergo a transition from a monolayer (region (i)) to a multilayer (region (ii)) through a first collapse plateau. Then, the multilayer continues to collapse through a second collapse plateau until it degrades at the end of region (iii). The presence of NMP on the water surface delays the surface pressure and molecular surface area of the first collapse plateau, suggesting that NMP tends to better stabilize the IL monolayer. Its presence contributed to the early degradation of the multilayer. Despite the presence of NMP, the thermodynamic properties of the IL Langmuir film remain the same as those of the free-solvent IL Langmuir film.

4.2.2 Π-A isotherm : GO

Figure 4.5 (a) and Figure 4.5 (b) show respectively the Π-A isotherm and the compressibility of GO Langmuir prepared in methanol $(GO)_{methanol}$ as studied by Bonatout et al.. Since methanol is a volatile solvent, $(GO)_{methanol}$ Langmuir film can be considered solvent free after 15 min from the deposition. As mentioned in section 3.3.5 of chapter 3, the amphiphilicity of GO sheets is strongly dependent on the size of the sheets. GO colloidal solutions consist of a polydispersion of sheets, some of which do not have the proper amphiphilic balance to form a Langmuir film. These sheets will therefore not be able to remain adsorbed on the water surface and will drown in the subphase. It is impossible to know the exact number of sheets remaining on the surface. The variation in surface pressure ($mN.m^{-1}$) is therefore plotted versus the variation in trough surface area per the volume of the deposited solution ($cm^2.mL^{-1}$).

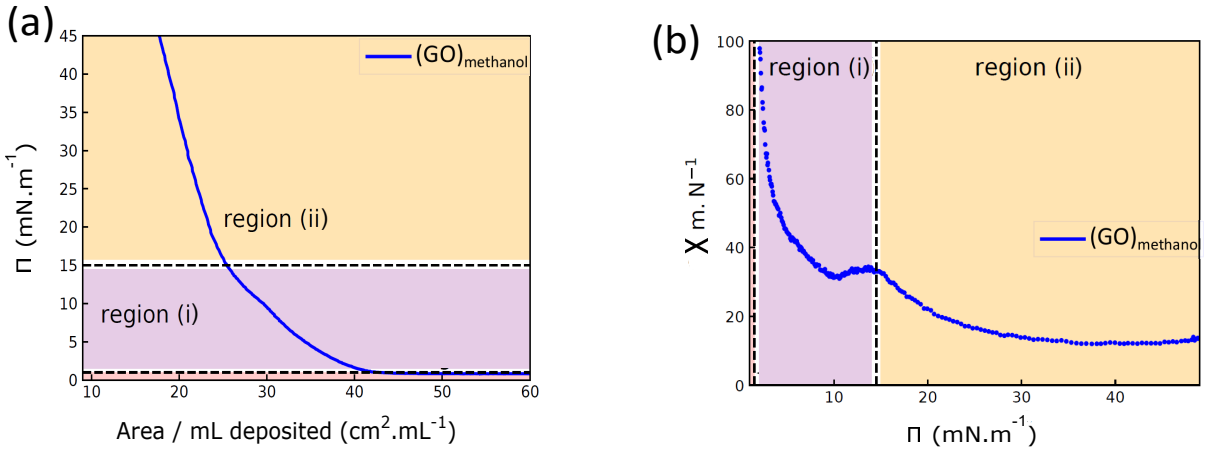

Figure 4.5: Π-A isotherm of $(GO)_{methanol}$ Langmuir film deposited at the air-water interface at 20°C (reproduced from [39], [99]).

According to Bonatout et al. [39, 99], the Π-A isotherm exhibits two increasing regions: region (i) and region (ii).

For surface areas greater than $A_{trough} \sim 40$ cm^2.mL^{-1}, the surface pressure of the film is $\Pi = 0$ mN.m^{-1} and the compressibility tends towards infinity. The film is in a coexistence of phases, in which one of the phases is a diluted phase. **The plateau is followed by region (i) which is limited between the isotherm lift-off and Π = 15 mN.m^{-1}.** It includes a pseudo-plateau observed at $\sim \Pi = 10$ mN.m^{-1}. The compressibility of this region is $\chi = 33.4$ m.N^{-1} which indicates a (LE) phase. **It is followed by a region (ii) of compressibility that extends from Π = 15 mN.m^{-1} to Π = 45 mN.m^{-1}.** The compressibility at the end of this region is χ= 15 m.N^{-1} which corresponds to a (LC) phase. At the end of this region, the film collapses.

Figure 4.6 (a) and Figure 4.6 (b) show respectively the Π-A isotherm and the inverse of compressibility of GO Langmuir prepared in NMP, $(GO)_{NMP}$. To form the film, 680 µL of a dispersion of GO in NMP of a concentration 0.057 mMol.L^{-1} (0.01 mg.mL^{-1}) were deposited on the water surface. This amount is equivalent to the amount that GO sheets occupy in Langmuir mixed film. The variation in surface pressure (mN.m^{-1}) is plotted versus the variation in trough surface area (cm^2).

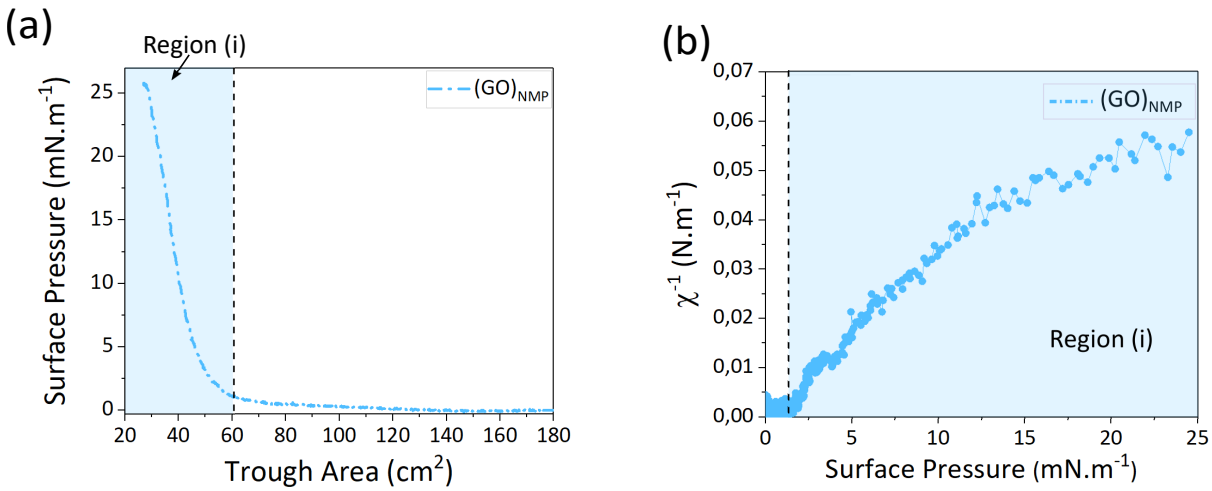

Figure 4.6: Π-A isotherm of $(GO)_{NMP}$ Langmuir film deposited at the air-water interface at 20°C.

The Π-A isotherm exhibit one increasing region : region (i).

For surface areas greater than $A_{trough} \sim 60$ cm^2, the surface pressure of the film is $\Pi = 0$ mN.m^{-1} and the inverse of the compressibility is $\chi^{-1} = 0$ N.m^{-1}. The film is in a coexistence of phases, in which one of the phases is a diluted phase. **The plateau is then followed by region (i) which extends from $A_{trough} \sim$ 60 cm^2 to A_{trough} = 27 cm^2.** The surface pressure increases from $\Pi = 0$ mN.m^{-1} to $\Pi = 26$ mN.m^{-1} and $A_{trough} = 27$ cm^2. The film did not reach higher surface pressure, as the compression has reached its limit in our trough. The compressibility of region (i) decreases gradually until it reaches χ= 18 m.N^{-1} at $\Pi = 26$ mN.m^{-}. It indicates that the film is in a (LE) phase.

The Π-A isotherm of the free-solvent GO Langmuir film presents two increasing regions : the first one corresponds to a (LE) phase and the second one to a (LC) phase. That of the $(GO)_{NMP}$ Langmuir film presents only one increasing region which corresponds to a (LE) phase. The presence of the NMP in the film appears to increase its compressibility.

4.2.3 Π-A isotherm : $[C_{20}mim]^+[NTf_2]^-$ + GO

Figure 4.7 (a) and Figure 4.7 (b) show respectively the Π-A isotherms and the inverse of compressibility of $(GO + [C_{20}mim]^+[NTf_2]^-)_{NMP}$ Langmuir film. To form the film, 680 µL of the mixture solution with a concentration of 0.047 $mg.mL^{-1}$ were deposited on the water surface. Since the mixture contains GO sheets, the Π-A isotherm represents the variation of $\Pi(A_{trough})$. The quantities of each of GO and IL in the mixed film are equivalent to those of each of the pure films studied previously.

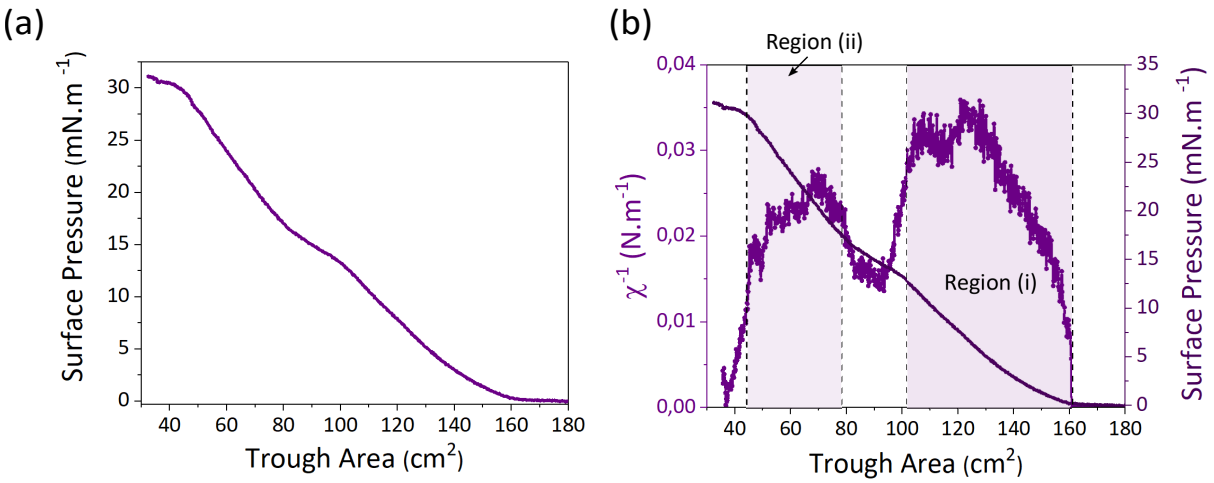

Figure 4.7: (a) Π-A isotherm of $(IL+GO)_{NMP}$ Langmuir film deposited at the air-water interface and (b) its inverse compressibility.

The Π-A isotherms of $(GO + [C_{20}mim]^+[NTf_2]^-)_{NMP}$ Langmuir mixed film exhibits two increasing regions : region (i) and region (ii).

For surface areas greater than $A_{trough} = 162$ cm^2, the surface pressure and the inverse of the compressibility of the film are respectively $\Pi = 0$ $mN.m^{-1}$ and $\chi^{-1} = 0$ $N.m^{-1}$. The film undergoes a plateau of coexistence of phases, one of which is the diluted phase. **The plateau is then followed by region (i) which is limited between A_{trough} = 162 cm^2 and A_{trough} = 103 cm^2.** The surface pressure increases from $\Pi = 0$ $mN.m^{-1}$ to $\Pi = 12.5$ $mN.m^{-1}$. In this region, the inverse of the compressibility increases to χ^{-1} = 0.035 $N.m^{-1}$ (χ = 28 $m.N^{-1}$). At $A_{trough} = 103$ cm^2, the slope of the inverse of the compressibility drops indicating the beginning of the formation of a plateau. It extends to ($\Pi = 16.5$ $mN.m^{-1}$; A_{trough}= 82 cm^2). **The plateau is then followed by region (ii) which is limited between A_{trough}= 82 cm^2 and A_{trough}= 42 cm^2.** The surface pressure increases from $\Pi = 16.5$ $mN.m^{-1}$ to $\Pi = 30$ $mN.m^{-1}$. In this region, the film is more compressible that it was in region (i). The inverse of the compressibility reaches $\chi^{-1} = 0.025$ $N.m^{-1}$ (χ = 40 $m.N^{-1}$). At $\Pi = 30$ $mN.m^{-1}$ another plateau started to

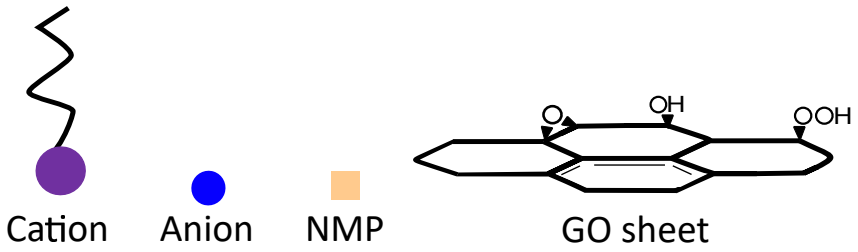

Figure 4.8: Schematic illustration of the cation, anion, NMP and GO sheets on the basis of which our XRR models were built.

form and is assumed to correspond to film collapse.

Discussion

The schematic illustration of cations, anions, NMP and GO sheets is shown in Figure 4.8. On their basis, we have built models to describe the possible configuration of the mixed film's components. The lift-off area of pure IL film is at A = 1.17 nm^2.$molecule^{-1}$, which corresponds in our case to A_{trough} = 225 cm^2. The lift-off area of pure GO film is at A_{trough} = 60 cm^2. In the mixed film, GO sheets could thus occupy a maximum of 23% of the surface occupied by the IL molecules. The lift-of of the mixed film is at A_{trough} = 162 cm^2. Two possible configurations can be considered to describe the two compounds of the mixed film at the lift-off :

1. First configuration :
   Suppose a monolayer of GO sheets and a monolayer of IL molecules are horizontally segregated at the water surface, as illustrated in Figure 4.9.
   At the lift off (A_{trough} = 162 cm^2), GO sheets must occupy A_{trough} = 60 cm^2 and

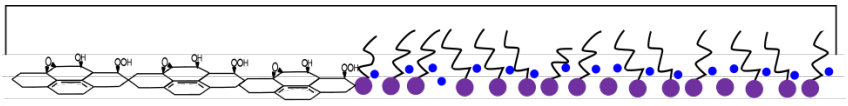

Figure 4.9: Schematic representation of the possible **first configuration of the layer in contact with water**.

   the IL molecules A_{trough} = 102 cm^2. In such as case, the surface occupied by the IL molecules would be half ($\sim$ 0.45%) of the surface that must be occupied by all IL molecules (A_{trough} = 225 cm^2). One must therefore consider a second monolayer of IL that must be stacked on top of the layer in contact with water, as illustrated in Figure 4.10. The layer in contact with air would be formed by the 55% of the deposited IL molecules which are supposed to occupy 76% of the trough surface, as illustrated in Figure 4.10. The orientation of IL as illustrated in this model does not necessarily reflect the true one, and further study is required to determine it.

2. Second configuration :
   Suppose a monolayer of GO sheets and a monolayer of IL molecules are vertically segregated at the water surface. The segregation would consist of a stack of one layer in contact with water and one layer in contact with air. GO sheets can

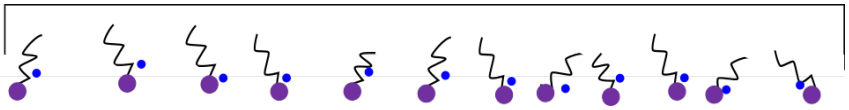

Figure 4.10: Schematic representation of the possible **first configuration of the layer in contact with air.**

occupy a maximum surface A_{trough} = 60 cm^2 which represents only 37 % of the surface occupied by the mixed film. The layer in contact with water cannot then be formed of pure GO sheets. The stack should consist of a layer in contact with water formed of IL molecules and a layer in contact with air formed of GO sheets. The IL molecules, in the layer in contact with water, would occupy A_{trough} = 162 cm^2, as illustrated in Figure 4.11 , which represents only 72% of the deposited IL. Therefore, 28% of the deposited IL must be either embedded in the subphase or

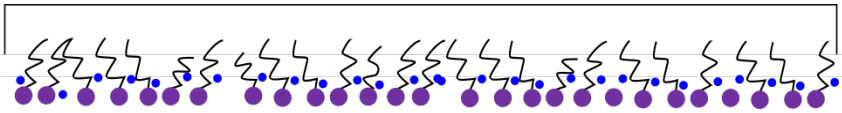

Figure 4.11: Schematic representation of the possible **second configuration of the layer in contact with water.**

occupying the layer in contact with air. Since this IL tends to be hydrophobic, it cannot sink into the aqueous subphase. Thus, 28% of the IL consider to be in the layer in contact with air with GO sheets. GO sheets do not fully cover the surface, the 28% IL could therefore either stack on next to GO sheets on top of the layer in contact with water ((Figure 4.12 (a)) or stack on top of the GO sheets (Figure 4.12 (b)). The orientation of IL as illustrated in this model does not necessarily reflect the true one, and further study is required to determine it.

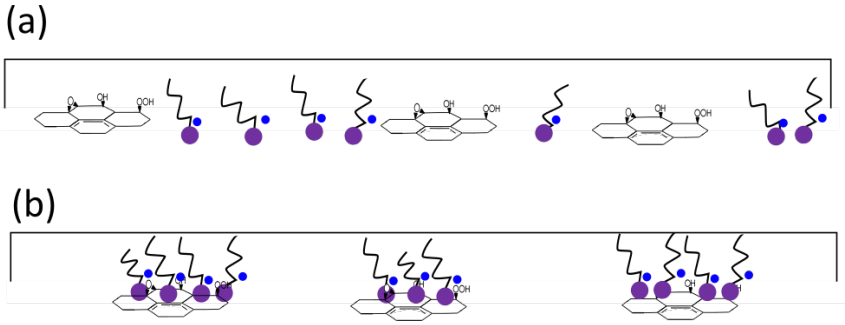

Figure 4.12: Schematic representations of the possible **second configuration of the layer in contact with air.**

At the lift-off, the film must be composed of two layers stacked vertically. Two configurations can be considered to describe the stacking. The first one consists in having the layer in contact with water formed of a monolayer GO sheets and a monolayer of IL molecules and the layer in contact with air of IL molecules. The second configuration consists in having the water contact layer formed of IL molecules solely and the air contact layer formed of GO sheets and IL molecules.

After the lift off, the mixed film is in the region (i) which is of compressibility χ = 28 m.N^{-1} which corresponds to (LE) phase. Then, at Π = 12.5 mN.$^{-1}$, a plateau begins to form, through which, the surface of the trough allocated to the film is reduced by 20 %. The plateau is then followed by region(ii) of compressibility χ = 40 m.N^{-1}. The film in region (ii) becomes more compressible than it was in region(i). In principle, as the surface pressure increases, the compressibility of the film should decrease. As shown in Chapter 3, section 3.2.1, the collapse of the IL Langmuir monolayer into a multilayer, across a plateau, is evidenced by an increase in the compressibility of region (ii) relative to that of region (i). The plateau observed in the isotherm of the mixed film may therefore correspond to the collapse of 20 % of IL molecules collapse.

In order to determine the configuration and a possible organization of the bilayer, structural studies such as XRR, GIXD and AFM measurements are required.

4.3 Characterization by X-ray scattering at the air-water interface

4.3.1 XRR measurements

The density profile of the (GO + $[C_{20}mim]^+[NTf_2]^-)_{NMP}$ mixed Langmuir film, deposited at the air-water interface, was probed by XRR along the axis perpendicular to the interface. The measurements were performed at PETRA III, beamline P08. The photon energy of the monochromatic X-ray photons was 18 KeV. The evolution of the reflectivity spectra of the Langmuir mixed film was followed along its compression. The XRR data were adjusted using GenX, a software to adjust the X-ray specular reflectivity spectra and/or neutron reflectivity spectra [135]. The adjustment proceeds by creating a model composed of layers at the interface between the subphase and the atmosphere. GenX then calculates the electron density profile, expressed in electron.Å^{-3}, of the model using a differential evolution algorithm based on Parratt's recursion formula. Depending on the fitting parameters, the model initially defined is validated or invalidated. We have chosen to convert the electron density "dens" obtained for each layer of our model into mass density "ρ" . To make the conversion, we used the following formula:

$$\rho = dens \times 10^{24} \times M \times u \tag{4.4}$$

"ρ", the mass density, is expressed in g.cm^{-3}. "dens", the electron density, is expressed in electron.Å^{-3}. "M" is the molar mass of the components that compose the layers and "u" is the relative atomic mass and is equal to : 1u = 1.66054$\times$10^{-24} g.

The IL molecule is composed of an anion and a cation. The theoretical density of $[C_{20}mim]^+[NTf_2]^-$, is supposed to be equal to the average of the densities of the $[C_{20}mim]^+$ and $[NTf_2]^-$. It thus corresponds to :

$$\rho_{IL-Theo} = \frac{\rho_{cation} + \rho_{anion}}{2} \tag{4.5}$$

The densities of the cation and the anion are calculated using the following equation :

$$\rho = \frac{M}{V \times N_A} \tag{4.6}$$

Where M is the molar mass, N_A is the Avogadro number and V is the volume of the entity. The volume of the $[C_{20}mim]^+$ is V_{cation} = 697 Å^3 and that of the $[NTf_2]^-$ is V_{anion} = 235 Å^3 $\Longrightarrow$ ρ_{cation} = 0.86 g.cm^{-3} and ρ_{anion} = 1.97 g.cm^{-3}. The estimated theoretical density of IL is therefore $\rho_{IL-Theo}$ = 1.42 g.cm^{-3}.

For GO, the estimated molecular formula of its elementary cell [136] is $C_2O_1H_{0.5}$ $\Longrightarrow$ M = 40.5 g.mol^{-1}. The area of its elementary cell is assumed to be equal to that of a graphene sheet (A = 5.1 Å^2) [137]. Its thickness is estimated to be equal to d = 10 Å [138]. The theoretical density of GO, according to Equation 4.6, is therefore $\rho_{GO-Theo}$ = 1.32 g.cm^{-3}.

The first XRR measurement was performed at (Π = 11 mN.m^{-1}; A_{trough} = 108 cm^2), just before the observed plateau at $\Pi_{plateau}$ = 12.5 mN.m^{-1} (see Figure 4.13). Figure 4.14 (a) and Figure 4.14 (b) show respectively the XRR spectrum adjusted using a model describing the film with a monolayer and its corresponding electron density profile. The fitting parameters are as follows :

- A monolayer that is very dense (ρ = 1.73 g.cm^{-3}), thick (d = 18.2 Å) and very rough (σ = 12.34 Å)

However, the fit does not correctly describe the reflectivity spectrum for $Q_z > 0.2$ nm^{-1}. The enormous roughness of this layer relative to its thickness and its high density suggest that the film could be formed by a bilayer instead of a monolayer. We have therefore abandoned the model of a monolayer and defined a model of a bilayer.

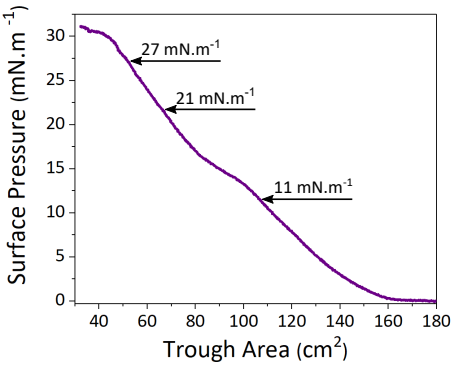

Figure 4.13: Π-A isotherm of $(IL+GO)_{NMP}$ Langmuir film deposited at the air-water interface.

Figure 4.15 (a) and Figure 4.15 (b) show respectively the XRR spectrum adjusted using a model describing the film with a bilayer and its corresponding electron density profile. The fit has converged to the following parameters :

1. First layer L_1, in contact with water, of density (ρ = 1.33 g.cm^{-3}) , thickness (d = 11 Å) and roughness (σ = 1.78 Å).
2. Second layer L_2, in contact with air, of density (ρ = 0.94 g.cm^{-3}), thickness (d = 12 Å) and roughness (σ = 5.92 Å).

According to the macroscopic study of $(GO + IL)_{NMP}$ Langmuir film (Figure 4.7), two possible configurations proved to be able to describe the stacking of the bilayer. The first suggests that the layer in contact with water L_1 is formed by (GO + IL) and the layer in contact with air L_2 by IL. The second suggests that the layer in contact with water is formed of IL and the layer in contact with air by (GO + IL). According to XRR

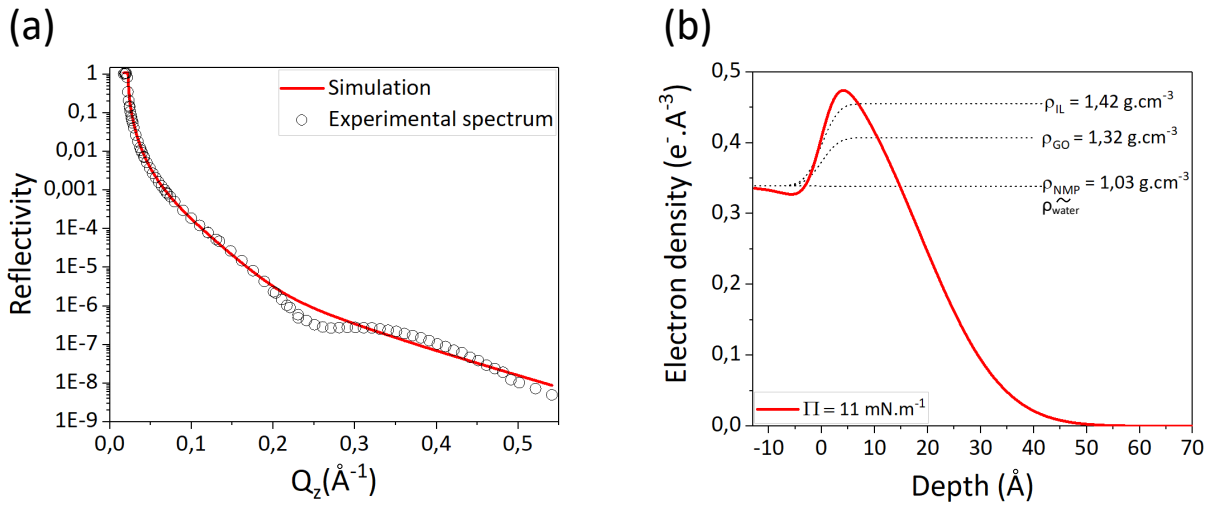

Figure 4.14: (a) XRR spectrum obtained at $\Pi = 11$ mN.m^{-1} adjusted by a model of a monolayer and (b) its corresponding electron density profiles.

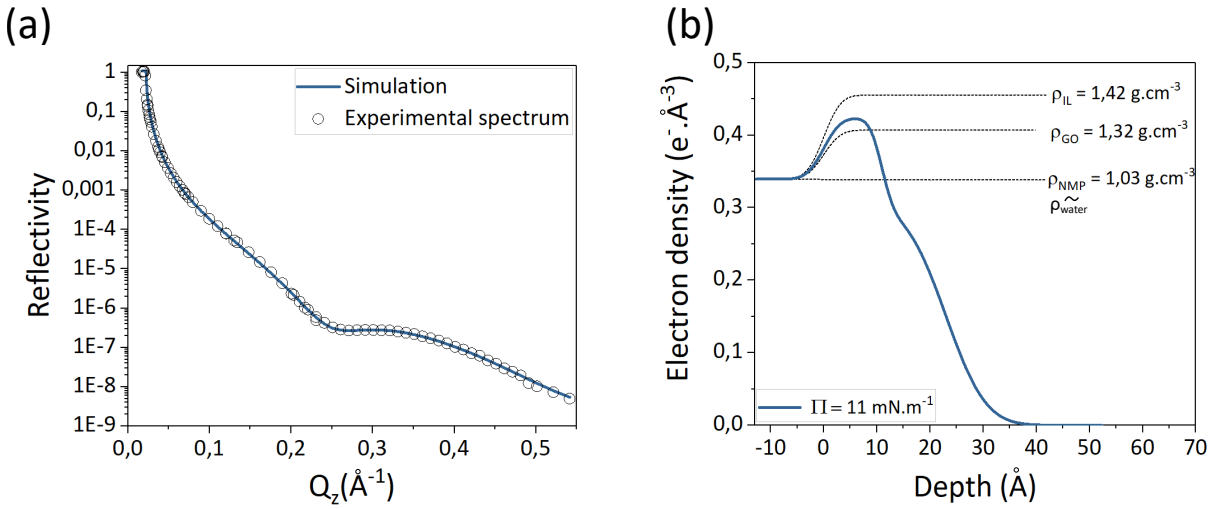

Figure 4.15: (a) XRR spectrum obtained at $\Pi = 11$ mN.m^{-1} adjusted by a model of a bilayer and (b) its corresponding electron density profiles.

adjustment parameters, the density of L_1 ($\rho = 1.33$ g.cm^{-3}) is close to that of IL and GO. However, the density of L_2 ($\rho = 0.94$ g.cm^{-3}) is 46% lower than that of IL ($\rho = 1.42$ g.cm^{-3}) and 28% lower than that of GO ($\rho = 1.32$ g.cm^{-3}). L_2 cannot therefore be formed by pure IL molecules, which requires adopting the second configuration (Figure 4.11 and Figure 4.12 (a) or (b)).

The density of L_1 is 6% lower than the theoretical density of IL. In such a case, it is quite acceptable to consider that L_1 is formed by pure IL molecules. However, according to the macroscopic study of the $(IL)_{NMP}$ film, NMP proved to remain, in modest quantity, adsorbed on the water surface. The density of NMP is $\rho_{NMP} = 1.03$ g.cm^{-3}. L_1 could therefore be formed of 23% of NMP against 77% of IL. At $\Pi = 11$ mN.m^{-1}, L_1 occupy $A_{trough} = 108$ cm^2. Imidazolium rings and NMP have an affinity for water and each other. Therefore, they can be considered, on the water surface, interacting with each other. The surface occupied by L_1 could thus consist of NMP molecules occupying $A_{trough} = 25$ cm^2 (23% of $A_{trough} = 108$ cm^2) and IL molecules occupying $A_{trough} = 83$

cm^2 (77% of A_{trough} = 108 cm^2). Regarding the thickness of L_1 (d = 11 Å), the alkyl chains should to be tilted in the air. As for anions, this XRR measurement could not provide rigorous information about them. However, because of their hydrophobicity and electrostatic interaction with the Imidazolium rings, it is suggested that they should be in contact with air but close to the rings.

According to the macroscopic study (Figure 4.7), in region (i), 28% of the total IL molecules must be in L_2. If the 72% of the total IL occupy A_{trough} = 83 cm^2 in L_1 $\Longrightarrow$ the remaining 28% of the total IL should occupy A_{trough} = 32 cm^2 in L_2. On the other hand GO sheets could occupy a surface up to a A_{trough} = 60 cm^2 in L_2. One of two possible models can describe the configuration of IL and GO in L_2. The first model M_1 is illustrated in Figure 4.16. It suggests that IL molecules prefer to stack on top of each other and be separated horizontally from GO sheets. In such a case, the area occupied by L_2 must correspond to A_{trough} = 32 + 60 = 92 cm^2. Since the thickness of L_2, according to XRR, is d = 12 Å, the alkyl chains of the IL molecules of L_2 should be interdigitated with those of L_1. The anions are supposed to be close to the rings.

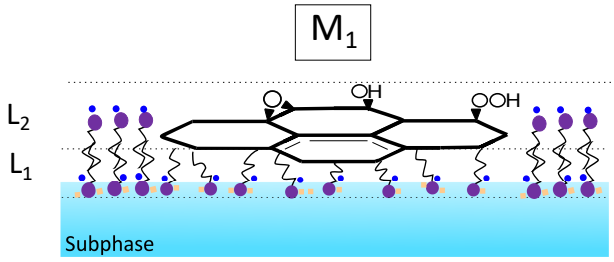

Figure 4.16: Schematic representations of the model M_1 describing the IL and GO stack configurations at Π = 11 $mN.m^{-1}$.

The second model M_2 is illustrated in Figure 4.17. It suggests that the IL molecules prefer to stack on top of GO sheets. In such a case, the area occupied by L_2 must correspond to that occupied by GO sheets which is A_{trough} = 60 cm^2. Regarding the thickness of L_2 the IL molecules should be lying horizontally and in contact with GO sheets. The anions are as well supposed to be close to the rings.

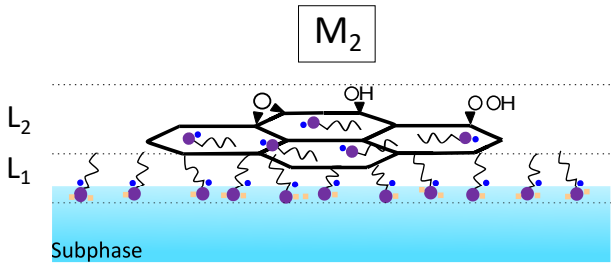

Figure 4.17: Schematic representations of the model M_2 describing the IL and GO stack configurations at Π = 11 $mN.m^{-1}$.

We notice that in the model M_2, the IL molecules at the interface with the GO sheets are perpendicular in L_1 but lying horizontally in L_2 (Figure 4.17). The main difference between the two layers lies in the environment surrounding the IL molecules. In L_1, they are limited between **two interfaces which are the water surface and the GO**

sheets. In L_2, they are limited between **two interfaces which are the GO sheets and the air**. The behavior of IL molecules at the interface with the GO sheets appears to be determined by the nature of the second interface limiting the molecules.

On the basis of the two proposed models, we deduce that L_2 can occupy a maximum surface of A_{trough} = 92 cm^2 (in M_1) or A_{trough} = 60 cm^2 (in M_2). This indicates that about 15% (in M_1) or 45% (in M_2) of the surface of L_2 at this surface pressure is free $\Longrightarrow$ L_2 is not very dense. As XRR measurements provide the average density of a layer, the low density of L_2 compared to that of the GO sheets and the IL molecules can therefore be justified.

We then performed XRR at (Π = 21 $mN.m^{-1}$; A= 67 cm^2), after the observed plateau at Π = 12.5$mN.m^{-1}$ (see Figure 4.13). Figure 4.18 (a) and Figure 4.18 (b) show respectively the adjusted XRR spectrum and the corresponding electron density profile. We also used the bilayer model to describe $(GO + IL)_{NMP}$ Langmuir mixed film. The fit well converged to a bilayer characterized by the following parameters :

1. First layer L_1, in contact with water, of density (ρ = 1.39 $g.cm^{-3}$) , thickness (d = 10 Å) and roughness (σ = 2.62 Å).

2. Second layer L_2, in contact with air, of density (ρ = 1.15 $g.cm^{-3}$), thickness (d = 18 Å) and roughness (σ = 5.56 Å).

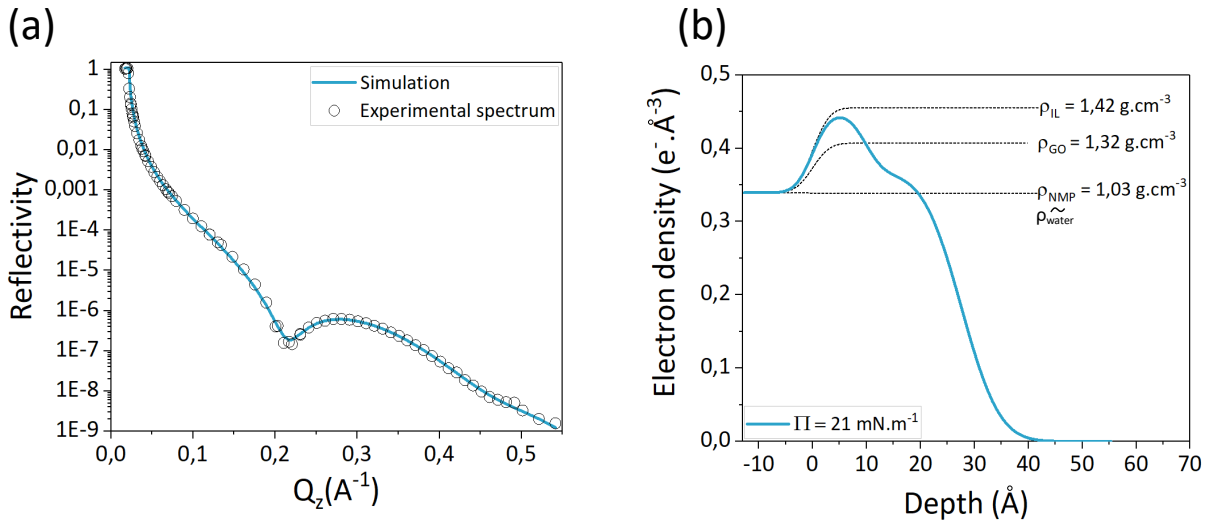

Figure 4.18: (a) XRR spectrum obtained at Π = 21 $mN.m^{-1}$ adjusted and (b) its corresponding electron density profiles.

The evolution of adjustment parameters from Π = 21 $mN.m^{-1}$ to Π = 27 $mN.m^{-1}$ is as follows :

– L_1 becomes 4% denser, keeps almost the same thickness and becomes 32% rougher.

– L_2 becomes 18% denser, 33% thicker and 6% less rough.

By compressing the film from (Π = 11 $mN.m^{-1}$; A_{trough}= 108 cm^2) to (Π = 21 $mN.m^{-1}$; A= 67 cm^2), the surface of the trough is reduced by 40%. If L_1 keeps the same

thickness, it should become 40% denser but in practice it only becomes 4% denser. Hence about 36% of the components of L_1 must have left it either to L_{21} or to the subphase. On the other hand, L_2 has gained 18% in density, which could be due to the transition of molecules from L_1 to L_2. This transition is not enough to explain the loss of 36% of L_1 and it must be considered that some molecules should have drowned in the subphase. IL molecules, thanks to their alkyl chains and the nature of their anions, are less hydrophilic than NMP. It is therefore plausible to consider that IL molecules are the ones that must have left L_1 for L_2 and NMP molecules are the ones that must have plunged into the water. The transition of IL from L_1 to L_2 through the plateau at $\Pi = 12.5$ mN.m^{-1} is in agreement with the macroscopic study. The final composition of L_1 corresponds roughly to 8% of NMP versus 92% of IL ($0.08\rho_{NMP} + 0.92\rho_{IL} = \rho_{L_1} = 1.39$ g.cm^{-3}). As L_1 has almost the same thickness at $\Pi = 21$ mN.m^{-1} as at $\Pi = 11$ mN.m^{-1}, its configuration can be considered to remain the same. As L_2 has increased in thickness, so the IL molecules must be oriented towards the air. In this regard, three possible configurations can be considered :

1. If one assumes that at $\Pi = 11$ mN.m^{-1}, the stack was described by M_1 (Figure 4.16) : the IL molecules in L_2 should stack on top of each other and thus remain horizontally segregated with GO as illustrated by the model M_3 in Figure 4.19.

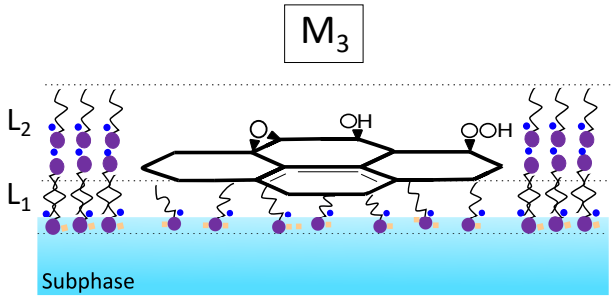

Figure 4.19: Schematic representation of the model M_3 describing the IL and GO stack configurations at $\Pi = 21$ mN.m^{-1}.

2. If one assumes that at $\Pi = 11$ mN.m^{-1}, the stack was described by M_2 (Figure 4.17), the molecules of IL in L_2 should behave according to one of two possible configurations :

   i They stack vertically on top of the IL of L_1, thus segregate horizontally with GO as illustrated by the model M_4 in Figure 4.20.

   ii They stack vertically on top of the IL molecules, those lying parallel to GO sheets, thus segregate vertically with GO as illustrated by the model M_5 in Figure 4.21. Since the alkyl chains are hydrophobic, they are expected to be oriented towards the air and the imidazolim rings to be in contact with the lying parallel IL molecules . The interaction between the vertical IL and the lying parallel ones could occur between chain-(rings+anion) or (rings+anion)-(rings+anion) or (rings+anion)-carbon basal plane. Based solely on XRR measurement, no rigorous information on the nature of their interaction can be deduced. It is therefore suggested to be in contact with air and close to the

Imidazolium rings.

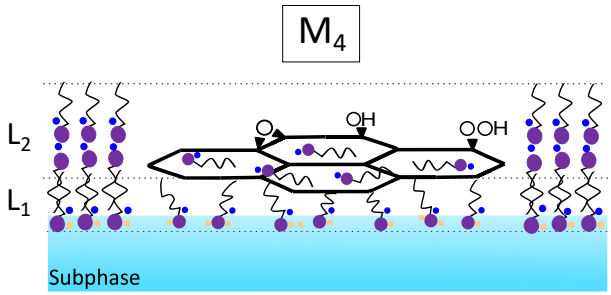

Figure 4.20: Schematic representation of the model M_4 describing the IL and GO stack configurations at $\Pi = 21$ mN.m^{-1}.

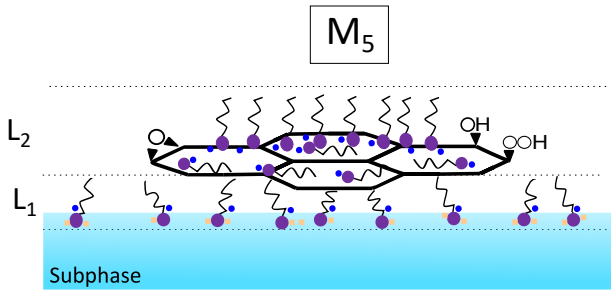

Figure 4.21: Schematic representation of the model M_5 describing the IL and GO stack configurations at $\Pi = 21$ mN.m^{-1}.

In order to follow the evolution of the density profile of the bilayer, we performed XRR at $\Pi = 27$ mN.m^{-1} (see Figure 4.13). Figure 4.22 (a) and Figure 4.22 (b) show respectively the adjusted XRR spectrum and its corresponding electron density profile. We also used the model of a bilayer. The fit well converged to a bilayer characterized by the following parameters :

1. First layer L_1, in contact with water, of density; $\rho = 1.3$ g.cm^{-3} , thickness; d = 12 Å and roughness; $\sigma = 3.31$ Å.

2. Second layer L_2, in contact with air, of density; $\rho = 1.23$ g.cm^{-3}, thickness; d = 19 Å and roughness; $\sigma = 6.04$ Å.

The evolution of adjustment parameters from $\Pi = 21$ mN.m^{-1} to $\Pi = 27$ mN.m^{-1} is as follows :

– L_1 becomes 6% less dense, 16% thicker and 20% rougher.

– L_2 becomes 6% denser, 5%thicker and 8% rougher.

By compressing the film from ($\Pi = 21$ mN.m^{-1}; A= 67 cm^2) to ($\Pi = 27$ mN.m^{-1}; A= 52 cm^2), the surface of the trough is reduced by 22%. The thickness of L_1 has increased by 16% at $\Pi = 27$ mN.m^{-1} and its density decreases by 6% while that of L_2 increases by 6%. It is therefore plausible to consider that 6% of IL molecules must have left L_1 for L_2. One could consider that the decrease of 22% in the surface area has resulted in the

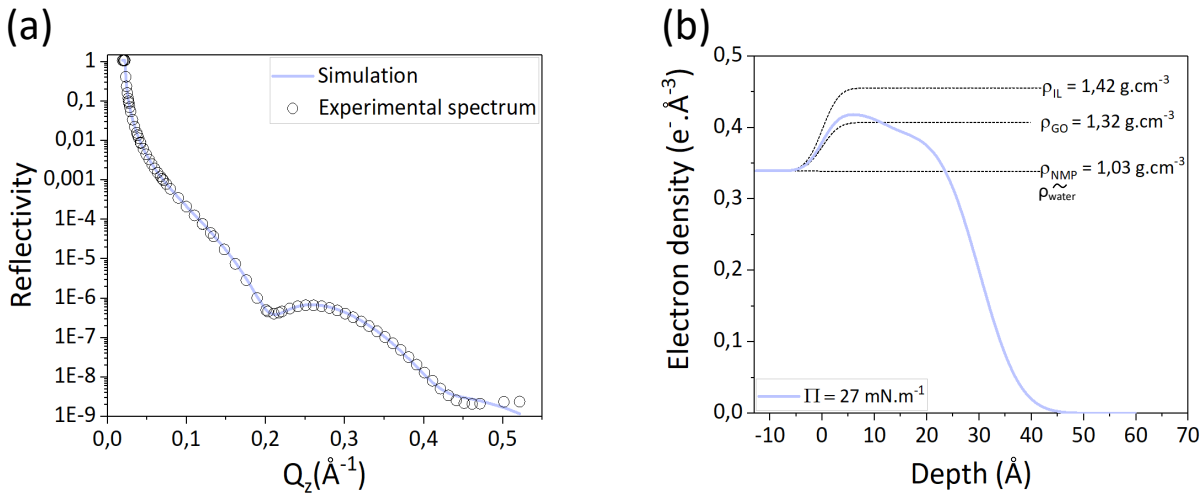

Figure 4.22: (a) XRR spectrum obtained at $\Pi = 27$ mN.m^{-1} adjusted and (b) its corresponding electron density profile.

increase of 16% the thickness of L_1 and in the transition of 6% IL from L_1 to L_2. This result is in agreement with the macroscopic study of the film (Figure 4.7). The thickness of the two layers suggests that the bilayer must have kept the same configuration as at $\Pi = 21$ mN.m^{-1}.

Figure 4.23 (a) and Figure 4.23 (b) present respectively the XRR spectra and their electron density profiles along the compression of the film. Table 4.2 shows the XRR adjustment parameters of the bilayer at different surface pressure. Figure 4.24 shows the evolution of these parameters along the compression of the bilayer.

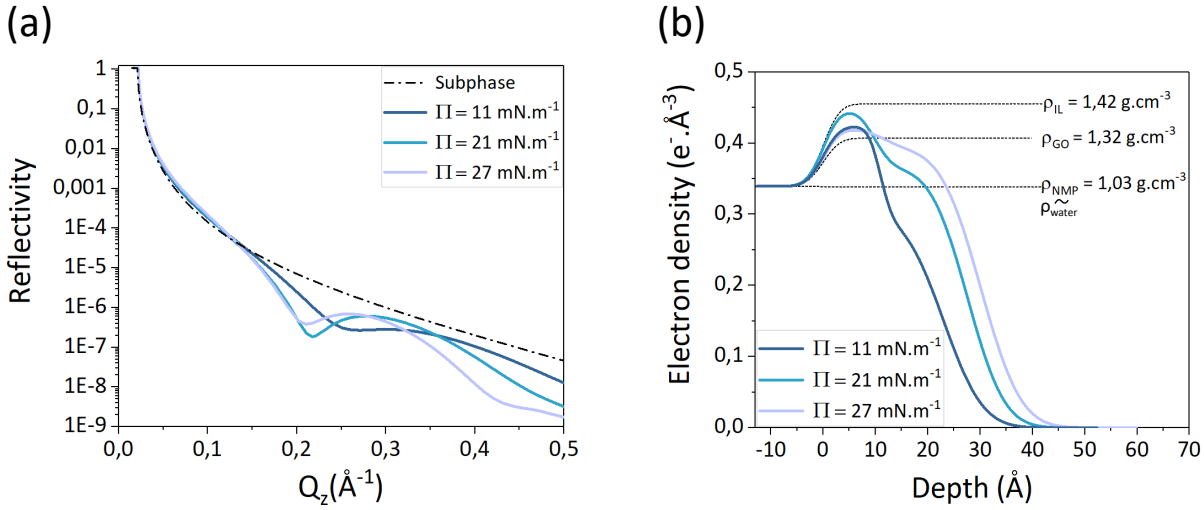

Figure 4.23: (a) The evolution of XRR spectra and (b) their corresponding electron density profiles obtained at different surface pressure.

	Layers	ρ (g.cm^{-3})	d (Å)	σ (Å)
$\Pi = 11$ mN.m^{-1}	L_1	1.33	11	1.78
	L_2	0.94	12.10	5.92
$\Pi = 21$ mN.m^{-1}	L_1	1.39	10	2.62
	L_2	1.15	18	5.56
$\Pi = 27$ mN.m^{-1}	L_1	1.30	12	3.31
	L_2	1.23	19	6.04

Table 4.2: Adjustment parameters of the bilayer model proposed to describe XRR spectra of $(GO + IL)_{NMP}$ Langmuir mixed film at different surface pressures.

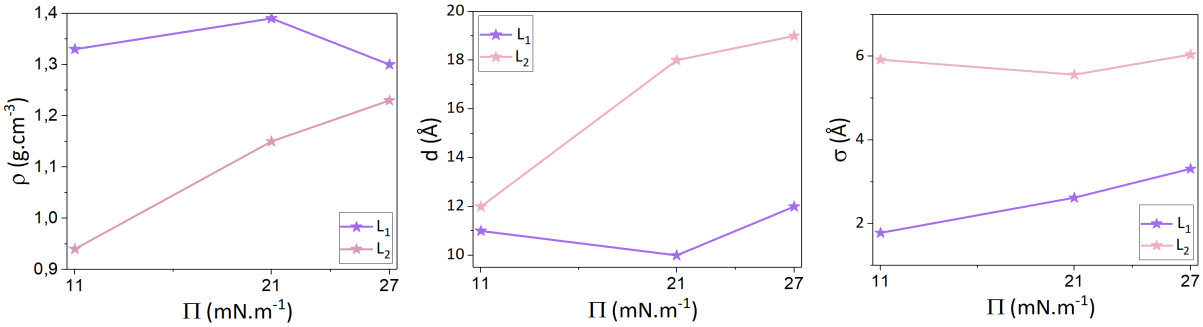

Figure 4.24: The evolution of (from left to right): the mass density, thickness and roughness of the layers along the different surface pressures.

The possible combinations of the models that could describe the bilayer along its compression are presented in the Table 4.3. The first includes M_1 and M_3, the second includes M_2 and M_4 and the third includes M_2 and M_5.

	Models		
11 mN.m^{-1}	M_1 - Figure 4.16	M_2 - Figure 4.17	M_2 - Figure 4.17
21 and 27 mN.m^{-1}	M_3 - Figure 4.19	M_4 - Figure 4.20	M_5 - Figure 4.21

Table 4.3: The possible combinations of the models describing the bilayer along its compression.

XRR measurements are in agreement with the macroscopic study. The mixed film is formed by a stack of a bilayer : a layer in contact with water (L_1) and a layer in contact with air (L_2). L_1 consists of IL and NMP molecules while L_2 consists of IL molecules and GO sheets. Through a plateau observed at $\Pi = 12.5$ mN.m^{-1}, some IL molecules from L_1 migrate to L_2 and some NMP molecules drown in the subphase. On the basis of XRR, five models have been proposed to describe the stack along its compression. From three model (M_2, M_4 and M_5), it was suggested that the interaction at the interface between IL and GO could be influenced by the nature of the second interface limiting the IL molecules. In order to reduce the choice to the appropriate combination of models and to highlight a possible organization of the compounds, we performed GIXD on water surface.

4.3.2 GIXD measurements

We performed GIXD measurements on (GO + IL)$_{NMP}$ Langmuir mixed film deposited at the air-water interface. These measurements were also carried out at PETRA III, beamline P08 at an energy of 18 Kev, using the LISA diffractometer. We investigated the organization of the mixed film at three different surface pressures (11, 21 and 27 mN.m^{-1}) (see Figure 4.25).

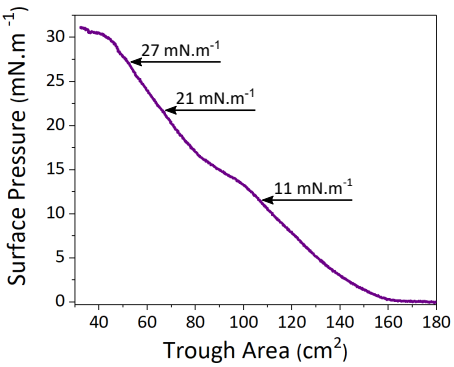

Figure 4.25: Π-A isotherm of (IL+GO)$_{NMP}$ Langmuir film deposited at the air-water interface.

At Π = 11 mN.m^{-1}, we did not succeed in observing any diffraction peaks, which indicates that the film is not organized. This is in agreement with the macroscopic study that indicates that the film at this surface pressure is in a (LE) phase, thus not very dense. At Π = 21 mN.m^{-1}, we observed an out-of plane diffraction signal. Figure 4.26 (a) and Figure 4.26 (b) show respectively the diffraction map and the integrated intensity of the signal over Q$_z$. Then at Π = 27 mN.m^{-1}, we observed an out-of plane diffraction signal. Figure 4.27 (a) and Figure 4.27 (b) show respectively the diffraction map and the integrated intensity of the signal over Q$_z$ at Π = 27 mN.m^{-1}.

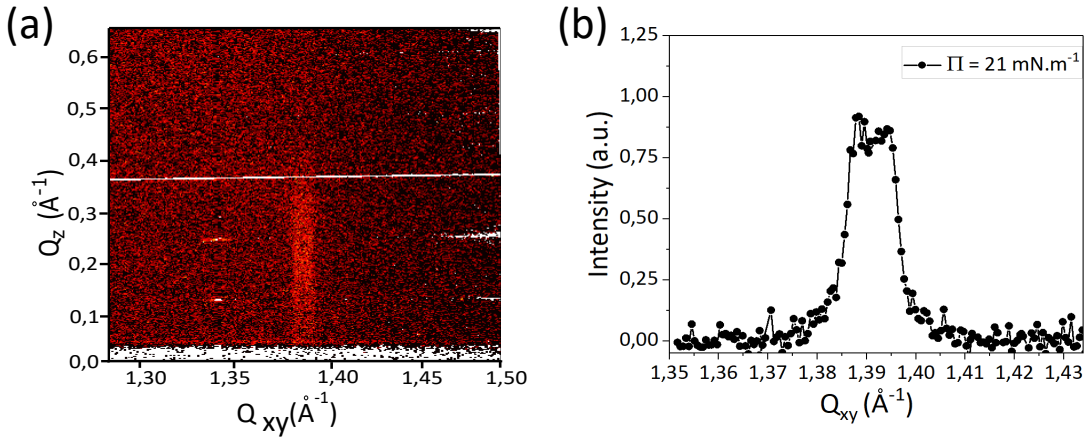

Figure 4.26: (a) The GIXD diffraction map and (b) the integrated intensity over Q$_z$ of the GIXD signal from (GO + IL)$_{NMP}$ Langmuir mixed film at Π = 21 mN.m^{-1}.

We first assumed that the signal observed at Π = 21 mN.m^{-1} and then at Π = 27 mN.m^{-1}, consists of one peak. We adjusted it integrated intensity by a Lorentzian function, after removing the background noise. The adjustment converged to a peak centered at Q$_{xy}$ = 1.391 Å at Π = 21 mN.m^{-1} and at Q$_{xy}$ = 1.388 Å at Π = 27 mN.m^{-1}. The lattice parameters at Π = 21 mN.m^{-1} are therefore smaller than that at Π = 27 mN.m^{-1}. In principle, the increase in the surface pressure of the film should allow a better organization of the structure in a more compact network. The network parameters should therefore decrease or at least remain the same as the film is compressed, from Π = 21 mN.m^{-1} to Π = 27 mN.m^{-1}. In this respect, we have suggested that the signal, at both

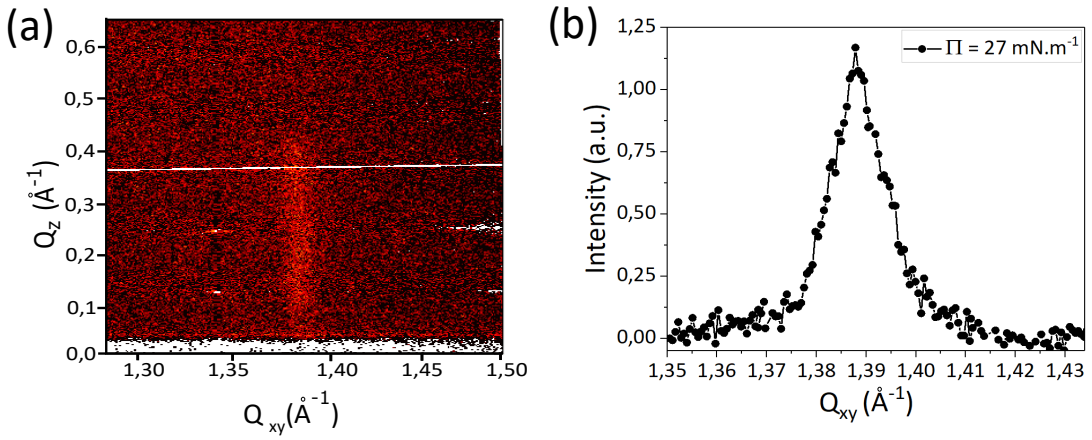

Figure 4.27: (a) The GIXD diffraction map and (b) the integrated intensity over Q_z of the GIXD signal from $(GO + IL)_{NMP}$ Langmuir mixed film at $\Pi = 27$ mN.m^{-1}.

surface pressures, may be formed of two peaks instead of one peak.

We adjusted the integrated intensities of the peaks by Lorentzian functions, as shown in Figure 4.28 (a) and Figure 4.28 (b). The first peak is centered at $Q_{xy} = 1.391$ Å^{-1} and the second one at $Q_{xy} = 1.388$ Å^{-1}. The rodscans of the two peaks are indiscernible as their Q_{xy} are so close. We have therefore shown in Figure 4.29 (a) the rodscan at $Q_{xy} = 1.391$ Å^{-1}, obtained at $\Pi = 21$ mN.m^{-1} and in Figure 4.29 (b) the rodscan at $Q_{xy} = 1.388$ Å^{-1}, obtained at $\Pi = 27$ mN.m^{-1}. They were adjusted by a square sinus cardinal function. The maximum of the rodscans is obtained around $Q_z = 0.2$ Å^{-1}, which indicates that the structure is tilted. The adjustment parameters of the integrated intensities and the rodscans are gathered in Table 4.4.

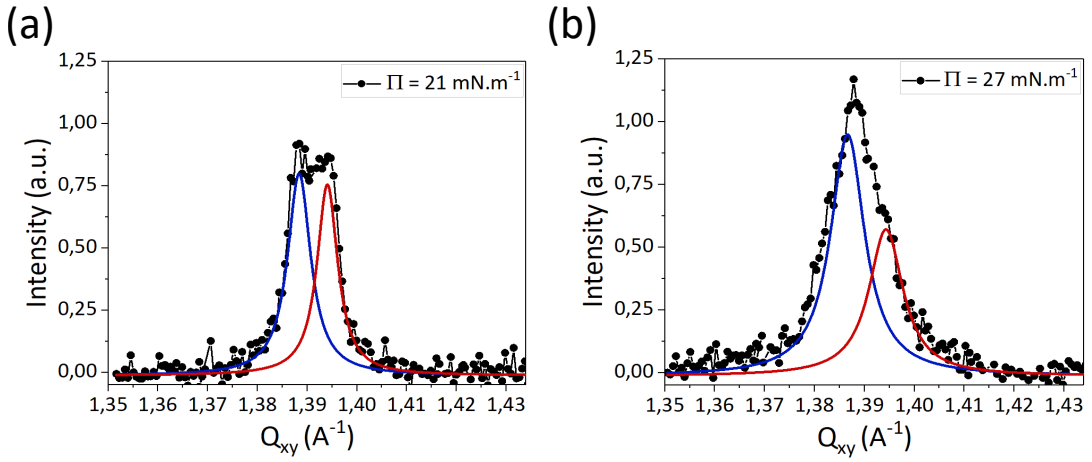

Figure 4.28: The integrated intensity of the signal observed (a) at $\Pi = 21$ mN.m^{-1} then (b) at $\Pi = 27$ mN.m^{-1}, adjusted by two Lorentzian functions.

The peaks are indexed according to a rectangular lattice composed of two molecules at $\Pi = 21$ mN.m^{-1} and at $\Pi = 27$ mN.m^{-1}. The first peak, centered at $Q_{xy} = 1.391$ Å^{-1}, corresponds to the peak (02) and the second one, centered at $Q_{xy} = 1.388$ Å^{-1}, corresponds to the peak degenerate (11) and $(1\bar{1})$. The lattice parameters correspond to a = 5.21 Å and b = 9.05 Å and to an area A = 47 Å^2. The area of the unit cell is

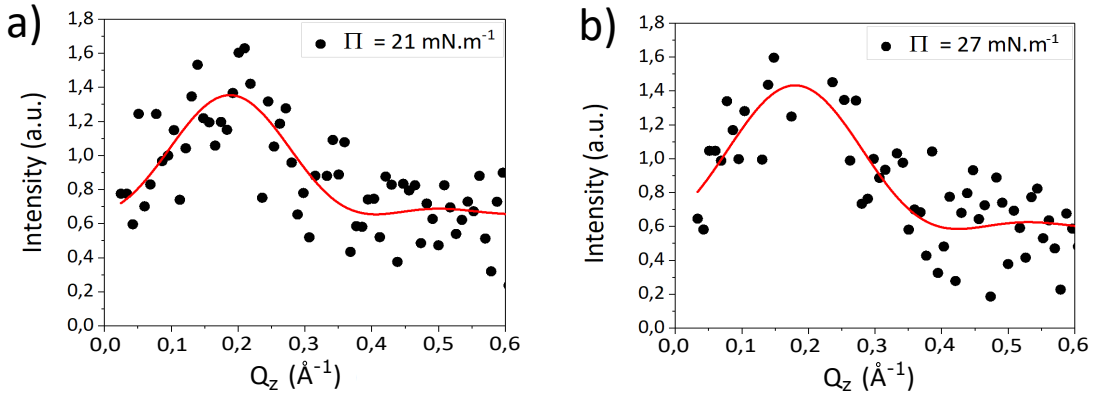

Figure 4.29: The profiles of the rodscans of the diffraction peak a) centered at Q_{xy} = 1.391 Å^{-1}, observed at Π = 21 mN.m^{-1} and b) centered at Q_{xy} = 1.388 Å^{-1}, observed at Π = 27 mN.m^{-1}.

Π (mN.m^{-1})	Index	Q_{xy} (Å^{-1})	ΔQ_{xy}(Å^{-1})	Peak Area (a.u.)	Q_z (Å^{-1})	ΔQ_z(Å^{-1})	Peak Area (a.u.)
21	(02)	1.388	0.0056	0.007	-	-	-
	(11)	1.391	0.0051	0.006	0.19	0.22	7
27	(02)	1.388	0.0083	0.013	0.18	0.24	8.48
	(11)	1.391	0.0083	0.008	-	-	-

Table 4.4: Adjustment parameters of diffraction peak of $(GO + IL)_{NMP}$ Langmuir mixed film deposited at the air-water interface at Π = 21 mN.m^{-1} and Π = 27 mN.m^{-1}.

therefore A = 23.5 Å^2.molecule^{-1} which is in the range of the cross section of an alkyl chain. The distance between Bragg planes, corresponding to Q_{xy} = 1.388 Å^{-1}, is d = 4.53 Å^{-1} and the one corresponding to Q_{xy} = 1.391 Å^{-1} is d = 4.52 Å^{-1}. They are comparable to the typical distance between Bragg planes formed of alkyl chains (d = 4.15 Å^{-1}). The FWHM of the adjusted rodscans averages about ΔQ_z = 0.23 Å^{-1} which indicates that the thickness of the structure is about 27 Å. It is in agreement with the length of an alkyl chain composed of 20 carbon atoms. On the basis of these results, one can presume that the diffracted peaks are relative to the organization of the IL molecules, slightly tilted, in a rectangular network. The maximum of the intensity of the rodscans is approximately Q_z = 0.2 Å^{-1} indicating that the IL molecules are 7° tilted with respect to the vertical to the interface. Both peaks are out-of-plane, the azimuth of the IL molecules is therefore $\psi = 0°$ indicating that the molecules are oriented towards the next nearest neighbor (NNN). As a reminder, the tilt is the inclination of the molecule's axis with respect to the z-axis. The azimuth is the direction of the tilt, so when $\psi = 0°$ the axis of the molecule is oriented in the direction of the y-axis. Figure 4.30 is a sketch showing the tilt and orientation of the molecule.

According to the macroscopic study and XRR measurements, the IL molecules occupy the two layers of the mixed film stack. The thickness of L_1, the layer in contact with water ($\sim$ 10Å) suggests that the IL in this layer cannot be elongated. On the other hand, L_2, the layer in contact with air, is 18 Å thick and rough (σ = 6Å). Since this layer is not dense, its roughness in relation to its thickness suggests that the layer could be thicker. The organized structure must therefore belong to L_2. The IL molecules in this layer

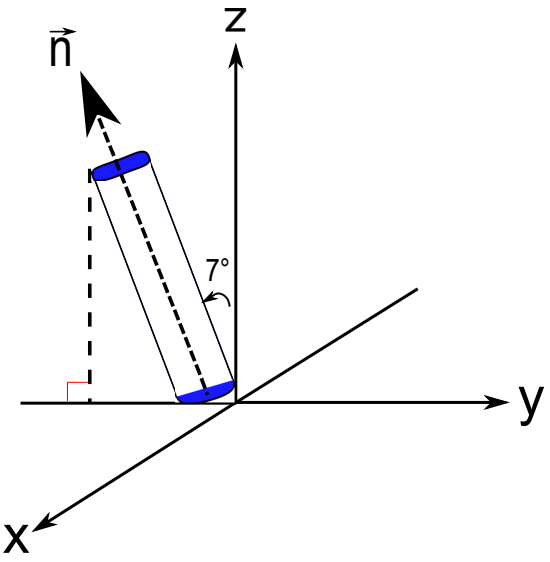

Figure 4.30: Schematic representation of the tilt and the direction of IL molecules in the rectangular lattice.

can adopt different configurations according to the three models (M_3, M_4, M_5) proposed by XRR. One thing is sure: this structure cannot be relative to the IL molecules that are lying parallel to the GO sheet. In order to narrow down the possibilities of properly describing the bilayer stack, we have transferred the films onto Si/SiO_2 wafers and studied them by the AFM.

4.4 Characterization by AFM on Si/SiO_2 solid substrates

In order to detect a possible influence of NMP, we studied pure films by AFM before proceeding to the study of the mixed film. Using the Langmuir-Blodgett procedure, we transferred the films to silicon wafers, at different surface pressures. The silicon wafers were cleaned with Piranha, so that their surfaces (SiO_2) were hydrophilic. We then studied them by AFM.

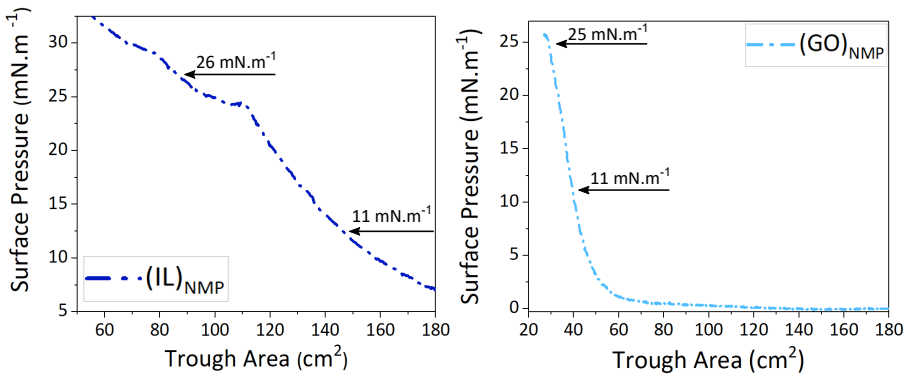

Figure 4.31: Π-A isotherms of (to left) $(IL)_{NMP}$ and (to right) $(GO)_{NMP}$ Langmuir films deposited at the air-water interface.

$(IL)_{NMP}$ Langmuir films were transferred at $\Pi = 11$ mN.m^{-1} then at $\Pi = 26$ mN.m^{-1} (see Figure 4.31 (to left)). $(GO)_{NMP}$ Langmuir films were transferred at $\Pi = 11$ mN.m^{-1} then at $\Pi = 25$ mN.m^{-1} (see Figure 4.31 (to right)).

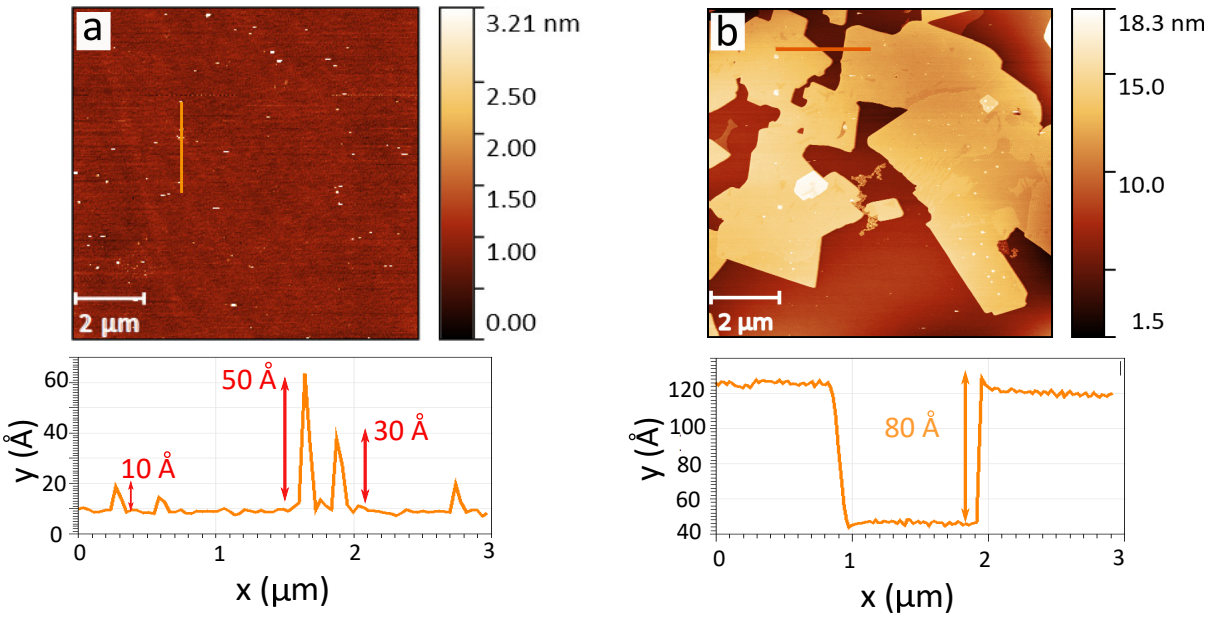

Figure 4.32: AFM topographic images and their corresponding profiles of $([C_{20}mim]^+[NTf_2]^-)_{NMP}$ Langmuir film transferred on Si/SiO_2 substrates by Langmuir-Blodgett technique at (a) $\Pi = 11$ mN.m^{-1} and at (b) $\Pi = 26$ mN.m^{-1}.

Figure 4.32 (a) shows the AFM topographic image of $(IL)_{NMP}$ Langmuir film transferred at $\Pi = 11$ mN.m^{-1}. We observe a homogeneous surface, on which defects of thickness varying between 10 Å and 50 Å exist. The homogeneous surface was also observed by AFM in the free-solvent IL film. It indicates either the transfer of an IL monolayer covering the entire surface of the silicon wafer. Or the failure of the transfer, because the monolayer is not dense. Defects can be impurities coming from the silicon wafer or can come from IL and/or NMP molecules. Based on the literature, Chun Yau et al. [139] have demonstrated that NMP degrade, polymerize and form particulates under sonication. The size and abundance of these particulates on wafers and in solutions depends on the sonication time. These defects may therefore correspond to NMP particulates. Thus, the NMP do not appear to interfere in the structure of the IL transferred on the silicon wafer.

Figure 4.32 (b) shows the AFM topographic image of $(IL)_{NMP}$ Langmuir film transferred at $\Pi = 26$ mN.m^{-1}. We observe a film of 80 Å thickness and defects distributed over its surface. The thickness of the film is consistent with a multilayer of IL molecules. The defects can be attributed to NMP particulates. The free-solvent IL film at $\Pi = 26$ mN.m^{-1} was also formed as a multilayer. NMP can therefore be considered as not interfering in the structure of the IL film on the silicon wafer.

Figure 4.33 (a) shows the AFM topographic image of $(GO)_{NMP}$ Langmuir film transferred at $\Pi = 11$ mN.m^{-1}. We observe an non dense film of 10 Å thickness and some defects of 30 Å thick. The thickness of the film corresponds to a monolayer of GO sheets.

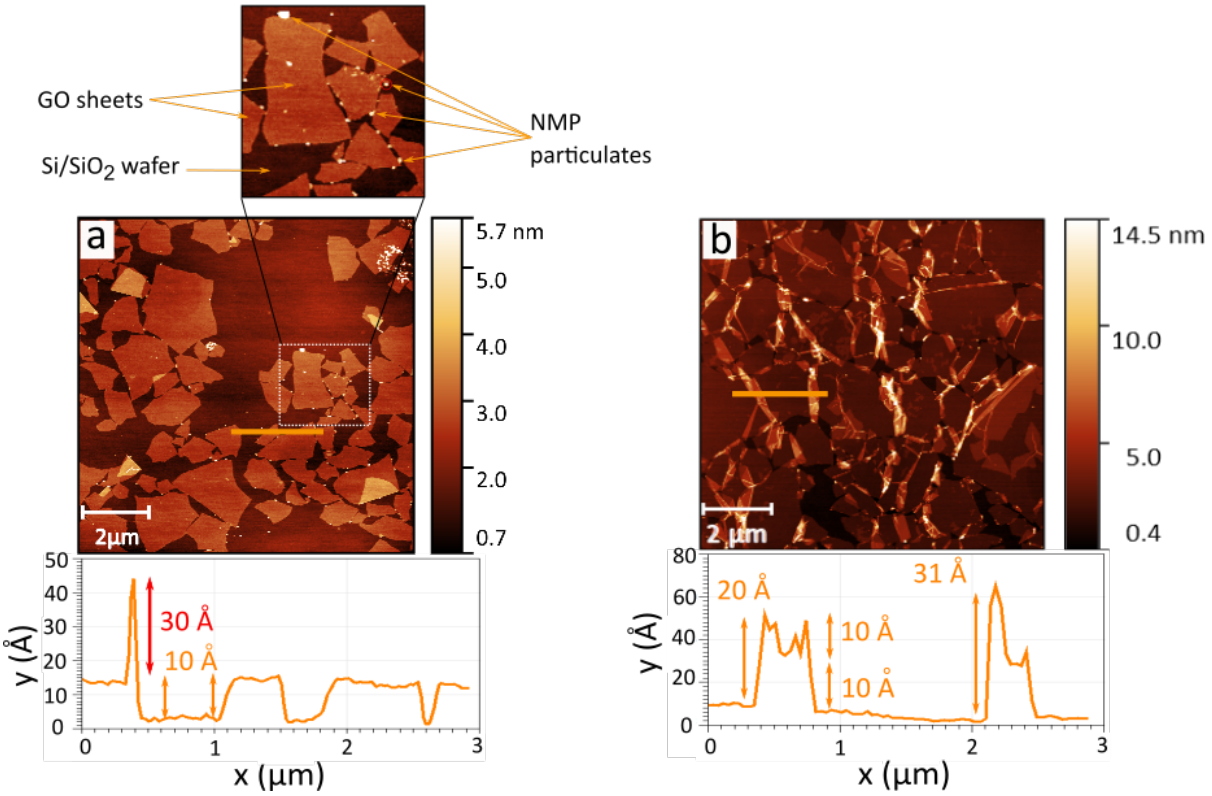

Figure 4.33: AFM topographic images and their corresponding profiles of $(GO)_{NMP}$ Langmuir film transferred on Si/SiO_2 substrates by Langmuir-Blodgett technique at (a) $\Pi = 11$ mN.m^{-1} and at (b) $\Pi = 25$ mN.m^{-1}.

The defects may correspond to NMP particulates. The free-solvent GO Langmuir film at $\Pi = 11$ mN.m^{-1} was as well formed as a monolayer but was denser than $(GO)_{NMP}$ Langmuir film. Thus, in addition to the particulates, NMP could also be formed into a thin film that occupies the free surface between GO sheets. Although, the NMP shows to reduce the density of the GO monolayer, it does not interfere in its structure.

Figure 4.33 (b) shows the AFM topographic image of $(GO)_{NMP}$ Langmuir film transferred at $\Pi = 25$ mN.m^{-1}. We observe a dense film of GO sheets, interacting with each other. The edges of GO sheets appear folded and forming domains 30 Å thick. This result is similar to that observed with the free-solvent GO Langmuir film transferred at this pressure. NMP can therefore be considered as not interfering with GO structures at $\Pi = 25$ mN.m^{-1}.

We conclude that the presence of NMP does not hinder or interfere with the organization of $([C_{20}mim]^+[NTf_2]^-)_{NMP}$ and $(GO)_{NMP}$ Langmuir film deposited on solids substrates.

We then studied (GO + $[C_{20}mim]^+[NTf_2]^-)_{NMP}$ Langmuir mixed films transferred at Π = 11 $mN.m^{-1}$ then at Π = 26 $mN.m^{-1}$ (see Figure 4.34).

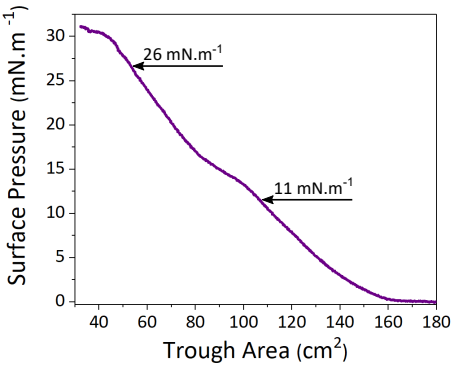

Figure 4.34: Π-A isotherm of $(IL+GO)_{NMP}$ Langmuir film deposited at the air-water interface.

Figure 4.35 shows the AFM topographic and phase images of $(GO+IL)_{NMP}$ Langmuir film transferred at Π = 11 $mN.m^{-1}$. We observe a layer of 8 Å thick covering almost the entire surface. This layer is covered by a non dense upper layer of 14 Å thick. We also observe a layer that correspond to the deepest region according to the topographic image. This layer is about 8° phase shifted from the two layers. It is thus suggested to attribute it to the silicon wafer. The thickness of the lower layer (8 Å) is in agreement with that of L_1 (10 Å), based on XRR. It is therefore suggested to be formed of NMP and IL molecules. The thickness of the upper layer (14 Å) is in agreement with that of L_2 (12 Å), based on XRR. It is therefore suggested to be formed of GO sheets and IL molecules. However, the theoretical thickness of GO sheets is 10 Å, which is 4 Å less than that of the upper layer, according to the AFM topographic image. Moreover, the upper layer is only 2° phase-shifted with respect to the lower layer, the one assumed to be composed of NMP and IL molecules. This modest phase shift could be the result of the interaction of the AFM tip with materials of similar natures. GO sheets in L_2 must thus be covered with IL molecules of 4 Å thick. This thickness is in the range order of that of an Imidazolium ring [3] and of a horizontal $[NTf_2]^-$ [67]. IL must be lying parallel to GO sheets in L_2. In this respect, M_2 (Figure 4.17), the model suggested following the XRR measurements, must be adopted to correctly describe the stack at Π = 11 $mN.m^{-1}$.

Figure 4.36 shows the AFM topographic and phase images of $(GO+IL)_{NMP}$ Langmuir film transferred at Π = 26 $mN.m^{-1}$. We observe a layer of 9 Å thick covered by a non dense layer of 47 Å thick. We also observe a layer that corresponds to the deepest region according to the topographic image. This layer is 15° phase shifted from the other two layers. It is thus suggested to attribute it to the silicon wafer. The thickness of the lower layer (9 Å) is in agreement with that of L_1 (10 Å), based on XRR. The lower layer is therefore suggested to be formed of NMP and IL molecules. The upper layer is only 2° phase-shifted with respect to the lower layer suggesting that the two layers are composed of materials of similar natures. The upper layer appears as formed by a stack of at least two layers, as shown in the zoomed image. The thickness of the first one is 16 Å, which could correspond to that of a monolayer of GO sheets covered IL molecules lying parallel. The thickness of the second one is 31 Å which is in the range of the that of elongated $[C_{20}mim]^+[NTf_2]^-$ molecules. The upper layer could therefore be formed by a stack of three layers: a monolayer of elongated IL molecules perpendicular to a monolayer of IL molecules lying parallel to a monolayer of GO sheets. The thickness of the upper layer, estimated from AFM, differs from that estimated from XRR. According to XRR measurements, L_2 is rough (σ = 6 Å) which suggests that it could be thicker. According to AFM measurements, the upper layer is not dense. Since XRR measurements provide the average thickness of a layer, the upper layer must appear thinner, in XRR, than it

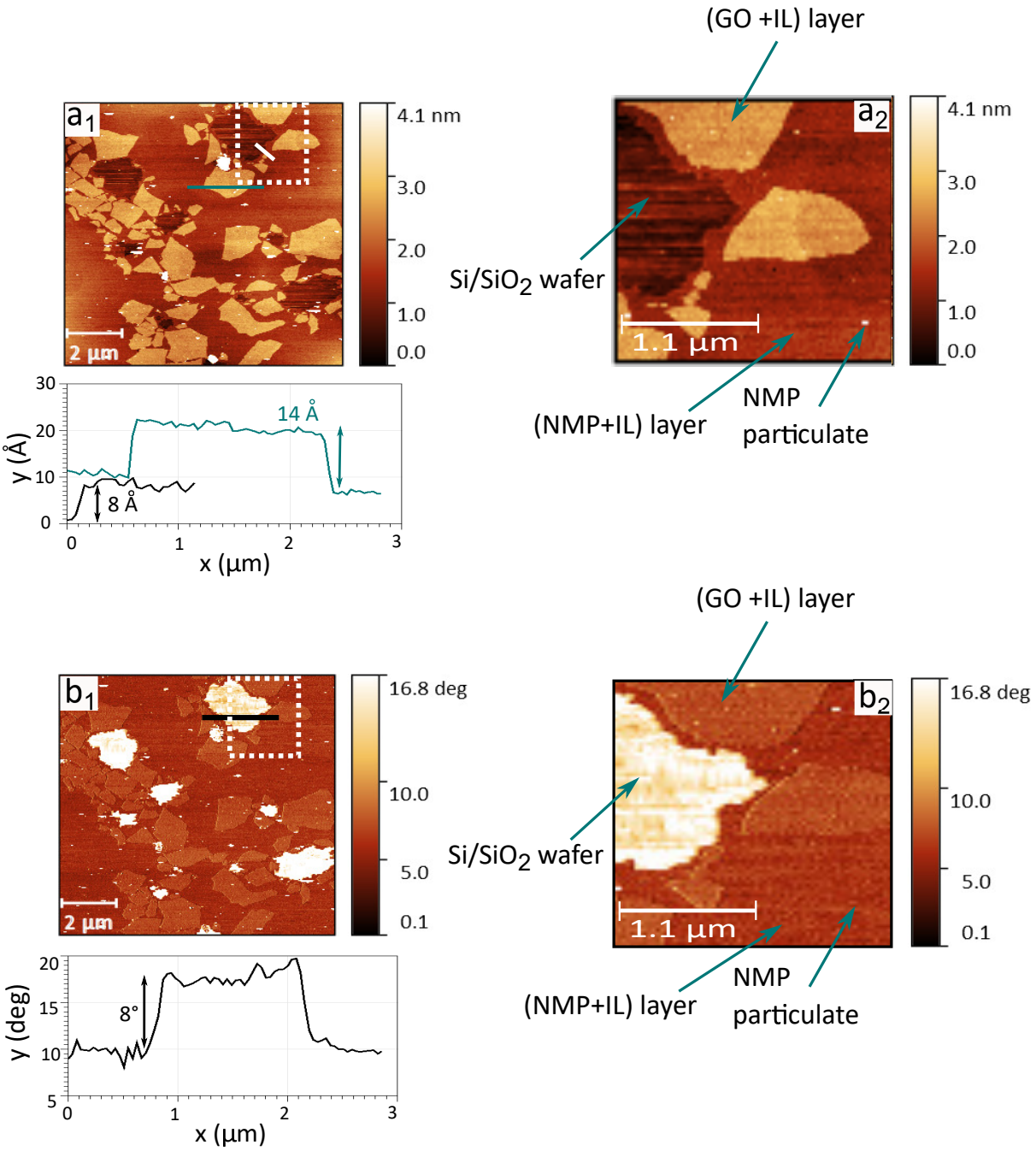

Figure 4.35: AFM topographic and phase images of (GO + $[C_{20}mim]^+[NTf_2]^-)_{NMP}$ Langmuir mixed film transferred on Si/SiO_2 wafer by Langmuir-Blodgett technique at $\Pi = 11$ mN.m^{-1}.

actually is. Therefore, the upper layer observed in AFM can be attributed to L_2, the layer in contact with air as described by XRR. The configuration deduced from AFM is in agreement with that proposed in model M_5 (Figure 4.21).

We evidenced by GIXD measurements the organization of a monolayer of IL molecules, almost perpendicular to the interface, in a rectangular lattice. The thickness of this structure is equal 30Å. It is in agreement with that of the layer of IL molecules standing perpendicular on top of the lying parallel IL molecules to GO sheets in L_2. We therefore

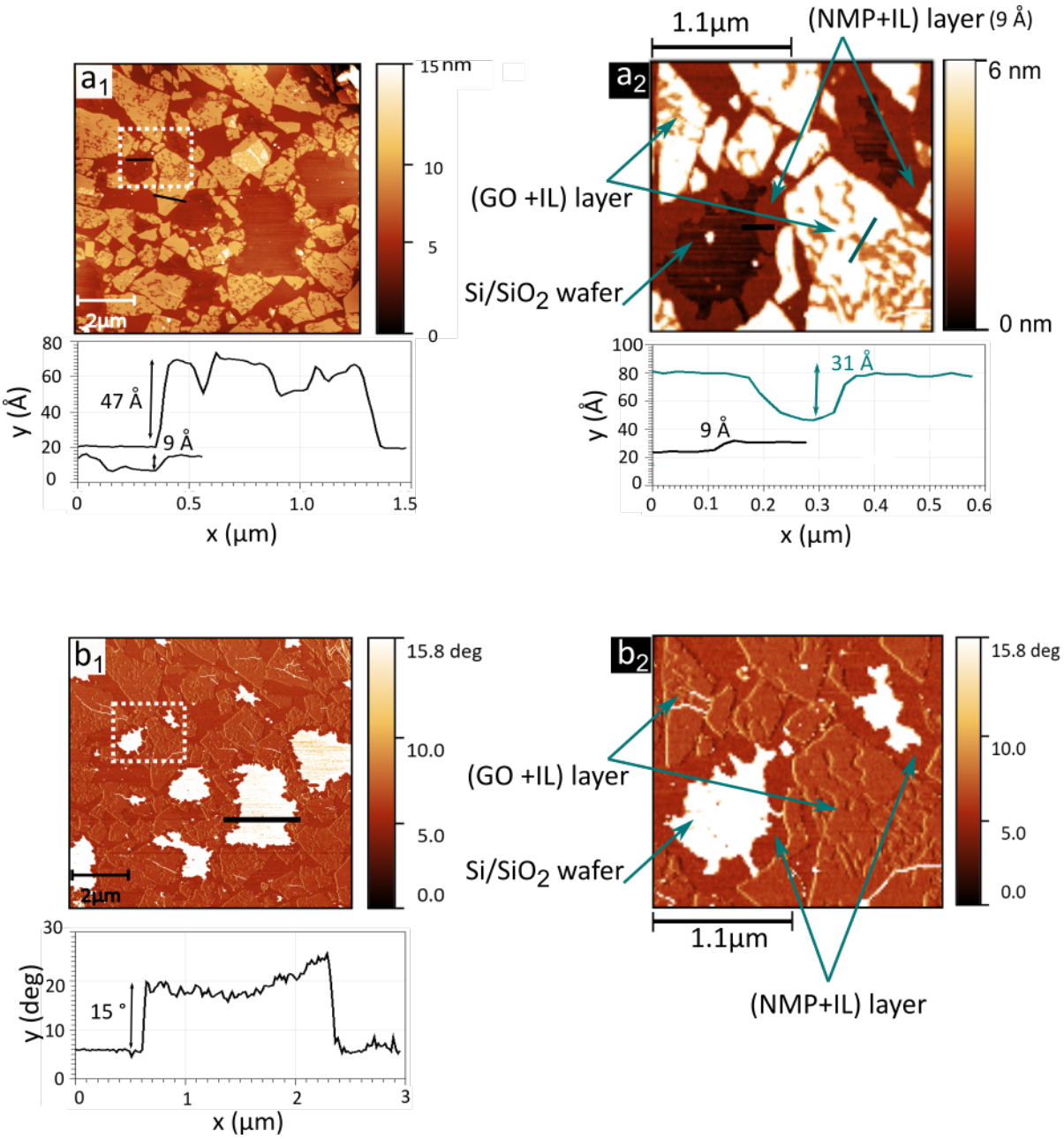

Figure 4.36: AFM topographic and phase images of (GO + $[C_{20}mim]^+[NTf_2]^-)_{NMP}$ Langmuir mixed film transferred on Si/SiO_2 wafer by Langmuir-Blodgett technique at $\Pi = 26$ mN.m^{-1}.

suggest that the IL molecules that have migrate from L_1 to L_2, get organized perpendicular on top of the lying parallel IL molecules.

4.5 Discussion

On the basis of the study of $(GO+IL)_{NMP}$ Langmuir film, we showed that GO sheets despite being amphiphilic, prefer to interact with the alkyl chains instead of water. GO sheets can therefore be considered to have tendency to be more hydrophobic. We also showed that the IL molecules are almost perpendicular to GO sheets, when they are at the interface with water (L_1), but lie parallel to GO sheets, when they are at the interface with air (L_2). According to the literature, the Imidazolium rings as well as the alkyl chains prefer to lie parallel to the graphene surface in contact with vacuum, due to Π-Π interaction between the rings and the graphene [3, 2, 4]. However, in L_1, the Imidazolium rings appear to prefer to interact with water rather than with the basal plane of GO. The interaction between the Imidazolium rings and water therefore dominates the Π-Π interaction between the rings and GO sheets in L_1. So depending on the preferential interaction of the Imidazolium rings, either with the GO interface or with the second interface, the IL molecules choose to be perpendicular or to lie parallel to the GO surface. Thus, the orientation of the IL molecules at the interface with the GO sheets is determined by the nature of the second interface that limits the IL.

The configuration of L_2, the layer in contact with air, is in agreement with the literature. According to the MDS studies of Moghadam et al. [2], the EDL of IL molecules at the interface with graphene, in contact with vacuum, is composed of two particular layers separated by IL molecules in bulk. The first is the layer adsorbed on the graphene surface and composed of lying parallel IL molecules. The second one is the vacuum layer, in contact with the vacuum and composed of perpendicular and/or tilted IL molecules. We can therefore suggest that the IL molecules at the interface with the GO sheets behave in the same way as when they are at the interface with the graphene.

On the basis of this study, it was practically impossible to deduce rigorous information about the position and orientation of anions in the IL layers. We will only state that the anions are supposed to be in contact with air and Imidazolium rings because of their hdrophobicity and electrostatic interactions.

4.6 Conclusion

According to the macroscopic study, XRR and AFM measurements, the mixed film is formed by a stack of two layers. The layer in contact with water, L_1, is occupied by IL tilted molecules and NMP. The layer in contact with air, L_2, is occupied by GO sheets and lying parallel IL molecules. Through a plateau observed at $\Pi_{plateau} = 12.5$ mN.m^{-1}, some of the IL molecules migrate from L_1 to the top of the IL molecules lying parallel to GO sheets in L_2. According to GIXD measurements, the transited IL molecules get organized almost perpendicular in a rectangular lattice on top of the lying parallel IL, in L_2. The configurations of the layers can be described by the model M_2 at $\Pi < \Pi_{plateau} = 12.5$ mN.m^{-1} and by the model M_5 at $\Pi > \Pi_{plateau} = 12.5$ mN.m^{-1} (as illustrated in Figure 5.31). The presence of NMP in L_1 is modest. It appears to stabilize pure GO and pure IL Langmuir films at the air-water interface.

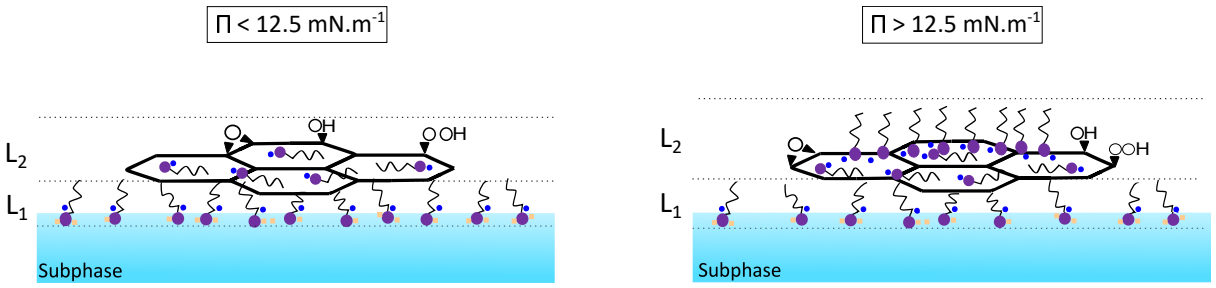

Figure 4.37: The models M_2 and M_5 which describe the bilayer respectively at $\Pi < 12.5$ mN.m^{-1} and $\Pi > 12.5$ mN.m^{-1}.

Two main conclusions can be drawn from this study :

1. GO sheets tend to be hydrophobic as they prefer to interact with the alkyl chains of IL rather than with water.

2. The interaction between IL molecules and GO sheets, at their interface, depends on the second interface limiting the IL molecules. IL molecules are almost perpendicular to the surface of GO sheets when they are at the interface with water. However, they lie parallel to GO sheets when they are at the interface with air.

4.7 Perspective

According to the literature, GO sheets dispersed in aqueous solutions are negatively charged at their edges due to the deprotonation of the carboxylic acid into -COO$^-$ [96]. Our measurements were performed on the water surface and GO sheets initially came from a water dispersion. The mixed films are thus supposed to be formed of GO sheets negatively charged at their edges. The interaction between IL and GO sheets in aqueous medium is of ionic interaction type between the cation of IL and -COO$^-$ decorating GO edges [140]. Our results showed that IL molecules managed to go beyond the edges of the GO sheets and reach their basal planes. This interaction between IL and GO appeared to be similar to that between IL and graphene based on the MDS studies [3, 2, 4]. It is therefore assumed that a charge screening may have permit IL molecules not to be trapped by the electrostatic interaction with GO edges. We observed that NMP molecules coexist with IL molecules in contact with water. This suggests that NMP molecules may have played the role of charge screening. In this respect, it is necessary to repeat our study on the mixed film but using a water-immiscible solvent.

The amount of IL molecules in our mixed films was a bit critical because it saturates the surface of the trough from the beginning of the measurement. On the other hand, the amount of GO sheets in the mixed films was only 26% of the surface occupied by IL molecules. It is therefore necessary to repeat the study using less IL molecules. It is also interesting to vary the concentration ratio between the GO sheets and the IL molecules.

Chapter 5

$[C_{20}mim]^+[NTf_2]^-$ Langmuir films deposited on subphases containing gold ions

Contents

Studies have shown that the introduction of gold nanoparticles into supercapacitors improves their performance. In this chapter, $[C_{20}mim]^+[NTf_2]^-$ Langmuir films are studied on subphases containing gold anionic complexes. One of our goals is to understand the interaction between the IL molecules and gold ions. Another objective is to perform surface X-ray radiolysis to form gold nanostructures using the IL film as a template. We show that at low concentration of gold ions, the IL spread over the ionic subphase behaves in the same way as that spread over pure water. Surface X-ray radiolysis leads to the formation of gold nanoparticles with a size of about 15 nm. On the other hand, we show that at a high concentration of gold ions, the IL over the ionic subphase behaves in a radically different way than that spread over the ionic subphase. GIXD measurements show the formation of an inorganic/organic superstructure that is assumed to form only above a threshold concentration of gold ions. This structure prevents gold complexes from being reduced and thus from forming nanoparticles by surface X-ray radiolysis.

5.1 $[C_{20}mim]^+[NTf_2]^-$ Langmuir films on subphases containing gold ions

We studied the thermodynamic behavior of $[C_{20}mim]^+[NTf_2]^-$ Langmuir film spread over Gold(III) chloride trihydrate $H[AuCl_4]\cdot 3H_2$ salts solutions. The IL molecules were dissolved in chloroform in a concentration of $C_{molecules} = 2$ mmol.L^{-1}. The number of IL molecules deposited on the surface corresponds to a molecular area of A = 1.33 nm^2.molecule^{-1}. The concentration of gold ions was defined as the number of gold ions per IL molecule $r_{ions/molecules}$ as defined in Chapter 3 in Equation 3.11. We worked with 2 different concentrations of gold ions: the first one corresponds to $r_{AuCl_4^-/IL} = 30$ while the second one to $r_{AuCl_4^-/IL} = 600$. The isotherms of both systems were performed at the same temperature (20°C) and at the same compression velocity (15 cm^2). We also added ethanol in the subphase at a concentration of about 10^{-2} mol.L^{-1} as we planned to later try to reduce gold ions by surface X-ray radiolysis at the synchrotron. In order to avoid the reduction of $[AuCl_4]^-$ in the subphases, we worked in a room sheltered from light.

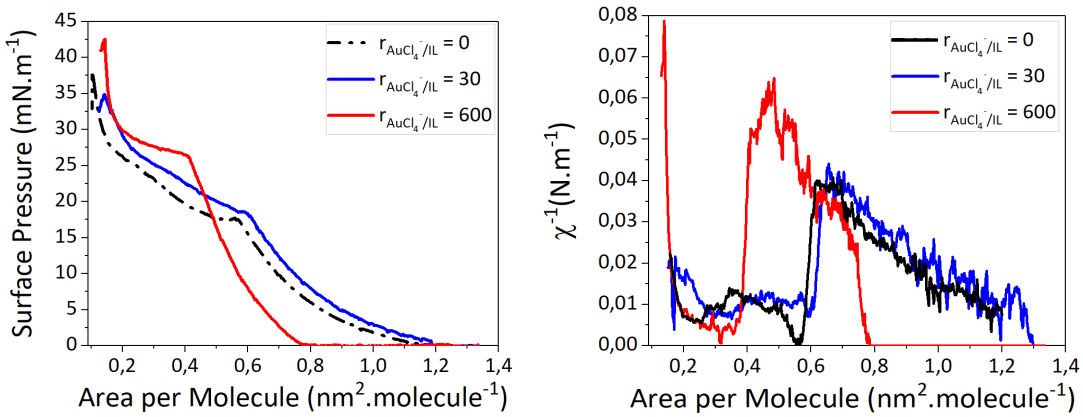

Figure 5.1: Π-A isotherms and the inverse of the compressibilities of $[C_{20}mim]^+[NTf_2]^-$ spread over pure water subphase (- - -), over a subphase containing 30 $[AuCl_4]^-$/IL (—) and over a subphase containing 600 $[AuCl_4]^-$/IL (—)

Figure 5.1 shows the Π-A isotherms of IL Langmuir films as a function of the concentration of $[AuCl_4]^-$ ions compared to that measured over pure water subphase. We notice that for a subphase of low concentration of $[AuCl_4]^-$ ($r_{AuCl_4^-/IL} = 30$) the film evolves in a rather similar way to the one spread over pure water. However, it behaves in a radically different way when the concentration of $[AuCl_4]^-$ in the subphase is 20 times higher ($r_{AuCl_4^-/IL} = 600$). Based on these observations, it can be concluded that, firstly, gold ions interact with IL molecules and, secondly, that the behavior of the IL film varies according to the concentration of gold ions.

In order to understand how the concentration of gold ions guides the behavior of the IL Langmuir film, we studied both films by BAM, AFM and GIXD. We also tried to reduce gold ions by surface radiolysis using the IL Langmuir film as a template. We will start by studying the IL Langmuir film spread over a subphase containing gold ions of a concentration corresponding to $r_{AuCl_4^-/IL} = 30$.

5.2 Subphase's concentration : $r_{AuCl_4^-/IL} = 30$

5.2.1 Macroscopic thermodynamic study on the aqueous subphase

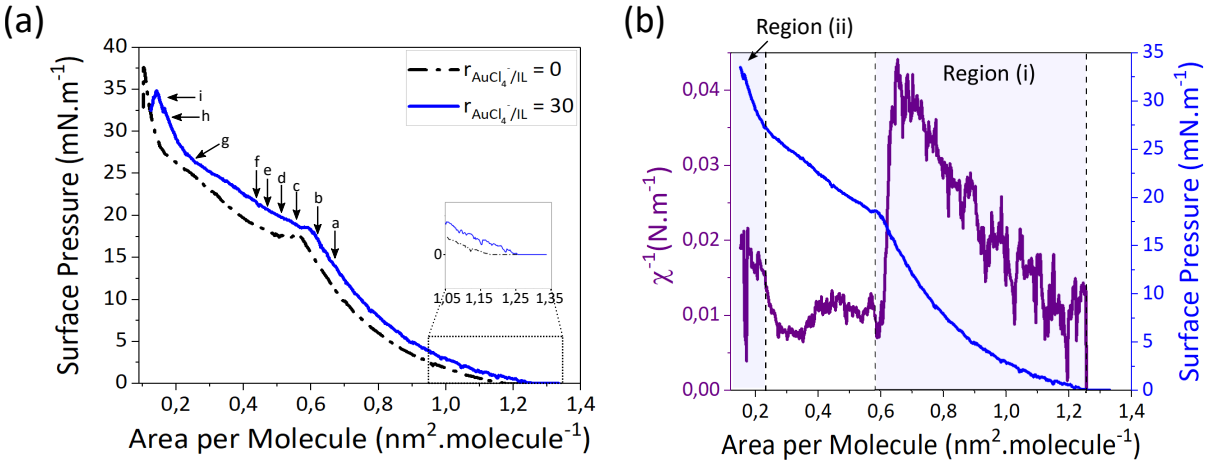

Figure 5.2: (a) Π-A isotherm and (b) inverse of the compressibility of $[C_{20}mim]^+[NTf_2]^-$ Langmuir film spread over a subphase containing 30 $[AuCl_4]^-$/IL.

Figure 5.2 (a) and Figure 5.2 (b) represent respectively the Π-A isotherm and the inverse of the compressibility of $[C_{20}mim]^+[NTf_2]^-$ Langmuir film spread over a subphase containing gold ions of a concentration corresponding to $r_{AuCl_4^-/IL} = 30$. It is possible to identify two increasing regions : region (i) and region (ii) and a plateau, other than the one obtained at $\Pi = 0$ mN.m^{-1}.

For molecular areas greater than A = 1.25 nm^2.molecule^{-1}, the surface pressure of the film is $\Pi = 0$ mN.m^{-1} and the inverse of the compressibility is $\chi^{-1} \sim 0$ N.m^{-1}. This indicates that the film is in a phase coexistence in which one of the phases is a diluted phase. **The plateau is followed by region (i) which is limited between A = 1.25 and A = 0.59 nm^2.molecule^{-1}.** In this region, the surface pressure increases gradually

from 0 $mN.m^{-1}$ to Π = 18.5 $mN.m^{-1}$. The inverse of the compressibility increases until χ^{-1} = 0.04 $N.m^{-1}$ (χ = 22 $m.N^{-1}$). At A = 0.59 $nm^2.molecule^{-1}$, the slope of the inverse of the compressibility drops, indicating the beginning of the formation of a plateau. It extends to (A = 0.22 $nm^2.molecule^{-1}$; Π = 27 $mN.m^{-1}$). **The plateau is then followed by region (ii) which extends to (A = 0.14 $nm^2.molecule^{-1}$; Π = 34.5 $mN.m^{-1}$).** The inverse of the compressibility in this region decreases to χ^{-1} = 0.02 $N.m^{-1}$ (χ = 50 $m.N^{-1}$). At Π = 34.5 $mN.m^{-1}$, the surface pressure drops indicating film collapse.

Discussion

By comparing the Π-A isotherm of IL Langmuir films measured on a subphase containing 30 $[AuCl_4]^-$/IL to that measured on pure water , it can be noticed that both have globally the same profile. However, the lift-off is reached at a molecular area (A = 1.25 $nm^2.molecule^{-1}$) 6% higher than that reached by the film spread on pure water (A = 1.17 $nm^2.molecule^{-1}$). Bai et al. [141] have studied the behavior of $[C_{16}mim]^+[Br]^-$ Langmuir film spread on subphases of different gold ions concentrations. They demonstrated that due to the electrostatic interaction between $[AuCl_4]^-$ anions and $[C_{16}mim]^+$ cations, $[AuCl_4]^-$ anions are adsorbed on the surface. This was emphasized by the observation of the increase of the lift-off area of $[C_{16}mim]^+[Br]^-$ Langmuir film as the concentration of $[AuCl_4]^-$ increases. One may suggest that the 6% increase in the lift-off area of the $[C_{20}mim]^+[NTf_2]^-$ film, when spread over a subphase containing 30 $[AuCl_4]^-$/IL, results from the electrostatic interaction between $[AuCl_4]^-$ and $[C_{20}mim]^+$. After the lift-off, the film passes to region (i). In this region, the compressibility of the film spread on the ionic subphase (χ = 23 $N.m^{-1}$) is slightly lower than that of the film spread on the pure water subphase (χ = 25 $N.m^{-1}$). Both compressibilities indicate that the films are in (LE) phase and formed as monolayers.

At the end of region (i), a plateau starts at (A= 0.59 $nm^2.molecule^{-1}$; Π = 18.5 $mN.m^{-1}$), when the subphase is ionic and at (A= 0.56 $nm^2.molecule^{-1}$; Π = 17.5 $mN.m^{-1}$), when it is pure water. The plateau is formed at a higher surface pressure and 5% greater molecular area when the subphase is ionic. This increase must be due to the interaction between $[AuCl_4]^-$ and $[C_{20}mim]^+$. The gold ions thus appear to stabilize the (LE) phase of the monolayer . Across the plateau, the molecular area of the film is reduced by a factor of 2.7, when the subphase is ionic. When it is pure water, the monolayer collapses into a multilayer by passing across two collapse plateaux, through which the molecular surface area is reduced by a factor of 3.2. The IL monolayer spread over the ionic subphase is therefore assumed to as well collapse through the plateau into a multilayer. In contrast to the film spread on pure water, collapse only occurs through one plateau.

After the plateau, both films enter region (ii) where they become more compressible than before the plateau. In principle, the higher the surface pressure of the film, the less compressible it is. However, if one considers that the monolayer spread on the ionic subphase collapses to a multilayer through the plateau, the system becomes 3D. Therefore, 2D compressibility can no longer be an adequate description of the film state and 3D compressibility must be considered. It is related to 2D compressibility by the relation χ_{3D}= eχ_{2D}, where e is the layer thickness.

Then, the surface pressure drops at (A = 0.14 $nm^2.molecule^{-1}$; Π = 34.5 $mN.m^{-1}$)

when the subphase is ionic and at ($A = 0.10$ nm^2.molecule^{-1}; $\Pi = 37.5$ mN.m^{-1}) when it is pure water. The final collapse of the film is therefore achieved earlier when the gold ions are absorbed on the surface. The adsorption of gold ions on the surface induces repulsion forces, which could be the reason for the stabilization of the non-dense monolayer before the plateau. At ($A = 0.14$ nm^2.molecule^{-1}; $\Pi = 34.5$ mN.m^{-1}), the film is very dense. The repulsion forces in such a case could therefore be the reason for its early degradation.

We then performed BAM measurements on the film during its compression on a subphase containing 30 $[AuCl_4]^-$/IL. We followed its evolution from $\Pi = 16$ mN.m^{-1}, through the transition plateau, to $\Pi = 33$ mN.m^{-1}.

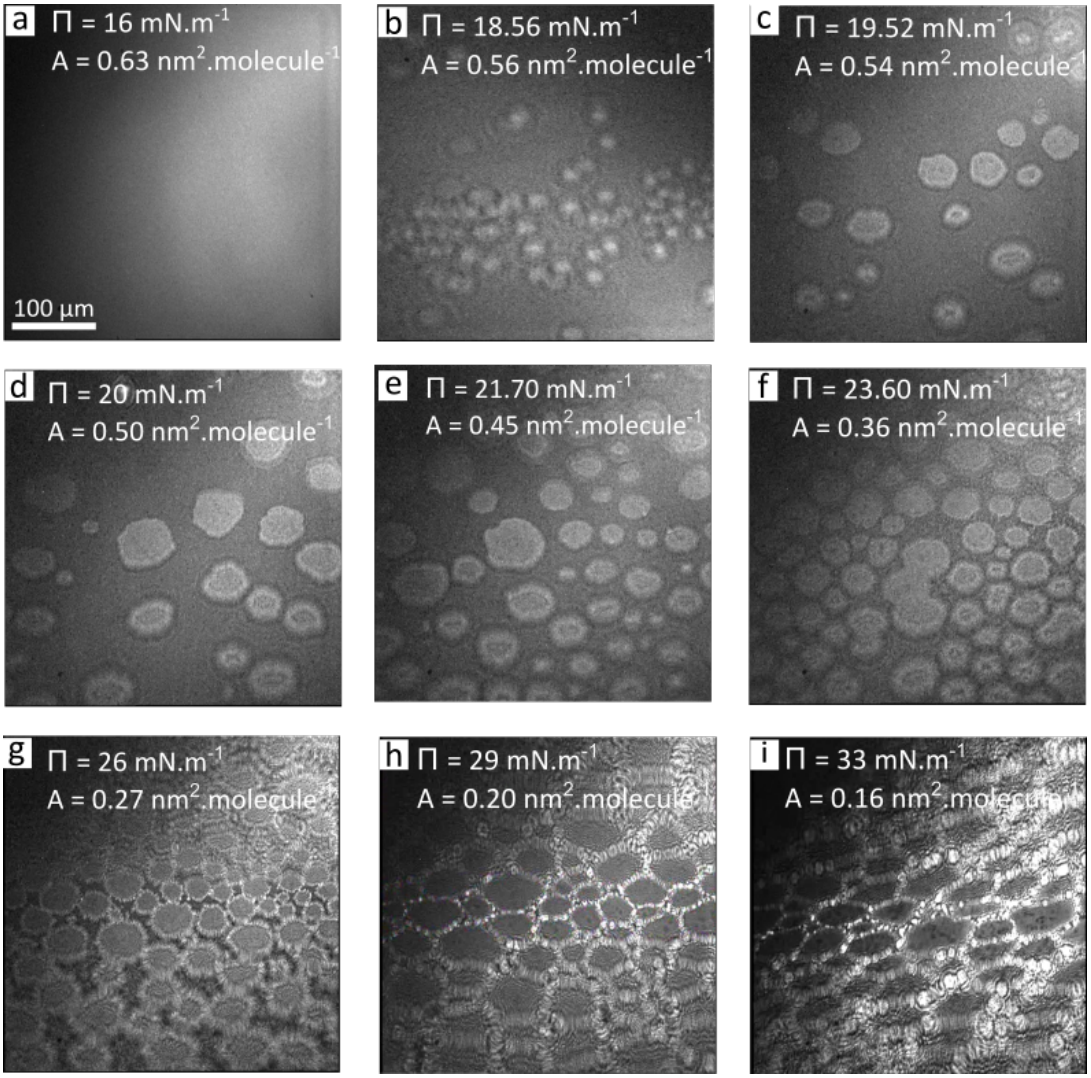

Figure 5.3: BAM images obtained on $[C_{20}mim]^+[NTf_2]^-$ Langmuir film spread over subphase containing containing 30 $[AuCl_4]^-$/IL along its compression.

Before the plateau (Figure 5.3(a)), no contrast is observed and the film appears in a homogeneous phase. When the plateau is reached at $\Pi = 18.5$ mN.m^{-1} (Figure 5.3(b)), we begin to observe a coexistence between circular plates domains, which are at the origin of the intense reflection, embedded with the homogeneous layer (in dark) which was observed before the plateau. The domains are comparable to that observed when the

film was spread over pure water suggesting that both films undergo the same transition. As the compression proceeds, but still on the plateau (Figure 5.3(c-d-e-f)), the circular plates increase in density. At Π = 26 mN.m^{-1}, A =0.27 nm^2.molecule^{-1} (Figure 5.3(g)), the film being close to the end of the plateau, we begin to observe another contrast attributed to granular domains. They are at the origin of the intense reflection and appear surrounding the circular plates. After the plateau (Figure 5.3(h)), the circular plates surrounded by the granular domains has coalesced together and the dark domains are no longer observed indicating the end of the film transition. The granular domains were not observed on pure water. At Π = 33 mN.m^{-1} and A =0.16 nm^2.molecule^{-1} (Figure 5.3(i)) we observe an increase in the intensity of the domains, which suggests that the film becomes dense.

Basically, on the macroscopic scale, both, the film spread on pure water and the film spread on the subphase containing 30 $[AuCl_4]^-$/IL, appear to undergo a transition from a monolayer to a multilayer across the plateau. However, in addition to circular plates and homogeneous phase observed by BAM in both films, granular domains were observed only when the subphase contains gold ions. Could granular domains be related to the interaction of gold anions with IL film? Would it be possible to highlight new domains of IL on solid substrates? We have therefore transferred the films to silicon wafers and studied them at AFM.

5.2.2 Transfer on solid substrates before irradiation

Using the Langmuir-Blodgett procedure, we transferred the films on silicon wafers cleaned with a Piranha solution (thus hydrophilic). We will focus on two transfers, one at Π = 16 mN.m^{-1} (before the plateau) and another at Π = 32 mN.m^{-1} (after the plateau) (see Figure 5.4), characterized by AFM.

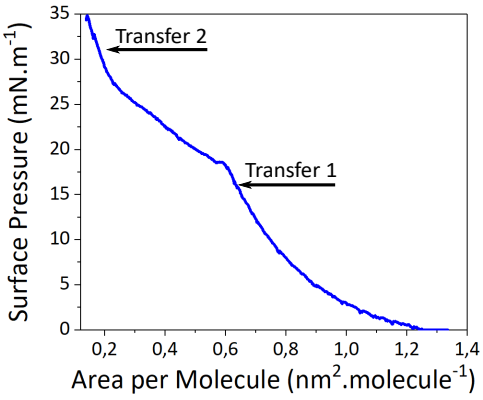

Figure 5.4: Π-A isotherm of the IL Langmuir film spread over a subphase containing 30 $[AuCl_4]^-$/IL.

Figure 5.5 (a) and Figure 5.5 (b) are respectively the topographic and the phase images obtained at Π = 16 mN.m^{-1}. The surface of the wafer appears quite homogeneous despite some defects of 50 nm thick. The homogeneity of the surface suggests that either the monolayer covers the entire surface or the transfer of the monolayer has failed. The film at this surface pressure is in phase (LE), so it is not dense. This could explain a possible failure in transferring the monolayer to a solid substrate. The defects are 5° shifted in phase with respect to the homogeneous surface. They could come from the film or from the silicon surface. The non-observance of such defects by BAM measurements is due to the limited resolution of BAM.

Figure 5.6 (a_1) and Figure 5.6 (a_2) are respectively the topographic image and its zoomed image obtained at Π = 32 mN.m^{-1}. Figure 5.6 (b_1) and Figure 5.6 (b_2) are

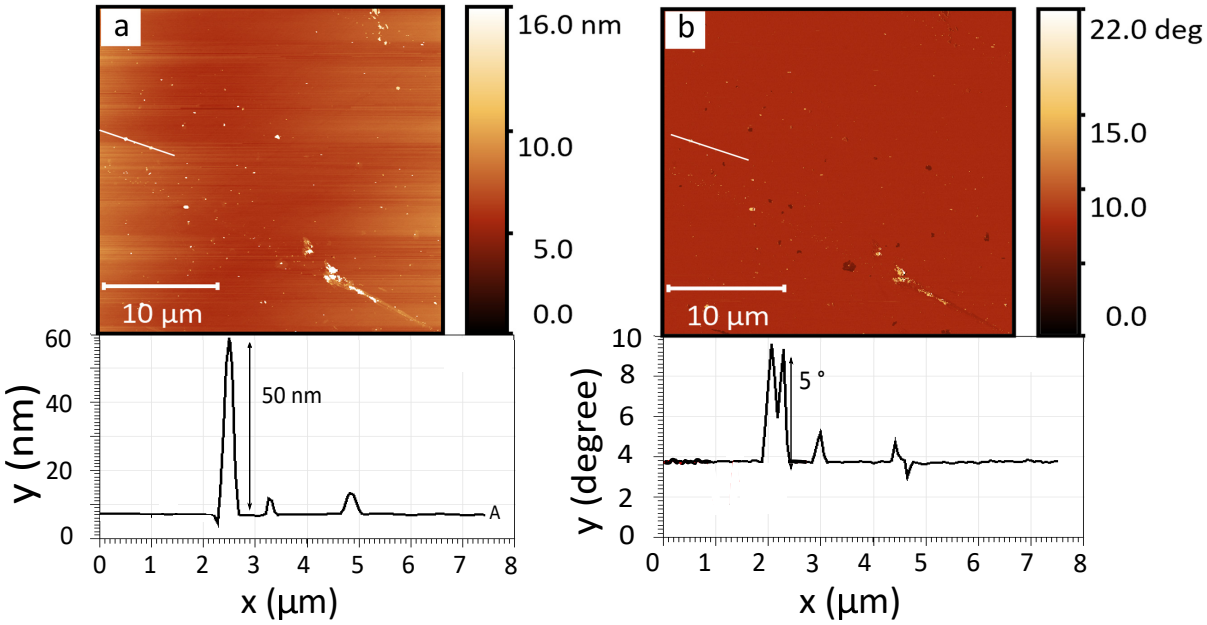

Figure 5.5: (a) AFM topographic and (b) phase images measured on $[C_{20}mim]^+[NTf_2]^-$ Langmuir films spread over a subphase containing 30 $[AuCl_4]^-$/IL transferred by Langmuir-Blodgett on Si/SiO_2 wafers at $\Pi = 16$ mN.m^{-1}.

respectively the phase image and its zoomed image obtained at $\Pi = 32$ mN.m^{-1}. We observe domains of 16 nm thick (Profile A) and 125 nm thick (Profile B) distributed on a homogeneous surface. In the zoomed images (Figure 5.6 (a_2 - b_2)), we observe a "hole" in the homogeneous surface, as pointed out by the white circle (Profile C) and domains of 2.1 nm thick (Profile D). The presence of the hole makes it possible, on the one hand, to identify this homogeneous surface as a homogeneous layer of the film and, on the other hand, to measure its thickness of approximately 1.5 nm. The 16 nm thick domains (Profile A) and the hole (Profile C) are respectively 32° and 36° phase shifted with respect to the homogeneous layer (1.5 nm thick). These two domains are the most out of phase in the system with respect to the homogeneous surface. As the hole (profile C) conforms to the lowest layer, we suggest to attribute it to the surface of silicon which is a hard material. The phase resemblance between the silicon and the 16 nm thick domains (profile A) suggests that they are also formed of a hard material. As the 16 nm thick domains are not in the same horizontal plane as the silicon surface, we suggest to attribute them to gold. The 2.1 nm thick domains and their contours (Profile D) are respectively -5° and 30° phase shifted with respect to the homogeneous layer. The phase of the plane of these domains (-5°) is the lowest one in the system. Since IL molecules are the softest materials in the system, these domains should be attributed to them. Their thickness is in agreement with that of a monolayer of tilted $[C_{20}mim]^+[NTf_2]^-$ molecules: the Imidazolium rings in contact with the silicon wafer and the alkyl chains oriented towards the air. The contours, 30° phase shifted, are of the same phase and level as the surface of the silicon. We therefore suggest that the IL layer may be separated from the homogeneous layer. The 125 nm thick domains (profile B) are 12° phase shifted with respect to the homogeneous layer. This phase shift is intermediate between that of gold and IL domains. These domains (Profile B) must therefore be formed of a mixture of gold and IL molecules. As for the homogeneous layer, there are not enough information to estimate its nature.

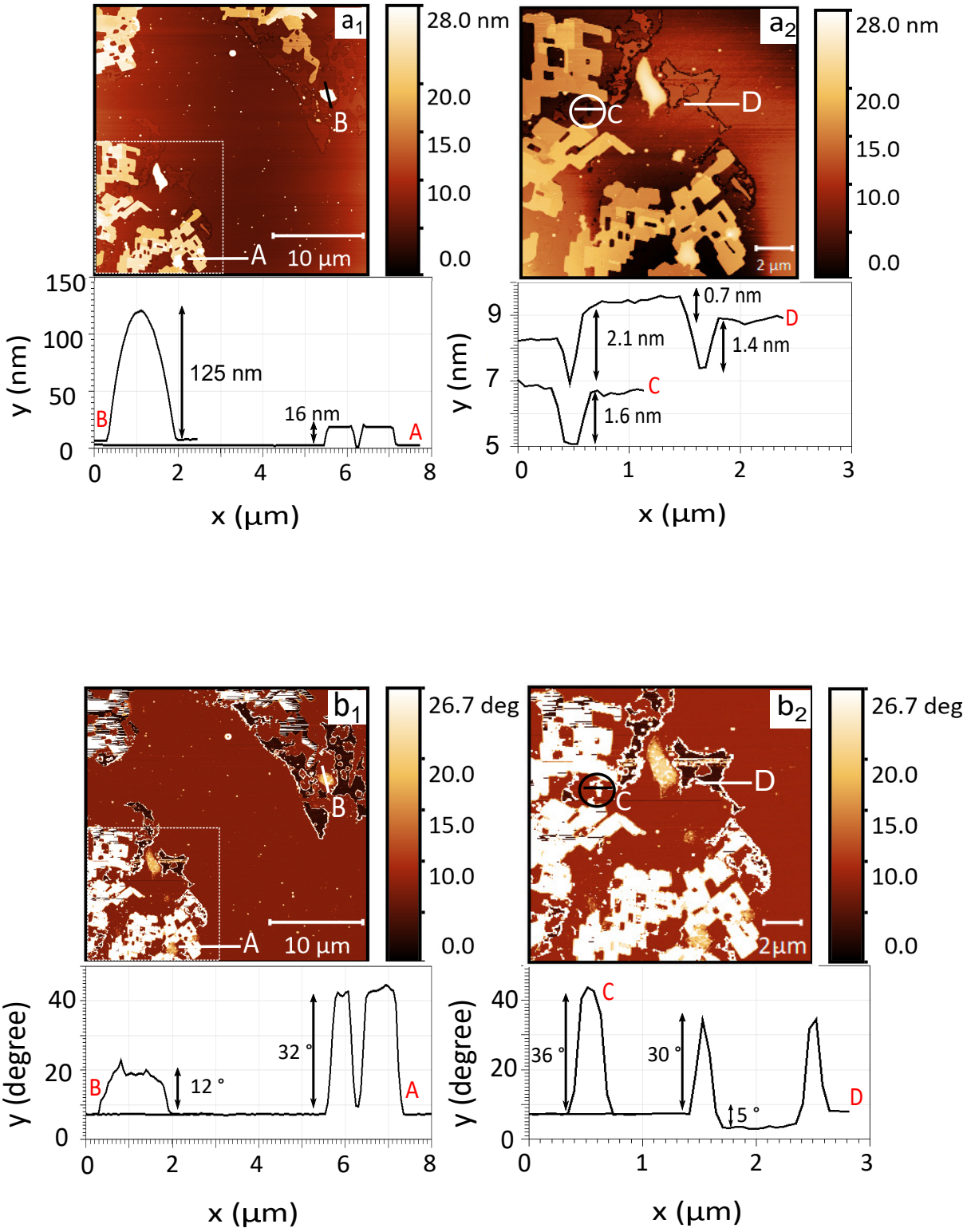

Figure 5.6: AFM topographic (a_1, a_2) and phase (b_1, b_2) images measured on $[C_{20}mim]^+[NTf_2]^-$ Langmuir films, spread over a subphase containing 30 $[AuCl_4]^-$/IL transferred by Langmuir-Blodgett on Si/SiO_2 wafers $\Pi = 32$ mN.m^{-1}.

Discussion

Before the plateau, the homogeneous surface is observed when we try to transfer the IL film from the surface of the pure as well as the ionic subphase. In both cases, the surface could correspond either to the silicon surface due to the possible failure of transfer or to the transfer of the monolayer which covers completely the surface. suggesting that the films may not be transferred to solid substrates. However, after the plateau, the domains observed on silicon wafers differ depending on whether the film was transferred from the surface of the pure water or ionic subphase. The interaction of gold ions shows to modify the multilayer domains obtained after the plateau. A structural characterization of the IL Langmuir film spread over a subphase containing 30 $[AuCl_4]^-$/IL, using GIXD is therefore necessary.

5.2.3 Characterization by X-ray scattering on aqueous subphase

GIXD measurements

We performed GIXD measurements to determine a possible organization of the film induced by the adsorption of gold ions at the surface of a subphase containing 30 $[AuCl_4]^-$/IL. These measurements were carried out at SIRIUS beamline at SOLEIL, at an energy of 12 Kev.

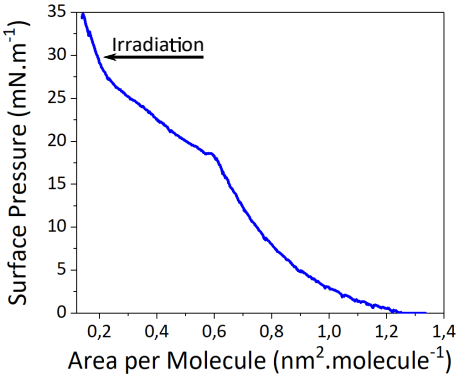

Figure 5.7: Π-A isotherm of the IL Langmuir film spread over a subphase containing 30 $[AuCl_4]^-$/IL.

For surface pressures lower than that of the transition plateau, we did not succeed in observing any diffraction peak. However, at $\Pi = 30$ mN.m^{-1}, after the transition plateau, we observed only one diffraction peak with the form of an in-plane Bragg rod as showed in Figure 5.8(a). The intensity of the integrated peak over Q_z is plotted as a function of Q_{xy} in Figure 5.8(b). The peak is adjusted by a Lorentzian function and the adjustment parameters are collected in Table 5.1. The correlation length of this structure is about $\xi = 6$ nm. The peak can be indexed according to a triply degenerated peak (11) of a hexagonal lattice. The distance between the diffracted planes is d = 0.41 nm and is close to the typical distance between diffracted planes of alkyl chains arranged in a network (d $\sim$ 0.42 nm [37]). The parameter and the area of the hexagonal unit cell composed of one molecule are calculated respectively as follows: a = 0.47 nm and A = 0.19 nm^2. This lattice parameter is close to the that formed of alkyl chain (d $\sim$ 0.48 nm). This area is consistent with the cross section of an alkyl chain (A $\sim$ 0.18 nm^2).

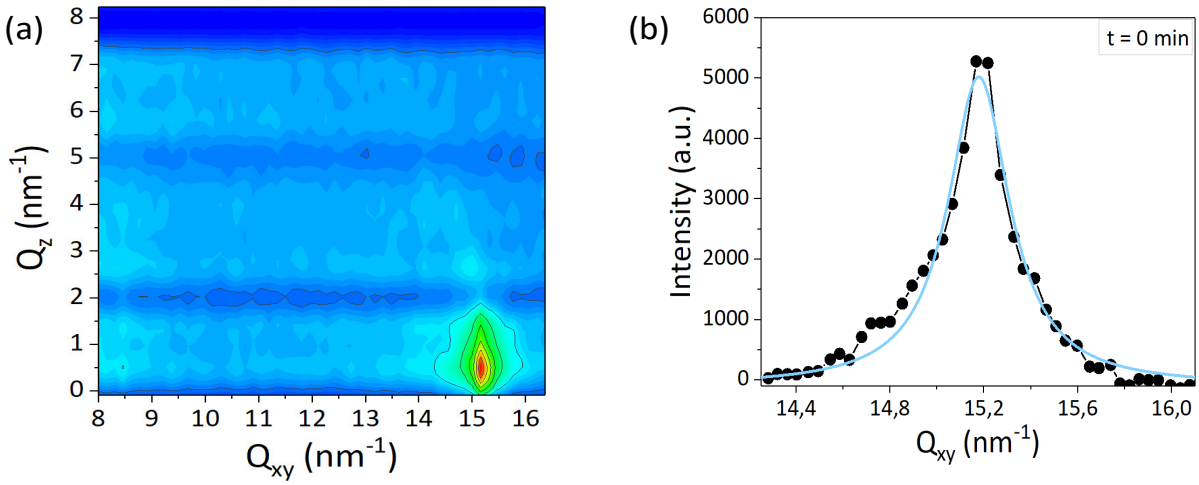

Figure 5.8: The X-ray diffraction (a) map, (b) intensity integrated over Q_z in the horizontal plane of $C_{20}mim]^+[NTf_2]^-$ Langmuir film over a subphase containing gold ions of a concentration corresponding to $r_{AuCl_4^-/IL} = 30$, at $\Pi = 30$ mN.m^{-1}.

Q_{xy} (nm^{-1})	FWHM ΔQ_{xy}(nm^{-1})	correlation length ξ (nm)	Peak area (a.u.)
15.17	0.32	6	2573

Table 5.1: Adjustment parameters of the diffraction peak obtained at $Q_{xy} = 15.17$ nm^{-1} integrated over Q_z of $[C_{20}mim]^+[NTf_2]^-$ Langmuir film spread over a subphase containing gold ions of a concentration corresponding to $r_{AuCl_4^-/IL} = 30$, at $\Pi = 30$ mN.m^{-1}.

Figure 5.9 represents the profile of the rodscan at $Q_{xy} = 15{,}17$ nm^{-1}. At the critical angle, a sharp and intense peak, called Vineyard peak [142, 41], is observed. This peak results from the reflection of the waves at the interface at angles smaller than the angle of incidence of the total reflection. It is not related to the vertical organization of the structure so we will not analyze it. The rodscan exhibits a second peak other than the Vineyard peak whose intensity can be adjusted by a square sine cardinal function. The adjustment parameters are collected in Table 5.2. The maximum of this profile is at $Q_z \sim 0$ nm^{-1} so the organized structure is perpendicular to the surface of the subphase. From the FWHM of this peak, the thickness of the structure can be estimated to be z = 2.6 nm. This thickness corresponds to the length of an elongated alkyl chain composed of 20 atoms (2.7 nm). One thus can conclude that this diffraction peak is associated to the organization of the chains of IL molecules in a hexagonal lattice, perpendicular to the surface of the subphase.

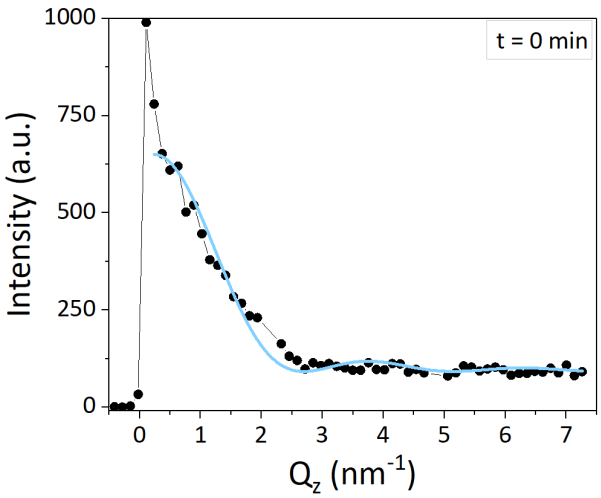

Figure 5.9: The profile of the rodscan at Q_{xy} = 15,17 nm^{-1} of $[C_{20}mim]^+[NTf_2]^-$ Langmuir film spread over a subphase containing gold ions of concentration corresponding to $r_{AuCl_4^-/IL}$ = 30

Q_{xy} (nm^{-1})	Q_z (nm^{-1})	FWHM ΔQ_z(nm^{-1})	height z (nm)	Peak area (a.u.)
15.17	0	2.45	2.6	558

Table 5.2: Adjustment parameters of the rodscan profile at Q_{xy} = 15.17 nm^{-1} of $[C_{20}mim]^+[NTf_2]^-$ Langmuir film spread over a subphase containing gold ions of a concentration corresponding to $r_{AuCl_4^-/IL}$ = 30.

Discussion

GIXD measurements showed that the IL molecules are arranged in a hexagonal lattice, perpendicular to the surface of the subphase containing 30 $[AuCl_4]^-$/IL , at Π = 30 $mN.m^{-1}$ (after the plateau). However, the diffraction spectrum obtained on the IL Langmuir film spread over pure water exhibits 9 diffraction peaks, after the plateau. According to Tassler et al. [11], the film is organized in a coexistence of a 3D structure and a rectangular network formed of interdigitated alkyl chains. The diffraction peak centered around Q_{xy} = 15.17 nm^{-1}, is common between the diffraction spectra obtained on the IL Langmuir film spread on pure water and the one spread on a subphase containing 30 $[AuCl_4]^-$/IL. The interaction of gold anions with the IL thus appears to prevent the 3D structure and stabilize the 2D network. According to the peak centered at Q_{xy} = 15.17, the correlation length of the structure is ξ = 7 nm on the pure water and ξ = 6 nm on the ionic subphase. They are considerably short compared to those of conventional films. The order range of the IL structure is therefore short but the same regardless of the type of subphase.

The IL Langmuir films spread over pure water and over a subphase of a concentration corresponding to 30 $[AuCl_4]^-$/IL behave globally in a similar way. Both undergo a transition from a monolayer to a multilayer across the plateau. However, the adsorption of gold ions shows to prevent the 3D structure of IL Langmuir film and stabilizes the 2D one.

Muller et al.[10] have demonstrated that surface X-ray radiolysis of a condensed Langmuir film spread over an aqueous metal ions subphase results in the formation of metal crystalline structures oriented by the organic monolayer. Bai et al. [141] have also demonstrated that IL Langmuir monolayers can be used as shape-control template to gold crystal structures formed through interfacial reduction of $[AuCl_4]^-$ by formaldehyde gas. We therefore irradiate our film by X-rays in a grazing incidence geometry to attempt to reduce the anions and form crystalline shapes controlled by the IL monolayer.

5.2.4 Surface X-ray radiolysis

We performed a surface X-ray radiolysis on the IL Langmuir film spread over a subphase containing 30 $[AuCl_4]^-$/IL. After compressing the film to Π = 32 mN.m^{-1} (see Figure 5.7), to a condensed and organized phase, we irradiated it for 2.5 hours (150 min) at a grazing incidence geometry. We probed the planar structure of the surface by GIXD during the irradiation time. Measurements were performed at the SIRIUS beamline at SOLEIL under an energy of 12 Kev.

As expected, at the beginning of the irradiation, only the diffraction peak attributed to the organization of the IL monolayer (centered at Q_{xy} = 15.17 nm^{-1}) is observed (Figure 5.8). After only 20 minutes of irradiation, we begin to observe the appearance of two diffraction rings. After 150 min of irradiation, the intensity of one of the diffraction rings becomes considerable, as shown in Figure 5.10(a). The intensities of both rings were integrated azimuthally (at constant Q) and represented in Figure 5.10(b).

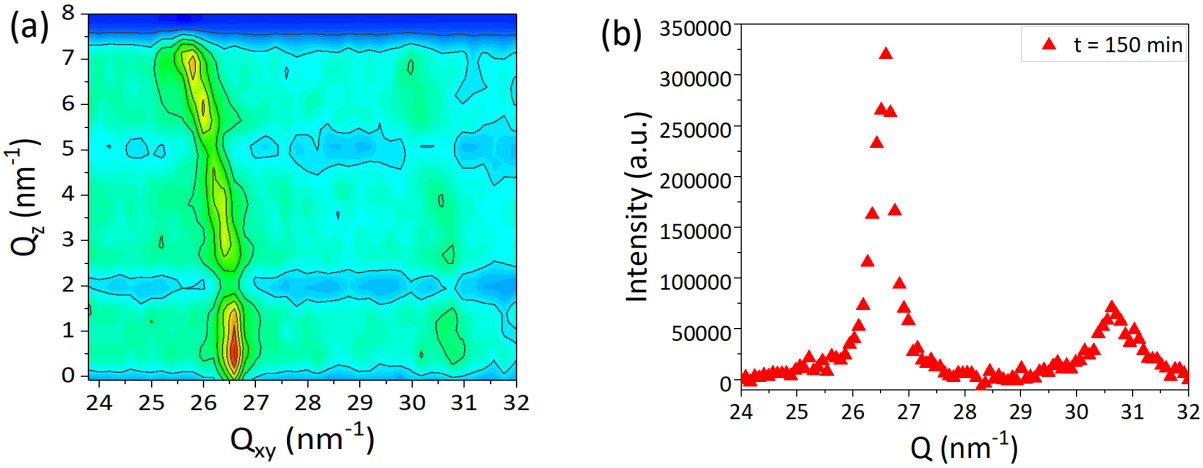

Figure 5.10: The X-ray diffraction map (a) and (b) the azimuthally integrated intensities of the two diffraction rings after 150 minutes of irradiation.

The diffraction by a powder composed of disoriented crystals is evidenced by the formation of a ring-shaped diffraction peak on the detector. According to the literature, the intense peak centered at Q = 26.58 nm^{-1} corresponds to the (111) diffraction peak of gold and the less intense peak centered at Q = 30.7 nm^{-1} corresponds to the (200) diffraction peak of gold [115]. These two diffraction rings are thus associated with the formation of disoriented gold nanostructures NPs. The evolution of the signals from the organic structure and the inorganic structure during the 150 min of irradiation is respectively shown in Figure 5.11 (a) and Figure 5.11 (b). We adjusted the integrated

intensities relative to gold and those relative to IL structures by Lorentzian functions. After 150 min of irradiation, the signal from the organization of the organic layer decreases by 1.8 times (from 2573 a.u. to 1424 a.u.) while that from the growth of NPs increases to 180300 a.u.. It appears that the growth of the inorganic structures disorganizes the organic layer or simply reduces the irradiated zone specific to the organic structure, by occupying the surface.

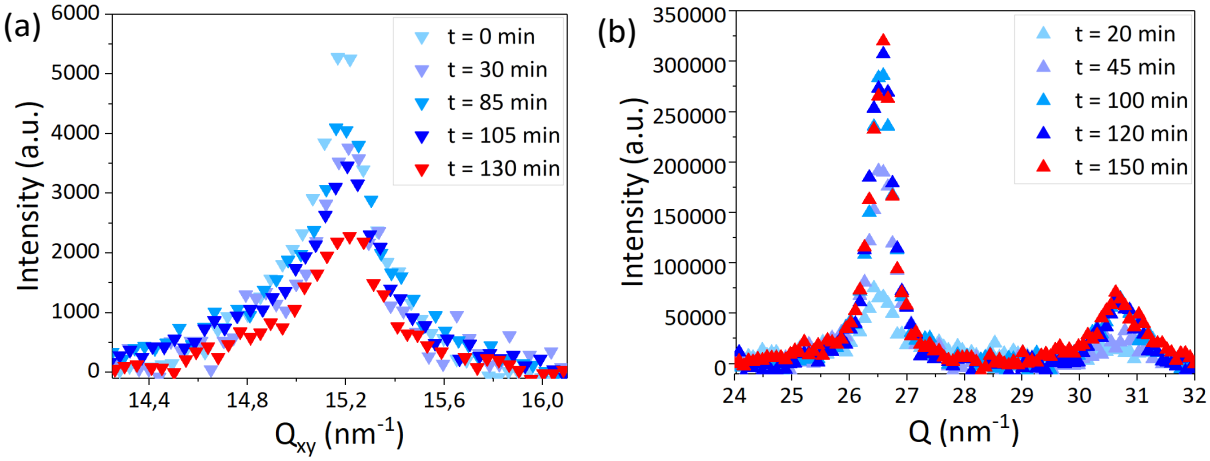

Figure 5.11: The GIXD signals as a function of the time irradiation coming from (a) the organic structure and (b) the inorganic structure.

The increase in signal intensity associated with the growth of gold NPs is mainly due to the increase in their number but also in their size . We adjusted the intensities of the peaks centered at Q = 26.58 nm^{-1} by Lorentzian functions and estimated the size of the formed gold NPs from the FHMW ΔQ as d = $\frac{2\Pi}{\Delta Q}$. Table 5.3 shows the evolution of the estimated diameter and size of gold NPs, estimated to be spherical, as a function of irradiation time. Since the intensity of the diffracted signal is proportional to the irradiated volume, we will estimate in Table 5.3 the growth rate of gold NPs volume. It is calculated between two consecutive measures as follows : $\frac{(V_{i+1}-V_i)}{(t_{i+1}-t_i)}$ and the evolution of the integrated intensity of the peak centered at Q = 26.58 nm^{-1}.

Time (min)	FHMW (nm^{-1})	size (nm)	volume (nm^3)	Growth rate (nm^3.min^{-1})	Peak area (a.u.)
0	-	0	0	0	0
20	0.56	11	700	35	56500
45	0.49	13	1200	20	154000
100	0.38	16	2100	16	183000
120	0.40	16	2100	-	201000
150	0.38	17	2600	10	180300

Table 5.3: The evolution of the estimated size of gold disoriented nanoparticles and the intensity of the peak centered at Q = 26.58 nm^{-1} as a function of irradiation time.

Between t = 0 min and t = 20 min, the volume of gold NPs increases from 0 to 700 nm^3 and the growth rate of the structure is 35 nm^3.min^{-1}. As the irradiation time increases,

the growth rate gradually decreases to 10 $nm^3.min^{-1}$ and the NP size stabilizes around 16 nm ($\sim$ 2000 nm^3) after 150 min. It appears that the growth rate of gold NPs is reduced as a function of irradiation time or that the experiment has reached its resolution. In order to better describe the evolution of the number and size of the gold structures: the evolution of the integrated intensity (I) of the peak at Q = 26.58 nm^{-1} and the evolution of the volume (V) of the NPs were plotted as a function of the irradiation time, as shown in Figure 5.12.

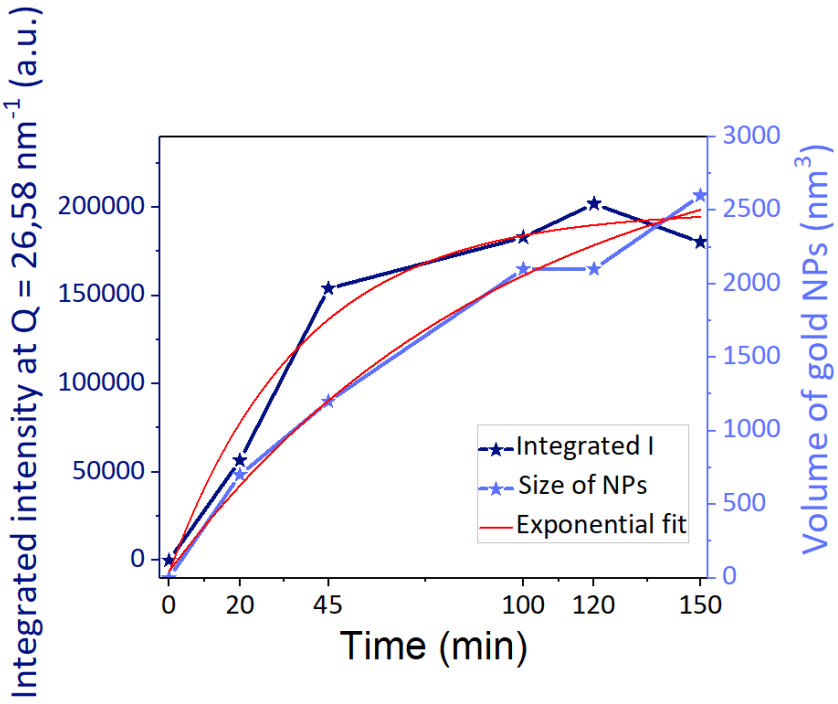

Figure 5.12: The evolution of the area of the integrated intensity of the peak centered at Q = 26.58 nm^{-1} (in blue navy) and that of the size growth of gold NPs (in purple) as a function of irradiation time.

We fitted each curve by exponential functions as follows :

$$I = 200000 - 205400 \exp\left(\frac{-t}{37}\right)$$
$$V = 3164 - 3120 \exp\left(\frac{-t}{97}\right)$$

According to the adjustment, it can be noticed that it takes 5τ= 5*97 = 485 min of irradiation for the diffraction peak area attributed to gold NPs formation to reach its maximum intensity at 200000 a.u.. It takes 5τ= 5*97 = 485 min for NPs to reach their maximum volume $\sim$ 3200 nm^3 (d $\sim$ 18 nm). It appears that as the duration of irradiation increases, the evolution of the number and size of NPs formed is hindered. This could be due to constraints imposed by organic molecules on the surface, which may have had an impact on the growth mechanism of NPs. Or it could be due to the limited number of gold ions initially dissolved in the subphase. Or it could be due to the limited resolution of the experiment.

In order to understand the reason that hinder the growth of gold structures, we will first calculate the number of gold atoms N_{atom} that exist, supposedly that all the ions

were reduced. We will assume that the nanoparticles are of spherical shapes. From the calculated N_{atom}, we will estimate the maximum number of spherical gold NPs of diameter $\sim$ 16 nm, possible to be obtained. Then we will compare it with the maximum number of gold NPs of diameter $\sim$ 16 nm, that could occupy the surface of the trough ($A_{trough} \sim 200$ cm^2, at the time of the measurement).

The volume of the subphase of the trough at SIRIUS beamline at SOLEIL is $V_{subphase}$ = 450 mL. The concentration of gold ions in the subphase is C = 0.12×10^{-4} mol.L^{-1}. N_A, the Avogadro number $\sim 6.022\times 10^{23}$. Supposedly that all the ions were reduced to atoms, the number of gold atoms N_{atom} would correspond to :

$$N_{atom} = C \times V_{subphase} \times N_A = 3252 \times 10^{15}\text{atoms} \tag{5.1}$$

The molecular weight of a gold atom is M = 197 g.mol^{-1} and its weight density being ρ = 19 g.cm^3. The volume of a gold atom V_{atom} is thus calculated as follows :

$$V_{atom} = \frac{M}{\rho \times N_A} = 0.017 \text{ nm}^3 \tag{5.2}$$

The volume of a gold NP (V_{NP}) of 16 nm corresponds to that of a sphere of 16 nm diameter. It is therefore worth V_{NP} = 2144 nm^3. This volume could be roughly formed by 13 $\times10^4$ gold atoms of V_{atom} = 0.017 nm^3. As $N_{atom} = 3252\times10^{15}$, the maximum number of gold NPs that could be formed is approximately $N_{NPs} = 2\times10^{13}$.

The surface occupied by a NP of 16 nm diameter corresponds approximately to S_{NPs} = 200×10^{-14} cm^2. Given that the available trough area is A_{trough} = 200 cm$_2$, the maximum number of NPs that could occupy the surface is roughly $N_{NPs} = 10^{14}$.

The maximum number of gold NPs that can be formed $N_{NPs} = 2\times10^{13}$ when it can occupy the available area of the trough $N_{NPs} = 10^{14}$. We can thus notice that the number of NPs formed is 5 times lower than that which could occupy the surface of the trough. It is therefore quite plausible to consider that after 150 min of irradiation, the system has almost reached its limit of gold NPs formation in size and number due to the limited number of gold ions initially dissolved.

5.2.5 Transfer on solid substrates after irradiation

At the end of the radiolysis, we observed the formation of a gold filament on the same path as that followed by the incident wave as shown in Figure 5.13. We transferred by Inverse Langmuir-Schaefer the film and then performed AFM on and near the filament.

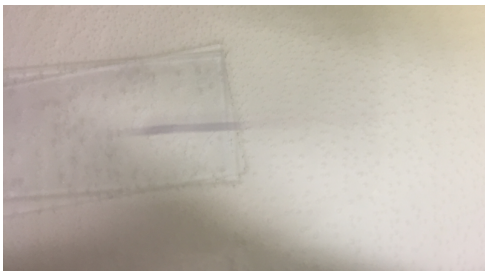

Figure 5.13: Photograph of the irradiated surface of $[C_{20}mim]^+[NTf_2]^-$ Langmuir film deposited on a subphase containing 30 $[AuCl_4]^-$/IL for 8 hours.

Figure 5.14 corresponds to the AFM topographic image obtained by probing the gold filament. We observe domains consisting of an agglomeration of NPs of 10 to 55 nm vertical size. As we probe the region of the path of the incident wave, the number of gold structures must be very significant, which explains the agglomeration of the NPs. However, since the AFM tip is not infinitely sharp, the measured lateral size of the NPs is convoluted by the tip.

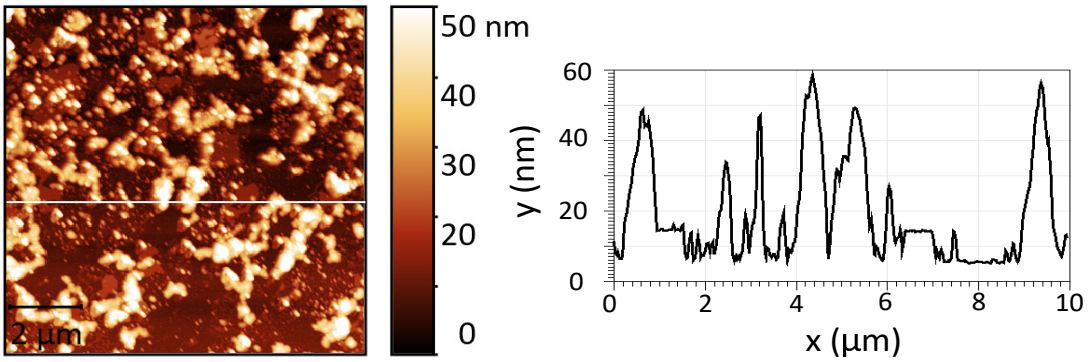

Figure 5.14: AFM topographic image measured on the gold filament transferred by Inverse Langmuir-Schaefer onto Si/SiO_2 substrate after 8 hours of irradiation.

Figure 5.15 correspond to AFM topographic and phase images obtained by probing the region close to the gold filament. A quasi-monodispersion of spherical domains is observed with a lateral size between 50 nm and 65 nm and a vertical size between 7 nm and 17 nm. The vertical size of the NPs s in agreement with the one obtained from GIXD measurements. However, their lateral size is convoluted by the AFM tip which is not perfectly sharp. The NPs appear to be dispersed over an almost homogeneous surface on which there is a small spot 0.9 nm thick. The homogeneous surface and this spot are shifted in phase by only 2.3°, which is too small to be considered relative to different nature domains. It is possible that the significant difference in their thicknesses is at the origin of this phase shift. They may be attributed to the organic layer. On the other hand, the spherical domains are 10° phase shifted with respect to the homogeneous layer, which suggests that they are of different natures.

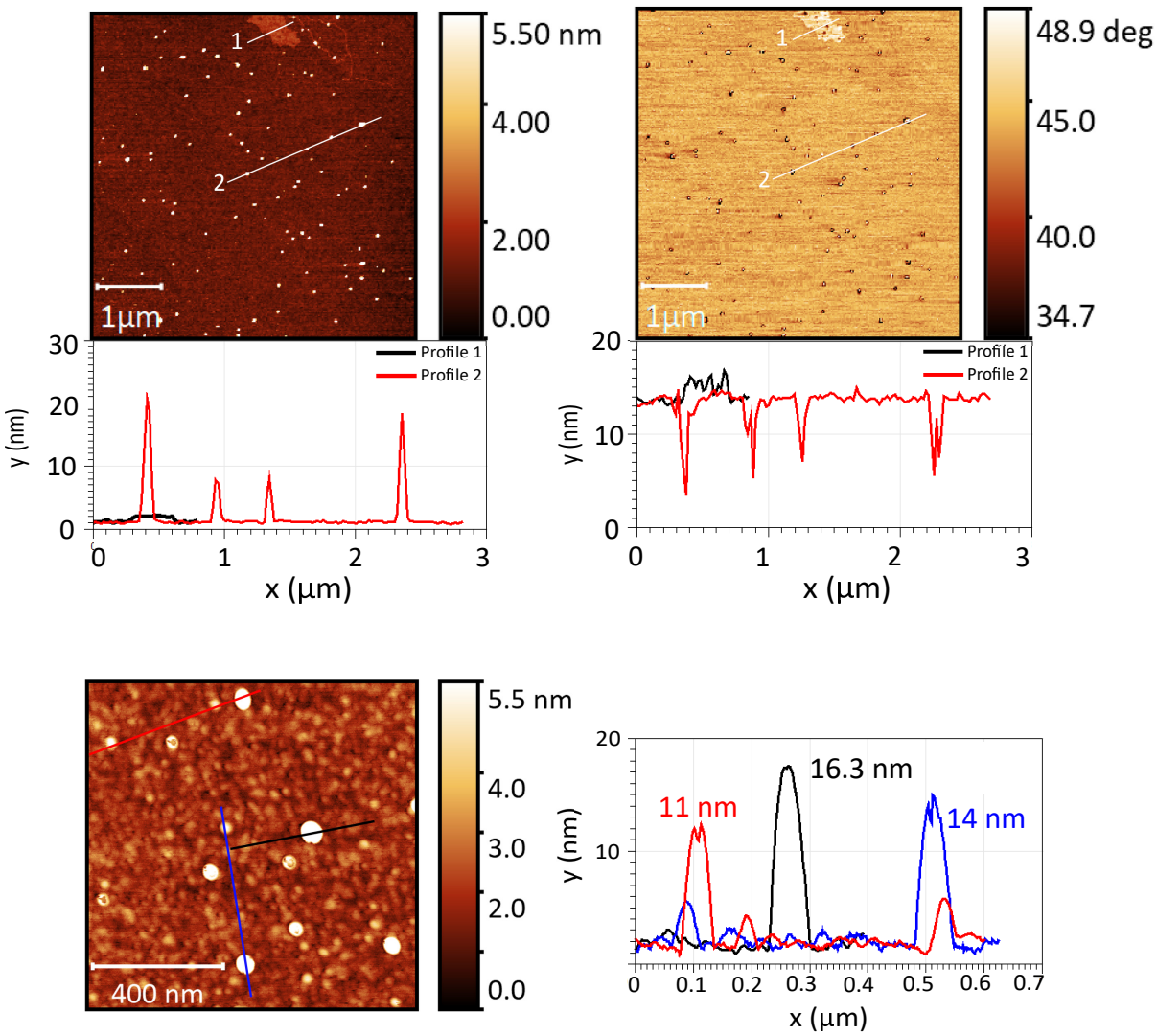

Figure 5.15: AFM topographic and phase images measured on the region close to the gold filament transferred by Inverse Langmuir-Schaefer onto Si/SiO_2 substrate after 8 hours of irradiation.

We succeeded in forming gold spherical nanoparticles of a size of 16 nm by surface X-ray radiolysis, using the IL Langmuir film as a template. After 2.5 h of irradiation, the growth in size and number of the gold NPs saturated due to the limited number of dissolved gold ions. The intensity of the signal coming from the organization of the IL film decreases as the inorganic structures grow.

5.3 Subphase's concentration : $r_{AuCl_4^-/IL} = 600$

Based on the literature, Dupres et al. [119] have demonstrated that organic and inorganic superstructures, in some cases, can form when the concentration of inorganic ions in the subphase exceeds a threshold concentration. It is therefore tempting to increase the concentration of gold ions in the subphase. We repeated the same study, but multiplying by 20 the number of $[AuCl_4]^-$ ions per molecule $[C_{20}mim]^+[NTf_2]^-$. The concentration of the subphases thus corresponds to $r_{AuCl_4^-/IL} = 600$.

5.3.1 Macroscopic thermodynamic study on the aqueous subphase

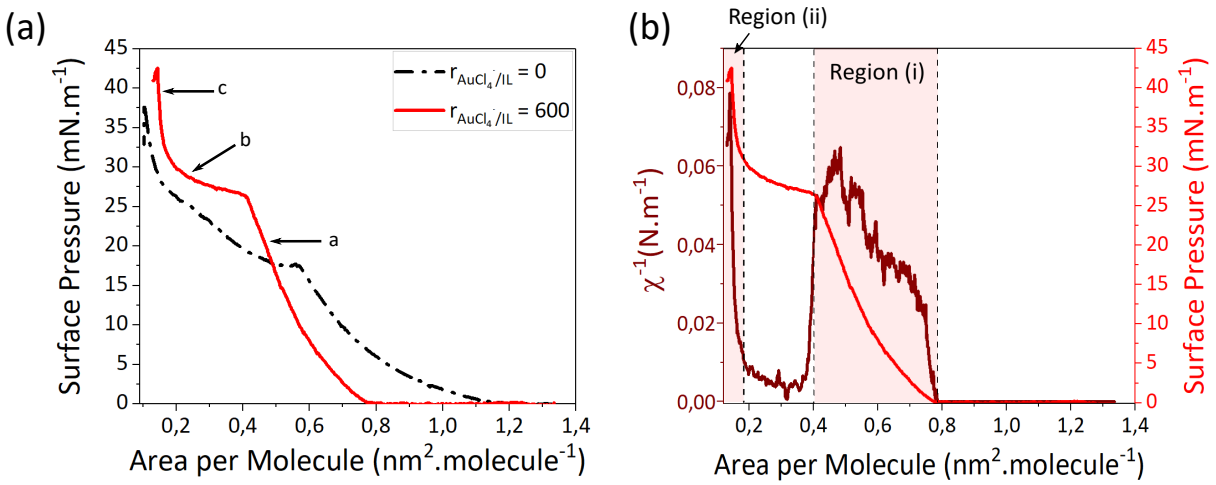

Figure 5.16: (a) Π-A isotherm and (b) inverse of the compressibility of $[C_{20}mim]^+[NTf_2]^-$ Langmuir film spread over a subphase containing 600 $[AuCl_4]^-$/IL.

Figure 5.16 (a) and Figure 5.16 (b) show respectively the Π-A isotherm and the inverse of the compressibility of $[C_{20}mim]^+[NTf_2]^-$ spread over a subphase containing 600 $[AuCl_4]^-$/IL. Two increasing regions can be identified: region (i) and region (ii) and a plateau, other the one obtained at $\Pi = 0$ mN.m^{-1}.

For molecular areas greater than A = 0.78 nm^2.molecule^{-1}, the surface pressure of the film is $\Pi = 0$ mN.m^{-1} and the inverse of the compressibility is $\chi^{-1} \sim 0$ N.m^{-1}. This indicates that the film is in a phase coexistence in which one of the phases is a diluted phase. **The plateau is followed by region (i) which is limited between A = 0.78 nm^2.molecule^{-1} and A = 0.40 nm^2.molecule^{-1}.** In this region, the surface pressure increases gradually from $\Pi = 0$ mN.m^{-1} to $\Pi = 26$ mN.m^{-1}. The inverse of the compressibility increases until $\chi^{-1} = 0.062$ N.m^{-1} ($\chi = 16$ N.m^{-1}). At A = 0.40 nm^2.molecule^{-1}, the slope of the inverse of the compressibility drops indicating the beginning of the formation of a plateau. It extends to (A = 0.19 nm^2.molecule^{-1} ; $\Pi = 30$ mN.m^{-1}). **The plateau is then followed by region (ii) which is limited between A = 0.19 nm^2.molecule^{-1} and A = 0.14 nm^2.molecule^{-1}.** The surface pressure increases to $\Pi = 42.5$ mN.m^{-1} and then drops, indicating film collapse. The film in this region becomes less compressible ($\chi = 12$ m.N^{-1}).

Discussion

By comparing the Π-A isotherm of IL Langmuir films measured on a subphase containing 600 $[AuCl_4]^-$/IL to that measured on pure water, it can be noticed that the film behave drastically in a different way. The lift-off (A = 0.78 nm^2.molecule^{-1}) is reached at a molecular area 33% less than when the film was spread on pure water (A = 1.17 nm^2.molecule^{-1}). After the lift-off, the film is in region (i) and is of a compressibility of $\chi = 16$ mN.m. This compressibility is at the limit of that of a (LE) phase and a (LC)

phase and is considered to be formed as a monolayer.

The presence of a large number of $[AuCl_4]^-$ on the surface might have led to competition with $[NTf_2]^-$ to be in the electrostatic interaction with $[C_{20}mim]^+$. $[AuCl_4]^-$ anions might therefore have replaced $[NTf_2]^-$ in the IL Langmuir film. The area occupied by an Imidazolium ring is assumed to be the same regardless the nature of the subphase. In this context, it is necessary to compare the cross section area of $[AuCl_4]^-$ with that of $[NTf_2]^-$.

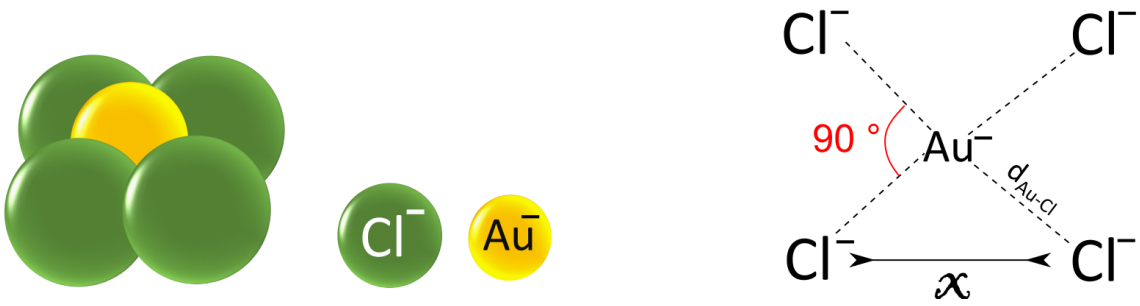

Figure 5.17: Illustration of the square planar geometry of $[AuCl_4]^-$.

$[AuCl_4]^-$ is a complex of a plane square geometry [143] as illustrated in Figure 5.17. It is characterized by having the gold ion in the center, bounded to 4 chloride ions with a binding angle of 90°. The average Au-Cl bond length is $d_{Au-Cl} \sim 0.23$ nm [143] and the average distance between two chloride is "x". On water surface, the complex is free to adopt a horizontal or vertical configuration. If it chose the horizontal one, its cross section area would correspond to $A_{Au-Cl} = x^2$. However, if it chose the vertical one, its cross section area would correspond to $A_{Au-Cl} = x \times d_{Cl}$ where "d_{Cl}" is the diameter of a chloride ion. The radius of a chloride ion is $r_{Cl} = 0.184$ nm [144]. The distance between two chlorides is therefore estimated as follows :

$$x = \sqrt{d_{Au-Cl}^2 + d_{Au-Cl}^2}$$

One obtains $x \sim 0.33$ nm. The cross section area of $[AuCl_4]^-$ is estimated to be $A_{Au-Cl} = 0.10$ nm^2, when it is horizontal and $A_{Au-Cl} = 0.12$ nm^2, when it is vertical. According to the macroscopic characterization of the IL at the air-water interface, $[NTf_2]^-$ is supposed to be in a horizontal configuration at the lift-off. Its cross section area, in this case, is estimated to be $A_{[NTf_2]^-} = 0.28$ nm^2. The cross section area of $[AuCl_4]^-$ is therefore 64% or 57% less than that of $[NTf_2]^-$. However, the lift-off area of the film spread over the subphase containing 600 $[AuCl_4]^-$/IL is 33 % less than that of the film spread over pure water. The area occupied by two $[AuCl_4]^-$, in a horizontal configuration, corresponds to 0.20 nm^2 which is 29% less of the cross section of $[NTf_2]^-$. One can therefore suggest that, at the surface of the subphase, $[NTf_2]^-$ may have got replaced by 2 complexes of $[AuCl_4]^-$. According to the literature [145, 146], IL molecules are characterized by their ability to extract gold. The extraction mechanism occurs through the exchange of anions between an IL anion and a gold anion complex. The exchange results in a product formed by the IL cation and the anionic gold complex and another product formed by the IL anion and the counter anion of the gold complex. This mechanism could therefore explain the replacement of one $[NTf_2]^-$ by one $[AuCl_4]^-$ at the surface. However, it appears that on the surface, there are 2 $[AuCl_4]^-$ for one $[C_{20}mim]^+$. The presence of the second

$[AuCl_4]^-$ could be indispensable to the reach thermodynamic equilibrium between the charged subphase and the charged surface.

At (A = 0.40 nm^2.molecule^{-1}; Π = 26 mN.m^{-1}), a plateau starts. The cross section area of an Imidazolium ring vertical to the surface is 0.3 nm^2 and that of $[AuCl_4]^-$ vertical to the surface is 0.1 nm^2. The molecular area at the beginning of the plateau (A = 0.40 nm^2.molecule^{-1}) thus corresponds to one $[C_{20}mim]^+$ and one $[AuCl_4]^-$. During film compression one of the two $[AuCl_4]^-$ must therefore have passed to the subphase. The plateau ends at (A = 0.19 nm^2.molecule^{-1} ; Π = 30 mN.m^{-1}). The molecular area of the film is therefore reduced by a factor of 2 across the plateau. One might suggest that Langmuir film undergoes a transition to a multilayer through the plateau.

After the plateau, the film is in region (ii). It has a compressibility of χ = 12 m.N^{-1}, which corresponds to a film (LC). The film in region (ii) is assumed to be formed as a multilayer film. It degrades at Π = 42.5 mN.m^{-1}, when the surface pressure decreases.

We then performed BAM measurements on the film during its compression. before the plateau, at Π = 20 mN.m^{-1} (Figure 5.18(a)) a homogeneous surface is observed. This observation is consistent with the Π-A isotherm which suggested that the film is in a (LE) single phase. When compressed to a surface pressure on the plateau, to Π = 28.23 mN.m^{-1}, (Figure 5.18(b)), a coexistence of light gray domains with dark domains is observed, indicating a phase transition region. The observed domains are completely different from those observed during the phase transition of the IL film spread over pure water or over a subphase containing 30 $[AuCl_4]^-$/IL. The phase transition that the film undergoes may have been altered by replacing $[NTf_2]^-$ by $[AuCl_4]^-$. After this plateau, at Π = 40 mN.m^{-1} (Figure 5.18(c)), the film appears in a homogeneous phase, brighter than before the plateau. This indicates the transition of the film to a denser phase.

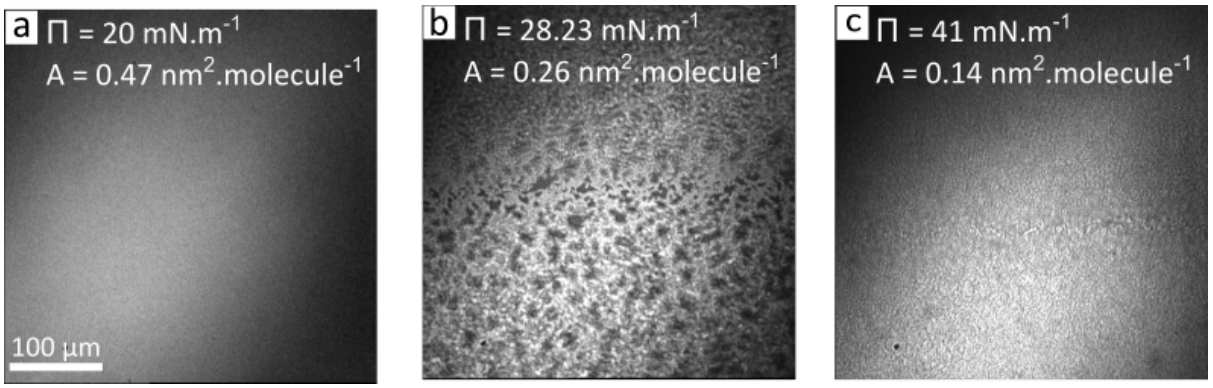

Figure 5.18: BAM images obtained along the compression of $[C_{20}mim]^+[NTf_2]^-$ Langmuir film spread over a subphase containing gold ions of a concentration corresponding to $r_{AuCl_4^-/IL}$ = 600

BAM measurements are consistent with those of the Π-A isotherm. The film undergoes a phase transition from a phase to a denser one across the transition plateau. The domains obtained on 600 $[AuCl_4]^-$/IL subphase are different from those obtained on pure water and on 30 $[AuCl_4]^-$/IL subphase. Are these domains relative to a different organization of the film?

5.3.2 Transfer on solid substrates before irradiation

Using the Langmuir-Blodgett procedure, we transferred the films on silicon wafers cleaned with a Piranha solution. We will focus on two transfers, one at $\Pi = 25$ mN.m^{-1} (before the plateau) and another at $\Pi = 33$ mN.m^{-1} (after the plateau) (see Figure 5.22), characterized by AFM.

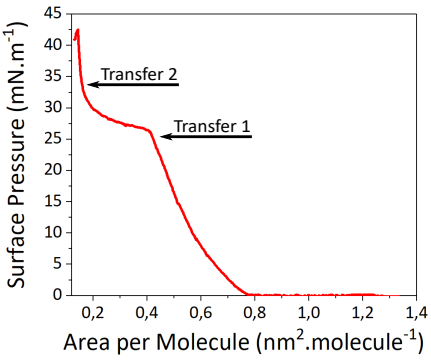

Figure 5.19: Π-A isotherm of the IL Langmuir film spread over a subphase containing 600 $[AuCl_4]^-$/IL.

Figure 5.20 (a) and Figure 5.20 (b) are respectively the AFM topographic and phase images of the film transferred at $\Pi = 25$ mN.m^{-1}. We observe a homogeneous surface covered with columnar domains. The domains consist of a stack of four layers: three thin layers (3.9 nm, 4.2 nm, 4 nm thick (Profile 1)) and one thick layer (60 nm thick (Profile 2)). The total thickness of the columnar domains corresponds to ~ 72 nm.

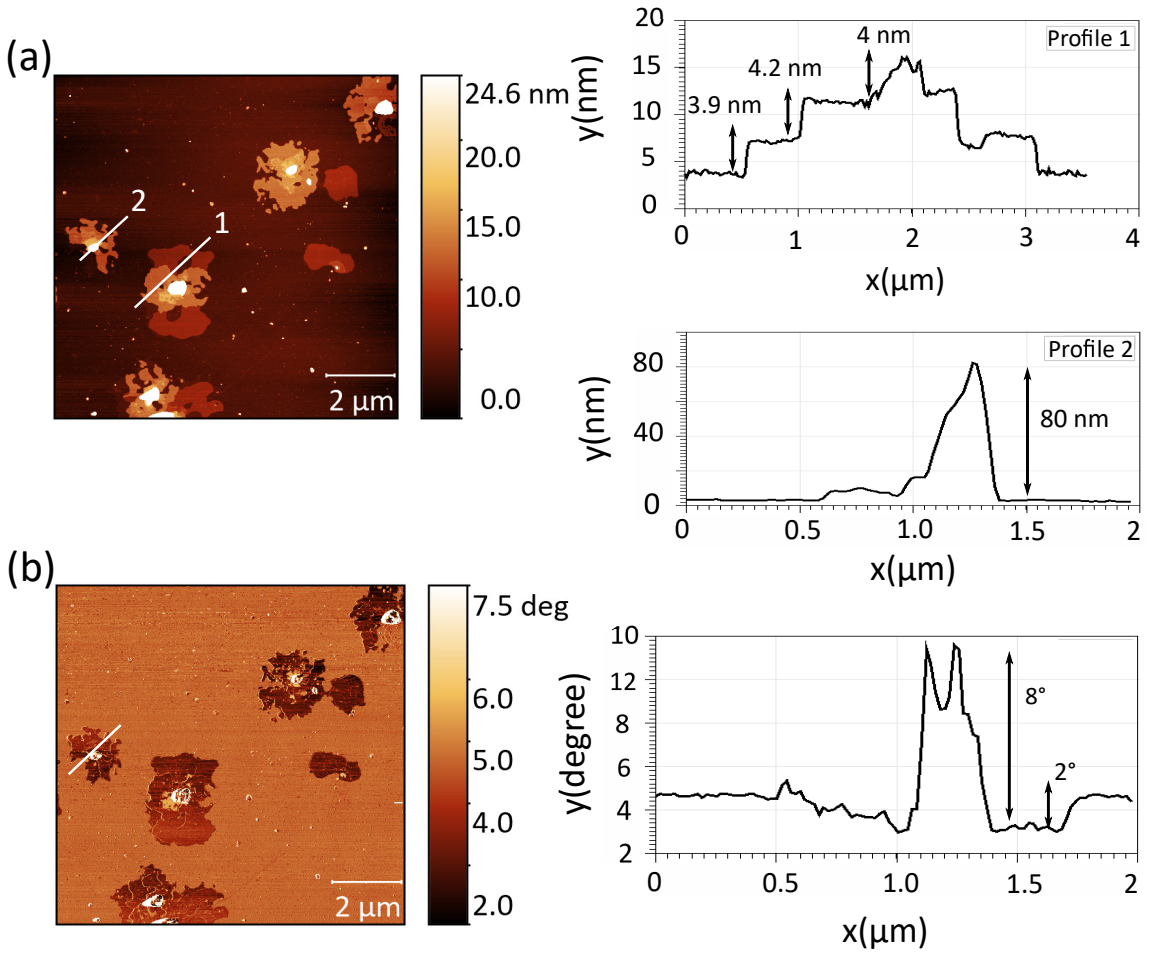

Figure 5.20: AFM topographic (a) and phase (b) image measured on $[C_{20}mim]^+[NTf_2]^-$ Langmuir films spread over a subphase containing 600 $[AuCl_4]^-$/IL, transferred by Langmuir-Blodgett on Si/SiO_2 wafers at $\Pi = 25$ mN.m^{-1}.

The thickness of each thin layer of Profile 1 is slightly higher than that of IL molecules (3.2 nm thick). They are of the same phase. Thin layers may therefore be formed of a mixture of gold and IL. They are 1.6° phase shifted with respect to the homogeneous surface, suggesting that it could just as well be formed from a mixture of gold and IL. The thick layer (Profile 2) is 8.6° phase shifted with respect to the homogeneous layer. It may correspond to gold domains.

Figure 5.21 (a) and Figure 5.21 (b) are respectively the AFM topographic and phase images of the the film transferred at $\Pi = 33$ mN.m^{-1}. We observe a homogeneous surface covered with columnar domains. The domains observed before the plateau seem to have merged into larger domains and cover almost the entire surface. Each thin layer becomes 8 nm thick while the thick layers become 36 nm thick. The thickness of the thin layers has almost doubled as the film passes through the transition plateau. On the other hand, the inorganic thick layers lost almost half of their thickness. The total thickness of the columnar domains corresponds to 80 nm. It has therefore increased by only 8 nm compared to the thickness before the plateau.

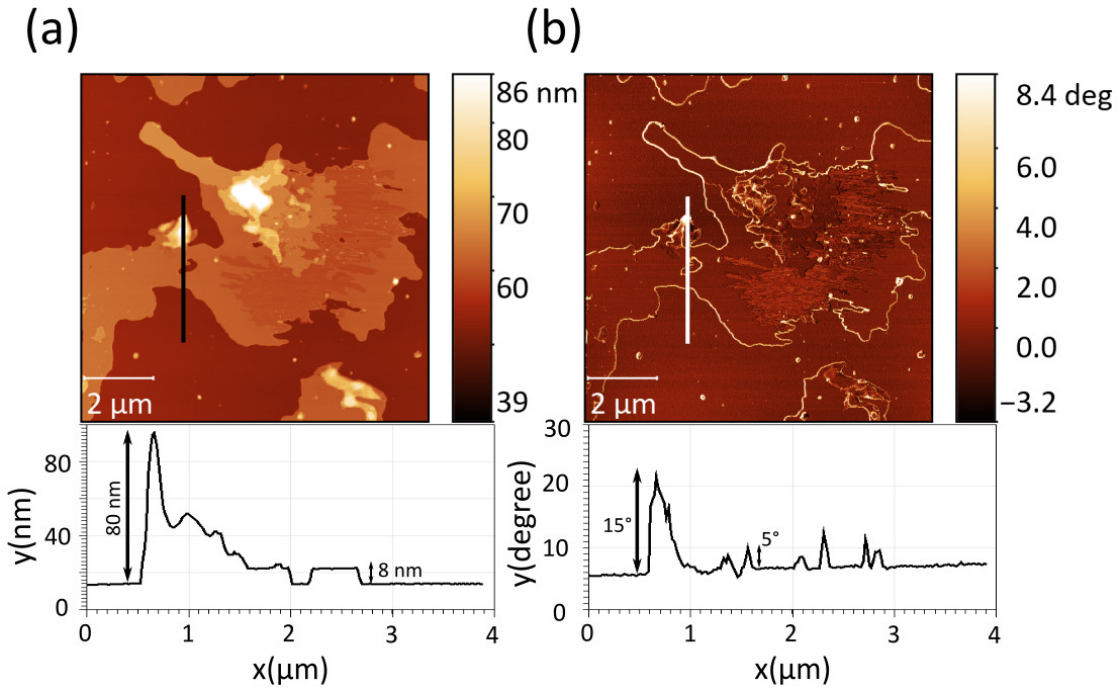

Figure 5.21: AFM topographic (a) and phase (b) image measured on $[C_{20}mim]^+[NTf_2]^-$ Langmuir films spread over a subphase containing 600 $[AuCl_4]^-$/IL, transferred by Langmuir-Blodgett on Si/SiO_2 wafers at $\Pi = 33$ mN.m^{-1}.

Discussion

According to the AFM images, the deposited film, before the plateau, is formed of columnar domains of 72 nm thick. They correspond to a stack of inorganic and organic layers. The film, on solid substrates, appears to have collapsed before the plateau, which is in discrepancy with the macroscopic study on the aqueous ionic subphase. $[AuCl_4]^-$ within a few angstroms of the subphase surface must be homogeneously dispersed due to their solvation in water. The film on the ionic aqueous subphase, before the plateau, can be formed as a monolayer. When interacting with a solid substrate, gold ions tend to form aggregates. This phenomenon can induce the collapse of the IL film in multilayers domains, as observed by AFM. Then the film undergoes a transition through the plateau where the columnar domains gain 8 nm in thickness. It thus collapses further across this plateau. AFM and the macroscopic study are in agreement that the plateau is a collapse plateau. According to macroscopic measurements, 2 complexes of $[AuCl_4]^-$ appear to have replaced $[NTf_2]^-$ on the water surface. On the basis of these measurements alone, it is not possible to provide further information on the position of $[NTf_2]^-$. The configuration of the film appears to depend on the nature of the substrate, whether aqueous or solid.

The behavior of the IL film vary radically when the concentration of the subphase is 20 times higher in gold ions. Will it be possible to detect changes in the organization of the film by GIXD performed on the ionic aqueous subphase? Is the structure modification of the film at the macroscopic scale a characteristic of a superstructure?

5.3.3 Characterization by X-ray scattering on aqueous subphase

In order to reveal a possible new structure of the IL film, we performed a GIXD on the IL film spread on a subphase containing 600 $[AuCl_4]^-$/IL. We then proceeded to irradiate it for several hours in an attempt to reduce the gold ions and to form crystalline structures by surface X-ray radiolysis. We followed by GIXD the evolution of the diffraction signal and by XRF the evolution of the fluorescence signals of gold and chloride on the surface.

GIXD measurements

The concentration of the subphase in gold ions corresponds to $r_{AuCl_4^-/IL} = 600$. The measurements were carried out at SIRIUS beamline at SOLEIL, at an energy of 8 Kev.

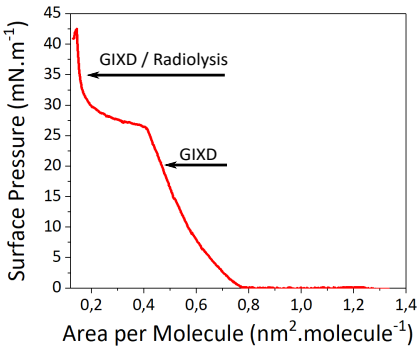

Figure 5.22: Π-A isotherm of the IL Langmuir film spread over a subphase containing 600 $[AuCl_4]^-$/IL.

We performed GIXD on the film obtained at $\Pi = 20$ $mN.m^{-1}$ (before the plateau) (see Figure 5.22). Figure 5.23 (a) and Figure 5.23 (b) represent respectively the X-ray diffraction map and the intensity of the diffraction signals integrated over Q_z.10 diffraction peaks, after 30 min of irradiation, were observed. The peaks are fitted by Lorentzian functions and the adjustment parameters are collected in Table 5.4. The rodscans of the peaks

are represented in Figure 5.24 and Figure 5.25.

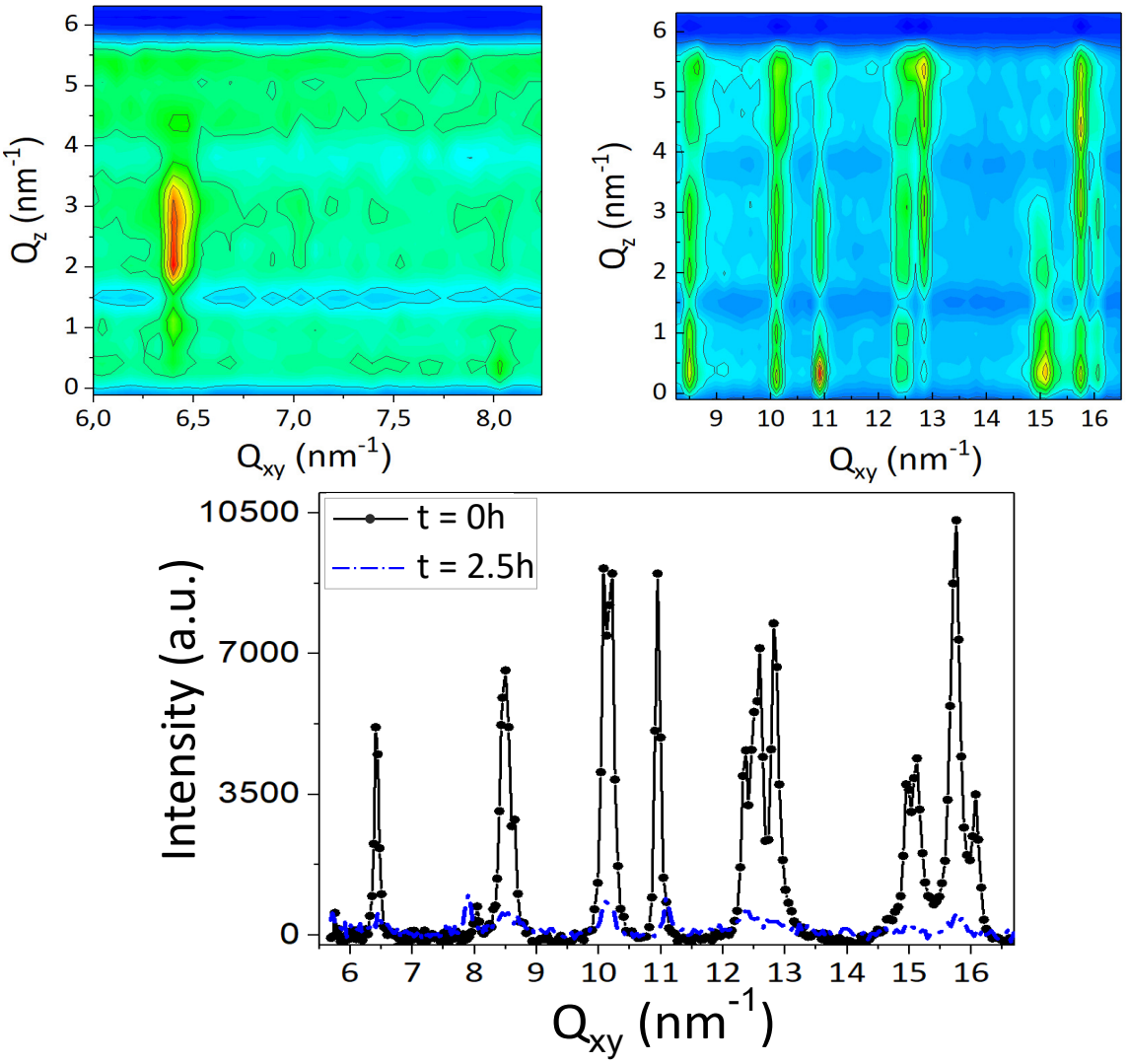

Figure 5.23: The X-ray diffraction (a) map and (b) intensities integrated over Q_z of the IL Langmuir film over a subphase containing 600 $[AuCl_4]^-$/ IL, at Π = 20 mN.m^{-1}.

Q_{xy} (nm^{-1})	ΔQ_{xy}(nm^{-1})	Peak area (a.u.)	Correlation length ξ (nm)
6.42	0.077	720	26
8.49	0.17	1977	12
10.15	0.19	2959	11
10.95	0.09	1274	22
12.55	0.20	2099	10
12.84	0.11	1390	18
14.96	0.12	560	17
15.11	0.17	1092	12
15.74	0.16	2785	13
16.07	0.11	530	18

Table 5.4: Adjustment parameters of the diffraction peaks integrated over Q_z of the IL Langmuir film spread over a subphase containing 600 $[AuCl_4]^-$/ IL, at $\Pi = 20$ mN.m^{-1}.

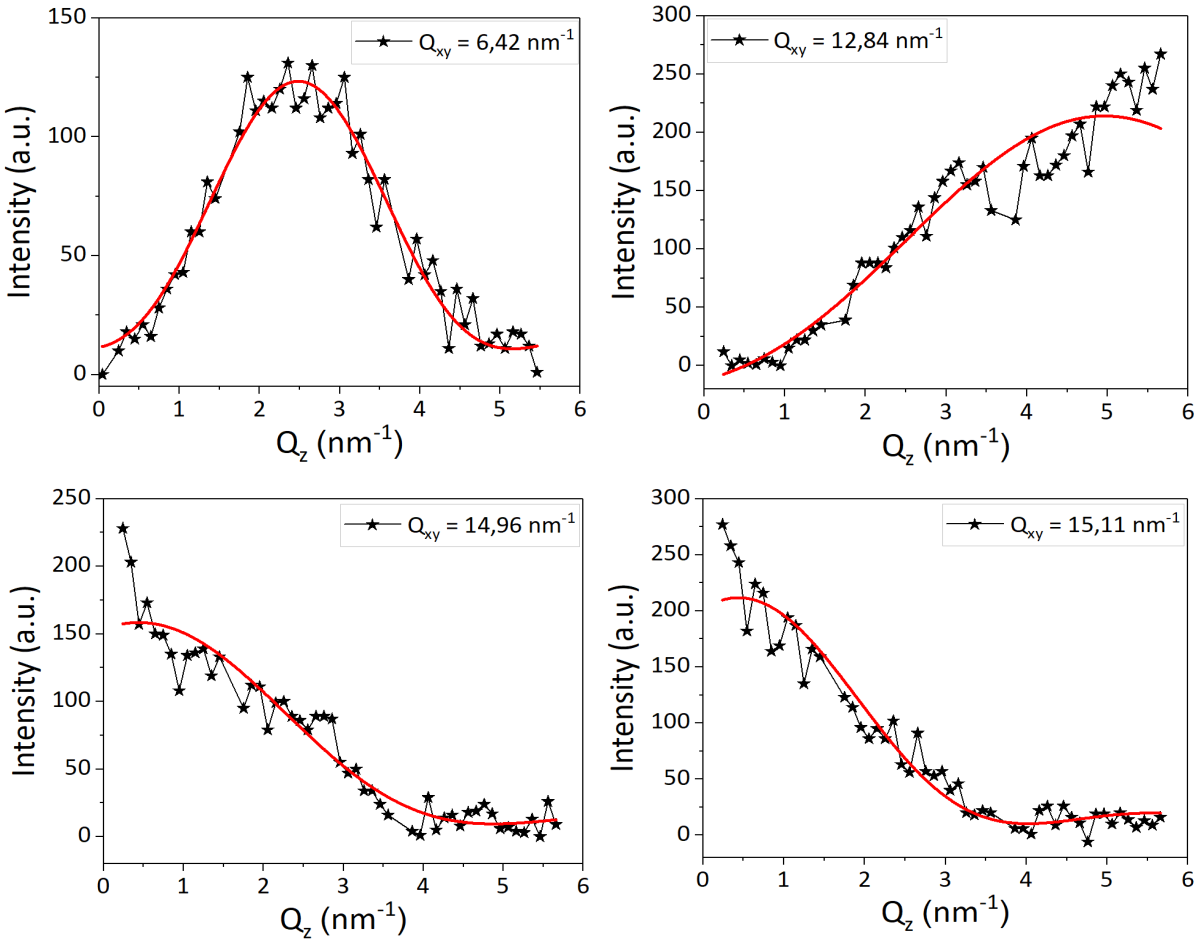

Figure 5.24: "Profile A" of the rodscans of the peaks relative to the organic structure obtained at $\Pi = 20$ mN.m^{-1}.

Depending on the intensity of the oscillations observed in the rodscans, two types of rodscan profiles can be identified. The first one, which we will call “Profile A”, exhibits one strong primary maximum (oscillation) and weak secondary maxima (Figure 5.24).

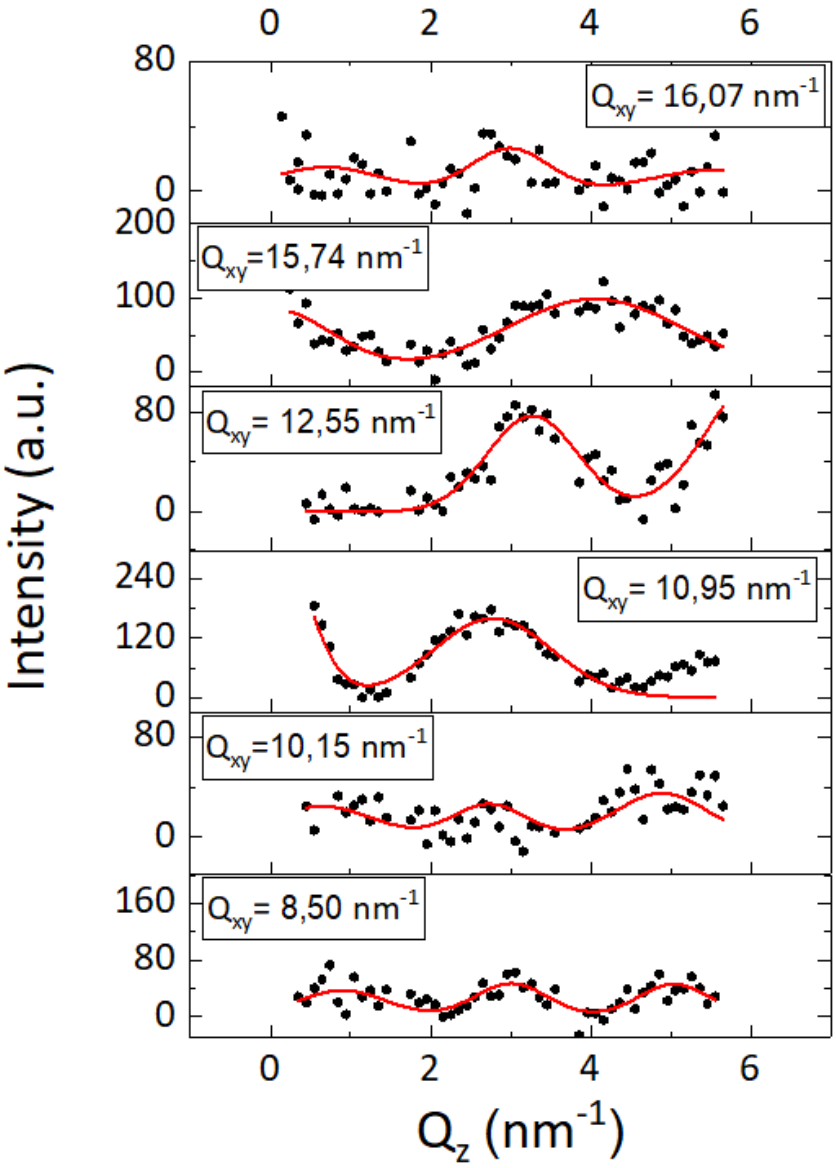

Figure 5.25: "Profile B" of the rodscans of the diffraction peaks relative to the organization of the inorganic structure coexisting with the IL Langmuir film at $\Pi = 20$ mN.m^{-1}.

This profile of rodscans can be adjusted by a square sine cardinal function. The rodscan of the peak centered at $Q_{xy} = 15.11$ nm^{-1}, the one relative to the organization of the alkyl chains of the IL, is of this profile. We therefore suggest to attribute the rodscans of "Profile A" to the organization of the organic layer of IL film. However, according to Tassler et al. [11], Langmuir IL film spread over pure water is not organized before the collapse plateau. Therefore, this organic structure can be purely formed of alkyl chains and Imidazolium rings, organized due to the presence of surface charges. It may also include anions of gold complexes within it. The adjustment parameters of these rodscans of "Profile A" are gathered in Table 5.5. The peak centered at $Q_{xy} = 6.42$ nm^{-1} is the only one whose rodscan profile is entirely in the range of the resolution of the experiment. It therefore provides the most accurate thickness of the structure which is estimated to be equal to z = 2.53 nm. Its maximum of the intensity is centered at $Q_z = 2.43$ nm^{-1}, which indicates that it is out-of-plane. The diffraction plane are therefore 20° tilted (t) with

respect to the vertical to the interface. The length of the alkyl chains in this structure is calculated as follows : $d = \frac{z}{\cos(t)} = 2.7$ nm, which is in agreement with the length of elongated alkyl chains composed of 20 carbons. The peak centered at $Q_{xy} = 12.84$ nm^{-1} is an harmonic peak of that centered at $Q_{xy} = 6.42$ nm^{-1}. It is possible to index this structure according to a 2D oblique lattice as follows : $Q_{xy}^{[1\,\bar{1}]} = 6.42$ nm^{-1}; $Q_{xy}^{[2\,\bar{2}]} = 12.84$ nm^{-1}; $Q_{xy}^{[0\,2]} = 14.96$ nm^{-1} and $Q_{xy}^{[1\,1]} = 15.11$ nm^{-1}. The parameters of this lattice correspond to : $a_1 = 1.6$ nm; $b_1 = 1.32$ nm; $\gamma = (\vec{a_1}, \vec{b_1}) = 140°$ and its area is $A_1 = a_1 b_1 \sin(140) = 1.35$ nm^2. At $\Pi = 20$ mN.m^{-1}, the molecular area, as measured by the Π-A isotherm is approximately 0.48 nm^2 (see Figure 5.22). The obtained lattice therefore contains about 3 IL molecules.

Q_{xy} (nm^{-1})	Q_z (nm^{-1})	ΔQ_z (nm^{-1})	Peak area (a.u.)	Thickness (nm)	tilt(°)
6.42	2.48	2.66	112	2.53	21
12.84	4.97	5.89	585	1.06	21
14.96	0.44	4.43	149	1.41	0
15.11	0.44	3.58	201	1.75	0

Table 5.5: Adjustment parameters of "Profile A" of the rodscans of the diffraction peaks relative to the organization of the IL Langmuir film layer, at $\Pi = 20$ mN.m^{-1}.

The second rodscan profile lacks the strong primary maximum and the oscillations appear of almost same intensities (Figure 5.25). This profile, which we will call "Profile B", cannot be adjusted by a square sine cardinal function. Their profile consists of periodic oscillations that can be adjusted by Gaussian functions. The adjustment parameters of the rodscans of "Profile B" are gathered in Table 5.6. Q_{xy}, Q_z and ΔQ_z are expressed in (nm^{-1}) and I in (a.u.). These peaks are assigned to an inorganic structure coexisting with the organic structure. They can be indexed in a hexagonal lattice as follows : $Q_{xy}^{[2\,2]} = 8.49$ nm^{-1}; $Q_{xy}^{[2\,3]} = 10.15$ nm^{-1}; $Q_{xy}^{[3\,2]} = 10.95$ nm^{-1}; $Q_{xy}^{[40]} = 12.55$ nm^{-1}; $Q_{xy}^{[5\,0]} = 15.74$ nm^{-1}. The peak centered at $Q_{xy} = 16.07$ nm^{-1} is of low intensity and is not well defined like the others. We will exclude its contribution to the inorganic structure. The parameters of the corresponding cell are : $\gamma = (\vec{a_2}, \vec{b_2}) = 120°$; $a_2 = b_2 = 2\Pi/(a_2^* \sin(120)) = 2.34$ nm and its area is $A_2 = a_2^2 \sin(120) = 4.74$ nm^2. One notices that $a_2 = \frac{3}{2} a_1$, where a_1 is one of the parameters of the organic structure obtained at $\Pi = 20$ mN.m^{-1}. Then, we multiply by 2 the indexation along the direction of $\vec{a_2}$ of the inorganic structure. The peaks become indexed as follows : $Q_{xy}^{[4\,2]} = 8.49$ nm^{-1}; $Q_{xy}^{[4\,3]} = 10.15$ nm^{-1}; $Q_{xy}^{[6\,2]} = 10.95$ nm^{-1}; $Q_{xy}^{[8\,0]} = 12.55$ nm^{-1}; $Q_{xy}^{[10\,0]} = 15.74$ nm^{-1}. The parameter of the inorganic network in the direction of $\vec{a_2}$ is thus 3× the one in the direction of $\vec{a_1}$ of the organic network. This result indicates that the two structures are commensurate in the direction of one axis and form a superlattice.

From the distance peak-to-peak and the FHMW of the oscillations, we have estimated the thickness and periodicity of the inorganic structure and have represented them in Table 5.7.

From the periodicity of the inorganic structures, it is estimated that they are formed

Q_{xy}	Q_{z1}	Q_{z2}	Q_{z3}	ΔQ_{z1}	ΔQ_{z2}	ΔQ_{z3}	I_1	I_2	I_3
8.50	0.9	3	5.04	1.08	0.90	0.88	50	52	50
10.17	0.63	2.73	4.89	1.29	0.90	1.13	40	30	50
10.95	0.9	2.81	-	0.9	1.22	-	385	232	-
12.55	3.30	6.12	-	1.13	1.33	-	108	180	-
15.74	0	4.05	-	1.52	2.21	-	163	272	-
16.07	0.7	2.99	5.52	1.34	0.96	1.54	25	25	25

Table 5.6: Adjustment parameters of "Profile B" of the rodscans of the diffraction peaks relatives to the organization of the inorganic structure in a coexistence with the IL Langmuir film at $\Pi = 20$ mN.m^{-1}.

Q_{xy}	Average ΔQ_z (nm^{-1})	Average peak-to-peak distance d(nm^{-1})	Average thickness of the structure z(nm)*	Average Oscillation period T(nm)**	Number of layers in the structure N***
8.50	0.95	2.07	6.61	3.03	2
10.17	1.10	2.13	5.71	2.94	2
10.95	1.06	1.91	5.92	3.28	2
12.55	1.23	2.82	5.10	2.30	2
15.74	1.86	4.05	3.37	1.55	2
16.07	1.28	2.41	4.91	2.61	2

Table 5.7: Parameters of the inorganic structure formed in a coexistence with of the organic Langmuir film, at $\Pi = 20$ mN.m^{-1} (*z = $\frac{2\Pi}{\Delta Q_z}$; **T = $\frac{2\Pi}{d}$; *** N = $\frac{z}{T}$)

of two layers, each about 2 to 3 nm. This structure is therefore 3D. Its thickness is too great to be purely composed of gold complexes (0.3 nm thick). The thickness of an anion $[NTf_2]^-$ is ~ 0.9 nm. According to the macroscopic study, at this surface pressure, it is assumed that $[NTf_2]^-$ has been replaced by two $[AuCl_4]^-$ at the surface. $[NTf_2]^-$ is then favorable to interact with the gold counter-ion complex, which is in our case $[H]^+$, and for both to form a compound [145]. From this point of view, it is convenient to suggest that $[H]^+[NTf_2]^-$ could have formed an organized network with $[AuCl_4]^-$ in the 3D structure.

Surface X-ray radiolysis

We then attempt to form crystalline gold nanostructures by surface X-ray radiolysis directed by the IL Langmuir film during ~ 8 hour. As a function of irradiation time, the intensity from the diffraction peaks progressively decreases. After 2.5 hours, all the peaks disappear suggesting the degradation of the superstructure. We maintained the irradiation for more 5.5 hours. However, we did not succeed in observing any diffraction peak relative to the formation gold NPs. We did not either observe the gold filament. These results suggest that gold ions could not be reduced. It appears that the organization of gold complexes in networks have prevented their reduction.

We then performed another GIXD on the film at $\Pi = 35$ mN.m^{-1} (after the plateau).Figure 5.26 (a) and Figure 5.26 (b) represent respectively the X-ray diffraction map and the intensity of the diffraction signals integrated over Q_z, obtained at $\Pi = 35$ mN.m^{-1}. 7

diffraction peaks were immediately observed. The peaks are fitted by Lorentzian functions and the adjustment parameters are collected in Table 5.8.

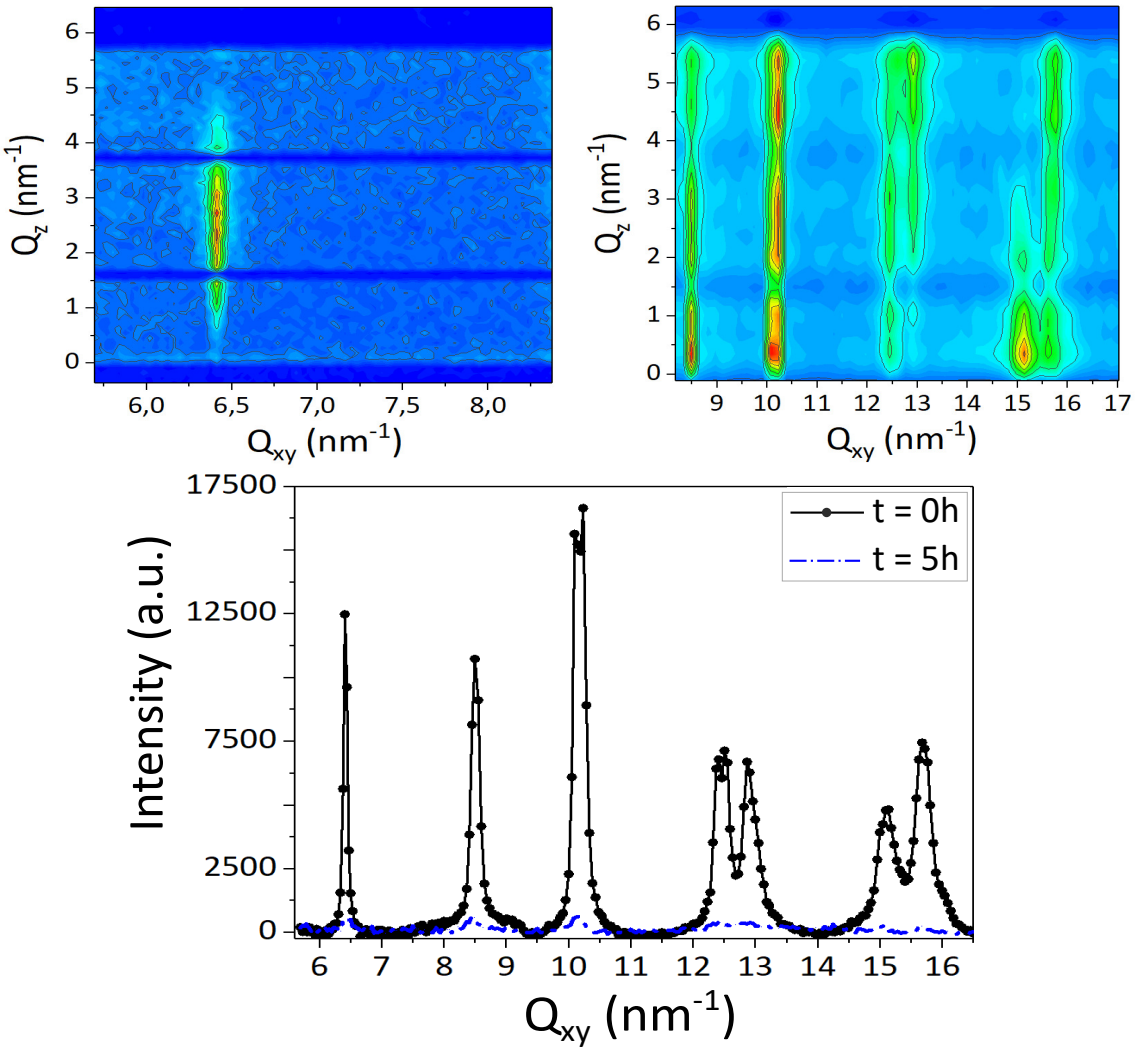

Figure 5.26: The X-ray diffraction (a) map and (b) intensities integrated over Q_z in the horizontal plane of the $[C_{20}mim]^+[NTf_2]^-$ Langmuir film spread over a subphase containing 600 $[AuCl_4]^-$/ IL, at Π = 35 mN.m^{-1}.

According to Tassler et al. [11], GIXD spectrum of $[C_{20}mim]^+[NTf_2]^-$ Langmuir film spread over pure water exhibits 9 diffraction peaks. Only the peak centered at Q_{xy} = 15.11 nm^{-1} is common between the structure obtained on pure water and on the ionic subphase. This peak is relative to the organization of alkyl chains. The correlation length of the structure detected from this peak is 7 nm on water surface and 6 nm on the ionic subphase. The order of the organization of the alkyl chains is therefore the same regardless of the nature of the subphase. The observed 7 diffraction peaks were evidenced as well before the plateau. The rodscans of the peaks are represented in Figure 5.27 and Figure 5.28.

Q_{xy} (nm^{-1})	FWHM ΔQ_{xy}(nm^{-1})	Peak area (a.u.)	correlation length ξ (nm)
6.41	0.064	1004	31
8.50	0.14	1891	14
10.17	0.19	4128	10
12.45	0.23	2099	9
12.91	0.25	1888	8
15.11	0.31	1775	6
15.70	0.28	2498	7

Table 5.8: Adjustment parameters of the diffraction peaks integrated over Q_z of the IL Langmuir film spread over a subphase containing 600 $[AuCl_4]^-$/ IL, at Π = 35 $mN.m^{-1}$.

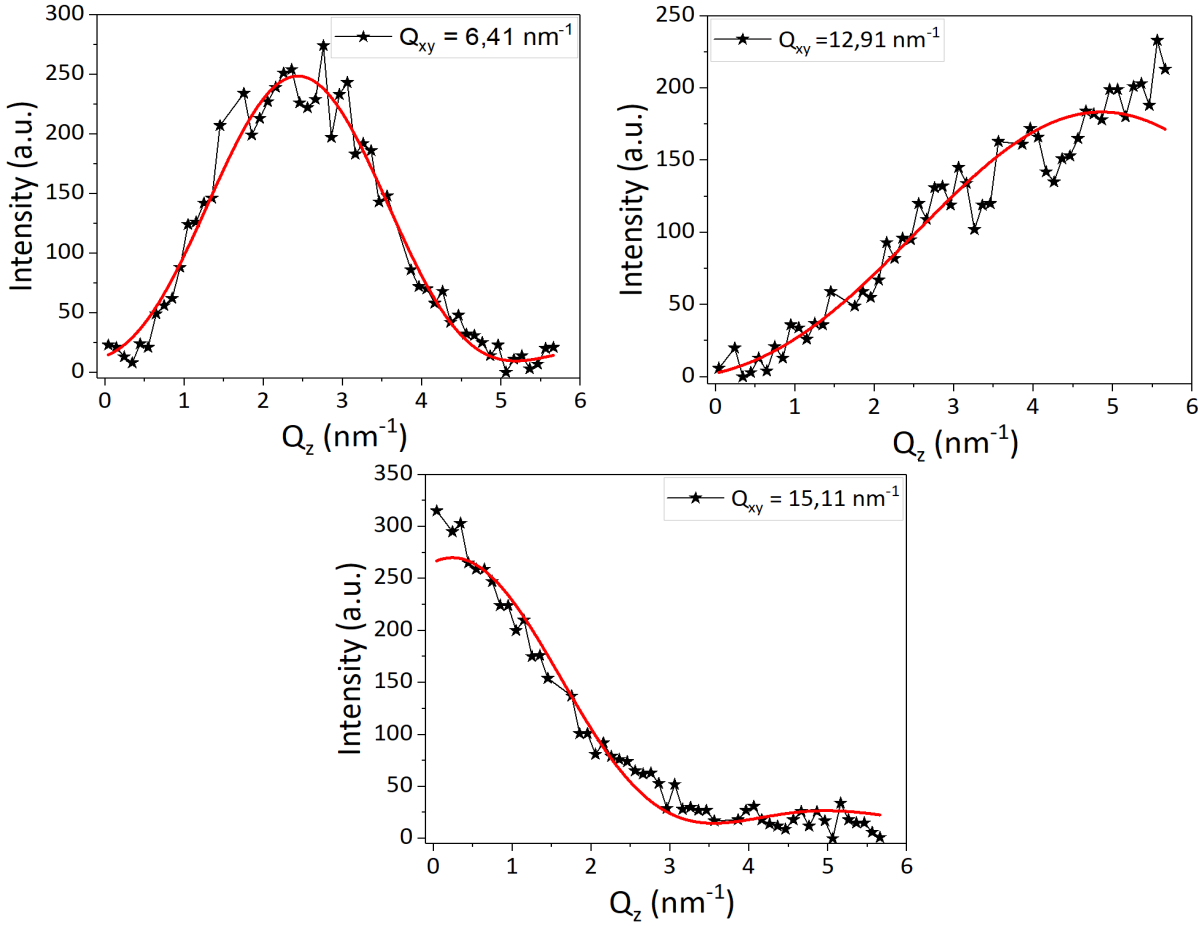

Figure 5.27: "Profile A" of the rodscans of the diffraction peaks relative to the organization of the IL Langmuir film at Π = 35 $mN.m^{-1}$.

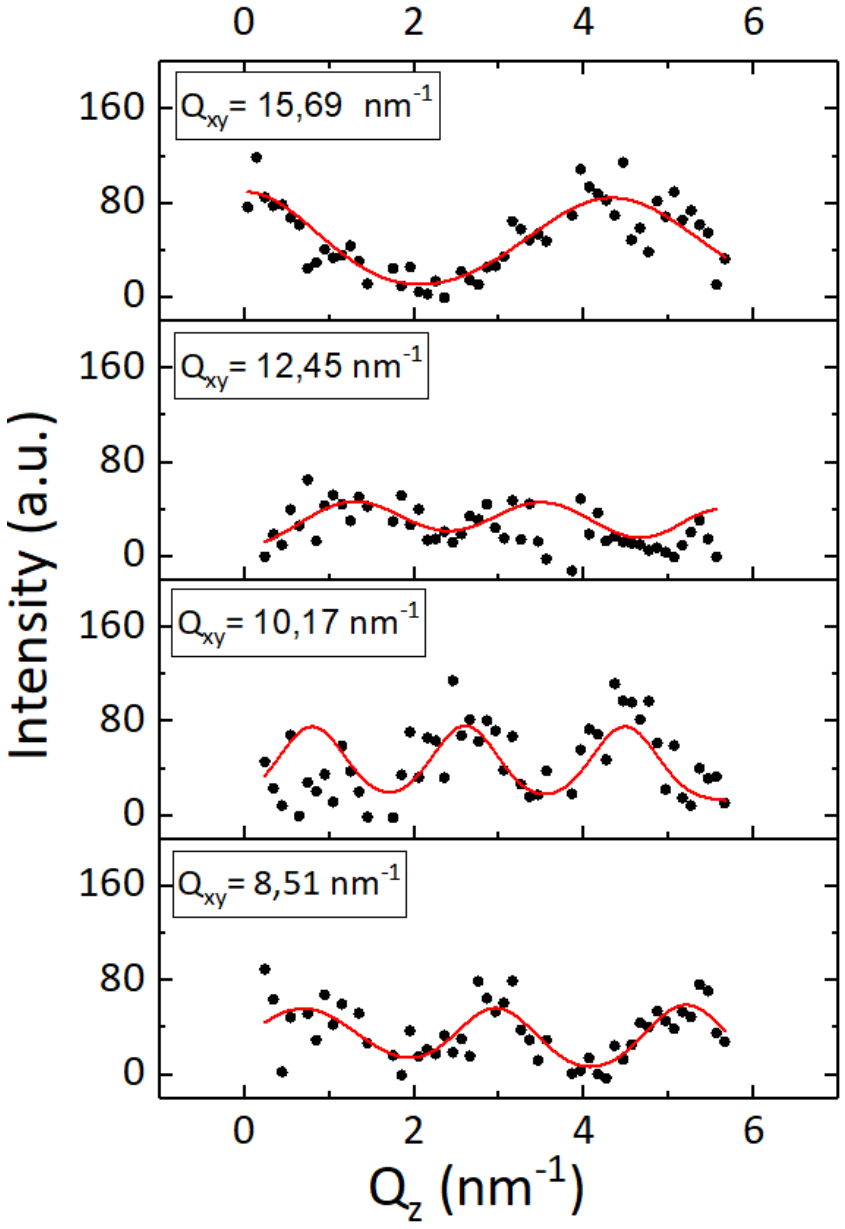

Figure 5.28: "Profile B" of the rodscans of the diffraction peaks relative to the organization of the inorganic structure coexisting with the IL Langmuir film at $\Pi = 35$ mN.m^{-1}.

Here again, it is possible to identify two profiles, "Profile A" (Figure 5.27) and "Profile B" (Figure 5.28) from the rodscan study as it was the case before the plateau. The rodscan of the peak, centered at $Q_{xy} = 15.11$ nm^{-1}, which is attributed to the organization of alkyl chains is of "Profile A". We therefore suggest to attribute the rodscans of "Profile A" (Figure 5.27) to the organization of the organic layer of IL film. These peaks are adjusted by a square sine cardinal function and the adjustment parameters are collected in Table 5.9. This organic structure can be purely formed of alkyl chains and Imidazolium rings, organized due to the presence of surface charges. It may also include anions of gold complexes within it. Here again, we are going to estimate the thickness of the structure from the rodscan of the peak centered at $Q_{xy} = 6.41$ nm^{-1}. One obtains z = 2.75 nm. The maximum of the intensity of this peak is located at $Q_z = 2.43$ nm^{-1}, which indicates that it is out-of-plane. The structure is therefore 21° tilted with respect to the vertical of the interface. The estimated length of the alkyl chains of this structure is about ~ 2.94 nm, which are in the range of the length of elongated alkyl chains composed of 20 carbon atoms. The peak centered at $Q_{xy} = 12.91$ nm^{-1} is an harmonic peak of that centered at $Q_{xy} = 6.41$ nm^{-1}. It is possible to index this structure according to a 2D rectangular lattice composed of 2 molecules as follows : $Q_{xy}^{[0\,1]} = 6.42$ nm^{-1}; $Q_{xy}^{[0\,2]} = 12.91$ nm^{-1} and the double degenerate peak (11) and $(1\bar{1})$ centered at $Q_{xy} = 15.11$ nm^{-1}. The parameter of this lattice correspond to : $\gamma = (\vec{a_1}, \vec{b_1}) = 90°$; $a_1 = 0.46$ nm; $b_1 = 0.97$ nm and its area is $A_1 = 0.44$ nm^2. The molecular area is therefore 0.22 nm^2 which is in the range of the cross section of an alkyl chain (~ 0.18 nm^2). Furthermore, at $\Pi = 35$ mN.$^{-1}$, the molecular area, as measured by the Π-A isotherm is approximately 0.2 nm^2 (see Figure 5.22), which is in agreement with GIXD measurements.

Q_{xy} (nm^{-1})	Q_z (nm^{-1})	ΔQ_z (nm^{-1})	Peak area (a.u.)	Thickness (nm)	tilt(°)
6.41	2.43	2.75	239	2.28	21
12.91	4.86	5.55	175	1.14	21
15.11	0.04	3.65	266	1.72	0

Table 5.9: Adjustment parameters of "Profile A" of the rodscans of the diffraction peaks relative to the organization of the IL Langmuir film obtained at $\Pi = 35$ mN.m^{-1}.

The second ones are of "Profile B" (Figure 5.28) and are assumed to be attributed to the inorganic structure that is formed in a coexistence with the IL Langmuir film. Their profile consists of periodic oscillations that can be adjusted by Gaussian functions. The adjustment parameters are collected in Table 5.10. These peaks are assigned to an inorganic structure coexisting with the organic structure, assumed to be the same as the one observed before the plateau. It is indexed according to a hexagonal lattice as follows: $Q_{xy}^{[2\,2]} = 8.50$ nm^{-1}; $Q_{xy}^{[2\,3]} = 10.17$ nm^{-1}; $Q_{xy}^{[4\,0]} = 12.45$ nm^{-1}; $Q_{xy}^{[5\,0]} = 15.74$ nm^{-1}. The parameters of the corresponding cell are : γ=($\vec{a}$,$\vec{b}$) = 120°; $a_2 = b_2 = 2\Pi/(a_2^* \sin(\gamma)) = 2.34$ nm and its area is $A_1 = 4.74$ nm^2. one notices that $a_2 = 5a_1$, where a_1 is one of the parameter of the organic structure obtained at $\Pi = 35$ mN.m^{-1}. This result indicates that the organic and inorganic structures are commensurate along the direction of $\vec{a_1}$ and thus form a superlattice.

Q_{xy}	Q_{z1}	Q_{z2}	Q_{z3}	ΔQ_{z1}	ΔQ_{z2}	ΔQ_{z3}	I_1	I_2	I_3
8.50	0.69	2.96	5.20	1.31	0.95	0.95	92	678	70
10.17	0.8	2.60	4.48	0.76	0.75	0.80	60	60	60
12.45	1.29	3.50	5.6	1.3	1.3	1	76	75	50
15.70	0	4.33	-	1.73	1.97	-	195	210	-

Table 5.10: Adjustment parameters of "Profile B" of the rodscans of the diffraction peaks relatives to the inorganic structure coexisting with the IL film at $\Pi = 35$ mN.m^{-1}.

From the distance peak-to-peak and the FHMW of the oscillations (Figure 5.28), the thickness and periodicity of the inorganic structure are estimated and gathered in Table 5.11.

Q_{xy}	Average ΔQ_z (nm^{-1})	Average peak-to-peak distance d (nm^{-1})	Average thickness of the structure z(nm)*	Average Oscillation period T(nm)**	Number of layers in the structure***
8.50	1.07	2.25	5.87	2.79	2
10.17	0.77	1.84	8.15	3.41	2
12.45	1.20	2.15	5.23	2.92	2
15.70	1.85	4.33	3.39	1.45	2

Table 5.11: Parameters of the inorganic structure coexisting with the IL Langmuir film, at $\Pi = 35$ mN.m^{-1} (*z = $\frac{2\Pi}{\Delta Q_z}$; **T = $\frac{2\Pi}{d}$; *** N = $\frac{z}{T}$)

From the periodicity of the inorganic structures, it is estimated that they are formed of two layers, each about 2 to 3 nm. This structure is therefore 3D. Its thickness is too great to be purely composed of gold complexes (0.3 nm thick). It is expected to be formed of $[H]^+[NTf_2]^-$ and $[AuCl_4]^-$ as it was the situation before the plateau.

Surface X-ray radiolysis

In an attempt to form crystalline gold nanostructures by surface X-ray radiolysis directed by the IL Langmuir film, the film was irradiated for ~ 8 hours. As a function of irradiation time, the intensities of the peaks decrease. After 2 hours of irradiation, the structures degrade completely. We did not succeed to observe any diffraction peak relative to the formation of gold crystalline nanostructures. We did not observe the gold filament as the one observed on the subphase containing 30 $[AuCl_4]^-$/ IL. One suggests that the organization of the inorganic structure in a coexisting with the organic structure may have prevented the gold ions from being reduced and coalescing into crystalline nanostructures.

XRF measurements

We also followed by XRF measurements the evolution of the fluorescence intensity of gold and chloride as showed in Figure 5.29. The peaks K_β of chloride and M_α of gold were adjusted by Gaussian functions along the irradiation. The intensity of these peaks were then normalized by that of the elastic peak. The normalized intensities are proportional

to the concentration of chloride and gold that are present in the irradiated volume which is close to the surface.

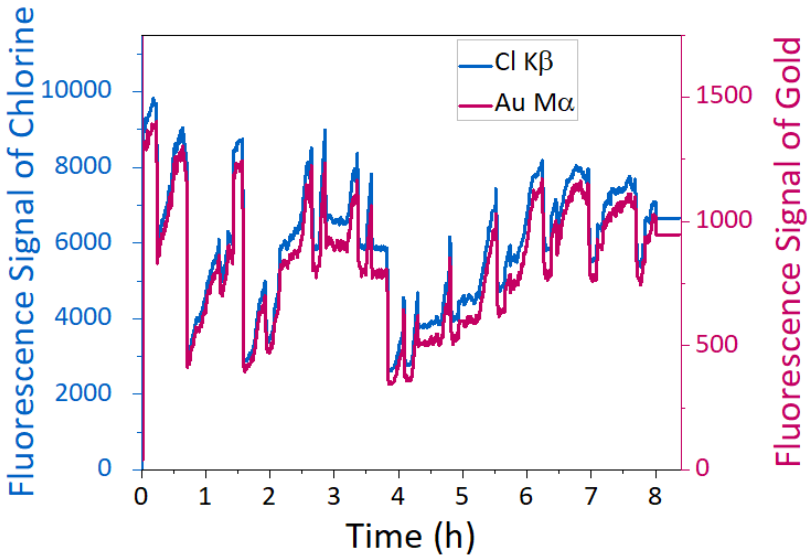

Figure 5.29: Evolution of the fluorescence intensity of gold and chloride as a function of the irradiation time.

We observe quasi-periodic fluctuations in the fluorescence intensities of gold and chloride over time. They are probably due to electronic problems and have no significance related to our measurement. After 8 hours of irradiation, the fluorescence intensity of gold decreases from 1300 a.u. to 950 a.u. and that of chloride from 9000 a.u. to 6000 a.u.. The intensities thus lose about 30% of their value after 8 hours of irradiation. In general, due to the evaporation of water's subphase during long measurements, it is required to constantly adjust the vertical position of the incident beam. This is done by moving the trough vertically until it is ensured that the detector detects the entire beam scattered by the irradiated surface of the trough. This process would allow the X-rays to penetrate the volume of the subphase and could induce the reduction of gold ions present on the surface as well as in the volume of the subphase. Consequently, unwanted crystalline gold nanostructures not directed and controlled by the IL Langmuir film would be formed. We therefore avoided performing height adjustment of the trough during this measurement. However, evaporation of water is unavoidable after 8 hours of irradiation. Consequently, the number of photons detected after 8 hours will be lower than at the beginning of the measurement. We therefore suggest that the 30% decrease in fluorescence intensity is due to the decrease in the number of photons detected after 8 hours of irradiation. However, although the fluorescence intensities of gold and chloride decrease over time, they evolve in an analogous manner. This indicates that the evolution of the concentration of gold on the surface follows the same one as that of $[AuCl_4]^-$. In contrast, the reduction of gold ions would be evidenced by a steady increase of the fluorescence intensity of gold without an increase of that of chloride.

Based on these results, we deduce that gold ions were not reduced by surface X-ray radiolysis. This is in agreement with the GIXD measurements which suggested that no crystalline gold nanostructures were formed. In order to confirm our hypotheses, we

studied the film transferred after 8 hours of irradiation on solid substrates by AFM.

5.3.4 Transfer on solid substrates after irradiation

After 8 hours of irradiation, we transferred the film by Inverse Langmuir-Schaefer procedure on a Si/SiO_2 wafer and studied it by AFM measurements. They wafers were cleaned with Piranha so the surface was hydrophilic.

Figure 5.30 (a) shows the AFM topographic image and Figure 5.30 (b) the AFM phase image of the film. We observe layers of 4.6 nm thick. We also observe poly-dispersed aggregation about tens of nanometer. They are phase shifted in about 10° with respect to the layers which indicates that they are of different nature. The thickness of the layers suggest that they may be attributed to the IL. The aggregation are therefore most probably relative to gold or to a gold/IL mixture. No NPs are observed on these images. One can thus confirm that gold ions were not reduced and did not form gold NPs.

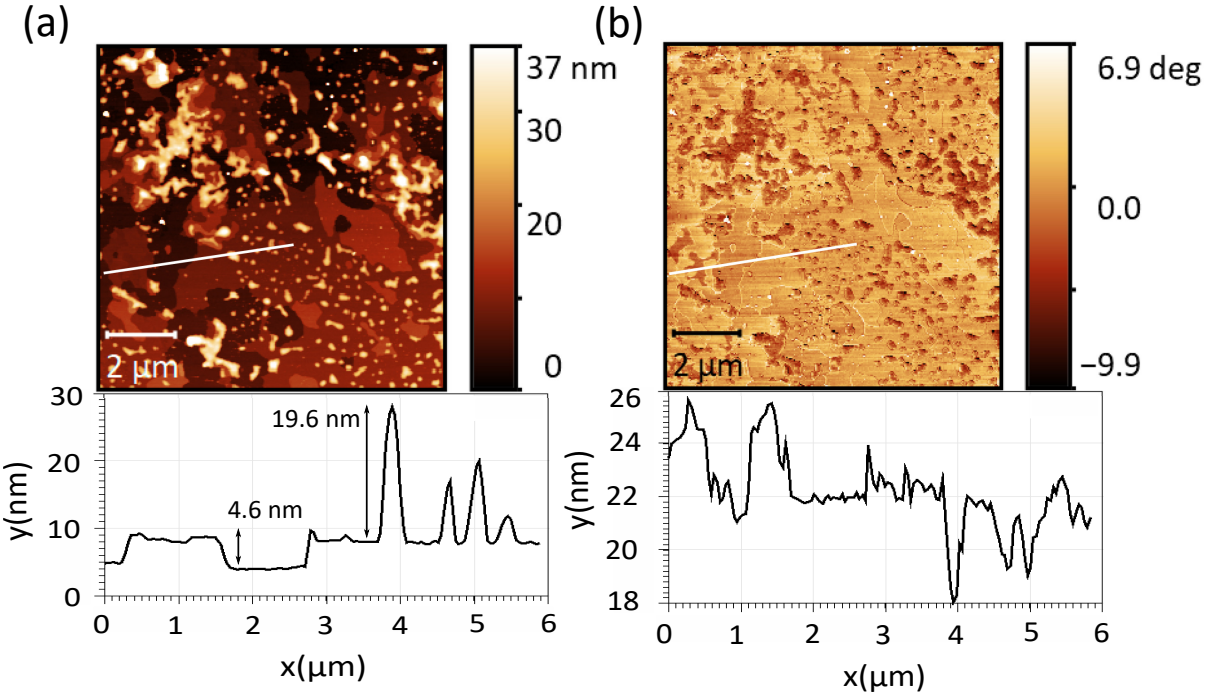

Figure 5.30: AFM topographic (a) and phase (b) image measured on $[C_{20}mim]^+[NTf_2]^-$ Langmuir films spread over a subphase containing 600 $[AuCl_4]^-$/IL transferred by Langmuir-Blodgett on Si/SiO_2 wafers at $\Pi = 35$ mN.m^{-1} after 8 hours of irradiation.

5.4 Discussion

We have shown that for a concentration corresponding to 600 $[AuCl_4]^-$/IL, an inorganic/organic superlattice form. The inorganic structure is assumed to be composed of $[AuCl_4]^-$ and $[H]^+[NTf_2]^-$, coexisting with the IL Langmuir film. We could not witness the superlattice when the subphases contained 30 $[AuCl_4]^-$/IL, suggesting that there is a concentration threshold to its appearance. The main difference in the macroscopic behavior of films as a function of gold concentration lies in the substitution of $[NTf_2]^-$ by

$[AuCl_4]^-$ in the IL film, only when the concentration of 600 $[AuCl_4]^-$/IL. It is suggested that this particular phenomenon could be the reason for the appearance of the superlattice, when the subphase contains 600 $[AuCl_4]^-$/IL.

Furthermore, at 600 $[AuCl_4]^-$/IL, surface X-ray radiolysis could not lead to the reduction of gold ions. Though this procedure is commonly used to reduce ions and has been shown to lead to the formation of gold NPs at 30 $[AuCl_4]^-$/IL. It appears as if the organization of the inorganic structure prevents the ions from being reduced. In other words, the interaction of $[AuCl_4]^-$, whether with $[NTf_2]^-$ or Imidazolium rings, is strong enough to capture $[AuCl_4]^-$, maintain the interaction with them and prevent them from being reduced.

5.5 Conclusion

At a low concentration of gold ions $r_{AuCl_4^-/IL} = 30$, the IL Langmuir film behaves in a way close to that spread on pure water. The adsorption of gold ions on the surface prevents the 3D organization of the film and organize it in a 2D network. Surface X-ray radiolysis of this system leads to the formation of about 15 nm gold NPs.

At a high concentration of gold ions $r_{AuCl_4^-/IL} = 600$, the IL Langmuir film behaves drastically and differently from that spread on pure water. It is suggested that a substitution of $[NTf_2]^-$ by $[AuCl_4]^-$ in the IL film must have taken place. Consequently, an inorganic/organic superstructure appears and the gold ion concentration is assumed to have exceeded a certain threshold. The organic and inorganic structures are commensurate along one direction. The formation of the superlattice prevents the gold ions from being reduced by surface X-ray radiolysis. Therefore, no gold crystalline nanostructure could be detected even after 8 hours of irradiation.

5.6 Perspective

Determining the concentration threshold for the formation of the inorganic structure coexisting with IL molecules could be a way to better understand the conditions governing its formation. It is done by gradually modifying the concentration of the subphase until the isotherm starts to behave drastically and differently.

It would be interesting to study the IL Langmuir film deposited on the subphases that contain metal cations. As IL molecule is formed by a cation and an anion, the adsorption of cations on the surface may induce phenomena different from those obtained following the adsorption of anions.

Discussion

One of the objectives of this thesis was to establish a general description of the behavior of IL molecules at the interface of GO sheets. This would allow a better understanding of the physico-chemical conditions for optimizing the surface interaction between the electrode (GO or graphene) and the electrolyte (IL) of supercapacitors. Initially, the hypothesis that was put forward was based on theoretical and simulation studies. It proposed that IL molecules, at the interface with GO sheets, form in a stack of layers. The layer adsorbed to GO sheets was proposed to be formed of lying parallel IL molecules. In fact, pure alkyl chains prefer to lie parallel to graphene sheets and Imidazolium rings via $\Pi - \Pi$ interactions with graphene also prefer to lie parallel to the sheets. The outermost layer of the stack was proposed to be formed of tilted or perpendicular IL molecules. It was also suggested that the orientation of alkyl chains should follow that of Imidazolium rings. To explore the hypothesis, we resorted to Langmuir procedure to elaborate such an interface and to XRR and GIXD measurements to investigate it at the air-water interface. The GO/IL interface was as well characterized by AFM measurement on solid substrates. The GO/IL Langmuir film was elaborated using a mixture of $[C_{20}mim]^+[NTf_2]^-$ (IL) and GO sheets dissolved in NMP, a non volatile and water-miscible solvent.

The macroscopic study showed that the mixed film was formed, at the air-water interface, by a stack of two main layers : L_1, the layer in contact with water and L_2, the layer in contact with air. The configuration of L_1 and L_2 depended on the surface pressures of the film, whether it is in the region preceding or following a phase transition plateau at $\Pi_{plateau}$ = 12.5 mN.m^{-1}. XRR and AFM measurements showed that before the plateau, L_1 was occupied by tilted IL molecules and a modest presence of NMP and L_2 by GO sheets covered with lying parallel IL molecules. Through the plateau, some of the IL molecules migrated from L_1 to the top of the IL molecules lying parallel to GO sheets in L_2. According to GIXD measurements, the migrated IL molecules to L_2 got organized,almost perpendicular, in a rectangular lattice. Based on these results, we proposed a model to describe the stacking configuration before the plateau ($\Pi < \Pi_{plateau}$ = 12.5 mN.m^{-1}) in Figure 5.31 (left) and another one after the plateau ($\Pi > \Pi_{plateau}$ = 12.5 mN.m^{-1}) in Figure 5.31 (right) .

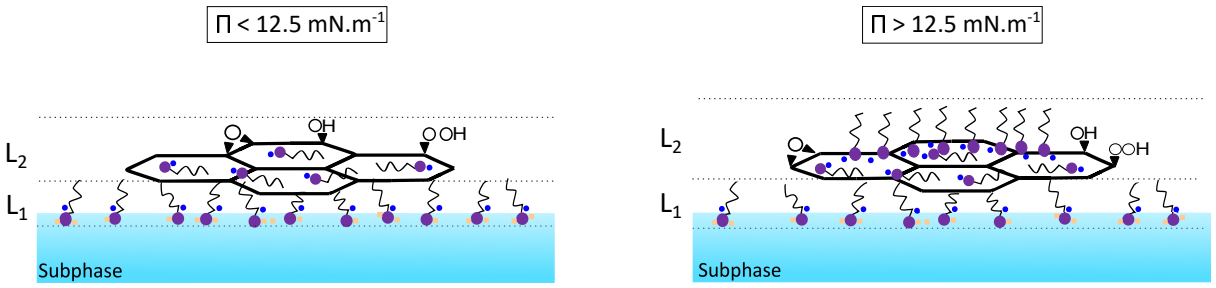

Figure 5.31: Models describing the stacking (to left) at $\Pi < 12.5$ mN.m^{-1} and (to right) at $\Pi > 12.5$ mN.m^{-1}.

The measurements show that the orientation of the IL molecules in the adsorbed layer to the GO surface in L_1, differs from that in L_2 : the molecules are tilted to GO sheets in L_1 but are lying parallel to them in L_2. This indicates that there is no lying parallel IL molecules in the layer adsorbed to the GO sheets in L_1 as is the case in L_2 and as initially proposed. The difference between the two layers lies in the environment surrounding the IL. In L_1, they are at the water interface on the one hand and at the GO interface on the other hand. However, in L_2, they are at the air interface on the one hand and at the GO interface on the other hand. It appears that the interaction between Imidazolium rings and water in L_1 is stronger than the Π-Π interaction between Imidazolium rings and GO sheets. In addition, although alkyl chains prefer to lie parallel to carbon planes, their orientation on GO sheets, when IL molecules are on the water surface, is not parallel. Based on these results, it can be confirmed that the orientation of the alkyl chains on GO sheets depends on the interaction between Imidazolium rings and GO sheets. Therefore, it can be stated that the interaction between IL molecules and GO sheets at their interface is determined by the interaction of the Imidazolium rings with the second interface (air, water....). These findings shed light on the role of the interface at which the IL molecules are located (air, water....) in determining their orientation at the interface with the GO sheets. It thus provides new insights into the interaction between the electrode (GO or graphene) and the electrolyte (IL) of supercapacitors. The measurements also indicate that the outermost layer of the IL stack in L_2, after the plateau, is tilted or perpendicular to GO surface (Figure 5.31 (right)). This result is in agreement with the literature.

The results also underline that GO sheets in the stack prefer to be in contact with the alkyl chains rather than water. Recall that the amphiphilicity of GO sheets depend on their sizes. Given that the studied GO sheets are of different size, it is assumed that some drown in the subphase and that some, which have an amphiphilic balance, remain adsorbed on the surface. Since the alkyl chains are hydrophobic, the remaining GO sheets, even though amphiphilic, might tend to be hydrophobic.

We also observed that the solvent (NMP) remains adsorbed in a modest quantity on the water surface. According to the literature, GO sheets dispersed in aqueous solutions are negatively charged at their edges due to the deprotonation of the carboxylic acid into -COO^- [96]. Our measurements were performed on water surface and GO sheets initially came from a water dispersion. GO sheets in the mixed film are thus supposed to be negatively charged at their edges. The interaction between IL and GO sheets in aqueous medium thus considers to take place between the cation of IL and -COO^- decorating GO edges. Our results showed that IL molecules managed to go beyond the edges of the GO

sheets and reach their basal planes. This interaction between IL and GO appears to be similar to that between IL and graphene based on the MDS studies [2, 3, 4]. We suggest that a charge screening may have permit the IL molecules not to be trapped by the electrostatic interaction with the edges of GO sheets. Since NMP is a neutral compound, it might have acted as the charge screening agent.

Based on the literature, the introduction of gold nanoparticles (NPs) between the electrode and the electrolyte of supercapacitors enhances their energy storage. Hence, the other objective of this thesis was to study the $[C_{20}mim]^+[NTf_2]^-$ Langmuir films deposited on aqueous subphases containing $[H]^+[AuCl_4]^-$. Then, we aimed to irradiate them by grazing incidence X-rays to reduce gold ions by surface radiolysis and form gold nanostructures directed by the IL films which acts as templates. Two concentrations of gold ions were investigated.

For a concentration of 30 gold ions per IL, the IL Langmuir film behaved in a way close to that spread on pure water. It collapsed from a monolayer to a multilayer through a plateau at $\Pi = 18.5$ mN.m^{-1}. The adsorption of gold ions on the surface prevented the 3D organization of the film and organized it in a 2D hexagonal network. Surface X-ray radiolysis performed on this system led to the formation of $\sim$ 15 nm gold NPs. For a concentration of 600 gold ions per IL, the IL Langmuir film behaved drastically and differently from that obtained on pure water. An anion substitution between the gold anionic complex $[AuCl_4]^-$ and the IL anion $[NTf_2]^-$ might have took place on the surface. Before and after a phase transition plateau observed at $\Pi = 26$ mN.m^{-1}, a superstructure along one direction appeared. It consisted of an inorganic structure formed underneath of an organic structure. The organic one was formed of the alkyl chains of the IL molecules. However, since anion substitution might have occurred in the Langmuir film, it is possible that the organic structure might also include gold ions, whose presence cannot be detected by GIXD. The inorganic structure was formed of $[AuCl_4]^-$ and probably $[H]^+$ and $[NTf_2]^-$. Before the plateau, the organic structure was organized in a 2D oblique lattice composed of 3 molecules. The inorganic one was composed of a 3D stack of 2D hexagonal networks. After the plateau, the inorganic structure kept the same organization as before the plateau, while the organic became organized in a rectangular lattice composed of 2 IL molecules. The performance of surface X-ray radiolysis on such a system could not lead to the reduction and the formation of gold nanostructures (NPs...) controlled by the IL film.

These results indicate that the formation of the superstructure is controlled by the concentration of gold ions in the subphase. Thus, there must be a certain threshold of concentration for its appearance. An important question associated with this result is what are the physico-chemical conditions that govern its attainment? It is not yet clear, but we speculate that the presence of $[NTf_2]^-$ at the surface might have reduced the solubility of gold ions in the water near the surface. In such a case, the threshold concentration could correspond to the limit of solubility of gold ions in the water near the surface. Another question also arises : why did the formation of the superstructure prevent surface X-ray radiolysis from forming gold NPs? In other terms, why the solvated electrons (one of the yields of radiolysis) could not reduce gold ions? We speculate that the anion substitution in the IL Langmuir film might have induced an electrostatic interaction between $[AuCl_4]^-$ and $[C_{20}mim]^+$. Consequently, gold ions that might exist in the organic

structure could not be free in the water near the surface. In addition, in the 3D structure, gold ions are arranged in a crystalline network and therefore are not free in the water near the surface. Hence, the engagement of gold in an interaction in the organic network or in the inorganic 3D crystal could have prevented them from being reduced by the solvated electrons. This might explain the failure of surface X-ray radiolysis in forming gold NPs. However, without at least determining the concentration threshold, it is not possible to confirm this speculation.

Conclusions and perspectives

In this work, we first sought to study IL ($[C_{20}mim]^+[NTf_2]^-$) Langmuir films mixed with GO sheets, and then to study IL Langmuir pure films deposited on gold ionic subphases, irradiated by grazing incidence X-rays. This research aimed to generalize our understanding of the behavior of IL molecules at the GO interface. Furthermore, it aimed at forming gold nanostructures, directed by the IL film, by surface X-ray radiolysis. The objective here is to understand the interaction between the electrode (graphene or GO) and the electrolyte (IL) of supercapacitors in order to improve their performance. The experimental techniques involved in the studies at the air-water interface are Π-A measurements, BAM, XRR, GIXD and XRF. The films were also investigated on solid substrates by AFM.

Langmuir mixed film of IL molecules and GO sheets was investigated at the air-water interface and on silicon wafers. The mixed film was prepared using a non volatile and water-miscible solvent (NMP). According to our measurements, the mixed film was formed by a stack of two layers at the air-water interface. The layer in contact with water, L_1, was occupied by IL tilted molecules and NMP. The layer in contact with air, L_2, was occupied by GO sheets covered with lying parallel IL molecules. Through a phase transition plateau observed at $\Pi_{plateau} = 12.5$ mN.m^{-1}, some of the IL molecules migrated from L_1 to the top of the IL molecules lying parallel to GO sheets in L_2. According to GIXD measurements, the transited IL molecules got organized almost perpendicular in a rectangular lattice of the following parameters: a = 5.21 Å and b = 9.05 Å and a molecular area A = 23.5 Å^2. Their alkyl chains were 7% tilted towards the next nearest neighbor (NNN). The lattice included 2 IL molecules. The configurations of the layers was described in Figure 5.31.

Here, three conclusions can be drawn :

1. Although alkyl chains tend to lie parallel to carbon planes, their orientation on GO sheets depends on the orientation of Imidazolium rings. When IL molecules are between water surface and GO sheets, the interaction of Imidazolium rings with water is stronger than the $\Pi - \Pi$ interaction with GO sheets. In such a case, Imidazolium rings prefer to be in water rather than to lie parallel to GO sheets. As a result, the alkyl chains prefer to be tilted towards GO surface rather than to lie parallel to it. However, when IL are between GO sheets and air, the interaction of Imidazolium rings with GO sheets is stronger than that with air. As a result, the Imidazolium rings as well as the alkyl chains lie parallel to GO sheets.

2. This study contributes to our understanding of the interaction of IL molecules, located at a certain interface (air, water....), with GO sheets. The findings state that the behavior of IL molecules at the interface with GO sheets is driven by

interaction of the Imidazolium rings with the second interface (air, water....). It is therefore not possible to generalize the type of interaction to describe the orientation of the IL molecules on the surface of GO sheets.

3. The remained adsorbed GO sheets, even though amphiphilic, tend to be hydrophobic as they prefer to interact with the alkyl chains rather than with water.

This research clearly illustrates that the interaction between IL molecules and GO sheets is not unique and general. It depends on the nature of the interface on which the IL molecules are located (water, air...). This raises the question of how changing the nature of the environments surrounding the electrolyte (IL) in supercapacitors can improve their energy storage density .
The amount of IL molecules used in the mixed films was a bit critical because it saturated the surface of the trough from the beginning of the measurements. On the other hand, the amount of GO sheets in the mixed films was only 26% of the surface occupied by IL molecules. From this perspective, it is crucial to repeat the study using less IL molecules. It is also interesting to vary the concentration ratio between the GO sheets and the IL molecules.
It would be interesting to vary the oxidation degree of GO sheets. This would allow us to verify whether there is a relation between the oxidation degree and the affinity of GO sheets to interact with alkyl chains rather than water.
As the solvent remains adsorbed on the surface of the water, it is necessary to repeat our study using a volatile solvent. This would allow us to test the efficiency of the solvent in the charge screening between the GO edges and the IL molecules.

Then, the IL pure Langmuir film was deposited on gold ionic subphases of different concentrations. We demonstrated that there is a threshold concentration in gold ions above which, an inorganic/organic superstructure forms. Its appearance prevented gold ions from being reduced by surface X-ray radiolysis. However, gold nanoparticles (NPs) $\sim$ 15 nm were formed when the concentration of the subphase was below the concentration threshold.

For a concentration of 30 gold ions per IL, which appeared to be below the concentration threshold, the IL film behaved in a way close to that spread on pure water. The adsorption of gold ions on the surface prevented the 3D organization of the film. At Π = 30 mN.m^{-1} (after the plateau Π = 18.5 mN.m^{-1}), the IL molecules got organized in a 2D hexagonal lattice of the following parameter a = 0.47 nm and a molecular area A = 0.19 nm^2. Surface X-ray radiolysis performed on this system led to the formation of $\sim$ 15 nm gold NPs.
For a concentration of 600 gold ions per IL, which appeared to be above the concentration threshold, the IL Langmuir film behaved drastically and differently from that of pure water. The film underwent a phase transition plateau at Π = 26 mN.m^{-1}.

– Before the plateau, at Π = 20 mN.m^{-1}, GIXD measurements showed 10 diffraction peaks. From the study of their rodscans, it was possible to divide them into two profiles, relative to two structures in a coexistence : an organic structure and an inorganic structure. The organic one was formed of a 2D oblique lattice of the following parameters : a_1 = 1.6 nm; b_1 = 1.32 nm; $\gamma = (\vec{a_1}, \vec{b_1}) = 140°$ and an area $A_1 = a_1 b_1 \sin(140) = 1.35$ nm^2. This lattice included 3 IL molecules. The

inorganic one was formed of a 3D stack of 2D hexagonal networks of the following parameters : γ=($\vec{a_2}$,$\vec{b_2}$) = 120°; $a_2 = b_2 = 2\Pi/(a_2^* \sin(120)) = 2.34$ nm and an area $A_2 = a_2^2 \sin(120) = 4.74$ nm^2. The superstructure was commensurate along one direction.

– After the plateau, at $\Pi = 35$ mN.m^{-1}, GIXD measurements showed 7 diffraction peaks. Here again, it was possible, based on their rodscan's profiles to identify two structures. The peaks relative to the organic structure indicated the organization of a 2D rectangular lattice of the following parameters : $\gamma = (\vec{a_1}, \vec{b_1}) = 90°$; $a_1 = 0.46$ nm; $b_1 = 0.97$ nm and an area $A_1 = 0.44$ nm^2. This lattice included 2 IL molecules. The peaks relative to the inorganic structure indicated the organization of the same 3D stack as before the plateau. Here again, the superstructure was commensurate along one direction.

The organic structures were alkyl chains of IL molecules while the inorganic one was formed of gold anionic complexes $[AuCl_4]^-$ and probably $[H]^+[NTf_2]^-$.

The conditions for exceeding the threshold concentration and thus for the appearance of the superlattice are unclear. We suggest that the presence of $[NTf_2]^-$ at the surface might have reduced the solubility of gold ions in water near the surface. Consequently, gold ions were trapped in a 3D lattice probably with $[NTf_2]^-$. We also suggest that electrostatic interactions between $[AuCl_4]^-$ and $[C_{20}mim]^+$, following anion substitution, might have trapped some gold ions in the IL Langmuir film. Consequently, the solvated electrons could not interact with gold ions near the water surface (neither those of the inorganic structure nor those of the organic structure). This speculation could explain why surface radiolysis could not lead to the formation of gold NPs. To validate or reject this speculation, it is necessary to determine the concentration threshold. It can be done by gradually modifying the concentration of the subphase until the Π-A isotherm starts to behave drastically and differently.
It would also be interesting to study the IL Langmuir film deposited on subphases containing metal cations. As the IL molecule is formed by a cation and an anion, the adsorption of cations on the surface may induce phenomena different from those obtained following the adsorption of anions.

List of Figures

List of Tables

Bibliography

[1] H Helmholtz. "Studien über elektrische Grenzflächen". In: *Ann. Phys. Chem., Neue Folge* 7 (1879), pp. 337–382.

[2] Behnoosh Sadeghi Moghadam et al. "Molecular dynamics simulation of amino acid ionic liquids near a graphene electrode: effects of alkyl side-chain length". In: *Physical Chemistry Chemical Physics* 18.48 (2016), pp. 33053–33067.

[3] Ahmet Uysal et al. "Structural origins of potential dependent hysteresis at the electrified graphene/ionic liquid interface". In: *The Journal of Physical Chemistry C* 118.1 (2014), pp. 569–574.

[4] Sergey A Kislenko, Igor S Samoylov, and Ravil H Amirov. "Molecular dynamics simulation of the electrochemical interface between a graphite surface and the ionic liquid [BMIM][PF 6]". In: *Physical Chemistry Chemical Physics* 11.27 (2009), pp. 5584–5590.

[5] Michael P Down et al. "Fabrication of graphene oxide supercapacitor devices". In: *ACS Applied Energy Materials* 1.2 (2018), pp. 707–714.

[6] Wen Qian et al. "Surfactant-free hybridization of transition metal oxide nanoparticles with conductive graphene for high-performance supercapacitor". In: *Green chemistry* 14.2 (2012), pp. 371–377.

[7] M Sarno and M Casa. "Green and one-step synthesis for Ag/graphene hybrid supercapacitor with remarkable performance". In: *Journal of Physics and Chemistry of Solids* 120 (2018), pp. 241–249.

[8] Gyanaranjan Sahoo et al. "Nano gold decorated reduced graphene oxide wrapped polymethylmethacrylate for supercapacitor applications". In: *RSC advances* 7.4 (2017), pp. 2137–2150.

[9] A Safavi and S Zeinali. "Synthesis of highly stable gold nanoparticles using conventional and geminal ionic liquids". In: *Colloids and Surfaces A: Physicochemical and Engineering Aspects* 362.1-3 (2010), pp. 121–126.

[10] François Muller et al. "Synthesis of Nanostructured Metal- Organic Films: Surface X-ray Radiolysis of Silver Ions Using a Langmuir Monolayer as a Template". In: *Langmuir* 20.12 (2004), pp. 4791–4794.

[11] Stephanie Tassler et al. "Ability to form Langmuir monolayer and bilayer at the air-water-interface of 1-alkyl-3-methylimidazolium ionic liquids". unpublished.

[12] Mandapati Jayalakshmi and K Balasubramanian. "Simple capacitors to supercapacitors-an overview". In: *Int. J. Electrochem. Sci* 3.11 (2008), pp. 1196–1217.

[13] Adam Namisnyk and J Zhu. "A survey of electrochemical super-capacitor technology". In: *Australian Universities Power Engineering Conference*. University of Canterbury, New Zealand. 2003.

[14] Andrew Burke, Zhengmao Liu, and Hengbing Zhao. "Present and future applications of supercapacitors in electric and hybrid vehicles". In: *2014 IEEE International Electric Vehicle Conference (IEVC)*. IEEE. 2014, pp. 1–8.

[15] Paschalis Alexandridis and Bjoern Lindman. *Amphiphilic block copolymers: self-assembly and applications*. Elsevier, 2000.

[16] Zineb Guennouni. "Study of Langmuir films made of diblock copolymer PS-b-PAA and formation of non-organic nanostructures by reduction of silver ions in their vicinity." Theses. Université Pierre et Marie Curie, June 2014. URL: `https://tel.archives-ouvertes.fr/tel-01097435`.

[17] CECILE FRADIN. "Structure et elasticite des interfaces liquides : une etude par diffusion de rayons x sous incidence rasante." PhD thesis. UNIVERSITE PARIS 6, 1999.

[18] Frédéric Dubreuil. "Structure et déformation des films de Langmuir. Application aux copolymèresdiblocs neutres-chargés." PhD thesis. UniversitéPierre et Marie Curie - Paris VI, Apr. 2001. URL: `https://tel.archives-ouvertes.fr/tel-00001306/document`.

[19] Yasuhiro Iwasawa, Noboru Oyama, and Hironobu Kunieda. *Proceedings of the International Conference on Colloid and Surface Science*. Elsevier, 2001.

[20] Joseph E Greene. "Tracing the 4000 year history of organic thin films: From monolayers on liquids to multilayers on solids". In: *Applied physics reviews* 2.1 (2015), p. 011101.

[21] Da-Neng Wang et al. "Benjamin Franklin, Philadelphia's favorite son, was a membrane biophysicist". In: *Biophysical journal* 104.2 (2013), pp. 287–291.

[22] M Elizabeth derrick. "Agnes Pockels, 1862-1935". In: *Journal of Chemical Education* 59.12 (1982), p. 1030.

[23] Vladimir M Kaganer, Helmuth Möhwald, and Pulak Dutta. "Structure and phase transitions in Langmuir monolayers". In: *Reviews of Modern Physics* 71.3 (1999), p. 779.

[24] Eric Saint-Martinl. " Etude de la rigidité de courbure de monocouches de Langmuir en présence d'unpeptide antimicrobien." PhD thesis. UniversitéJoseph-Fourier - Grenoble I, 2007. URL: `https://tel.archives-ouvertes.fr/tel-00157944/document`.

[25] Tian Ma and Shouhong Wang. "DYNAMICAL THEORY OF THERMODYNAMICAL PHASE TRANSITIONS". In: (2017).

[26] AM Bibo, CM Knobler, and IR Peterson. "A monolayer phase miscibility comparison of long-chain fatty acids and their ethyl esters". In: *The Journal of Physical Chemistry* 95.14 (1991), pp. 5591–5599.

[27] IR Peterson et al. "Equivalent states of amphiphilic lamellae". In: *Langmuir* 8.12 (1992), pp. 2995–3002.

[28] Vladimir M Kaganer, Helmuth Möhwald, and Pulak Dutta. "Structure and phase transitions in Langmuir monolayers". In: *Reviews of Modern Physics* 71.3 (1999), p. 779.

[29] VM Kaganer and EB Loginov. "Crystallization phase transitions and phase diagram of Langmuir monolayers". In: *Physical review letters* 71.16 (1993), p. 2599.

[30] MK Durbin et al. "X-ray diffraction study of a recently identified phase transition in fatty acid Langmuir monolayers". In: *The Journal of Physical Chemistry* 98.7 (1994), pp. 1753–1755.

[31] Jens Als-Nielsen et al. "Principles and applications of grazing incidence x-ray and neutron scattering from ordered molecular monolayers at the air-water interface". In: *Physics Reports* 246.5 (1994), p. 254.

[32] Philippe Fontaine et al. "Fast and adjustable-resolution grazing-incidence x-ray liquid surface diffraction". In: *Review of scientific instruments* 75.10 (2004), pp. 3097–3106.

[33] K Kjaer et al. "Synchrotron x-ray diffraction and reflection studies of arachidic acid monolayers at the air-water interface". In: *The Journal of Physical Chemistry* 93.8 (1989), pp. 3200–3206.

[34] Jens Als-Nielsen and Des McMorrow. *Elements of modern X-ray physics*. John Wiley & Sons, 2011.

[35] Samy Remita et al. "X-ray radiolysis induced formation of silver nano-particles: A SAXS and UV–visible absorption spectroscopy study". In: *Nuclear Instruments and Methods in Physics Research Section B: Beam Interactions with Materials and Atoms* 263.2 (2007), pp. 436–440.

[36] Jan Kmetko et al. "The effects of divalent ions on Langmuir monolayer and subphase structure: A grazing-incidence diffraction and Bragg rod study". In: *The Journal of Physical Chemistry B* 105.44 (2001), pp. 10818–10825.

[37] Lisa Bardin. "Monocouches d'alcanes semi-fluorés". PhD thesis. Paris 6, 2010.

[38] Marcio Luis Ferreira Nascimento. "Brief history of X-ray tube patents". In: *World Patent Information* 37 (2014), pp. 48–53.

[39] Nathalie Bonatout. "Etude des films de Langmuir d'oxyde de graphène, de liquides ioniques et des systèmes mixtes". PhD thesis. Nov. 2017.

[40] Claire Laulhé. *Interaction rayons X / Matière -Diffraction des rayons X*. URL: `http://hebergement.u-psud.fr/l3papp/wp-content/uploads/2019/03/Chapitre-V.pdf`.

[41] Philippe Fontaine. "Polymérisation bidimensionnelles dans les couches de la Langmuir: le cas des n-alkyltrialkoxysilanes". PhD thesis. Lille 1, 1995.

[42] Klaus Martin Zimmermann. "Advanced analysis techniques for x-ray reflectivities: Theory and application". In: *Disserta tion* (2005).

[43] Lyman G Parratt. "Surface studies of solids by total reflection of X-rays". In: *Physical review* 95.2 (1954), p. 359.

[44] Frank Schreiber and Alexander Gerlach. "X-ray and neutron reflectivity for the investigation of thin films". In: *Website. www. physchem. ox. ac. uk/fs* (2013).

[45] Florin Abelès. "Recherches sur la propagation des ondes électromagnétiques sinusoıdales dans les milieux stratifiés-Application aux couches minces". In: *Annales de physique*. Vol. 12. 5. EDP Sciences. 1950, pp. 596–640.

[46] Sarah Bartlett. *Crystals for positive manifestation*. Fair Winds Press, 2017.

[47] Dieter Schwarzenbach. "The success story of crystallography". In: *Acta Crystallographica Section A: Foundations of Crystallography* 68.1 (2012), pp. 57–67.

[48] Rudolf Peierls. "Quelques propriétés typiques des corps solides". In: *Annales de l'institut Henri Poincaré*. Vol. 5. 3. 1935, pp. 177–222.

[49] John Michael Kosterlitz and David James Thouless. "Ordering, metastability and phase transitions in two-dimensional systems". In: *Journal of Physics C: Solid State Physics* 6.7 (1973), p. 1181.

[50] Amardeep Bharti and Navdeep Goyal. "Fundamental of Synchrotron Radiations". In: *Synchrotron Radiation*. IntechOpen, 2019.

[51] S Hénon and J Meunier. "Microscope at the Brewster angle: Direct observation of first-order phase transitions in monolayers". In: *Review of Scientific Instruments* 62.4 (1991), pp. 936–939.

[52] Sylvie Hénon. "Microscopie à l'angle de Brewster: transitions de phases et défauts d'orientation dans des films monomoléculairess". PhD thesis. Université Pierre et Marie Curie-Paris VI, 1993.

[53] Gerd Binnig, Calvin F Quate, and Ch Gerber. "Atomic force microscope". In: *Physical review letters* 56.9 (1986), p. 930.

[54] Bruker. *bruker AFM's probe*. URL: `https://www.brukerafmprobes.com/p-3884-ddesp-v2.aspx`.

[55] James L Dye. "The alkali metals: 200 years of surprises". In: *Philosophical Transactions of the Royal Society A: Mathematical, Physical and Engineering Sciences* 373.2037 (2015), p. 20140174.

[56] Paul Walden. "Molecular weights and electrical conductivity of several fused salts". In: *Bull. Acad. Imper. Sci.(St. Petersburg)* 1800 (1914).

[57] Filippo Ferdeghini. "Liquides ioniques sous confinement nanométrique unidimensionnel". PhD thesis. Paris 6, 2015.

[58] Sven Herrmann. *New synthetic routes to polyoxometalate containing ionic liquids: an investigation of their properties*. Springer, 2015.

[59] John S Wilkes. "A short history of ionic liquids—from molten salts to neoteric solvents". In: *Green Chemistry* 4.2 (2002), pp. 73–80.

[60] Michael E Van Valkenburg et al. "Thermochemistry of ionic liquid heat-transfer fluids". In: *Thermochimica Acta* 425.1-2 (2005), pp. 181–188.

[61] Peter Wasserscheid and Thomas Welton. *Ionic liquids in synthesis*. John Wiley & Sons, 2008.

[62] Ali Eftekhari. "Supercapacitors utilising ionic liquids". In: *Energy Storage Materials* 9 (2017), pp. 47–69.

[63] Linpo Yu and George Z Chen. "Ionic liquid-based electrolytes for supercapacitor and supercapattery". In: *Frontiers in chemistry* 7 (2019), p. 272.

[64] T Welton. "Ionic liquids in green chemistry". In: *Green Chemistry* 13.2 (2011), pp. 225–225.

[65] Alessandro Triolo et al. "Nanoscale segregation in room temperature ionic liquids". In: *The Journal of Physical Chemistry B* 111.18 (2007), pp. 4641–4644.

[66] MG Montalbán et al. "Effect of temperature, anion, and alkyl chain length on the density and refractive index of 1-alkyl-3-methylimidazolium-based ionic liquids". In: *Journal of Chemical & Engineering Data* 60.7 (2015), pp. 1986–1996.

[67] John D Holbrey, W Matthew Reichert, and Robin D Rogers. "Crystal structures of imidazolium bis (trifluoromethanesulfonyl) imide 'ionic liquid'salts: the first organic salt with a cis-TFSI anion conformation". In: *Dalton Transactions* 15 (2004), pp. 2267–2271.

[68] Thorben Sieling and Izabella Brand. "In Situ Spectroelectrochemical Investigation of Potential-Dependent Changes in an Amphiphilic Imidazolium-Based Ionic Liquid Film on the Au (111) Electrode Surface". In: *ChemElectroChem* 7.15 (2020), pp. 3233–3243.

[69] David B Cordes et al. "Ionic Liquid-Based Routes to Conversion or Reuse of Recycled Ammonium Perchlorate". In: *Chemistry–A European Journal* 15.48 (2009), pp. 13441–13448.

[70] Kostya S Novoselov et al. "Two-dimensional atomic crystals". In: *Proceedings of the National Academy of Sciences* 102.30 (2005), pp. 10451–10453.

[71] *Graphene – the perfect atomic lattice*. URL: `https://www.nobelprize.org/prizes/physics/2010/illustrated-information/`.

[72] Prakash R Somani, Savita P Somani, and Masayoshi Umeno. "Planer nano-graphenes from camphor by CVD". In: *Chemical Physics Letters* 430.1-3 (2006), pp. 56–59.

[73] Andre Konstantin Geim. "Graphene: status and prospects". In: *science* 324.5934 (2009), pp. 1530–1534.

[74] DV Badami. "X-ray studies of graphite formed by decomposing silicon carbide". In: *Carbon* 3.1 (1965), pp. 53–57.

[75] William S Hummers Jr and Richard E Offeman. "Preparation of graphitic oxide". In: *Journal of the american chemical society* 80.6 (1958), pp. 1339–1339.

[76] Golap Kalita and Masaki Tanemura. "Fundamentals of Chemical Vapor Deposited Graphene and Emerging Applications". In: *Graphene Materials-Advanced Applications* (2017).

[77] Abhijeet Ojha. "Two dimensional films and three-dimensional macro-structures from the aqueous dispersion of graphene oxide: Synthesis, rheology, and applications". PhD thesis. 2020.

[78] Daniel R Dreyer, Rodney S Ruoff, and Christopher W Bielawski. "From conception to realization: an historial account of graphene and some perspectives for its future". In: *Angewandte Chemie International Edition* 49.49 (2010), pp. 9336–9344.

[79] Zongyou Yin et al. "Graphene-based materials for solar cell applications". In: *Advanced energy materials* 4.1 (2014), p. 1300574.

[80] Usman Khan et al. "Graphene tribotronics for electronic skin and touch screen applications". In: *Advanced materials* 29.1 (2017), p. 1603544.

[81] Guangya Jiang et al. "An efficient flexible graphene-based light-emitting device". In: *Nanoscale Advances* 1.12 (2019), pp. 4745–4754.

[82] Fan Zhang et al. "A high-performance supercapacitor-battery hybrid energy storage device based on graphene-enhanced electrode materials with ultrahigh energy density". In: *Energy & Environmental Science* 6.5 (2013), pp. 1623–1632.

[83] Ulrich Hofmann and Rudolf Holst. "Über die Säurenatur und die Methylierung von Graphitoxyd". In: *Berichte der deutschen chemischen Gesellschaft (A and B Series)* 72.4 (1939), pp. 754–771.

[84] G Ruess. "Über das graphitoxyhydroxyd (graphitoxyd)". In: *Monatshefte für Chemie und verwandte Teile anderer Wissenschaften* 76.3-5 (1947), pp. 381–417.

[85] Werner Scholz and HP Boehm. "Untersuchungen am graphitoxid. VI. Betrachtungen zur struktur des graphitoxids". In: *Zeitschrift für anorganische und allgemeine Chemie* 369.3-6 (1969), pp. 327–340.

[86] Anton Lerf et al. "13C and 1H MAS NMR studies of graphite oxide and its chemically modified derivatives". In: *Solid State Ionics* 101 (1997), pp. 857–862.

[87] Heyong He et al. "A new structural model for graphite oxide". In: *Chemical physics letters* 287.1-2 (1998), pp. 53–56.

[88] Tamás Szabó et al. "Evolution of surface functional groups in a series of progressively oxidized graphite oxides". In: *Chemistry of materials* 18.11 (2006), pp. 2740–2749.

[89] Daniel R Dreyer, Alexander D Todd, and Christopher W Bielawski. "Harnessing the chemistry of graphene oxide". In: *Chemical Society Reviews* 43.15 (2014), pp. 5288–5301.

[90] Anton Lerf et al. "Structure of graphite oxide revisited". In: *The Journal of Physical Chemistry B* 102.23 (1998), pp. 4477–4482.

[91] Wenqin Wu et al. "Highly efficient removal of Cu (II) from aqueous solution by using graphene oxide". In: *Water, Air, & Soil Pollution* 224.1 (2013), p. 1372.

[92] Rafal Sitko et al. "Adsorption of divalent metal ions from aqueous solutions using graphene oxide". In: *Dalton transactions* 42.16 (2013), pp. 5682–5689.

[93] Andrew T Smith et al. "Synthesis, properties, and applications of graphene oxide/reduced graphene oxide and their nanocomposites". In: *Nano Materials Science* 1.1 (2019), pp. 31–47.

[94] Qi Qiao et al. "Graphene oxide model with desirable structural and chemical properties". In: *Carbon* 143 (2019), pp. 566–577.

[95] Igor Levchenko et al. "Scalable graphene production: perspectives and challenges of plasma applications". In: *Nanoscale* 8.20 (2016), pp. 10511–10527.

[96] Félix Mouhat, François-Xavier Coudert, and Marie-Laure Bocquet. "Structure and chemistry of graphene oxide in liquid water from first principles". In: *Nature communications* 11.1 (2020), pp. 1–9.

[97] Jaemyung Kim et al. "Graphene oxide sheets at interfaces". In: *Journal of the American Chemical Society* 132.23 (2010), pp. 8180–8186.

[98] Ayrat M Dimiev, Lawrence B Alemany, and James M Tour. "Graphene oxide. Origin of acidity, its instability in water, and a new dynamic structural model". In: *ACS nano* 7.1 (2013), pp. 576–588.

[99] Nathalie Bonatout et al. "How exfoliated graphene oxide nanosheets organize at the water interface: evidence for a spontaneous bilayer self-assembly". In: *Nanoscale* 9.34 (2017), pp. 12543–12548.

[100] Mi Wang. "Irradiated assisted corrosion of stainless steel in light water reactors-focus on radiolysis and corrosion damage". In: (2013).

[101] F Crumière et al. "LET effects on the hydrogen production induced by the radiolysis of pure water". In: *Radiation Physics and Chemistry* 82 (2013), pp. 74–79.

[102] Gérard Baldacchino et al. "Importance of radiolytic reactions during high-LET irradiation modalities: LET effect, role of O 2 and radiosensitization by nanoparticles". In: *Cancer Nanotechnology* 10.1 (2019), pp. 1–21.

[103] M Breitenkamp, A Henglein, and J Lilie. "Mechanism of the reduction of lead ions in aqueous solution (a pulse radiolysis study)". In: *Berichte der Bunsengesellschaft für physikalische Chemie* 80.10 (1976), pp. 973–979.

[104] Julien Grand et al. "Nanoparticle alloy formation by radiolysis". In: *The Journal of Physical Chemistry C* 122.24 (2018), pp. 12573–12588.

[105] P Radvanyi and MM Be. "The discovery of radioactivity; La decouverte de la Radioactivite". In: (1996).

[106] Pierre Curie and Andre Debierne. "Sur la radio-activité induite et les gaz activés par le radium". In: *Compt. rend* 132 (1901), pp. 768–770.

[107] Jay A LaVerne. "Radiation Chemistry: Yields of Chemical Species". In: ().

[108] Friedrich Giesel. "Ueber radium und radioactive Stoffe". In: *Berichte der deutschen chemischen Gesellschaft* 35.3 (1902), pp. 3608–3611.

[109] F Giesel. "Ueber den Emanationskörper aus Pechblende und über Radium". In: *Berichte der deutschen chemischen Gesellschaft* 36.1 (1903), pp. 342–347.

[110] John D Zimbrick. "Radiation chemistry and the Radiation Research Society: a history from the beginning". In: *Radiation research* 158.2 (2002), pp. 127–140.

[111] JP Keene. "Kinetics of radiation-induced chemical reactions". In: *Nature* 188.4753 (1960), pp. 843–844.

[112] Edwin J Hart and JW Boag. "Absorption spectrum of the hydrated electron in water and in aqueous solutions". In: *Journal of the American Chemical Society* 84.21 (1962), pp. 4090–4095.

[113] Jacqueline Belloni et al. "Radiation-induced synthesis of mono-and multi-metallic clusters and nanocolloids". In: *New Journal of Chemistry* 22.11 (1998), pp. 1239–1255.

[114] Virginie Trupin Wasselin. "Processus primaires en chimie sous rayonnement. Influence du transfert d'energie lineique sur la radiolyse de l'eau". PhD thesis. Paris 11, 2000.

[115] Louis Bondaz. "Formation de nano-objets métalliques par radiolyse d'ions en présence d'auto-assemblages de polyélectrolytes". In: (2018).

[116] Ahmet Uysal et al. “Reverse self-assembly:(111)-oriented gold crystallization at alkylthiol monolayer templates”. In: *Physical review letters* 107.11 (2011), p. 115503.

[117] S Cantin et al. “Observation of a two-step mechanism in the formation of a superstructure of cadmium-behenic acid Langmuir monolayer: Evidence of an intermediate structure”. In: *Physical Review E* 70.5 (2004), p. 050601.

[118] F Leveiller et al. “Crystallinity of the double layer of cadmium arachidate films at the water surface”. In: *Science* 252.5012 (1991), pp. 1532–1536.

[119] Vincent Dupres et al. “Superlattice formation in fatty acid monolayers on a divalent ion subphase: Role of chain length, temperature, and subphase concentration”. In: *Langmuir* 19.26 (2003), pp. 10808–10815.

[120] Sophie Cantin et al. “Evolution toward the X phase of fatty acid Langmuir monolayers on a divalent cation solution”. In: *Langmuir* 26.2 (2010), pp. 830–837.

[121] Alae El Haitami et al. “Inorganic mixed phase templated by a fatty acid monolayer at the air–water interface: the Mn and Mg case”. In: *Physical Chemistry Chemical Physics* 20.9 (2018), pp. 6629–6637.

[122] Jérémy Pignat. “Films cristallins organiques-inorganiques à l’interface eau-air”. PhD thesis. Cergy-Pontoise, 2006.

[123] Venkatramana Losetty, Cecilia Devi Wilfred, and M Chandra Shekar. “Synthesis and study of ionic interactions by volumetric, transport, FT-IR and computational methods of alkyl imidazolium acetate ionic liquid with molecular solvents (DMSO, DMF & EG) at T=(293.15–363.15) K”. In: *Journal of Molecular Liquids* 224 (2016), pp. 480–491.

[124] Chengna Dai et al. “Separation of benzene and thiophene with a mixture of N-methyl-2-pyrrolidinone (NMP) and ionic liquid as the entrainer”. In: *Fluid Phase Equilibria* 388 (2015), pp. 142–150.

[125] Dimitrios Konios et al. “Dispersion behaviour of graphene oxide and reduced graphene oxide”. In: *Journal of colloid and interface science* 430 (2014), pp. 108–112.

[126] JI Paredes et al. “Graphene oxide dispersions in organic solvents”. In: *Langmuir* 24.19 (2008), pp. 10560–10564.

[127] CMR. *Diméthylformamide - Site CMR*. URL: `https://www.substitution-cmr.fr/index.php?id=112&tx_kleecmr_pi3%5Buid%5D=196&tx_kleecmr_pi3%5Bonglet%5D=2&cHash=0394fe1c51`.

[128] The National Institute for Occupational Safety and Health (NIOSH). *Ethylene glycol*. URL: `https://www.cdc.gov/niosh/npg/npgd0272.html`.

[129] DDBST GmbH. *Vapor Pressure of N-Methyl-2-pyrrolidone*. URL: `http://www.ddbst.com/en/EED/PCP/VAP_C284.php`.

[130] Dannie C. Middleton. *Preventing Adverse Health Effects from Exposure to: Dimethylformamide (DMF)*. URL: `https://www.cdc.gov/niosh/docs/90-105/default.html`.

[131] Matthew J Large et al. “Understanding solvent spreading for Langmuir deposition of nanomaterial films: A Hansen solubility parameter approach”. In: *Langmuir* 33.51 (2017), pp. 14766–14771.

[132] Gholam R Vakili-Nezhaad, Hamid Modarress, and Gholam A Mansoori. "Solvent Extraction of Aromatic Components from Lube-Oil Cut by N-methylpyrrolidone (NMP)". In: *Chemical Engineering & Technology: Industrial Chemistry-Plant Equipment-Process Engineering-Biotechnology* 22.10 (1999), pp. 847–853.

[133] Frank Fusiak. *Method of activating N-methyl-2-pyrrolidone (NMP) varnish and paint remover solvents for removal of organic coatings*. US Patent 5,334,331. Aug. 1994.

[134] Mallikarjuna N Nadagouda and Rajender S Varma. "Green and controlled synthesis of gold and platinum nanomaterials using vitamin B2: density-assisted self-assembly of nanospheres, wires and rods". In: *Green Chemistry* 8.6 (2006), pp. 516–518.

[135] Matts Björck and Gabriella Andersson. "GenX: an extensible X-ray reflectivity refinement program utilizing differential evolution". In: *Journal of Applied Crystallography* 40.6 (2007), pp. 1174–1178.

[136] Tom Dyer, Ngamta Thamwattana, and Rouhollah Jalili. "Modelling the interaction of graphene oxide using an atomistic-continuum model". In: *RSC advances* 5.94 (2015), pp. 77062–77070.

[137] Jean-Noel Fuchs and Mark Oliver Goerbig. "Introduction to the physical properties of graphene". In: *Lecture notes* 10 (2008), pp. 11–12.

[138] Sasha Stankovich et al. "Graphene-based composite materials". In: *nature* 442.7100 (2006), pp. 282–286.

[139] Hin Chun Yau et al. "Sonochemical degradation of N-methylpyrrolidone and its influence on single walled carbon nanotube dispersion". In: *Chemical Communications* 51.93 (2015), pp. 16621–16624.

[140] Yanyu Liang et al. "Dispersion of graphene sheets in organic solvent supported by ionic interactions". In: *Advanced materials* 21.17 (2009), pp. 1679–1683.

[141] Xiangtao Bai et al. "Synthesis and characterization of microscale gold nanoplates using Langmuir monolayers of long-chain ionic liquid". In: *Crystal Growth and Design* 8.10 (2008), pp. 3840–3846.

[142] George H Vineyard. "Grazing-incidence diffraction and the distorted-wave approximation for the study of surfaces". In: *Physical Review B* 26.8 (1982), p. 4146.

[143] Magdolna Hargittai et al. "Molecular Structure, Bonding, and Jahn- Teller Effect in Gold Chlorides: Quantum Chemical Study of AuCl3, Au2Cl6, AuCl4-, AuCl, and Au2Cl2 and Electron Diffraction Study of Au2Cl6". In: *Journal of the American Chemical Society* 123.7 (2001), pp. 1449–1458.

[144] Atomistic Simulation Group in the Materials Department of Imperial College. *Database of Ionic Radii*. URL: `http://abulafia.mt.ic.ac.uk/shannon/ptable.php`.

[145] Nicolas Papaiconomou et al. "Efficient removal of gold complexes from water by precipitation or liquid–liquid extraction using ionic liquids". In: *Green chemistry* 14.7 (2012), pp. 2050–2056.

[146] Nicolas Papaiconomou et al. "Selective extraction of gold and platinum in water using ionic liquids. A simple two-step extraction process". In: *Dalton Transactions* 42.6 (2013), pp. 1979–1982.